Computational fluid-dynamics investigations of vortex generators for flow-separation control

by

Florian von Stillfried

Doctoral Thesis

Royal Institute of Technology School of Engineering Sciences Linné FLOW Centre Department of Mechanics SE - 100 44 Stockholm

Akademisk avhandling som med tillstånd av Kungliga Tekniska högskolan i Stockholm framlägges till offentlig granskning för avläggande av teknologie doktorsexamen onsdagen den 16 maj 2012 kl. 10:15 i F3, Lindstedtsvägen 26, Kungliga Tekniska högskolan, Stockholm.

©Florian von Stillfried, maj 2012 US–AB, Stockholm 2012

Abstract

Many flow cases in fluid dynamics face undesirable flow separation due to adverse pressure gradients on wall boundaries. This occurs, for example, due to geometrical reasons as in a highly curved turbine-inlet duct or on flow-control surfaces such as wing trailing-edge flaps within a certain angle-of-attack range. Here, flow-control devices are often used in order to enhance the flow and delay or even totally eliminate flow separation. Flow control can e.g. be achieved by using passive or active vortex generators (VGs) for momentum mixing in the boundary layer of such flows. This thesis focusses on such passive and active VGs and their modelling for computational fluid dynamics investigations.

First, a statistical VG model approach for passive vane vortex generators (VVGs), developed at the Royal Institute of Technology Stockholm and the Swedish Defence Research Agency, was evaluated and further improved by means of experimental data and three-dimensional fully-resolved computations. This statistical VVG model approach models those statistical vortex stresses that are generated at the VG by the detaching streamwise vortices. This is established by means of the Lamb-Oseen vortex model and the Prandtl lifting-line theory for the determination of the vortex strength. Moreover, this ansatz adds the additional vortex stresses to the turbulence of a Reynolds-stress transport model. Therefore, it removes the need to build fully-resolved threedimensional geometries of VVGs in a computational fluid dynamics mesh. Usually, the generation of these fully-resolved geometries is rather costly in terms of preprocessing and computations. By applying VVG models, the costs are reduced to that of computations without VVGs. The original and an improved calibrated passive VVG model show sensitivity for parameter variations such as the modelled VVG geometry and the VVG model location on a flat plate in zero- and adverse-pressure-gradient flows, in a diffuser, and on an airfoil with its high-lift system extracted. It could be shown that the passive VG model qualitatively and partly quantitatively describes correct trends and tendencies for these different applications.

In a second step, active vortex-generator jets (VGJs) are considered. They were experimentally investigated in a zero-pressure-gradient flat-plate flow at Technische Universität Braunschweig, Germany, and have been re-evaluated for our purposes and a parameterization of the generated vortices was conducted.

Dependencies of the generated vortices and their characteristics on the VGJ setup parameters could be identified and quantified. These dependencies were used as a basis for the development of a new statistical VGJ model. This model uses the ansatz of the passive VVG model in terms of the vortex model, the additional vortex-stress tensor, and its summation to the Reynolds stress tensor. Yet, it does not use the Prandtl lifting-line theory for the determination of the circulation but an ansatz for the balance of the momentum impact that the VGJ has on the mean flow. This model is currently under development and first results have been evaluated against experimental and fully-resolved computational results of a flat plate without pressure gradient.

Descriptors: flow-separation control, vane vortex generator, vortex generator jet, zero-pressure-gradient turbulent boundary layer, adverse-pressure-gradient turbulent boundary layer, statistical modelling, turbulence, Reynolds stress-transport model, computational fluid dynamics

Preface

This doctoral thesis is written within the area of fluid mechanics and mainly investigates computational studies regarding vortex generators. In particular, this thesis examines statistical vortex-generator models which were applied in wall-bounded turbulent flows. One main focus of this work was a thorough evaluation study of passive vortex-generator models and its application in zero-and adverse-pressure-gradient flat-plate boundary-layer flows, in asymmetric diffuser flow, as well as on an airfoil with a deployed short-chord flap. Another main focus of this contribution was to parameterize and model the vortices from vortex-generator-jet experiments that were carried out at Technische Universität Braunschweig, Germany, and to determine the model parameter dependencies on the experimental vortex-generator-jet setup parameters. As a result, a new formulation for a statistical vortex-generator-jet model was derived and evaluated against experimental and fully-resolved computational results.

This thesis is subdivided into two parts. In the first part, background on vortex generators, the governing equations, the basic concepts and methods for the statistical-modelling approach, and a short discussion of selected results are presented. The second part of this thesis includes in total four journal papers, three of them either published or accepted for publication, and which are adjusted to comply with the present thesis format, as well as one conference proceedings paper. A digital version of this thesis is available for download on the KTH library homepage on http://www.kth.se/en/kthb.

Stockholm, May 2012 Florian von Stillfried

V



Contents

Abstract	iii
Preface	v
Part I. Overview and summary	
Chapter 1. Introduction	1
Chapter 2. Background	4
2.1. Passive Vane Vortex Generators	4
2.2. Active Vortex Generator Jets	7
Chapter 3. Governing Equations	10
Chapter 4. Vortex Generator Modelling	13
4.1. Existing Vane Vortex Generator Models	13
4.2. User Challenges of VG Models	15
4.3. Statistical Vortex Generator Models	16
4.4. Statistical Vane Vortex Generator Model	19
4.5. Statistical Vortex Generator Jet Model	24
Chapter 5. Selected Results and Discussion	28
5.1. Original VVG Model in APG Flat-Plate Flow	28
5.2. Comparison of the VVG models	28
5.3. VVG Model Applications	32
5.4. Parameterization of VGJ Experiments	34
5.5. Evaluation of the Statistical VGJ Model	36
Chapter 6. Summary of Appended Papers	39
Chapter 7. Concluding Remarks and Outlook	43
Chapter 8. Papers and Authors' Contributions	45

Acknowledgements	48
References	50
Part II. Papers	
Paper 1. Vortex-Generator Models for Zero- and	
Adverse-Pressure-Gradient Flows	57
Paper 2. Evaluation of a Vortex Generator Model in	
Adverse Pressure Gradient	
Boundary Layers	89
Paper 3. Evaluating and Parameterizing Round	
Vortex-Generator Jet Experiments	
for Flow Control	121
Paper 4. A Statistical Vortex-Generator-Jet Model for	
Turbulent Flow-Separation Control	157
Paper 5. Application of a Statistical Vortex Generator	
Model on the Short-Chord Flap of a	
Three-Element Airfoil	183

Part I Overview and summary

CHAPTER 1

Introduction

The demand to design more efficient flow-separation control systems such, for example, new high-lift configurations for future aircraft which enable better low-speed behaviour during takeoff and landing, increased safety, and less environmental impact is becoming more important for the aircraft industry. At the same time, reduction of the complexity of existing flow-separation control systems is not only a trend but necessary in order to, for the example of a high-lift system, advance flight safety, reduce overall weight, lower fuel emissions, increase the operating distance, just to mention a few. For this case, it can be stated that the high-lift system has a meaningful impact on the total performance of the aircraft, economically as well as ecologically. Not only the aircraft industry faces such demands, other industries that develop and use fluid-mechanical processes are constantly in the need to improve products to either be and remain competitive, and/or to fulfil legal requirements as, for example, certification processes due to changing regulations on different markets throughout the world.

Flow-separation control can be a very effective way for improving existing fluid-dynamical systems, and a powerful tool in the conceptual design process from the very beginning of a product-development cycle. The term "flow-separation control" in fluid dynamics is generally used when a wall-bounded fluid flow is modified by flow-separation-control devices such as, for example, vortex generators (VGs). The general benefit from applying VGs in wall-bounded flows is a possible delay and/or prevention of boundary-layer separation and thereby, an increase of the overall system efficiency. In the limit of the operational envelope, fluid-dynamical systems may not perform properly without flow-separation control.

When flow-separation control is necessary, equipping control surfaces with VGs is a common procedure; see figures 1.1 and 1.2. Such VGs mix the fluid near those surfaces and push higher-momentum-containing fluid closer towards the wall, and vice versa. This increases the near-wall velocity and the near-wall momentum, and consequently the stability of the flow in terms of separation delay and/or prevention. During a product-development phase, an increasing amount of computational analysis is used nowadays, and VGs generally have the disadvantage of being computationally costly and time-consuming when included in a detailed analysis. Computational grids often fully resolve VGs, leading to a large amount of additional nodes in their vicinity, which causes

1

2 1. INTRODUCTION



FIGURE 1.1. Deployed flaps and spoilers uncover VGs close to the leading edge on a flap during landing.



FIGURE 1.2. VGs against buffeting effects on a main wing during cruise flight.

high computational costs. Therefore, VGs are often neglected in computational analyses. In a later stage during an experimental evaluation, VGs are, on the other hand, often included in for example wind- or water-tunnel investigations so that their impact can be studied thoroughly. This is a disadvantage for the product-design process that may benefit from a detailed computational analysis from the very beginning of the product-development cycle.

Different techniques to include VGs in computations are typically used: fully-resolved, partly-resolved, and fully-modelled approaches exist. Fully-resolved three-dimensional VGs and corresponding vortex structures are fully

embedded in the computational mesh, typically leading to very fine mesh sizes in their vicinity. Partly-resolved approaches model the VGs by, for example, volume forces that are added to the governing equations. Still, the generated vortex structures need to be fully resolved and a high mesh density, comparable to the fully-resolved approach, is needed downstream of the VGs. Fully-modelled approaches go one step further: they also model the generated vortex structures downstream of the modelled VGs. This approach further reduces the mesh size compared to the partly-resolved approach. Nevertheless and due to the increased modelling, it is necessary to further verify results for the partly- and the fully-modelled approaches by means of comparisons against experimental and/or fully-resolved computational results.

This thesis mainly discusses the development and evaluation of fully-modelled VG models for passive and active flow-separation control and provides comparative studies regarding fully-resolved computational analyses and experiments. It includes the application and the evaluation of a statistical method that may be used for including VGs in a computational analysis during the early design process. A considerable advantage of the statistical method is that it removes the actual need to include VG geometries and vortex structures within a computational grid. Normally, this leads to a significant larger number of nodes and thus, longer preprocessing, computation and postprocessing time. Instead, the physical impact of the vortices on the mean flow in terms of additional vortex stresses is modelled. This results in negligible additional computational costs when compared to computations without flow-separation control, but to tremendous savings when compared to three-dimensional computations with fully-resolved VGs.

CHAPTER 2

Background

Vortex generators generate streamwise vortex structures that typically mix the boundary layer in wall-bounded flows. This increases the mean-streamwise velocity near the wall, as well as an average momentum transport towards it. As a result, the boundary-layer velocity profile becomes fuller where high-momentum fluid is pushed towards the wall and less full where it is pushed away. In total, VGs maintain the flow to be more stable by boundary-layer mixing processes, resulting in delayed or even prevented boundary-layer separation. In the following, previous findings from research regarding passive and active VGs are presented.

2.1. Passive Vane Vortex Generators

For quite some time, passive vane vortex generators (VVGs) have been used in order to control flow separation. "Passive" refers to VGs that generate a streamwise vortex without requiring additional external energy. However, the additional benefit of using passive VVGs generally comes along with a somewhat increased overall drag. A way to avoid this drag penalty is to use VVGs that can be retracted when not needed, as can be seen for the adjustable control surfaces in figure 1.1. The presence of parasitic drag is a tradeoff situation for the designer, whereas it is not easy to predict drag penalties and the disadvantages of a fixed passive VVG system a priori. Typically, VVGs are installed normal to the surface, with a vane angle of incidence α towards the mean-flow direction. Flow-separation control with passive VVGs is by far the cheapest and fastest way to equip solid bodies and is therefore widely used in aeronautics and related industries nowadays. Many different research groups have evaluated VVGs experimentally and by means of computations, and it is well-proven that these devices can efficiently increase the overall performance of fluid-mechanical systems.

Pearcey (1961) suggested certain design criteria for successful boundary-layer flow control with VVGs. His studies encompassed different VVG designs as for example corotating and counter-rotating VGs, multiple-row systems, and VVGs of different geometries; see also figure 2.1. "Counter-rotating" setups, see figure 2.2(a), typically contain VVG pairs with vanes mounted in a mirror-inverted manner so that vortices with opposite-rotational directions are generated. This arrangement is common for the application of flow-separation control in two-dimensional flows when the spanwise velocity component is zero,

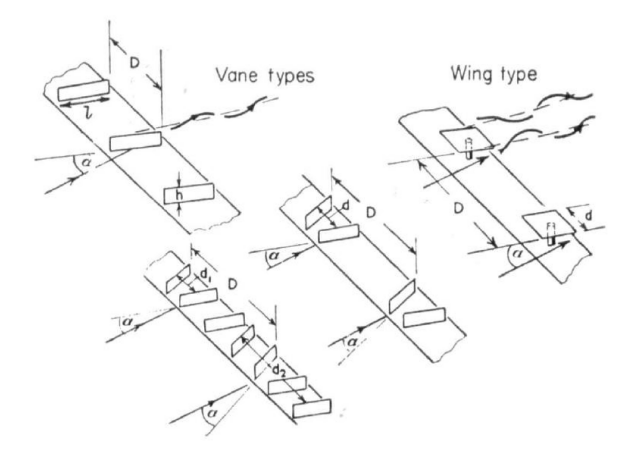


FIGURE 2.1. Types and notation of Pearcey's VVGs. [From Pearcey (1961).]

also used in this thesis. In contrast to that are "co-rotating" setups, see figure 2.2(b), where VVG vanes are installed in the same manner regarding α and therefore, produce vortices with the same rotational directions. This arrangement is typically found in three-dimensional flows on, for example, highly swept aircraft wings with strong cross-flows. Pearcey investigated parameters like the distance D between neighbouring VVG pairs, the distance d between two VVG vanes of a VVG pair, the VVG chord c^1 , and the vane angle of incidence α . By that, Pearcey carried out one of the most important studies for passive VVGs already more than 50 years ago.

More recent studies (Lin 2002; Yao et al. 2002) have shown that so-called subboundary-layer VVGs (SBVGs) have major advantages compared to standard VVGs with vane heights in the order of the local boundary-layer thickness δ_{99} , i.e., $h_{\rm VG}/\delta_{99}\approx 1$. SBVGs have a typical device height of $0.1\leq h_{\rm VG}/\delta_{99}\leq 0.5$, thus mixing the mean-flow momentum only within the boundary layer. This has been shown to be very efficient compared to standard VVGs. The VVGs which were studied in this thesis can be considered as SBVGs (although, $h_{\rm VG}/\delta_{99}\approx 0.65$ for the defined baseline VVG position in von Stillfried et al. (2011b,a)). A VVG streamwise-position variation study increased the ratio $h_{\rm VG}/\delta_{99}$ upstream of the baseline VVG position, and a decrease in skin-friction results could be observed, basically confirming Lin's findings.

A comprehensive research study for passive VVGs with counter- and corotating setups was carried out by Godard & Stanislas (2006) which was partly based on the findings from Lin (2002). Their motivation was to describe optimal parameters for VVGs for the flow over a bump, similar to the suction

¹In this thesis, c is defined as the streamwise projected VVG chord, i.e., the length of the chord along the VVGs becomes $c/\cos\alpha$.

6

side of an airfoil. For that, they studied previous results by several research groups and started from the optimal parameters given in Lin $et\ al.\ (1991)$. By successively varying the VVG parameters and measuring the overall performance in terms of skin-friction distributions at two spanwise symmetry planes, they could define optimum settings both for the counter- and the corotating systems. In terms of $h_{\rm VG}$, Godard & Stanislas identified that the skin-friction distributions increased with increasing $h_{\rm VG}$, which is in contrast to some results in existing literature. As a result of the study, Godard and Stanislas found that "the counter-rotating configuration is twice as efficient as the corotating one, which is already quite efficient". The setup for the optimum counter-rotating case by Godard & Stanislas is very close to the setup used by Lögdberg $et\ al.\ (2009)$ in the two-dimensional flat-plate boundary-layer experiments that were also utilized in the present work.

Pauley & Eaton (1988) have experimentally investigated VVG pairs and arrays with a ratio $h_{\rm VG}/\delta_{99}=1.5$, mounted in a zero-pressure-gradient (ZPG) flat-plate boundary layer, and mainly investigated spanwise vorticity contours. Different VVG setups were examined, as for example counter-rotating commonflow-up/down, pairs with different height ratios $h_{\rm VG}/\delta_{99}$, corotating and alternating arrays. They varied the angle of incidence α as well as the spacing d, and could show that a strong interaction of neighbouring vortices (for example, common-flow-up settings) caused a decrease of peak vorticity, whereas the streamwise development of the vortex circulation was primarily connected to the interaction with the wall and thus, skin friction. Vortices that were located closer to the wall (for example, counter-rotating common-flow-down setups) caused a larger skin-friction variation which, in turn, diminished the circulation. A conclusion of their work is that VVG pairs should be arranged in such a way that they produce common-flow-down vortex structures which could be confirmed by the results given in this thesis. Furthermore, corotating VVG

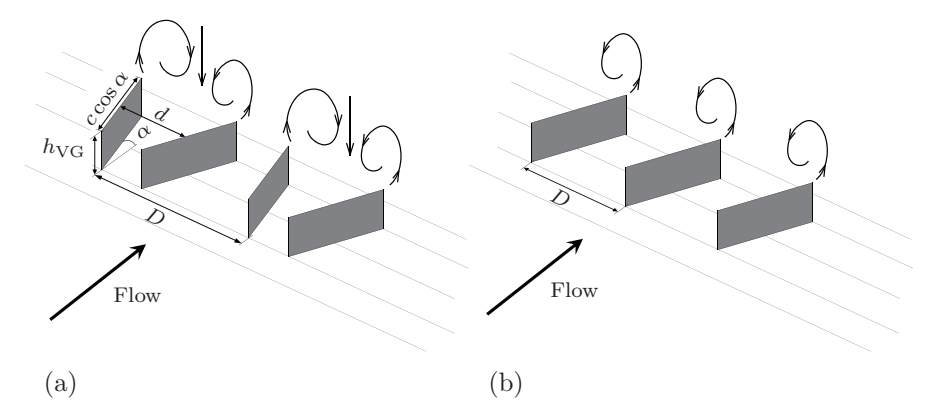


FIGURE 2.2. VVG setups and the notation that is used in this thesis: (a) counter-rotating common-flow-down, and (b) corotating (d=0) configurations.

arrays should provide a certain minimum distance D because vortex velocities may cancel out each other if VVGs are located too closely to each other.

Another interesting work was published by Barth et al. (2011), who have examined a dynamical VVG system which deploys/retracts the VVG actuators at very high frequencies. Their motivation was to investigate high-frequency and dynamically-retractable VVGs due to the general setup limitations for high-frequency blowing by active vortex-generator jets. Barth et al. (2011) could for example show that the dynamic VVGs mix the boundary layer by large-scale momentum and not as an effect of the turbulence scales, which supports the findings of Ortmanns & Kähler (2007) for vortex-generator jets; see also section 2.2. These results form an important information for the statistical modelling approaches which utilize the findings of Ortmanns & Kähler (2007) and Barth et al. (2011). Basically, it was shown that flow-separation is established by the large-scale momentum mixing from the streamwise vortices, and this concept is used for the statistical VG models which are presented in this thesis.

2.2. Active Vortex Generator Jets

Even though the concept of active flow control was investigated already as early as in the middle of the 20th century, it has only become more popular in the research community during the last 25 years. Unlike passive VVGs, active VGJs usually do not include any geometrical structures which penetrate from the surface into the mean flow. This has the advantage that VGJs do not contribute to parasitic drag in contrast to permanently deployed VVGs. Moreover, VGJs have the option to be activated when flow-separation control is needed, and to be deactivated when flow control is not needed. This feature makes this concept highly flexible and efficient.

VGJs create vortices by means of an injected jet with a velocity U_{VGJ} which enters the boundary-layer flow through the actuator exit of diameter Φ_{VGJ} in a direction characterized by the pitch and skew angles α and β , respectively; see figure 2.3. It is observed that, in this work, the skew angle $\beta=0^{\circ}$ is defined in the upstream direction. The jet injection is enabled by means of continuous or pulsating jet blowing. The higher amount of possible setup-parameter combinations make active VGJs, compared to passive VVGs, more complicated and time-consuming to investigate. This is one of the practical reasons for the dominance of experimental investigations in contrast to a smaller amount of computational studies.

Selby et al. (1992) present an important parametric study for co- and counter-rotating VGJ arrays, and a variation of the VGJ parameters $\alpha=15^{\circ}$ to 90°, $\beta=90^{\circ}$ to 180°, $\Phi_{\rm VGJ}=0.8$ to 4.8 mm, and the velocity ratio $\lambda=U_{\rm VGJ}/U_{\infty}=0.6$ to 6.8. The study has shown by means of pressure-distribution plots that increasing λ generally increased the performance of the flow-control system, which can be confirmed by the findings of an increase in vortex stresses for growing λ in this thesis; see appended Paper 4. In the same

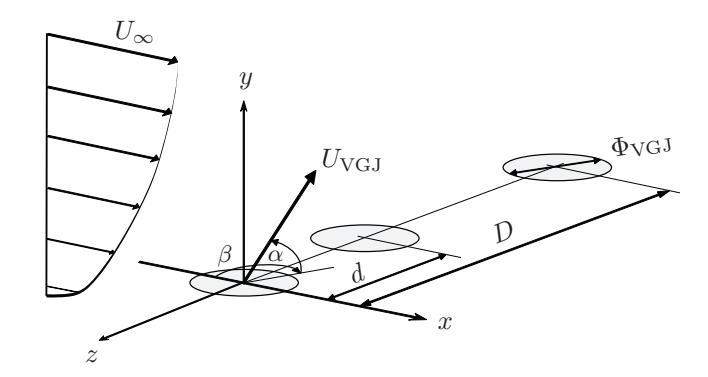


FIGURE 2.3. The VGJ actuator geometry and parameters, also showing the additional symmetry parameters d and D for pair and array configurations.

manner, Selby et al. (1992) demonstrated that efficiency increased with increasing α up to 25°, as well as for decreasing β to values between 90° and 120°. Moreover, counter-rotating VGJ arrays showed to have inferior performance when compared to corotating systems.

Also Johnston & Nishi (1990) have studied configurations of skewed and pitched co- and counter-rotating round VGJ arrays. It could be shown for $\beta = 90^{\circ}$, that the generated streamwise vortices were similar to those from passive VVGs, that the mixing in the boundary layer was associated with the streamwise vortices, and that the vortices successfully eliminated regions of separation. These findings support the similar vortex modelling ansatzes for the VVG and the VGJ models in this thesis. Johnston & Nishi (1990) showed that vortices from VGJs tended to dissipate faster than those from passive VVGs. Compton & Johnston (1992) showed that β between 90° and 135° maximized the vorticity of the streamwise vortex, and that the vortices were comparable to weak vortices from VVGs for velocity ratios $\lambda = 0.7$ to 1.3. In this thesis, it can be found that $\lambda = 2.5$ produces approximately equal strong VGJ vortex stresses when compared to the basic VVG setup by Lögdberg et al. (2009). On the other hand, increasing λ to 5.0 amplifies the vortex stresses by one order of magnitude, possibly providing advances for VGJ flow-separation control. Khan & Johnston (2000) investigated a smooth contoured actuatorexit nozzle and identified the strongest peak mean vorticity for $\lambda = 1.0$, $\alpha =$ 30° , and $\beta = 120^{\circ}$. They report a streamwise momentum defect in the vortex core and an increased turbulence level between the vortex and the wall. In another contribution, Johnston et al. (2002) investigated the effects of two different round actuator-inlet characteristics (the smooth-contoured actuator nozzle from Khan & Johnston (2000) and a sharp-edged inlet) on the vortex creation under identical boundary conditions. They showed the near-field charateristics for $x/\Phi_{VGJ} \leq 5$ of the sharp-edged inlet to be very different from the smooth-contoured inlet. This was probably due to the stalled region

which led to area blocking as well as to instabilities of the shear-layer inside the nozzle. A faster dissipation of the dominant vortex is the result, but the influence of the sharp edge damps out for $x/\Phi_{\rm VGJ}>10$, with results of both inlets becoming comparable to each other. The experimental results in this thesis provided two different inlet geometries for the single-jet (no duct) and the VGJ pair setup (sharp-edge duct). The findings of Johnston *et al.* (2002) are important for a valuation of results for different actuator inlet geometries, and for a sensitizing concerning the results interpretation.

Zhang & Collins (1997) investigated the near field behind a single round VGJ by means of mean-velocity contours and proposed $\alpha = 30^{\circ}$ and $\beta = 120^{\circ}$ for $\lambda = 1.0$ as suitable jet parameters, essentially in agreement with Khan & Johnston (2000). Zhang & Collins (1997) state that a single vortex was developed within $x/\Phi_{VGJ} \leq 10$, and that the vortex core moved away from the wall with increasing λ . Their findings are generally valid for the VGJ stress results from experiments; see appended Papers 3 and 4. Another important result was that they observed a significant influence of the freestream flow on the jet. Zhang (2003) investigated corotating VGJ arrays at $\alpha = 45^{\circ}$ and $\beta = 135^{\circ}$ with the same actuator type and the same boundary conditions as in Zhang & Collins (1997). Zhang claims that the vortices from the VGJ array had the same main characteristics compared to a single VGJ with a similar setup, and a similar presumption was made for the spanwise-averaged second-order statistics of single VGJ from experiments; cf. appended Paper 3. Moreover, Zhang states that, as a consequence of the vortex presence in the flow, turbulence production appeared to be the main mechanism to form the primary shear stresses.

Ortmanns & Kähler (2007) have examined single round VGJs in a watertunnel flat-plate turbulent boundary layer and have shown that the turbulent fluctuations are almost negligibly affected by the vortex structures. In particular, Ortmanns & Kähler state that the jet-boundary-layer interaction produced less turbulent fluctuations when compared to a free-jet flow. This is an important finding for the interpretations of results from experiments and computations. They conclude, similar to Barth et al. (2011) but in total contrast to Zhang (2003), that only the large-scale momentum transport was the origin of the mixing processes in the flow. Ortmanns (2008) and Mahmood & Radespiel (2009, 2011) investigated experimentally and computationally, respectively, the single round VGJ setup from Ortmanns & Kähler (2007). Ortmanns (2008) claimed that a fully-developed vortex was obtained for $\alpha = 45^{\circ}$ and $\beta = 90^{\circ}$ to 105° , but that a smaller pitch angle $\alpha = 30^{\circ}$ increased the overall flow-separation control performance. Ortmanns could show that increasing λ increased the vortex core wall-normal distance and radius in agreement with Zhang & Collins (1997). Moreover, Ortmanns (2008) showed that the vortex circulation was linearly dependent on λ .

CHAPTER 3

Governing Equations

This thesis covers to a large extent the concept, development and evaluation of statistical models for passive VVGs and active VGJs, complemented with computational investigations of fully-resolved flow-control devices. The computational investigations that are presented in this work rely on the RANS equations and therefore, a brief introduction of the governing flow equations is presented in this section. The incompressible turbulent flow is governed by the continuity equation and the Navier-Stokes equations that read

$$\frac{\partial u_i}{\partial x_i} = 0, (3.1)$$

$$\frac{\partial u_i}{\partial t} + u_j \frac{\partial u_i}{\partial x_j} = -\frac{1}{\rho} \frac{\partial p}{\partial x_i} + \frac{\partial}{\partial x_j} (2\nu s_{ij}), \tag{3.2}$$

with u_i and p as the instantaneous velocity and pressure fields, ρ and ν as the constant density and the kinematic viscosity, respectively. The instantaneous strain-rate tensor is denoted as $s_{ij} \equiv (u_{i,j} + u_{j,i})/2$. The strength of these equations is that they take all turbulence effects into account, from the smallest Kolmogorov scales up to the largest geometric flow scales. A direct-numerical solution (DNS) of equations (3.1) and (3.2) normally leads to an enormous amount of computational effort and thus, costs. Research is then mostly restricted to simple geometries and low-to-moderate Reynolds numbers, and thus has limited applicability for most engineering applications which often involve high Reynolds number turbulent flows. Therefore, statistical approaches are widely used, and the instantaneous flow-field variables are, for this purpose, decomposed into mean and fluctuating parts. The mean part is usually defined as the ensemble-average value over a large set of realizations, whereas the property of the fluctuating part is the vanishing ensemble-averaged value. According to this decomposition, see for example Pope (2000), the instantaneous velocity and pressure from equations (3.1) and (3.2) become

$$u_i = U_i + u_i', (3.3)$$

$$p = P + p', \tag{3.4}$$

denoting capital-letter quantities as the mean parts, and small-letter quantities with primes as the fluctuating parts. From the above definition of the

decomposition, it follows that the ensemble-averaged equations (3.3) and (3.4) read

$$\overline{u_i} \equiv U_i, \quad \overline{u_i'} = 0, \tag{3.5}$$

and

$$\overline{p} \equiv P, \quad \overline{p'} = 0.$$
 (3.6)

The decomposition of the instantaneous flow-field variables into a mean and a fluctuating part in equations (3.3) and (3.4) is commonly known as "Reynolds decomposition". Applying the Reynolds decomposition, i.e., plugging equations (3.3) and (3.4) into equations (3.1) and (3.2), followed by an ensemble-averaging yields the incompressible RANS mean-flow equations:

$$\frac{\partial U_i}{\partial x_i} = 0, (3.7)$$

$$\frac{\partial U_i}{\partial t} + U_j \frac{\partial U_i}{\partial x_j} = -\frac{1}{\rho} \frac{\partial P}{\partial x_i} + \frac{\partial}{\partial x_j} (2\nu S_{ij} - \overline{u_i' u_j'}), \tag{3.8}$$

where $S_{ij} \equiv (U_{i,j} + U_{j,i})/2$ defines the mean strain-rate tensor. By applying the Reynolds decomposition and multiplying equation (3.2) with the density ρ , the mean-flow momentum equation in equation (3.8) gains an additional turbulence-stress term $-\rho \overline{u'_i u'_j}$ on the right-hand side, known as the "Reynoldsstress tensor". It represents the additional internal turbulence stresses that emerge due to the velocity fluctuations and that act on the mean flow.

An equation for the Reynolds-stress tensor $-\rho \overline{u_i'u_j'}$ can be derived from the Navier-Stokes equations, but the problem lies in the generation of even higher-order moments like $\overline{u_i'u_j'u_k'}$. This is commonly called the "closure problem" of turbulence. Turbulence modelling is the art of finding additional equations for the Reynolds-stress term to close the system of equations, and to make it solvable. The aim is therefore to design a closed system of equations for the one-point quantities U_i , P and $\overline{u_i'u_j'}$. Therefore, the Reynolds-stress term needs to be modelled, containing only known quantities. The modelling of the Reynolds-stress tensor fills numerous books as well as journal papers, and is not part of this work and therefore not presented. From the existing modelling approaches, the concept of the differential Reynolds-stress model (DRSM) and the provision of transport equations for the individual tensor components is suitable for capturing their time and spatial development.

The Reynolds-stress-tensor transport equation is derived by means of subtracting equation (3.8) for the mean velocity U_i from equation (3.2) for the instantaneous velocity u_i . The resulting equation for $u'_i = u_i - U_i$ is then multiplied by u'_j , and combined with the corresponding equation with switched i and j indices. After averaging, we get

$$\frac{D\overline{u_i'u_j'}}{Dt} = \mathcal{P}_{ij} - \epsilon_{ij} + \Pi_{ij} + \mathcal{D}_{ij}. \tag{3.9}$$

The terms on the right-hand side of equation (3.9) represent the turbulence production tensor \mathcal{P}_{ij} , the dissipation-rate tensor ϵ_{ij} , the pressure strain-rate tensor Π_{ij} , and the turbulence diffusion \mathcal{D}_{ij} , respectively. Turbulence modelling is needed for the latter three terms, whereas the production tensor \mathcal{P}_{ij} is explicitly given if $u'_i u'_j$ is known:

$$\mathcal{P}_{ij} \equiv -\overline{u_i'u_k'}\frac{\partial U_j}{\partial x_k} - \overline{u_j'u_k'}\frac{\partial U_i}{\partial x_k},\tag{3.10}$$

and rotational mean-flow effects enter equation (3.10) naturally, providing a major advantage over, for example, simpler eddy-viscosity models. As stated before, the remaining three terms on the right-hand side in equation (3.9) need to be modelled, where the major challenge lies on the model for the redistributive pressure strain-rate tensor Π_{ij} , leading to various DRSM approaches in the literature. The interested reader is referred to relevant text books on the topic; see for example Wilcox (1988), or Pope (2000). The concept of the statistical VG modelling approach, which is based on the transport equation for $\overline{u_i'u_j'}$ and an extension for the Reynolds-stress tensor, is described in detail in section 4.3.

CHAPTER 4

Vortex Generator Modelling

4.1. Existing Vane Vortex Generator Models

Since the inclusion of VGs in a computational mesh is a rather cumbersome and time-consuming procedure, several research teams have developed models for passive VVGs in order to circumvent these difficulties. To my knowledge, the first work on VVG modelling, which is fully-integrated in a Navier-Stokes solver, was published by Bender et al. (1999) and is referred to as the Bender-Anderson-Yagle (BAY) VVG model in this thesis. As Bender et al. point out, only "the large-scale effects induced on the secondary flow by the vortex generators are of interest" for the designer of fluid-mechanical systems that use VVGs. A modelling approach that solely takes these large-scale effects into account is therefore assumed to be sufficient to model VVGs with much less computational effort and time. The BAY model is based on relations between the local flow-field primitive parameters and the geometrical-setup parameters of the VVG and it uses volume side lift forces L_i which substitute the resolved VVG geometries in a computational grid. The volume forces L_i , which describe the lift that originates from the modelled VVGs, are based on the lifting-line theory (LLT) by Prandtl (1921). The modelled forces are then applied on chosen cells V_i in the computational mesh. They represent the influence region of the modelled VVGs, and act perpendicular to the freestream and parallel to the wall. The volume cells V_i , which represent the forcing region for the BAY model, need to be specified manually. Therefore, the cell coarseness, and the fineness of the VVG-covering grid is given by the user. In particular, Bender et al. (1999) report the option to include L_i in small clustered cell regions for isolated VVGs, up to an entire spanwise field of cells for a tight array of VVGs with a small spanwise symmetry distance D. It is mentioned that the BAY model also includes an empirical calibration constant c_{BAY} . Bender et al. describe a dependency of results on the total number of grid cells $\Sigma V_i = V_M$ that represent the modelled VVGs (linear mode), as well as a dependency on the absolute value of c_{BAY} (asymptotic mode).

Dudek (2011) implemented the BAY model into the Wind-US Navier-Stokes solver, and could achieve good results when compared to fully-gridded VVG data and to experiments for a single VVG in a subsonic ZPG boundary layer, for a VVG array in a circular S-duct, and for counter-rotating VVG pairs in supersonic boundary-layer flow.

Jirásek (2005) presented a further development of the BAY model, calling it jBAY model. The proposal removes the need for user inputs regarding the definition of the cell volumes V_i that contain the original resolved VVG structures. Using the original BAY model could be cumbersome because VVGs can be very thin structures and it might be difficult to define the correct volume cells V_i . The dependency on the constant c_{BAY} may also involve further difficulties in obtaining a reliable model setup. VVG arrays in the original BAY model asymptotic mode are regarded as one large single VVG which covers the corresponding spanwise domain. The force L_i is applied on each grid point which is included in the volume for the modelled "single" VVG. For the case of VVG arrays, Jirásek (2005), in contrast to Bender et al. (1999), suggests the jBAY model that applies a spanwise-distributed lift force L_i on specific grid points. For that, the VVGs are considered to be infinitely thin structures which cut the mesh cells and edges, creating new grid points at intersections. The resulting volume force is projected to only these newly created grid points to reduce the application of the lifting-force terms. Jirásek tested the jBAY model with a universal constant $c_{\text{BAY}} = 10$ on three different cases and achieved excellent agreement of results when compared to fully-resolved VVG computations and experimental data. Therefore, the uncertainties connected to the original BAY model was removed by the jBAY model. Still, the flow structures downstream of the VVG forcing plane need to be resolved properly in order to achieve good results.

Wendt (2004) presented an emprical VVG model approach by means of a parameterization study for passive VVGs. Wendt carried out his research in a straight pipe turbulent boundary layer with VVGs either mounted in a single configuration or, in case of arrays, evenly distributed along a circumferential row at a constant streamwise position. The arrays investigated were both of corotating and of counter-rotating (including common-flow-down/up settings) types. His results cover an extensive study of the geometrical VVG setup as well as the general flow setup. It was shown that counter-rotating VVG arrays performed better when compared to a single VVG and found out that a corotating setup gave poorer results than a single VVG. Wendt used his results as a basis for developing a VVG model. By using the Lamb-Oseen vortex model and the LLT, he was able to model the streamwise peak vorticity ω_z and the vortex circulation Γ . The model results presented by Wendt (2004) show a very good agreement when compared to experiments with single VVGs.

Dudek (2006) implemented Wendt's model into the Wind-US Navier-Stokes solver. She evaluated Wendt's VVG model by means of VVG arrays in several different flow cases. The model results were compared to results from fully-resolved VVG computations and to experimental results. The conclusion of her work was that the empirical VVG model generated overall satisfactory results and could confirm the findings of Wendt (2004).

Another approach was presented by Gleyzes & Pailhas (2011), who have used the original BAY model for a triangular passive VVG to mimic an active

VGJ. Therefore, they had to find reasonable parameter values for the BAY-modelled VVG that created a comparable vortex from a VGJ. Whereas the VGJ actuator's setup was amongst others defined by $\alpha=30^\circ$, and the BAY-modelled equivalent VVG was found to give comparable results for an angle of incidence $\alpha=45^\circ$. Near-field data show differences in results due to the different vortex generation by VVGs and VGJs. Nevertheless, results in the far field show a fairly good agreement between the BAY-modelled VVGs, experiments, as well as computations with fully-gridded VGJs. Finally, Gleyzes & Pailhas (2011) state that there is no high sensitivity of the BAY model results for a VVG- α -range of $\pm15^\circ$ at such high α as 45°. In total, they experienced heavily reduced global CPU time, especially when taking the parameter variation study into account, and showed that the BAY model for passive VVGs could in principle be used for an analysis of active VGJs.

4.2. User Challenges of VG Models

The expression "VG modelling" already implies that the flow physics, which is predominating in such fluidic flows, is not realisticly captured. Instead, a general modelling approach reduces the physical description in such a way that results become satisfactory with the benefits of simpler preprocessing and reduced CPU time. Furthermore, VG models are used in combination with RANS turbulence models that already model the mean-flow characteristics and properties, and this reduces result accuracy per se. Moreover, VG modelling results strongly depend on the specific modelling concept. This could be observed in the foregoing section where the VVG model results from different sources have been compared to either experiments, and/or fully-resolved VVG computations. These approximated results have shown to be often very sactisfactory for the presented cases. Nevertheless, it remains unclear if the introduced VVG models could be able to predict different, or even more complicated flows, as well as a wide setup-parameter range reasonably correct. Unfortunately, the user of such VG models can never be totally confident about the computational results, at least unless a certain experience for the specific VG model and/or reference data from corresponding experiments exist. The long-term goal of VG modelling research is to elimante the latter issue, giving the user a more or less universal tool for a-priori-analyses of applied flow-separation control.

On the other hand, VG models involve many advantages in a computational analysis as mentioned previously. Parameter variations become less time-consuming due to reduced preprocessing complexity, as well as heavily reduced total computer processing times. Moreover, computational analyses using the same VG model make it possible to draw conclusions regarding the relative change in results, enabling the determination of trends and tendencies when setup parameters change.

4.3. Statistical Vortex Generator Models

This thesis deals mainly with two different statistical VG model approaches for passive and active flow-separation control. The two VG models are based on the formation of so-called additional vortex stresses that originate from the vortices. Before it is possible to determine these stresses, the vortex velocities that represent the actual generated vortices need to be modelled first. For that, a vortex model is required that makes it possible to analytically determine the vortex velocities for a specific VG setup. The Lamb-Oseen vortex model is used in this thesis, and it contains the following parameters: the vortex circulation Γ_{max} , the viscous core radius r_0 , and the vortex core location (h_c/z_c) . Based on the modelled vortex velocities, their spanwise-averaged second-order statistics, reading $\overline{V_iV_j}(y,z)$, can be determined. As a result, the $\overline{V_iV_j}(y,z)$ tensor can be used as an additional forcing term in the RANS momentum equation.

The principle difference between the VVG and the VGJ models, that are presented in the following sections, is the ansatz for the determination of the Lamb-Oseen vortex-model input paramaters $\Gamma_{\rm max}$ and r_0 , because VVGs and VGJs generate vortices in different ways. In this section, it is explained how the total vortex-velocity field $V_i(y,z)$ for a spanwise modelled VG array with a large number of VGs is treated in the turbulence description of a computational analysis, and how the additional vortex stress tensor is formed and finally added to the Reynolds-stress tensor.

4.3.1. Lamb-Oseen Vortex Model

The Lamb-Oseen vortex model was chosen for the statistical-modelling approach for passive VVGs and active VGJs since it has shown to model the cross-plane components $[V_y, V_z](y, z)$ for streamwise vortices reasonably well. The resulting vortex-velocity field in the radial direction reads

$$V_{\Phi}(r) = \frac{\Gamma_{\text{max}}}{2\pi r} \left[1 - e^{-\left(\frac{r}{r_0}\right)^2} \right], \tag{4.1}$$

with $\Gamma_{\rm max}$ for the vortex circulation, r_0 for the vortex core radius, and $r=\sqrt{\left(y-h_{\rm c}\right)^2+\left(z-z_{\rm c}\right)^2}$ is the radial distance from the vortex core $(h_{\rm c},z_{\rm c})$ in cartesian coordinates. As mentioned previoulsy, the two different VG models for passive VVGs and for active VGJs require different ansatzes for $\Gamma_{\rm max}$, r_0 and $(h_{\rm c},z_{\rm c})$. The details about how the specific vortex-model parameters are determined are given in sections 4.4 and 4.5.

After determining $\Gamma_{\rm max}$, r_0 and $h_{\rm c}$, the resulting induced VG array velocity field $V_i(y,z)$ is identified by means of a superposition of each single vortex-velocity field $V_{\Phi}(r)$ and its corresponding mirror image; see also figure 4.1. In order to obtain the additional turbulent vortex stresses for the statistical VG models, the induced velocity field $V_i(y,z)$ is split into its velocity components $V_y(y,z)$ and $V_z(y,z)$ in the wall-normal and the spanwise direction, respectively $(V_x=0)$ due to the choice of the two-dimensional Lamb-Oseen vortex model).

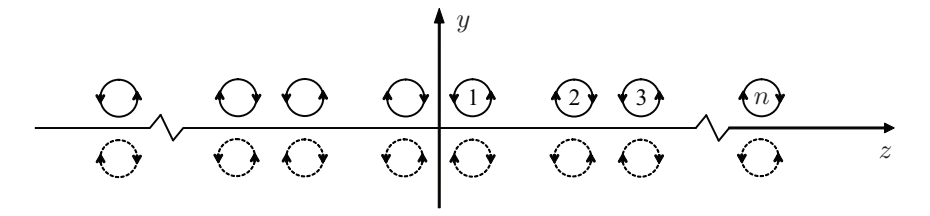


FIGURE 4.1. VG model forcing plane: vortex array with n VG pairs and mirror images for the analysis of the superimposed vortex-velocity field $V_i(y, z)$ from equation (4.2). [Image inspired by Törnblom & Johansson (2007).]

According to Törnblom & Johansson (2007), the velocity components for a counter-rotating common-flow-down VG array setup read

$$[V_x, V_y, V_z](y, z) = \sum_{n=1}^{\infty} (-1)^{n+1} \sum_{m=1}^{4} (-1)^{m+1} \frac{V_{\Phi}(r_m)}{r_m} [0, \Delta z_m, -\Delta y_m], \quad (4.2)$$

where

$$r_m = \sqrt{\Delta y_m^2 + \Delta z_m^2},\tag{4.3}$$

and

$$\Delta y_1 = y - h_n, \quad \Delta z_1 = z - z_n,$$
 $\Delta y_2 = y + h_n, \quad \Delta z_2 = z - z_n,$
 $\Delta y_3 = y + h_n, \quad \Delta z_3 = z + z_n,$
 $\Delta y_4 = y - h_n, \quad \Delta z_4 = z + z_n.$
(4.4)

The spanwise-averaged second-order statistics of the total additional vortex velocities $V_i(y, z)$ from equation (4.2) can now be determined and are assumed to act as additional turbulent vortex stresses within the statistical VG model ansatz and can then be added to the mean-flow turbulence; see section 4.3.3.

4.3.2. Velocity Triple Decomposition

The concept of the velocity triple decomposition makes it possible to formally add the additional total vortex-velocity field $V_i(y, z)$ from equation (4.2) to the mean-flow velocity U_i and the turbulent fluctuations u'_i from equation (3.5):

$$u_i(x, y, z, t) = U_i(y) + u'_i(x, y, z, t) + V_i(y, z).$$
(4.5)

The additional total velcocity field V_i can now, for example, be added to the mean flow U_i in a RANS computation. This resolves the mean-flow velocity U_i and the generated vortices V_i , thus only expressing the turbulent part u_i' by a conventional turbulence model. On the other hand, it is possible to solely resolve the mean-flow velocity U_i , and instead to add V_i to the turbulent fluctuations u_i' and thereby, treat the combination $u_i' + V_i$ in a turbulence

model. The two approaches perform differently in a computational analysis. The first one resolves the VGs and the generated vortices downstream of the VGs which requires a fully-resolved three-dimensional computational grid. This makes the first approach and its results highly grid dependent. The second proposal adds the additional vortex velocities within the turbulence model and, by that, a computational analysis may reduce to two-dimensional computational grids only. As a consequence, the results including the vortices become solely dependent on the turbulence model used. Still, the VG forcing plane¹, where the statistical vortex-stress terms are applied, needs to be adequately resolved in order to capture the modelled vortices within the turbulence model. The ansatz for adding V_i to u_i' within a statistical turbulence model is used for the statistical VG modelling approaches in this thesis, and the combined velocity field v_i' from the turbulence fluctuations u_i' and the vortex veloities V_i is defined as

$$v_i'(y, z, t) \equiv u_i'(y, z, t) + V_i(y, z).$$
 (4.6)

It is now possible to form the time- and spanwise-averaged second-order statistics of $v'_i(y, z, t)$ which, in turn, are used for a substitution of the original Reynolds-stress tensor by an extended Reynolds-stress tensor $\overline{v'_i v'_j}(y)$ which includes the modelled vortex stresses from $V_i(y, z)$.

4.3.3. Extended Reynolds Stress Tensor

As briefly mentioned in section 4.3.2, the concept of the statistical vortex modelling is to assume that the spanwise-averaged second-order statistics of the additional vortex-velocity field $V_i(y,z)$ from equation (4.2) act as additional stresses on the mean flow. By making this explicit assumption, the additional spanwise-averaged second-order statistics of the vortex-velocity field $V_i(y,z)$, or simply the vortex stresses, enter the DRSM equations through the combined stress tensor $-\rho \overline{v_i'v_j'}(y)$ for $v_i'(y,z,t)$ from equation (4.6). This substitutes the Reynolds-stress tensor $-\rho \overline{u_i'u_j'}(y)$ with the extended Reynolds-stress tensor for the combined stresses $-\rho \overline{v_i'v_j'}$, where

$$-\rho \overline{v_i' v_j'}(y) = -\rho \overline{(u_i' + V_i)(u_j' + V_j)},$$

$$= -\rho \left[\overline{u_i' u_j'}(y) + \Delta \overline{u_i' u_j'}(y) \right],$$
 (4.7)

and

$$\Delta \overline{u_i' u_j'}(y) \equiv \overline{V_i V_j}(y). \tag{4.8}$$

¹The term "forcing plane" is generally used in this thesis and denotes the plane normal to the freestream direction, and at the VG array position. Strictly valid only in three dimensions, the VG forcing plane reduces to a VG forcing line in two-dimensional flows.

The cross-product terms in equation (4.7) form the correlations $\overline{u_i'V_j}$ and $\overline{u_j'V_i}$. These contributions become zero, because their mean values are derived from a spanwise- and time-averaging of $u_j'V_i$, and because the velocity field $V_i(y,z)$ is steady. The additional vortex stresses² can be determined from the spanwise-average term

$$\Delta \overline{u_i' u_j'}(y) = \frac{1}{D} \int_{-D/2}^{D/2} V_i(y, z) V_j(y, z) dz.$$
 (4.9)

where the vortex-velocity field is given by equation (4.2). It is sufficient to integrate and spanwise-average the second-order statistics in equation (4.9) over a distance D since the vortex-velocity field $V_i(y,z)$ is periodic in the spanwise direction. Additional contributions $\Delta \overline{u_i'u_j'}(y)$ are, due to the choice of the Lamb-Oseen vortex model $(V_x=0)$, only nonzero for $\Delta \overline{v'v'}(y)$ and $\Delta \overline{w'w'}(y)$. Moreover, a wall-damping function, $[1-\exp(-20y/h)]$, is introduced and applied on equation (4.9), because the spanwise vortex-velocity component $V_z(y,z)$ at the wall boundary does not cancel out and would result in a finite value for $\Delta \overline{w'w'}(y=0)$.

In that way, a summation of the boundary-layer turbulence stresses $\overline{u_i'u_j'}(y)$ with the VG model vortex stresses $\Delta \overline{u_i'u_j'}(y)$ can be carried out. The vortex stresses $\Delta \overline{u_i'u_j'}(y)$ are thereby applied at the VG forcing plane, and from there, they influence the downstream development of the mean flow. The VVG model forcing plane is defined as the location of the vane trailing edge where the generated vortices detach. In terms of the VGJ model, the location of the jet exit center is defined as the VGJ forcing plane.

As described in chapter 3, a DRSM is suitable to properly describe the streamwise transport and development of the individual components of $\overline{u_i'u_j'}(y) + \Delta \overline{u_i'u_j'}(y)$. Furthermore and unlike simpler turbulence models, a DRSM enables to account for the energy transfer between the different components of the extended Reynolds-stress tensor $\overline{v_i'v_j'}(y)$. In particular, the vortex stress tensor $\Delta \overline{u_i'u_j'}(y)$ does not enable the normal and the important shear stresses, $\Delta \overline{u'u'}(y)$ and $\Delta \overline{u'v'}(y)$, respectively, and their production is instead established through $\mathcal{P}_{12} = \overline{v'v'}\frac{\partial V_x}{\partial y}$ in the transport equations for $\overline{u_i'u_j'}(y) + \Delta \overline{u_i'u_j'}(y)$ within the DRSM.

4.4. Statistical Vane Vortex Generator Model

The original statistical VVG model was initially proposed by Törnblom & Johansson (2007), and it is presented in this section. As mentioned in section 4.3.1, the values for Γ_{max} , r_0 , and (h_c, z_c) need to be determined with respect to the VG model used. The spanwise vortex core location z_c , which is initially a function of the VVG setup parameters d and D, as well as d and D must be

²From here on, the factor $-\rho$ is obmitted for better readability. Still, the term "stresses" is used for the remaining tensor.

explicitely given by the user in order to determine the total vortex-velocity field for VVG arrays from equation (4.4). Furthermore, empirical well-established values for r_0 and h_c enter the VVG model with $r_0 = 0.1 h_{\rm VG}$ according to Törnblom & Johansson (2007), and $h_c = h_{\rm VG}$ due to the distinct vortex shedding from the VVGs.

The central ansatz for the VVG model are very thin vanes which can be considered as small wings, mounted normal on the control surface; see also figures 1.1 and 2.2. The LLT is used for the determination of $\Gamma(y)$ across the vane, and thereby, the maximum value Γ_{max} . The spanwise circulation distribution $\Gamma(y)$ across a wing along the spanwise coordinate y is given by

$$\Gamma(y) = \frac{K}{2}U(y)c(y)\left[\alpha(y) - \frac{w(y)}{U(y)}\right],\tag{4.10}$$

where U(y) represents the incoming velocity distribution across the wing, c(y) the wing chord distribution, K the local section lift slope of the wing at zero angle of attack, and w(y) the downwash-velocity distribution

$$w(y) = \frac{1}{4\pi} \int_{-h}^{h} \frac{d\Gamma}{dy'} \frac{1}{y' - y'_0} dy'. \tag{4.11}$$

The term in squared brackets in equation (4.10) specifies the effective angle of attack

$$\alpha_{\text{eff}}(y) \equiv \alpha(y) - \frac{w(y)}{U(y)},$$
(4.12)

which develops due to the finite wing aspect ratio. The LLT strictly holds only for high-aspect-ratio wings for small angles of attack α in inviscid free-flight conditions. By means of modelling $\Gamma(y)$ for relatively small vanes that are mounted in a boundary-layer flow, some of its assumptions are not strictly valid as a result of: 1) a spanwise varying boundary-layer velocity profile U(y) instead of a constant freestream velocity U_{∞} ; 2) VVGs being wing-like vanes with very low aspect ratios; 3) possible neighbouring-vortex interaction; and 4) a rather high vane angle of incidence α towards the mean-flow direction. Therefore, the LLT should only be considered as an approximation to estimate the circulation distribution $\Gamma(y)$ across the vane. The circulation Γ_{max} is then used as an input parameter to the Lamb-Oseen vortex model from equation (4.1). A solution method for equations (4.10) and (4.11) is given in the next section.

4.4.1. Solution Method for the Lifting-Line Theory

In a next step on the way to model VVGs, it is necessary to solve equations (4.10) and (4.11) numerically by means of a Fourier series; see Glauert (1926). A suitable transformation for the y-coordinate of a single vane and its mirror image is given by

$$y(\theta) = -h_{VG}\cos(\theta),\tag{4.13}$$

with $0 \le \theta \le \pi$ as the new y-coordinate limits. The Fourier-series ansatz for equation (4.10) according to Glauert (1926) reads

$$\Gamma(\theta) = 4h_{VG}U_{ref} \sum_{n=1}^{\infty} A_n \sin(n\theta).$$
 (4.14)

The induced downwash $w(\theta)$ from equation (4.11) at a certain spanwise position θ in combination with equation (4.13) becomes

$$\frac{w(\theta)}{U_{\text{ref}}} = \frac{1}{4\pi} \int_0^{\pi} \frac{d\Gamma(\theta')}{d\theta'} \frac{d\theta'}{\cos \theta' - \cos \theta},$$

$$= \frac{1}{\pi} \int_0^{\pi} \frac{\sum_{n=1}^{\infty} n A_n \cos(n\theta')}{\cos \theta' - \cos \theta} d\theta',$$

$$= \sum_{n=1}^{\infty} n A_n \frac{\sin(n\theta)}{\sin \theta},$$
(4.15)

where the standard integral

$$\int_0^{\pi} \frac{\cos(n\theta') d\theta'}{\cos \theta' - \cos \theta} = \frac{\pi \sin(n\theta)}{\sin \theta}$$
 (4.16)

is used. Equations (4.14) and (4.15) are plugged into equation (4.10), leading to the system of equations

$$\sum_{n=1}^{\infty} A_n \sin(n\theta) (\mu(\theta)n + \sin\theta) = \mu(\theta) \frac{U(\theta)}{U_{\text{ref}}} \alpha(\theta) \sin\theta, \qquad (4.17)$$

where $\mu(\theta) = Kc(\theta)/8h_{\rm VG}$. This system of equations is solved by a truncation of the series at n=N colloation points for the vane and its mirror image, and solving at M=(N-1)/2 collocation points for the vane only, viz. $0 \le y \le h_{\rm VG}$ and $\frac{\pi}{2} \le \theta \le \pi$, respectively. The solution for A_n is then used to solve the circulation distribution $\Gamma(y)$ across the vane.

4.4.2. Original Statistical Vane Vortex Generator Model

When the circulation distribution $\Gamma(y)$ and its maximum value Γ_{max} are determined, the vortex velocities $V_i(y,z)$ from equations (4.1) and (4.2) and the vortex stresses $\Delta \overline{u_i'u_j'}(y)$ from equation (4.9) can be formed and added to the turbulence stresses $u_i'u_j'(y)$ at the VVG forcing plane.

A typical distribution of the turbulence stresses $\overline{u_i'u_j'}(y)$ for a ZPG boundary-layer flat-plate flow is given in figure 4.2. The additional vortex stresses $\Delta \overline{v'v'}(y)$ and $\Delta \overline{w'w'}(y)$ for a specific VVG setup, see figure 4.3, are then added to the turbulence stresses, resulting in the combined stresses in figure 4.4. These represent the combined stresses of the extended Reynolds-stress tensor which is treated by the transport equation of a DRSM turbulence model.

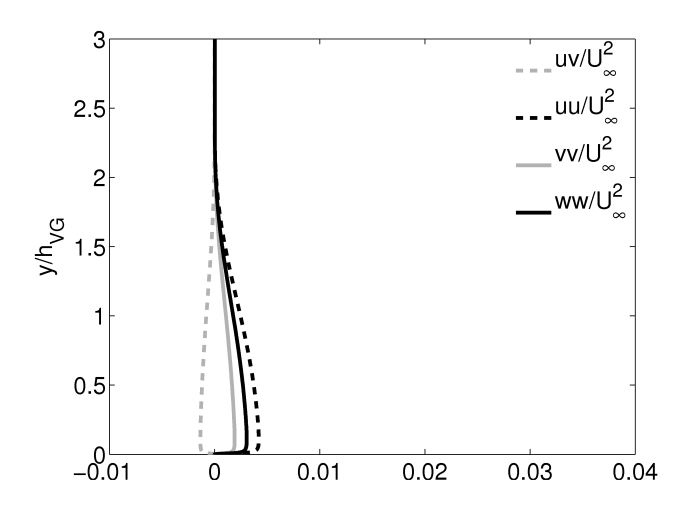


FIGURE 4.2. Nondimensional boundary-layer turbulence stresses at the VVG model forcing plane.

4.4.3. Improvement of the Statistical Vane Vortex Generator Model

Since the original proposal of the VVG model by Törnblom & Johansson (2007) did not account for the vortex-stress components $\Delta \overline{u'u'}(y)$ and $\Delta \overline{u'v'}(y)$, an improved VVG model is proposed on the basis of the original VVG model. A straightforward way to include also those correlations which contain products of u' seems to simply extend the Lamb-Oseen vortex model by a streamwise-velocity component V_x . The $\Delta \overline{u'u'}(y)$ component could be derived from this

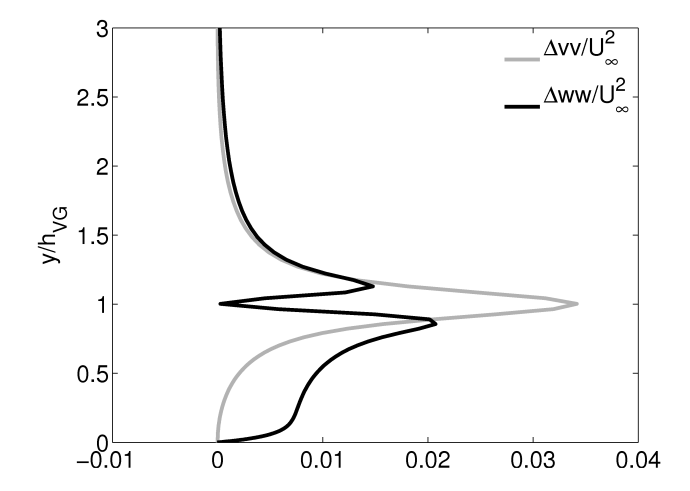


FIGURE 4.3. Nondimensional additional vortex stresses at the VVG model forcing plane. $U_{\infty}=26.5~\mathrm{m/s},~\alpha=\pm15^{\circ},~h_{\mathrm{VG}}/\delta_{99}=0.65.$

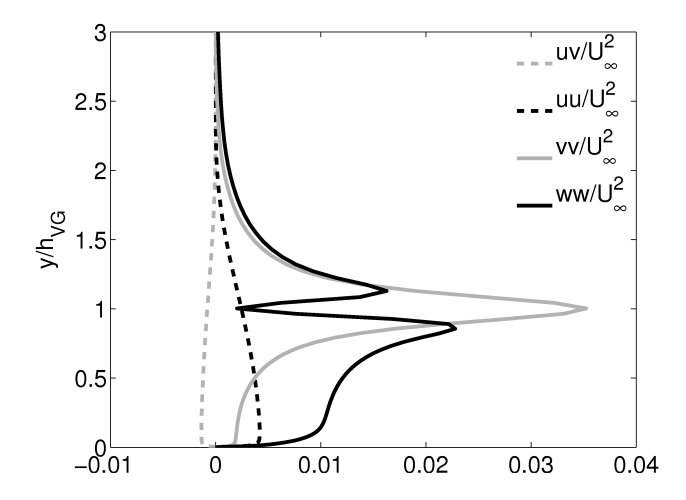


FIGURE 4.4. Nondimensional combined stresses, summation of the boundary-layer turbulence stresses from figure 4.2 and the additional vortex stresses from figure 4.3.

ansatz but not $\Delta \overline{u'v'}(y)$, because any streamwise vortex-velocity component V_x would not be correlated with the cross-plane vortex-velocity components V_y and V_z . Therefore, another approach for modelling both the $\Delta \overline{u'u'}(y)$ and the $\Delta \overline{u'v'}(y)$ is proposed here. The existing vortex-stress components $\Delta \overline{v'v'}(y)$ and $\Delta \overline{w'w'}(y)$ are used in order to model the remaining nonzero vortex-stress components $\Delta \overline{u'u'}(y)$ and $\Delta \overline{u'v'}(y)$. Also the mean strain-rate tensor S_{ij} is included in this ansatz and it accounts for the effects of the velocity gradient $\partial U(y)/\partial y$ in the boundary layer, with S_{ij} becoming zero at the boundary-layer edge. Thereby, it is ensured that the additional modelled vortex stresses become zero when the local boundary-layer edge is reached. The suggested $\Delta \overline{u'u'}(y)$ and $\Delta \overline{u'v'}(y)$ stresses read

$$\Delta \overline{u'u'}(y) = C_{uu} \cdot S(y) \frac{r_0^2}{\Gamma_{\text{max}}} \left[\Delta \overline{v'v'}(y) + \Delta \overline{w'w'}(y) \right],$$

$$\Delta \overline{u'v'}(y) = -C_{uv} \cdot S(y) \frac{r_0^2}{\Gamma_{\text{max}}} \left[\Delta \overline{v'v'}(y) + \Delta \overline{w'w'}(y) \right], \qquad (4.18)$$

where C_{uu} and C_{uv} denote nondimensional constants in order to account for the correct amplitude of the modelled stresses. The constants C_{uu} and C_{uv} were determined empirically by means of examining the improved VVG model in ZPG flat-plate boundary-layer flow, as well as a comparison against experimental data and resolved computations, and read

$$C_{uu} = 160,$$

 $C_{uv} = 80.$ (4.19)

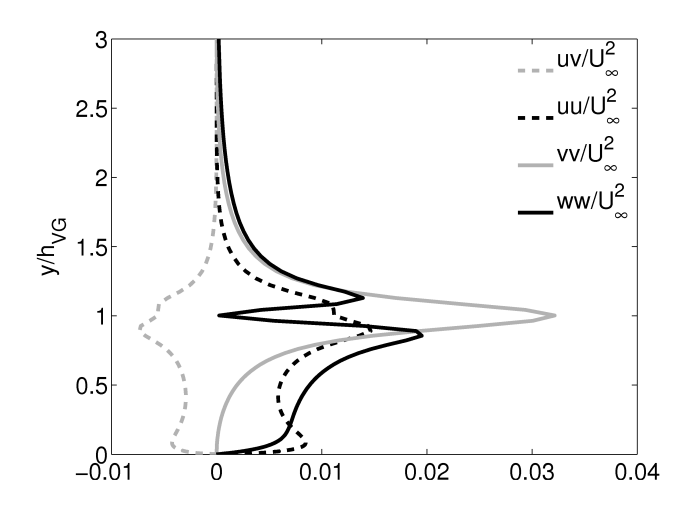


FIGURE 4.5. Nondimensional combined stresses for the improved VVG model at the VVG model forcing plane. $U_{\infty} = 26.5 \text{ m/s}, \alpha = \pm 15^{\circ}, h_{VG}/\delta_{99} = 0.65$; see also figure 4.3.

An example of the additional improved VVG stresses from equation (4.18) is given in figure 4.5. It can be seen how the two additional vortex stress distributions are mirrored and amplified by the coefficients C_{uu} and C_{uv} around the y-axis, and how they combine the characteristics of the $\Delta \overline{v'v'}(y)$ and $\Delta \overline{w'w'}(y)$ stresses. This improved VVG model has shown to have a better impact on the near-field stress development and thus, provides improved flow-separation control when compared to the original VVG model.

4.5. Statistical Vortex Generator Jet Model

It was shown that the distinct vortices which detach from the trailing edge of the VVG vanes can be modelled by an analytical derivation of the circulation $\Gamma_{\rm max}$ using the established theory of lifting lines by Prandtl. This concept cannot be assumed for modelling of VGJs. A different way of vortex generation by VGJs needs to be considered, and this section presents the development of the concept for the derivation of $\Gamma_{\rm max}$ for the statistical VGJ model. The derivation of the Lamb-Oseen vortex-model parameters $\Gamma_{\rm max}$, r_0 and $(h_{\rm c}, z_{\rm c})$ for the statistical VGJ model is mainly based on experiments from Ortmanns (2008) for single VGJ. The determination of suitable values was carried out via a least-squares data fitting of the experimental $U_{\Phi}(r)$ and the Lamb-Oseen vortex velocities $V_{\Phi}(r)$:

$$\min_{x} \|[U_{\Phi}(r) - V_{\Phi}(r)]\|_{2}^{2}. \tag{4.20}$$

It could be shown that the Lamb-Oseen vortex model represents the single VGJ vortices reasonably well (see figure 4.6). More details concerning the parameterization of the experimental vortices can be found in section 5.4 and in

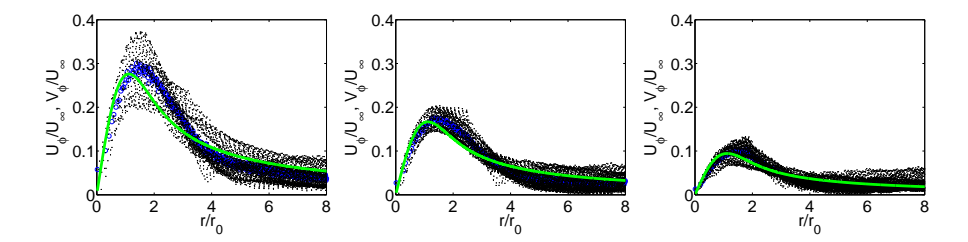


FIGURE 4.6. Nondimensional vortex velocity $U_{\Phi}(r/r_0)/U_{\infty}$ from experiments (dots), corresponding averaged values (circles), and the fitted vortex model $V_{\Phi}(r/r_0)/U_{\infty}$ (curve). Here: $U_{\infty} = 25 \text{ m/s}, \lambda = 2.5, \alpha = 45^{\circ}, \beta = 90^{\circ}$ at streamwise positions x = 50, 100, and 200 mm (from left to right).

appended Paper 3. Empirical values for r_0 and h_c and their dependencies on the VGJ setup parameters were derived from the parameterization of vortices from experiments. In contrast to the derivation of empirical values for r_0 and h_c , the vortex circulation $\Gamma_{\rm max}$ could be estimated from the the balance of the injected jet impulse and the added tangential momentum by an embedded boundary-layer vortex. This idealized model assumes a jet impulse $p_{\rm VGJ} = F_{\rm VGJ} \Delta t$ which is injected into the freestream during the time Δt into the boundary layer and that, in turn, creates a streamwise vortex when the jets deflects due to the mean boundary-layer flow. For the jet with a skew angle β , the magnitude of the momentum change $p_{\rm VGJ}$ can be estimated as

$$p_{\text{VGJ}} = F_{\text{VGJ}} \Delta t \sin \beta. \tag{4.21}$$

Due to the injected jet, the boundary layer experiences an increase of the cross-plane momentum by the fully-developed vortex. Likewise, the vortex momentum $p_{\rm V}$ of a fully-developed vortex which travels the streamwise distance x in Δt , see figure 4.7, reads

$$p_{V} = \int_{V} \rho U_{\Phi}(r) dV_{V},$$

$$= \rho \Delta x 2\pi \int_{0}^{R} U_{\Phi}(r) r dr.$$
(4.22)

As an evaluation of the experiments has shown, an upper integration boundary of $R=5r_0$ is reasonable, because a circular area with $R=5r_0$ contains most of the tangential vortex momentum. The injected jet impulse is suggested to be completely transformed, i.e., without any losses, into tangential vortex momentum. This balance enables the equation $p_{VGJ}=p_V$, which can be solved for Γ_{max} that enters equation (4.22) through the Lamb-Oseen vortex model. The expression for Γ_{max} is used to derive the modelled vortex velocities $V_i(y,z)$ for VGJs and enables the derivation of the vortex stresses for the

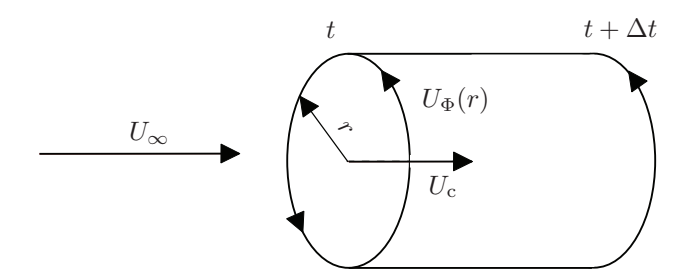


FIGURE 4.7. Schematic of a vortex tube of radius r and tangential velocity $U_{\Phi}(r)$ that travels the distance $\Delta x = U_{c}\Delta t$ during the time Δt .

statistical VGJ model. The Lamb-Oseen vortex model is then fully described by this ansatz, and the vortex model parameters read

$$\Gamma_{\text{max}} = C_{\Gamma} \sin \beta \left(\frac{\Phi_{\text{VGJ}}^2 \lambda^2 U_{\infty}}{r_0} \right),$$

$$r_0 = C_r \Phi_{\text{VGJ}} \sqrt{\lambda},$$

$$h_c = C_h \Phi_{\text{VGJ}} \lambda,$$
(4.23)

where C_{Γ} , C_r and C_h represent suitable nondimensional vortex-model parameters for $\Gamma_{\rm max}$, r_0 , and $h_{\rm c}$. The numerical value of $C_{\Gamma} = \pi/\left[2\left(10 - \sqrt{\pi}\right)\right] \approx 0.2$ for $R = 5r_0$ in equation (4.22). The specific scaling for r_0 and $h_{\rm c}$ was empirically derived from the parameterization of the single-jet vortices from experiments by Ortmanns (2008). Universal nondimensional values are proposed to be $C_r = 0.4$ and $C_h = 0.6$ based on the results for $\alpha = 30$ °.

Vortex stresses for chosen VGJ settings at the VGJ forcing plane for $C_{\Gamma} = 0.2$, $C_r = 0.4$, $C_h = 0.6$ are given in figures 4.8 and 4.9. From the plots in figure 4.8, and a comparison with the corresponding VVG case in figure 4.3, it can be observed that the VGJ $\Delta \overline{v'v'}(y)$ peak stresses have decreased by $\approx 30\%$, whereas the VGJ $\Delta \overline{w'w'}(y)$ peak stresses have grown by a factor >2 when compared to the VVG model. This is the result of the small pitch angle $\alpha = 30^{\circ}$ and the strong blowing perpendicular to the freestream direction for $\beta = 90^{\circ}$, whereas VVG vortices enable a naturally stronger wall-normal component, and are also less affected by the presence of the wall. This is due to the fixed vortex core location at the VVG forcing plane which is in contrast to vortices originating from VGJs.

In the case for increasing λ (see figure 4.9), the general observation is that the vortex stresses are strongly amplified when compared to the lower λ -case. An increase in λ from 2.5 to 5.0 results in an increase for the $\Delta \overline{v'v'}(y)$ and the $\Delta \overline{w'w'}(y)$ peak stresses by a factor >4.5 and >8, respectively, essentially enabling similar peak stresses for both vortex stress components. The vortex core for $\lambda=5.0$ is also located further away from the wall, compare with

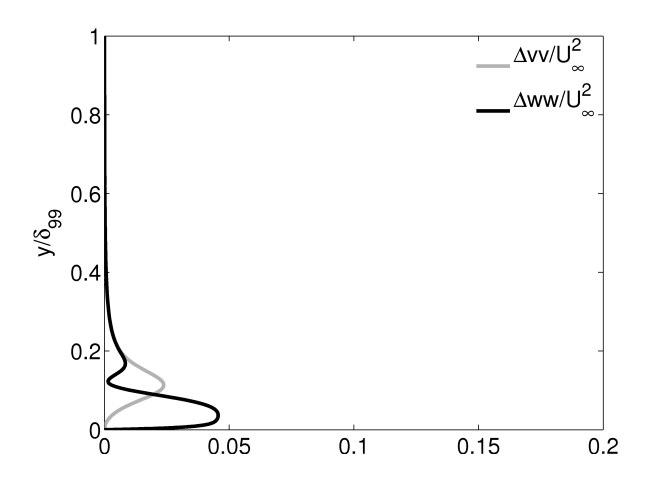


FIGURE 4.8. Nondimensional vortex-stress distributions at the VGJ model position from equation (4.23). $U_{\infty} = 25 \text{ m/s}$, $\lambda = 2.5$, $\Phi_{\text{VGJ}}/\delta_{99} = 0.07$.

 h_c in equation (4.23), and thereby enables, in combination with a relatively weaker-growing r_0 , a stronger $\Delta \overline{v'v'}(y)$ due to the decreasing wall influence. The figures 4.8 and 4.9 generally show how the VGJ model reacts sensitively to a velocity ratio change in equation (4.23). Furthermore, it can be observed that the $\Delta \overline{v'v'}(y)$ stresses for the given VGJ setup become more than four times stronger when compared to the efficient VVG model configuration from figure 4.3, which probably leads to more efficient flow-separation prevention by VGJs.

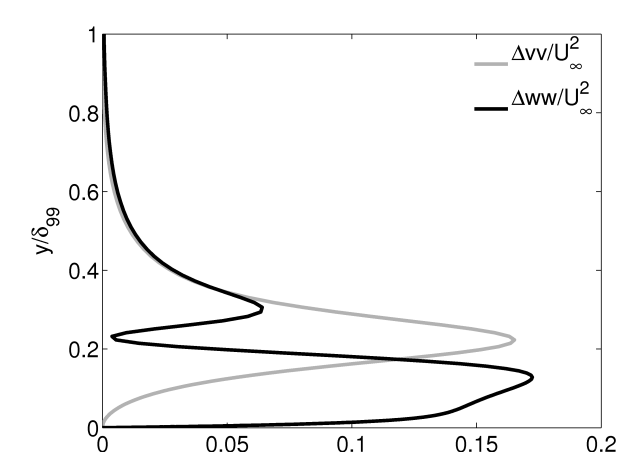


FIGURE 4.9. Nondimensional vortex-stress distributions at the VGJ model position from equation (4.23). $U_{\infty} = 25 \text{ m/s}$, $\lambda = 5.0$, $\Phi_{\text{VGJ}}/\delta_{99} = 0.07$.

CHAPTER 5

Selected Results and Discussion

5.1. Original VVG Model in Adverse-Pressure-Gradient Flat-Plate Flow

The original VVG model was applied in APG flat-plate boundary-layer flow and evaluated against computations of a fully-gridded VVG array, as well as corresponding experiments by Lögdberg *et al.* (2010). A sensitivity study of the VVG model position dependency on skin-friction results was carried out.

The VVG array was installed in the APG section on a flat plate with a counter-rotating common-flow-down setup and consisted of rectangular vanes with $\alpha=\pm15^{\circ}$. The local ratio of $h_{\rm VG}/\delta_{99}<0.7$. In experiments and computations, a distinct separation bubble was present when no flow control was applied; see for example $c_f<0$ in figure 5.1. Applying the fully-resolved VVGs, see the VG3D curve, the skin friction increased significantly and flow separation was prevented. The original VVG model, cf. the VG2D curve, showed a clear enhancement of the skin-friction, essentially preventing flow separation. Its impact on skin-friction increase was nonetheless not comparable to the VG3D computations.

In total, seven streamwise VVG forcing plane positions were examined, see also figure 5.2 for skin-friction results for $x_{\rm VG} \geq 1.25$ m. When the VVG model was applied at $x_{\rm VG} \leq 1.25$ m (not shown), the skin-friction distributions at the former separation-bubble location were increased for growing $x_{\rm VG}$. For the $x_{\rm VG} \geq 1.25$ m plots in figure 5.2, the opposite effect was observed: the further downstream the VVG forcing plane, the weaker the impact on the mean flow. This led to a decreased skin-friction distribution and eventually, separated flow occured. A conclusion from this study is that there existed an optimum VVG position for flow-separation control using the original VVG model at the beginning of the APG section close to $x_{\rm VG} = 1.25$ m. Nevertheless, the overall flow state was rather insensitive on the VVG position. Still, a minimum distance between the model forcing plane and the originally separated region was required in order to eventually overcome flow separation.

5.2. Comparison of the VVG models

The original and the improved VVG models were evaluated and compared against each other, as well as against fully-resolved VVG computations and against experiments by Lögdberg *et al.* (2009, 2010). The VVGs were applied

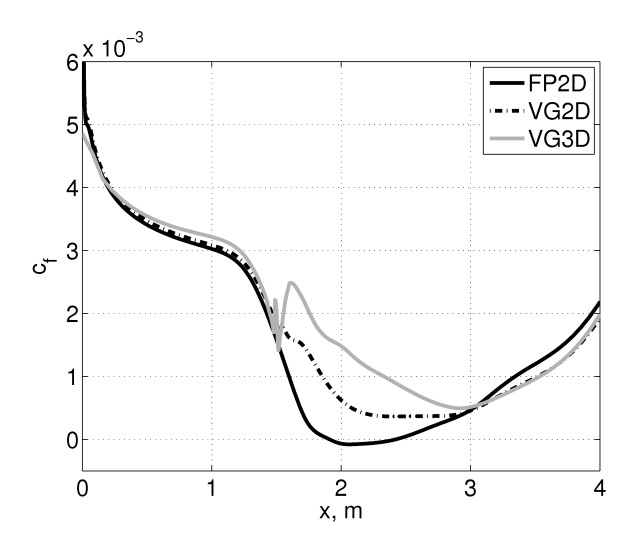


FIGURE 5.1. Local skin-friction coefficient distributions for computations without VVGs (FP2D), with the original VVG model (VG2D), and fully-gridded VVGs (VG3D). Here: baseline case for $x_{\rm VG}=1.54$ m.

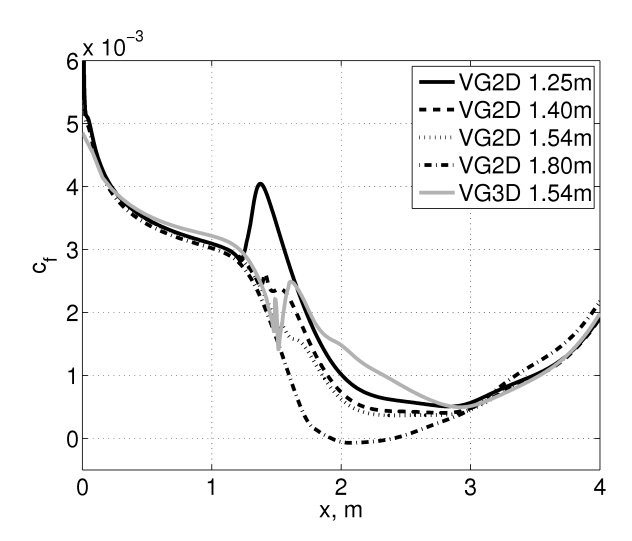


FIGURE 5.2. Local skin-friction coefficient distributions for a streamwise-position variation of the original VVG model forcing plane (VG2D) for 1.25 m $\leq x_{\rm VG} \leq$ 1.80 m. Results for the fully-resolved computations (VG3D) for the baseline case $x_{\rm VG} = 1.54$ m.

in ZPG and APG boundary-layer flat-plate flow; see also appended Paper 1. The ZPG experiments were carried out in the minimum-turbulence-level wind tunnel at KTH, and the APG case for the comparison study was the one given in section 5.1.

Figures 5.3 and 5.4 present the combined near-field and far-field $\overline{u'v'}(y)$ and $\overline{u'u'}(y)$ stress distributions for the ZPG case. Each of the top left distributions represents the initial distributions at the VVG model forcing plane. The original VVG model $\Delta \overline{u'v'}(y)$ stresses without the forcing term were initially zero but, when traveling downstream, primarily produced via the turbulence production \mathcal{P}_{12} , as can be seen from the top plots in figure 5.3. The $\overline{u'u'}(y)$ stresses were not provided by the original VVG model, and the variation in the streamwise direction was rather slow, as can be seen in the top plots in figure 5.4.

On the other hand, the results for the improved VVG model showed improved stress distributions for the $\overline{u'v'}(y)$ and the $\overline{u'u'}(y)$ stresses, matching the fully-resolved results well above the vortex center, viz. $y/h_{\rm VG} > 1$. Below the vortex center, the stress distributions showed a deficit when compared to the fully-gridded results, but they approached each other through turbulence production and redistribution further downstream. The improved model stresses converged reasonably well with fully-gridded results. With the beginning of the far field, the stresses for both VVG models approached and lay on top of each other for $x/h_{\rm VG} > 9.4$. The process of mutual approach is the result of the diffusive, productive, and redistributive effects within the DRSM. Both VVG models showed lower stress levels in the distant far field when compared to the fully three-dimensional computations and experiments, which resolved the vortex structures which have longer life times than the modelled vortex stresses.

As for the original VVG model in section 5.1, the APG flat-plate boundary-layer computations were carried out for the improved VVG model and compared to computations without VVGs, with the original VVG model, and also to fully-resolved VVG results; see also figure 5.5. The boundary conditions for the boundary layer without flow control and for the improved VVG model were identical to those for the original VVG model from section 5.1. The baseline case for a forcing plane at $x_{\rm VG}=1.54$ m was examined and is compared in figure 5.5. The improved VVG model gives a substantial increase of local skin-friction in the near-field transient. The increase of the skin-friction peak is almost identical to the fully-resolved data; cf. VG3D. The improved VVG model eliminated the separation bubble efficiently, and provided a more accurate prediction for separated flow, i.e. $c_f < 0$, as compared to the original VVG model.

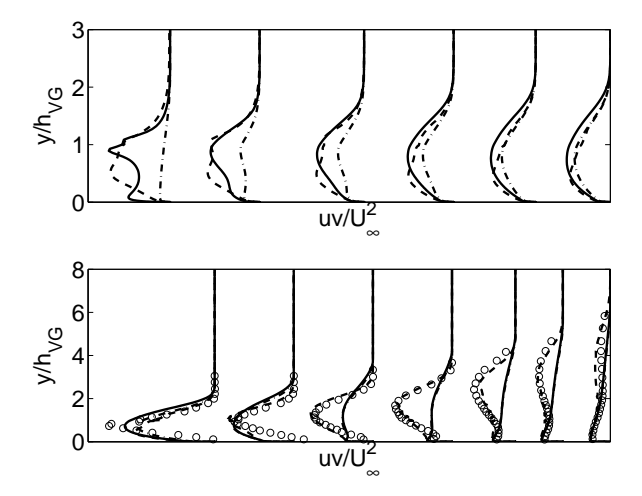


FIGURE 5.3. Original VVG model (broken line), improved VVG model (solid line), spanwise-averaged fully-resolved computational (dashed line), and spanwise-averaged experimental (circles) results for: near field $x/h=0.0,\,0.5,\,1.1,\,1.7,\,2.2,\,$ and 2.8 (top); far field $x/h=3.3,\,9.4,\,23,\,37,\,65,\,93,\,$ and 148 (bottom).

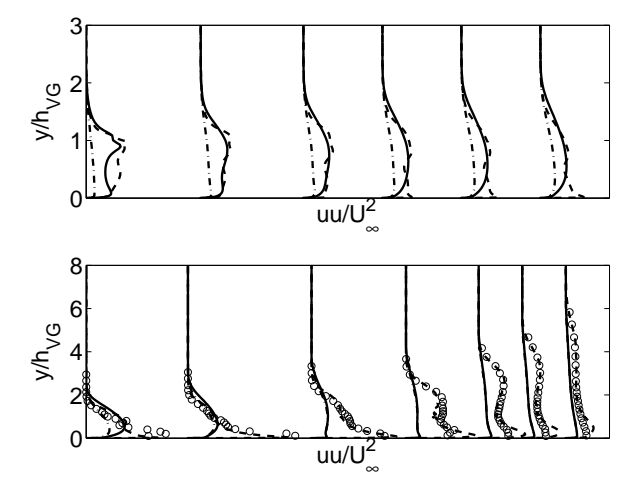


FIGURE 5.4. Original VVG model (broken line), improved VVG model (solid line), spanwise-averaged fully-resolved computational (dashed line), and spanwise-averaged experimental (circles) results: near field $x/h=0.0,\,0.5,\,1.1,\,1.7,\,2.2,\,\mathrm{and}\,2.8$ (top); far field $x/h=3.3,\,9.4,\,23,\,37,\,65,\,93,\,\mathrm{and}\,148$ (bottom).

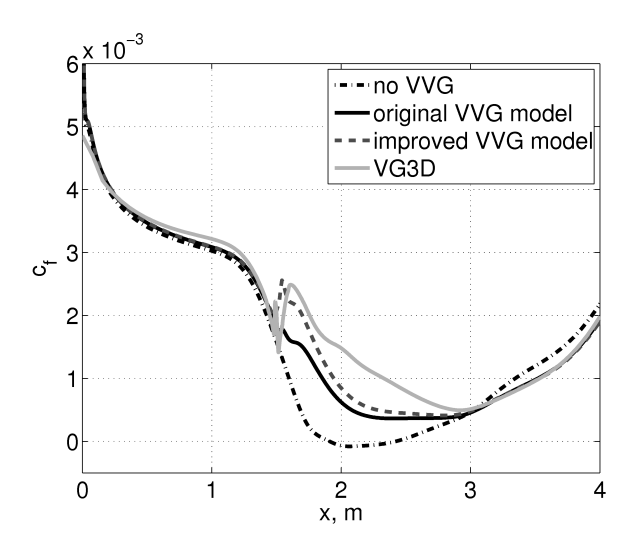


FIGURE 5.5. Local skin-friction coefficient distributions for the baseline case $x_{\text{VG}_{\text{TE}}} = 1.54 \text{ m}$: no VVGs applied, for the original and the improved VVG model computations, and for the spanwise-averaged fully-resolved computations (VG3D).

5.3. VVG Model Applications

5.3.1. HELIX Airfoil with Short-Chord Flap

The original VVG model was applied to model a corotating VVG array in the turbulent boundary layer of the HELIX airfoil short-chord flap; see also appended Paper 5. Several VVG settings were computationally investigated within this project and the initial VVG model position ($x_{\rm VG}=25\%~c_{\rm flap}$) was not capable to suppress separated flow as in corresponding experiments; see figure 5.6(a). The reason for this was found to be the large detached-flow region on the short-chord flap that was deployed at higher angle of attacks α when compared to a conventional high-lift system. In contrast to the VVG model RANS computations, flow-separation control worked well in the experiments as a result of the strongly fluctuating flow around the flap, which enabled the creation of streamwise vortices when attached flow impinged the VVGs. Such flow conditions could not be achieved by a RANS computation which solves for the steady-state ensemble-averages and cannot capture unsteady flow states.

Nevertheless, it could be shown that the VVG model could successfully prevent flow separation on the flap for different configurations. The main parameter was found to be the streamwise location of the VVG on the flap. Figure 5.6(b) shows the flow state for a setup with the VVG located further upstream in the permanent-attached flow region at 8% $c_{\rm flap}$. It can also be seen that the VVG model establishes attached flow around the entire short-chord flap. Furthermore, the modelled VVG shape and height were changed during in this

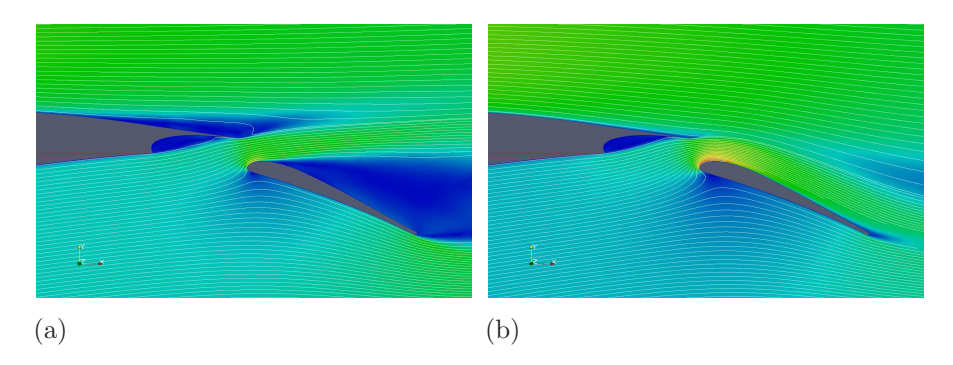


FIGURE 5.6. Velocity contours (blue: low velocity; red: high velocity), and streamline plots for: (a) the original airfoil without VVG model, and (b) the modified airfoil with the original VVG model applied.

study, and the mean flow showed some sensitivity for the setup parameters. As a result of the study, the VVG position can be said to be the most important VVG model parameter, followed by the VVG height which has a direct influence on the magnitude of $\Gamma_{\rm max}$ due to its dependency on the VVG tip velocity.

5.3.2. Plane Asymmetric Diffuser Flow

A further comparison between the original and the improved VVG models was carried out in the APG section of a plane asymmetric diffuser with an opening angle of 8.5°; see appended Paper 1. The 8.5° opening angle gives a weak separation which can be easily controlled, and this flow case was therefore suitable for an evaluation of the VVG models. Computations without any flow control revealed a separated region on the upper diffuser wall, see figure 5.7(a), which was in good agreement when compared to the experiments by Törnblom (2006). Applying the original VVG model established attached flow, see figure 5.7(b), and the pressure coefficient results showed a clear increase in static pressure on the upper wall (not shown here). When applying the improved VVG model, it could be observed how the streamlines were pushed further upward, and even how a slight separated region was generated on the lower diffuser wall; figure 5.7(c). Pressure coefficient curves showed a prevailing increase in static pressure throughout the diffuser when compared to the results for the original VVG model. As a result, the application of the improved VVG model led to a slightly higher pressure recovery at the diffuser exit, similar to that from the experiments with VVGs. In figure 5.7(c), it can be seen from the increased turbulence kinetic energy contours that the influence of the improved VVG model is stronger in the near field close to the upper wall.

Whether the results from the original or the improved VVG model results are correct could not be conclusively answered, because detailed velocity plots

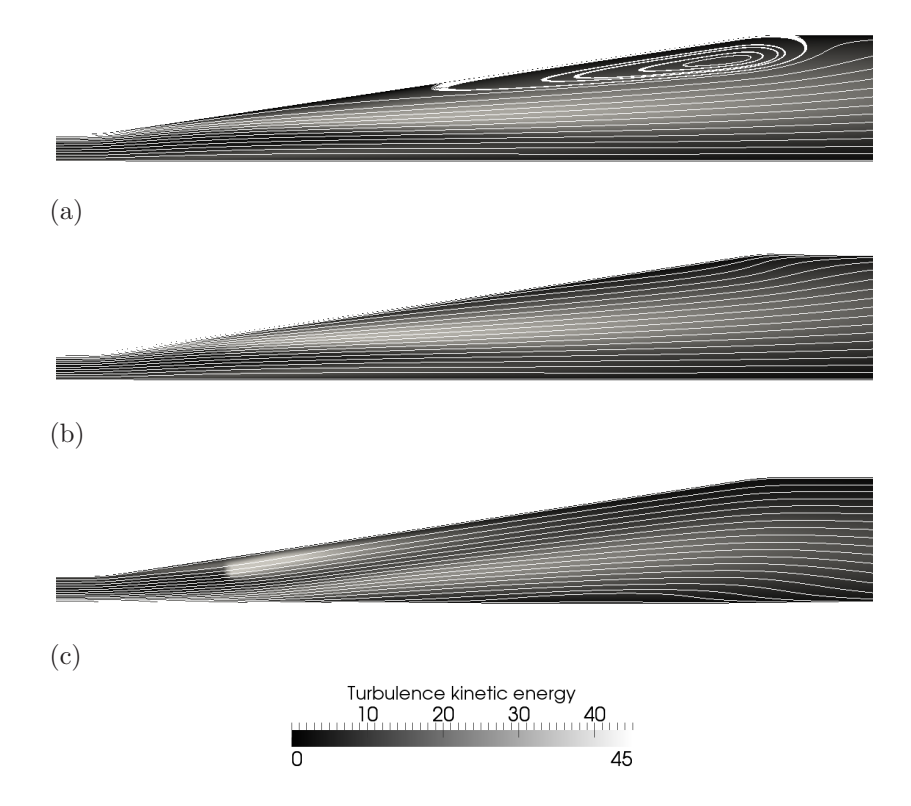


FIGURE 5.7. Turbulence kinetic-energy contours and streamlines for the computations: (a) without VG model, (b) with original VG model, and (c) with improved VG model.

within the diffuser, as well as a pressure-coefficient distributions on the lower wall were not available for experiments with VVGs. In total, it can be stated that the improved VVG model has a stronger impact on the near field characteristics, which led to a higher pressure recovery at the diffuser exit. But, on the other hand, this also gives fundamentally different flow states for the rather sensitive flow case of the plane asymmetric diffuser.

5.4. Parameterization of VGJ Experiments

As the motivation was to develop a statistical model also for active VGJs, a collaboration with the Institute of Fluid Mechanics of Technische Universität Braunschweig, Germany, was initiated by the author; see also appended Paper 3. Experimental results for single VGJs (Ortmanns 2008) and VGJ pairs (Casper 2011), comprising a broad range of parameter variations regarding α , β , U_{∞} , and λ were examined at KTH. The single-jet data were analysed using the velocity triple decomposition, and experimental vortex velocities $U_i(y, z)$ could be extracted from the analysis. The results could be used to carry out

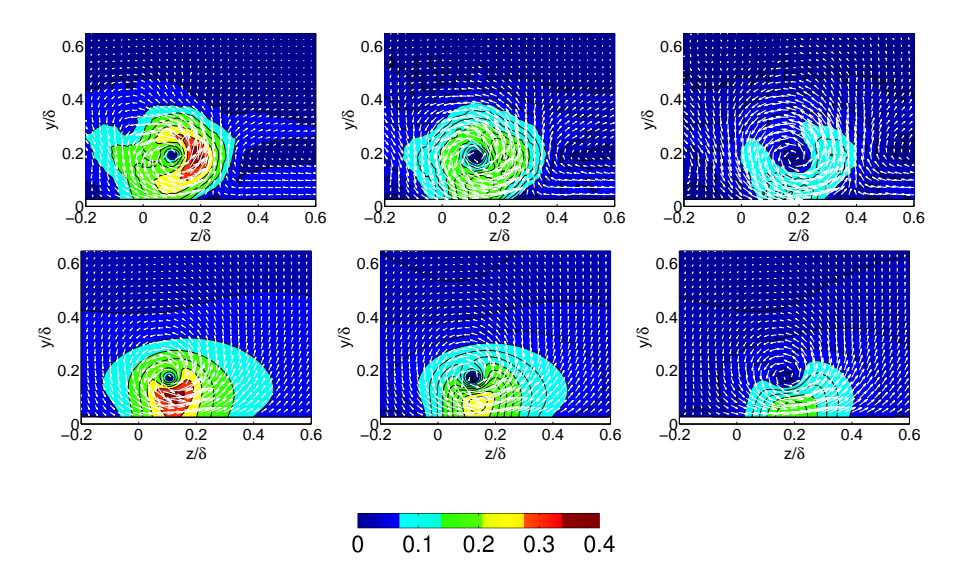


FIGURE 5.8. Experimental (top) and fitted (bottom) vortex-velocity fields $\sqrt{\left(V_y^2+V_z^2\right)}/U_\infty$ at streamwise positions $x=50,\ 100,\ \text{and}\ 200\ \text{mm}$ (from left to right.). Here: $U_\infty=25\ \text{m/s},\ \lambda=2.5,\ \alpha=45^\circ,\ \beta=90^\circ.$

a nonlinear least-squares data fitting between the experimental single-jet vortex velocities $U_i(y,z)$ and the Lamb-Oseen vortex-model velocity $V_i(y,z)$. The data fitting resulted in fitted parameters for Γ_{max} , r_0 , and (h_c, z_c) .

A comparison of the streamwise development of an experimental vortex and a fitted Lamb-Oseen vortex at three streamwise locations is presented in figure 5.8. A reasonably good agreement between experiments and the fitted vortex is given. Still, differences in the secondary-flow field can be observed because the Lamb-Oseen vortex model represents a simplified description of the experimental vortices. The experiments show secondary-vortex flow as well as peak velocities between the primary and secondary vortices, whereas the modelled vortex velocity develops its peak values between the wall and the vortex core. The fitted results are satisfactory, and figure 5.8 is representative for a broad parameter range of β , U_{∞} , and λ , for which the least-squares fitting worked well.

The results of the nonlinear least-squares data fitting for $r/r_0 \leq 8$ are presented in figure 4.6 in section 4.5. The general conclusion from this figure is that the modelling of experimental results was successfully accomplished by means of the Lamb-Oseen vortex model. Therefore, the Lamb-Oseen vortex model was used for the development of a statistical VGJ model; see section 5.5 and appended Paper 4.

5.5. Evaluation of the Statistical VGJ Model

5.5.1. Streamwise Development of VGJ Model Parameters

As stated in section 5.4, the Lamb-Oseen vortex model was chosen for the development of a statistical VGJ model. Therefore, the vortex-model parameters Γ_{max} , r_0 , and h_c needed to be determined in terms of the VGJ setup parameters α , β , λ , U_{∞} , and Φ_{VGJ} . For the determination of the parameters r_0 , and h_c , empirical results from the single-jet experiments by Ortmanns (2008) could be used. It was shown, that r_0 and h_c depend on the actuator exit diameter Φ_{VGJ} and the velocity ratio λ . The model coefficients for r_0 and h_c , reading C_r and C_h , and the streamwise development by means of the vortex-parameterization results from section 5.4 are plotted in figure 5.9.

 $C_{\rm r}$ can be observed to increase roughly linearly in the streamwise direction for all VGJ settings. The $\alpha=45^{\circ}$ results show a spread in results, but the reasons for this is unclear. However, the results are still close together when compared to the wide range of parameter settings that were used in the VGJ experiments. Nevertheless, an extrapolation to $x/\delta_{99}=0$ for the $\alpha=30^{\circ}$ results is proposed in order to determine inital setting for $C_{\rm r}$ for the statistical VGJ model. Thereby, a universal value $C_{\rm r}=0.4$, valid for all settings, was chosen for the application of the VGJ model in ZPG flat-plate boundary-layer flow; see appended Paper 4.

In case of $C_{\rm h}$, the same strategy as for $C_{\rm r}$ was used in order to determine a universal value for the VGJ model. The results for $\alpha=30^{\circ}$ lie very close to each other and describe a linear behaviour which can be utilized for a similar extrapolation as for $C_{\rm r}$. The $\alpha=45^{\circ}$ also show the spread in results. Here, a universal value $C_{\rm h}=0.6$ is suggested, which again represents the results for $\alpha=30^{\circ}$ very well.

The model coefficient for $\Gamma_{\rm max}$, C_{Γ} , was derived analytically in section 4.5. It was shown that $C_{\Gamma} \approx 0.2$. A comparison of the streamwise evolution for $\alpha = 30^{\circ}$ from experiments reveals C_{Γ} -values that lie close together around 0.2; see figure 5.9. The $\alpha = 45^{\circ}$ values show the typical spread which could be observed for the other nondimensional parameters. However, the agreement between the $\alpha = 30^{\circ}$ and the theoretical result for C_{Γ} confirms the idealized model that describes the balance and the transition of momentum between the jet and the vortex reasonably well. Therefore, it can be assumed that the theoretical derivation for C_{Γ} represents a suitable ansatz for the statistical VGJ model.

In total, it is suggested that $\alpha=30^\circ$ represents a good setup choice for VGJ flow-separation control, especially when taking the spread in results for $\alpha=45^\circ$ into account.

5.5.2. Application of the VGJ Model in ZPG Boundary-Layer Flow

Figure 5.10 shows the application of the statistical VGJ model in ZPG flat-plate boundary-layer flow in terms of a comparison of $\Delta \overline{v'v'}$ vortex stress results with

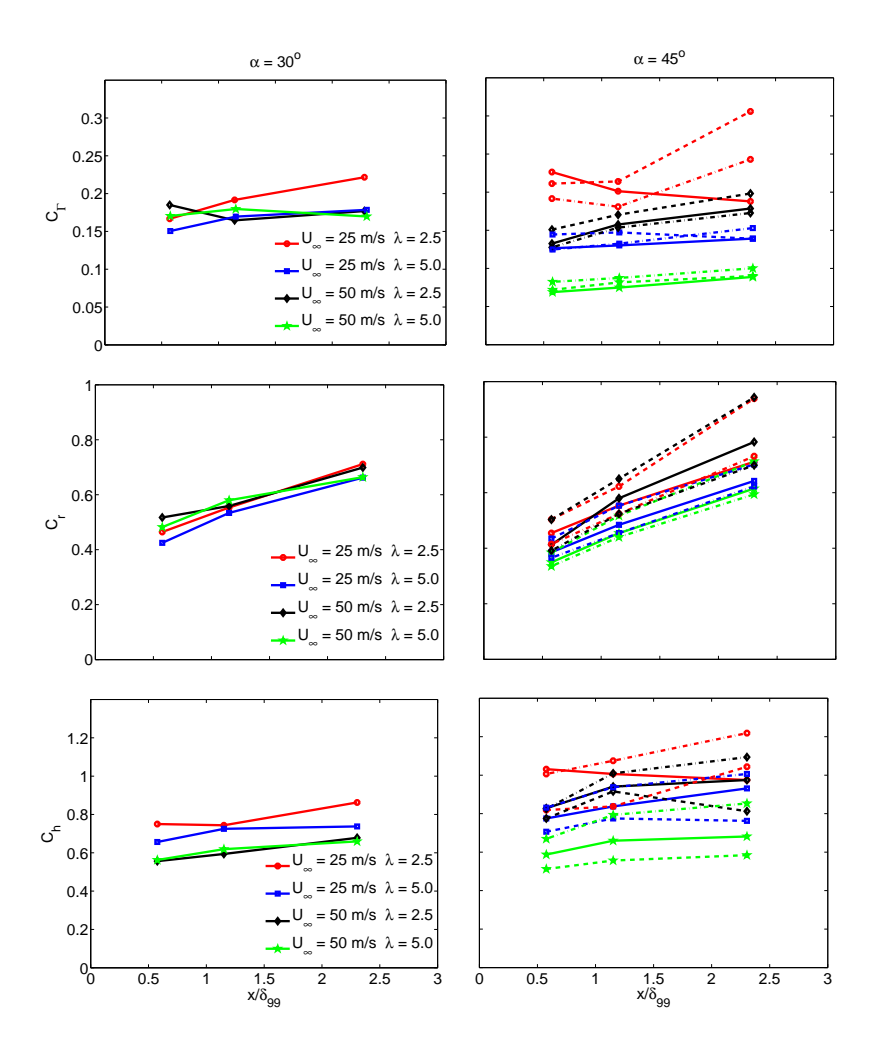


FIGURE 5.9. Streamwise development of the nondimensional VGJ model parameters for experimental results: circulation C_{Γ} , viscous core radius $C_{\rm r}$, and wall-normal location $C_{\rm h}$ for: $\alpha = 30^{\circ}$ and 45° , $\beta = 75^{\circ}$ (dashed line), 90° (solid line) and 105° (broken line).

corresponding data from fully-gridded VGJ computations, and experiments. The near-field reveals large vortex-stress differences between the VGJ model and the fully-gridded results, and the reason for this is very likely the vortex formation which takes time/space to develop in the three-dimensional computations. In case of the VGJ model, the vortex stresses already represent fully-developed vortices. Therefore, the vortex stresses do not coincide qualitatively

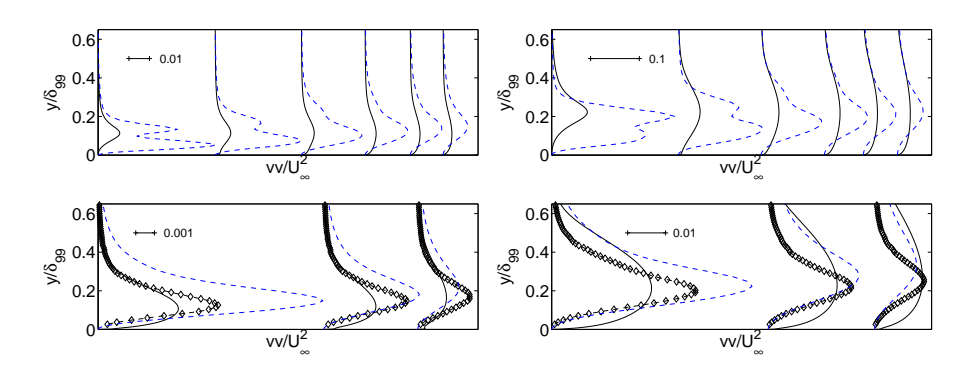


FIGURE 5.10. $\Delta \overline{v'v'}$ vortex-stress distributions. $\alpha = 30^{\circ}$, $\beta = 90^{\circ}$, $U_{\infty} = 25$ m/s, $\lambda = 2.5$ (left), and 5.0 (right): fully-gridded VGJs (dashed line), experiments (circles), and VGJ modelling results (solid line) at $x/\delta_{99} = 0$, 0.1, 0.2, 0.3, 0.4, 0.6 (top), and 0.6, 1.1, and 2.3 (bottom).

in the near field. On the other hand, it can be seen that the far-field stress distributions for the VGJ model represent the fully-resolved computations and the experiments qualitatively well. Still, the VGJ model underpredicts the stresses but the overall streamwise development is very satisfactory for this new VGJ model approach. However, the VGJ model should be tested more thoroughly in APG flows in order to investigate its applicability for more challenging flow conditions.

CHAPTER 6

Summary of Appended Papers

6.1. Paper 1

Vortex-Generator Models for Zero- and Adverse-Pressure-Gradient Flows.

This publication presents the application of the original and the improved VVG model for three different flow cases. First, basic studies, including the calibration and the evaluation of the original and the improved VVG models with experimental data were investigated in ZPG flat-plate boundary-layer flow; see also Lögdberg et al. (2009). The setup for the VVG models corresponds to the experimental setup, and a parameter study was carried out using the original VVG model. Based on a basic setup case, the local airfoil-section lift slope Kin the LLT, the viscous core radius r_0 in the vortex model, and the turbulent specific dissipation rate ω in the turbulence model were investigated independently of each other. It was shown that changing K had a weak impact on results, whereas the latter two parameters showed stronger dependencies. The improved VVG model constants from equation (4.19) were empirically determined, and it could be shown how the combined stresses improved in the near field downstream of the VVG. In summary, this study showed that the VVG models significantly changed the development and the distribution of stresses, including the near-field development close to the VVG forcing plane

Second, the VVG models were investigated in an APG flat-plate boundary-layer flow, comparable to the experiments by Lögdberg et al. (2010). It could be shown how the two VVG models performed under flow conditions including a separated region, comparable to the suction side of an airfoil. In total, the VVG model generally underpredicted skin-friction results compared to fully-resolved computations, even though the improved VVG model showed better results when compared to the original VVG model. Nevertheless, both VVG models successfully predicted attached flow on the flat plate, and this is in agreement with experiments and fully-resolved computational results.

In a last part, the VVG models were investigated in internal diffuser flow. The results showed that the VVG models generally underpredicted the increase of pressure-coefficient distributions in the expanding part in experiments. The VVG models were still capable of predicting the pressure recovery at the diffuser exit quantitatively correct. On the other hands, both VVG models predicted different flow states within the diffuser, but this could not be evaluated by experiments or fully-resolved computations. Nevertheless, the general findings

regarding the differences of flow-control capabilities between both VVG models from the APG flat-plate case could be confirmed by the diffuser flow case.

6.2. Paper 2

Evaluation of a Vortex Generator Model in Adverse Pressure Gradient Boundary Layers.

This paper presents the evaluation of the original VVG model in APG flatplate boundary-layer flow which was previously experimentally investigated by Lögdberg (2008). Lögdberg carried out studies including three different APG cases, whereas the computational investigations by the author concentrated on the most comprehensively studied case. The experiences and results from Paper 1 concerning the calibration of the VVG model were used and applied. Moreover, sensitivity studies of the VVG position upstream of the separation bubble complemented the previous research results. It could be shown by means of skin-friction as well as static-pressure distribution plots, that the VVG model showed strong sensitivity for the streamwise position, leading to a better separation prevention in terms of increased skin-friction results the further upstream the VVG model was applied within the APG region. If the VVG model was located too closely to the separated region, flow separation could not be prevented. The VVG was also positioned in the preceeding windtunnel ZPG region where the opposite flow-control effect was observed, i.e., decreasing skin-friction distributions for further upstream VVG positions.

Second, it could be shown that the original VVG model was capable of establishing the same overall flow states (attached/detached flow) as in experiments, i.e., when a VVG position variation, as well as a VVG height variation was investigated.

In total, this paper has shown that the original VVG model successfully describes the qualitative impact of passive VVGs on flow-separation control by means of the statistical-modelling approach and by using the original VVG model.

6.3. Paper 3

Evaluation and Parameterization of Round Vortex-Generator-Jet Experiments for Flow Control.

The aim of this study was to parameterize single-jet vortices in terms of the Lamb-Oseen vortex model, as well as to identify and to classify efficient VGJ parameter settings for flow-separation control. The contribution covers the evaluation of the VGJ experiments, previously carried out at Technische Universität Braunschweig, Germany. Single VGJs had been investigated over a broad VGJ parameter range, including variations of α , β , U_{∞} and λ . The vortex-velocity fields from experiments were parameterized by means of a nonlinear least-squares data fitting to the vortex model velocities. Thereby, fitted vortex-model parameters Γ_{max} , r_0 , and h_c for each single-jet setup were identified and thereby, allowed for the modelling of the vortex velocities from

experiments. It was shown that the Lamb-Oseen vortex model represented the experimental results well. From that, the spanwise-averaged vortex stresses $\Delta u_i'u_j'(y)$ of the modelled vortices could be derived and evaluated over a broad VGJ parameter setup range. A comparison of the single-jet vortex stresses to those for VGJ pairs in a counter-rotating common-flow-down configuration with a similar parameter setup was given, and the results showed high comparability between the single VGJs and the VGJ pairs.

In a second step, the fitted Lamb-Oseen vortex-model parameters $\Gamma_{\rm max}$, r_0 , and $h_{\rm c}$ were nondimensionalised and a results comparison study for $\alpha=45^{\circ}$ at the first near-field measurement plane was carried out. It could be shown that the most important VGJ parameters for the nondimensional parameters was the velocity ratio λ and that there occurs a variation for the skew angle β .

This contribution represented the starting point and provided essential information for the development of a statistical VGJ model for flow-separation control which is presented in Paper 4.

6.4. Paper 4

A Statistical Vortex-Generator-Jet Model for Turbulent Flow-Separation Control

This paper presents the ansatz for a statistical VGJ model and is, to a large extent, based on the findings of Paper 3. The Lamb-Oseen vortex model was chosen for the modelling of the vortex velocities, because it had shown satisfactory results in Paper 3. The statistical ansatz required the Lamb-Oseen vortex-model input parameters $\Gamma_{\rm max}$, r_0 , and $h_{\rm c}$, and in terms of the VGJ, a different approach was necessary when compared to the modelling of VVGs. The vortex generation was found to be fundamentally different for VGJs and therefore, an expression for $\Gamma_{\rm max}$ which did not originate from the LLT, needed to be determined. Empirical results for r_0 and $h_{\rm c}$, similar to the findings for VVGs, were also sought after.

The experimental results and the parameterization study from Paper 3 served as a starting point for the derivation of the fitted vortex-model parameters Γ_{max} , r_0 , and h_c . Based on that, nondimensional vortex-model parameters C_{Γ} , $C_{\rm r}$, and $C_{\rm h}$ as functions of the VGJ parameters β , Φ_{VGJ} , U_{∞} , and λ were successfully determined. Universal-valid empirical values for the nondimensional vortex-model parameters $C_{\rm r}$ and $C_{\rm h}$ were found based on the experimental results. An analytical expression for the vortex circulation $\Gamma_{\rm max}$, and a value for C_{Γ} were determined by inspecting the balance between the momentum of the injected jet and the momentum of the created fully-developed streamwise vortex further downstream in the flow. The analytical results for C_{Γ} could be confirmed by experimental results for the term C_{Γ} , and therefore, it is suggested that the expression for the vortex circulation $\Gamma_{\rm max}$ is reasonable. The determined nondimensional VGJ model parameters $C_{\Gamma} = 0.2$, $C_{\rm r} = 0.4$, and $C_{\rm h} = 0.6$ were used in the application of the VGJ model in ZPG flatplate flow. The analysis of results, as well as its comparison to the experiments

and fully-resolved computations gave satisfactory streamwise statistical vortexstress distributions. In the far field, where the vortices are fully-developed, results for the forced stresses compared mostly qualitatively well and a sensitivity of the VGJ model regarding λ and h_c could be observed. Nonetheless, in order to show the VGJ models's flow-separation capabilities, further evaluation studies should to be carried out.

6.5. Paper 5

Application of a Statistical Vortex Generator Model Approach on the Short-Chord Flap of a Three-Element Airfoil.

This conference paper presents the application of the original VVG model on the short-chord flap of the HELIX three-element airfoil. The challenge that is linked to the design of a short-chord is the higher flap deflection angle $\delta_{\rm F}$ which is required in order to achieve the same total lift force as for a conventional flap. Due to higher $\delta_{\rm F}$, flow separation is more likely to occur on a short-chord flap, and thus, VVGs may be a way to overcome separated flow on the suction side of the flap.

Experiments with the HELIX airfoil have shown that VVGs are able to prevent flow separation when applied at 25% flap chord c_{flap} . An application of the VVG model with a corresponding setup as from the experiments was, on the other hand, not capable of achieving attached flow on the flap. Therefore, different setup-parameter variations for the VVG model were investigated. Results for a streamwise-position variation of the VVG revealed that the DRSM-based VVG model does not work properly when the VVG is located in regions with heavily separated flows. It was found that flow-separation prevention was essentially enabled when the VVG was positioned very close to the flap leading edge. In the same manner, the VVG height has an impact on the flow-separation capabilities since higher vane-tip velocities generate stronger vortex stresses by the VVG model. However, successful flow-separation control could be shown up to 8% c_{flap} which is rather far upstream when compared to experiments (25% c_{flap}). The VVG model showed its capabilities and shortcomings for flow-separation control on an airfoil high-lift system and based on these results, a further development of the original VVG model could be motivated.

CHAPTER 7

Concluding Remarks and Outlook

This thesis deals with flow-separation control by means of VVGs as well as VGJs, and the methods to model these flow-separation-control devices in a statistical sense.

The statistical VVG model has been evaluated by means of different flow cases in this thesis: ZPG and APG flat-plate boundary-layer flow, APG diffuser flow, and the external flow around the HELIX three-element airfoil with a short-chord flap. It could be generally shown that the original VVG model predicts the influence of such passive flow-control devices qualitatively correct. Nevertheless, it could also be observed how the flow-control effect of the original VVG model was in many cases lower than expected, for example when compared to corresponding experiments or fully-resolved VVG computational results. As discussed in section 5.2, the $\overline{u'v'}$ Reynolds stresses are generated through the production term \mathcal{P}_{12} in the turbulence model that, in turn, need a certain streamwise distance to properly develop. This causes a large variation of the $\overline{u'v'}$ Reynolds stresses in the near field, as can be seen in figure 5.3. Nonetheless, the original VVG model showes very satisfactory results in an APG flat-plate boundary-layer and diffuser flow, preventing flow separation as predicted by fully-resolved computations and experiments.

An improved statistical VVG model was developed based on the original VVG model which enables a direct forcing of the additional vortex stresses $\Delta \overline{u'u'}$ and $\Delta \overline{u'v'}$. Thus, the important shear stresses $\Delta \overline{u'v'}$ can directly act from the improved VVG model forcing plane, and are able to to mix the boundary layer even in the very near field. The development of the improved VVG model represents a more comprehensive flow-separation-control model and its potential should be examined further in the future. The HELIX airfoil case represents an adequate flow case for that, because original VVG results are available; see section 5.3. The improved VVG model may be able to describe the prevention of flow separation also for VVG closer to 25% $c_{\rm flap}$, so that results may become more comparable to experiments.

In terms of flow-separation control with VGJs, experimental and computational data were analysed in this thesis. It was assumed that VGJ arrays may be represented by single VGJs when the design criteria of a certain minimum VGJ actuator distance D is fulfilled. A parameterization of the experimental single-jet results by means of a nonlinear least-squares data fitting led to a validation of the Lamb-Oseen vortex model to successfully represent fully-developed

vortices from single VGJs. Dependencies of the Lamb-Oseen vortex-model parameters on the VGJ parameters have shown that the vortex circulation Γ_{max} was dependent on the freestream Reynolds number, the velocity ratio λ , and, for high U_{VGJ} , also on the Mach number Ma. A higher value for λ increased the vortex strength and efficiency of the jet, whereas compressible effects for high λ showed opposite trends when compared to low Ma cases.

In another study, the statistical VGJ model was evaluated in ZPG flat-plate boundary-layer flow. The results showed reasonably good agreement with fully-resolved RANS computations, as well as with experiments. Parameter variations for λ and $U_{\rm VGJ}$ were carried out and vortex stress results downstream of the VGJ were presented. The VGJ model results are considered to be satisfactory for the first ansatz of this idealized statistical VGJ model.

For future studies, it is suggested to apply the VGJ model to APG boundary-layer flows, similar to those of the investigations for the VVG models. A direct comparison between VGJ model and corresponding fully-resolved VGJ computations may illustrate interesting differences concerning the flow-separation control capabilities of VGJs. An improved description of the VGJ model, similar to the improved VVG model, should be considered as a next logical step towards an enhanced VGJ model. Even though the vortex creation for active VGJs is fundamentally different compared to the distinct vortex-shedding from passive VVGs, such an improvement could ameliorate the flow-separation-control abilities of the VGJ model in the very near field behind the VGJ forcing plane.

In terms of the investigated flow cases for the VGJ model, LES analyses have the potential to also resolve for the small-scale turbulent eddies, as well as the momentum mixing in the shear layer between the incoming turbulent boundary layer and the jet. They may play, although the opposite was reported by some researchers, an important role in the final vortex creation, development and its decay. An option to extend the current VGJ model for periodic excitation would also be a consideration, which has shown to be more efficient than steady-jet blowing. One option could be to establish the time-dependent application of vortex stresses in the flow or, as a second and more realistic alternative, to find an expression for the given "steady blowing" statistical VGJ model in terms of nondimensional parameters C_{Γ} , C_{r} , and C_{h} that may represent an equivalent to the periodic excitation mode.

CHAPTER 8

Papers and Authors' Contributions

Paper 1

Vortex-Generator Models for Zero- and Adverse-Pressure-Gradient Flows F. von Stillfried (FS), S. Wallin (SW) & A.V. Johansson (AJ), 2012, AIAA Journal $\bf 50(4)$, pp. 855-866, DOI: 10.2514/1.J051169.

This work is of computational character on the development and the evaluation of two statistical VVG models for passive VVGs in ZPG and APG flat-plate boundary-layer flow. The computations, the data analysis, as well as the writing was done by FS with considerable help and supervision by SW and AJ. SW provided results for the diffuser study. Parts of these results have been presented and published in:

Statistical Modeling of the Influence of Turbulent Flow Separation Control Devices

F. VON STILLFRIED, S. WALLIN & A.V. JOHANSSON, 2009, 47^{th} AIAA Aerospace Sciences Meeting, Orlando, FL, USA, AIAA Paper 2009-1501.

Statistical Modeling of Vortex Generators in Pressure Gradient Boundary Layers

F. VON STILLFRIED, S. WALLIN & A.V. JOHANSSON, 2009, Sixth International Symposium on Turbulence and Shear Flow Phenomena, Seoul National University, Seoul, Korea, Conference Proceedings, Vol. II, pp. 647-652.

An Improved Passive Vortex Generator Model for Flow Separation Control F. von Stillfried, S. Wallin & A.V. Johansson, 2010, 5th AIAA Flow Control Conference, Chicago, IL, USA, AIAA Paper 2010-5091.

Paper 2

Evaluation of a Vortex Generator Model in Adverse Pressure Gradient Boundary Layers

F. VON STILLFRIED (FS), S. WALLIN (SW) & A.V. JOHANSSON (AJ), 2011, AIAA Journal $\bf 49(5)$, pp. 982-993, DOI: 10.2514/1.J050680.

This work is of computational character on the evaluation of the original statistical VVG model in APG flat-plate boundary-layer flow. The computations, the data analysis, as well as the writing was done by FS with considerable help and supervision by SW and AJ. Parts of these results have been presented and published in:

Statistical Modeling of Vortex Generators in Pressure Gradient Boundary Layers

F. VON STILLFRIED, S. WALLIN & A.V. JOHANSSON, 2009, Sixth International Symposium on Turbulence and Shear Flow Phenomena, Seoul National University, Seoul, Korea, Conference Proceedings, Vol. II, pp. 647-652.

Paper 3

Evaluating and Parameterizing Round Vortex Generator Jet Experiments for Flow Control

F. VON STILLFRIED (FS), S. WALLIN (SW), A.V. JOHANSSON (AJ), M. CASPER (MC) & J. ORTMANNS (JO), 2012, accepted for publication in AIAA Journal.

This work is of experimental and analytical character and deals with the evaluation of VGJs in a ZPG flat-plate boundary-layer flow. The experiments were carried out by JO and MC at Technische Universität Braunschweig, Germany. The data analysis and the writing was done by FS with considerable help and supervision by SW and AJ, as well as with inputs from JO and MC. Parts of these results have been presented and published in:

Evaluating Vortex Generator Jet Experiments for Turbulent Flow Separation Control

F. VON STILLFRIED, T. KÉKESI, S. WALLIN & A.V. JOHANSSON, 2011, European Turbulence Conference 13, Warsaw, Poland, *Journal of Physics: Conference Series 318 022038*, DOI:10.1088/1742-6596/318/2/022038.

Paper 4

 $A\ Statistical\ Vortex-Generator-Jet\ Model\ for\ Turbulent\ Flow-Separation\ Control$

F. VON STILLFRIED (FS), S. WALLIN (SW) & A.V. JOHANSSON (AJ), 2012, submitted to AIAA Journal.

This work is of computational character on the development of a statistical VGJ model for active VGJs. The data analysis and the writing was done by FS with considerable help and supervision by SW and AJ. Parts of these results have been presented and published in:

A Novel Modeling Approach for Vortex Generator Jet Flow Separation Control F. von Stillfried, S. Wallin & A.V. Johansson, 2012, 50th AIAA Aerospace Sciences Meeting, Nashville, TN, USA, AIAA Paper 2012-0742.

Paper 5

Application of a Statistical Vortex Generator Model Approach on the Short-Chord Flap of a Three-Element Airfoil

F. VON STILLFRIED (FS), S. WALLIN (SW) & A.V. JOHANSSON (AJ), 2009, presented at the KATnet II conference on Key Aerodynamic Technologies, 12-14 May, Bremen, Germany

This work is of computational character on the development of the original VVG model in APG boundary-layer flow of a three-element airfoil. The basic computational grid as well as the experimental data were provided by Ulf Tengzelius of FOI. The data analysis and the writing was done by FS with considerable help and supervision by SW and AJ.

Acknowledgements

No book is ever the product of only one individual's efforts, and it is clear that this one is not any different. I could never have realised it without the help and suggestions of many supportive friends and colleagues.

I would like to express my sincere thanks to my supervisors, Arne Johansson and Stefan Wallin, for their guidance and the very fruitful and enlightning meetings, as well as for their support during all the time. Moreover, I am very thankful for the numerous and accurate discussions with Arne and Stefan that significantly increased the quality of the submitted papers.

I am grateful for the support and the helpful comments of Ola Lögdberg of Scania AB, Sweden, concerning his experimental work on VVGs at KTH which were essential for the comparison studies that I carried out.

Moreover, I am glad to have experienced a very welcoming and friendly working atmosphere during my entire stay at the Institute of Fluid Mechanics of Technische Universität Braunschweig, Germany, and I especially thank Marcus Casper and Peter Scholz for the successful cooperation, the support, and the kind provision of experimental data within our collaborative research project on VGJs. Jens Ortmanns of Rolls-Royce Germany is highly acknowledged for the very kind and straightforward assistance concerning his former PhD project on VGJs.

During my time as a PhD candidate, I have been quite many times at FOI in Kista, and I have to mention at least the following colleagues for their support from which I benefitted during the last years: Peter Eliasson and Olof Grundestam for their comprehensive support concerning the CFD code Edge, Ulf Tengzelius who helped me with the HELIX airfoil case, Henrik Edefur for his assistance in mesh-generation techniques in ICEM, and Oskar Enoksson for the support regarding the tunnan computer cluster.

Many special thanks to my former and present office colleagues, as well as to everybody from the department who regularly played indoor hockey with me; good times I will never forget. Moreover, I have always experienced a very friendly working atmosphere at KTH Mechanics and I feel very much indebted to all the above individuals, and to those colleagues who have crossed my ways whose names I have not listed, and who have assisted, inspired, and enlightened me one way or another ever since I started working at KTH in September 2007.

Furthermore, the financial support of the Erich-Becker foundation of Fraport AG, Germany, is highly appreciated.

Last but not least I take full responsibilty for misapprehensions, omissions and oversimplifications in this thesis. Nonetheless, I hope that the rest of this book creates new insights and gives new knowledge to the flow-control community.

Thank you all.

Stockholm, May 2012 Florian von Stillfried

References

- Barth, T., Scholz, P. & Wierach, P. 2011 Flow Control by Dynamic Vane Vortex Generators Based on Piezoceramic Actuators. AIAA Journal 49 (5), 921 – 931.
- Bender, E. E., Anderson, B. H. & Yagle, P. J. 1999 Vortex Generator Modelling for Navier-Stokes Codes. *American Society of Mechanical Engineers, FEDSM* 99-6919.
- Casper, M. 2011 Personal communication.
- COMPTON, D. A. & JOHNSTON, J. P. 1992 Streamwise Vortex Production by Pitched and Skewed Jets in a Turbulent Boundary Layer. *AIAA Journal* **30** (3), 640 647.
- DUDEK, J. C. 2006 Empirical Model for Vane-Type Vortex Generators in a Navier-Stokes Code. AIAA Journal 44 (8), 1779 1789.
- Dudek, J. C. 2011 Modeling Vortex Generators in a Navier-Stokes Code. AIAA Journal **49** (4), 748 759.
- GLAUERT, H. 1926 The Elements of Aerofoil and Airscrew Theory, 1st edn. Cambridge University Press, London, UK.
- GLEYZES, C. & PAILHAS, G. 2011 Flow Control using Continuous Fluidic Vortex Generators. Validation of a Simple CFD Model of the Interaction Between a Boundary Layer and an Inclined Jet. AIAA Paper 2011-3849.
- GODARD, G. & STANISLAS, M. 2006 Control of a Decelerating Boundary Layer. Part 1: Optimization of Passive Vortex Generators. Aerospace Science and Technology 10 (3), 181 – 191.
- JIRÁSEK, A. 2005 A Vortex Generator Model and its Application to Flow Control. Journal of Aircraft 42 (6), 1486 – 1491.
- Johnston, J. P., Mosier, B. P. & Khan, Z. U. 2002 Vortex Generating Jets: Effects of Jet-Hole Inlet Geometry. *International Journal of Heat and Fluid Flow* 23, 744 749.
- JOHNSTON, J. P. & NISHI, M. 1990 Vortex Generator Jets Means for Flow Separation Control. AIAA Journal 28 (6), 989 994.
- Khan, Z. U. & Johnston, J. P. 2000 On Vortex Generating Jets. *International Journal of Heat and Fluid Flow* 21, 506 511.
- LIN, J. C. 2002 Review of Research on Low-Profile Vortex Generators to Control Boundary-Layer Separation. Progress in Aerospace Sciences 38, 389 – 420.
- LIN, J. C., SELBY, G. & HOWARD, F. 1991 Explority Study of Vortex-Generating Devices for Turbulent Flow Separation Control. AIAA 1991-0042.

- LÖGDBERG, O. 2008 Turbulent Boundary Layer Separation and Control. PhD thesis, Department of Mechanics, KTH Stockholm.
- LÖGDBERG, O., ANGELE, K. & ALFREDSSON, P. H. 2010 On the Robustness of Separation Control by Streamwise Vortices. *European Journal of Mechanics B/Fluids* **29** (1), 9 17.
- LÖGDBERG, O., FRANSSON, J. H. M. & ALFREDSSON, P. H. 2009 Streamwise Evolution of Longitudinal Vortices in a Turbulent Boundary Layer. *Journal of Fluid Mechanics* 623, 27 58.
- Mahmood, S. & Radespiel, R. 2009 RANS Simulation of Jet Actuation in a Boundary Layer-Flow using Chimera Grids. *Deutscher Luft- und Raumfahrtkongress, September 8-10, Aachen, Germany.*
- Mahmood, S. & Radespiel, R. 2011 Detached-Eddy Simulation of Vortex Generator Jet using Chimera Grids. *International Conference on Computational Fluid Dynamics, July 27-29, Paris, France.*
- ORTMANNS, J. 2008 Aktive Grenzschichtbeeinflussung mittels Pneumatischer Wirbelgeneratoren bei großen Reynoldszahlen. PhD thesis, Institut für Strömungsmechanik, Technische Universität Braunschweig.
- ORTMANNS, J. & KÄHLER, C. J. 2007 The Effect of a Single Vortex Generator Jet on the Characteristics of a Turbulent Boundary Layer. *International Journal of Heat and Fluid Flow* **28**, 1302 1311.
- Pauley, W. R. & Eaton, J. K. 1988 Experimental Study of the Development of Longitudinal Vortex Pairs Embedded in a Turbulent Boundary Layer. *AIAA Journal* **26** (7), 816 – 823.
- Pearcey, H. H. 1961 Part IV: Shock-Induced Separation and its Prevention by Design and Boundary Layer Control. In *Boundary Layer and Flow Control*, its *Principles and Applications* (ed. G. V. Lachmann), pp. 1170 1344. Pergamon, Oxford, UK.
- Pope, S. B. 2000 Turbulent Flows. Cambridge, UK: Cambridge University Press.
- PRANDTL, L. 1921 Applications of Modern Hydrodynamics to Aeronautics. *Tech. Rep* Rept. No. 116. NACA.
- Selby, G. V., Lin, J. C. & Howard, F. G. 1992 Control of Low-Speed Turbulent Separated Flow using Jet Vortex-Generators. *Experiments in Fluids* **12**, 394 – 400
- VON STILLFRIED, F., WALLIN, S. & JOHANSSON, A. V. 2011a Evaluation of a Vortex Generator Model in Adverse Pressure Gradient Boundary Layers. *AIAA Journal* 49 (5), 982 993.
- VON STILLFRIED, F., WALLIN, S. & JOHANSSON, A. V. 2011b Vortex-Generator Models for Zero- and Adverse-Pressure-Gradient Flow. AIAA Journal ${\bf 50}$ (4), 855-866.
- TÖRNBLOM, O. 2006 Experimental and Computational Studies of Turbulent Separating Internal Flows. PhD thesis, Department of Mechanics, KTH Stockholm.
- TÖRNBLOM, O. & JOHANSSON, A. V. 2007 A Reynolds Stress Closure Description of Separation Control with Vortex Generators in a Plane Asymmetric Diffuser. *Physics of Fluids* **19** (115108).
- WENDT, B. J. 2004 Parametric Study of Vortices Shed from Airfoil Vortex Generators. AIAA journal 42 (11), 2185 2195.

- Wilcox, D. C. 1988 Reassessment of the Scale Determining Equation for Advanced Turbulence Models. AIAA Journal 26 (11), 1299 1310.
- YAO, C.-S., LIN, J. C. & ALLAN, B. G. 2002 Flow-Field Measurement of Device-Induced Embedded Streamwise Vortex on a Flat Plate. AIAA Paper 2002-3162.
- Zhang, X. 2003 The Evolution of Co-Rotating Vortices in a Canonical Boundary-Layer with Inclined Jets. *Physics of Fluids* **15** (12), 3693 3702.
- Zhang, X. & Collins, M. W. 1997 Nearfield Evolution of a Longitudinal Vortex Generated by an Inclined Jet in a Turbulent Boundary Layer. *Journal of Fluids Engineering* **119**, 934-939.

Part II

Papers

Paper 1

Vortex-Generator Models for Zero- and Adverse-Pressure-Gradient Flows

By Florian von Stillfried, Stefan Wallin, and Arne V. Johansson

Royal Institute of Technology, 100 44 Stockholm, Sweden

AIAA Journal **50**(4), pp. 855 – 866, DOI: 10.2514/1.J051169.

A computational fluid-dynamics investigation, including passive vortex-generators (VGs) that generate streamwise counter-rotating vortex structures, usually requires a grid including fully-resolved VG geometries and vortex structures with a corresponding large number of grid points to obtain an accurate solution. An efficient way to avoid such a setup and time-consuming process in turbulent shear-layer flows is to introduce statistics-based vortex-generator modelling. The second-order statistics of the initial vortices are computed by using a vortex model in combination with the lifting-line theory. The statistics are added as additional turbulence stress terms to the equations within a differential Reynolds stress-turbulence model. In this investigation, results from statistical VG model computations for zero- and adverse-pressure-gradient flat-plate boundary-layer flows, as well as for the flow in a plane asymmetric diffuser, are evaluated against results from fully-resolved VG computations and experiments. It could be shown that the initial near-field forcing is too weak for the proposed VG model. An improved VG model description removes some drawbacks by adding additional statistical forcing terms. Results become more comparable, resulting in improved predictions when compared to experiments and fully-resolved computations.

1. Introduction

The operational envelope in aeronautical, as well as other engineering designs, is in many cases limited by turbulent boundary-layer separation. The possibility of controlling and delaying the separation region enables more efficient designs that can be used for improving the performance or for optimizing the design in order to reduce drag and weight. Turbulent boundary layers can be energized by generating streamwise vortices originating from vortex-generators (VGs) that increase the momentum mixing in the boundary layer and thus increase the near-wall velocity. This generally delays flow separation or even totally prevents the near-wall flow separation. Advantages of attached flow, compared to separated flow, are generally higher efficiency, lower drag generation, and

decreased dynamic loads. On the other hand, nonretractable passive VGs may generate a certain amount of additional drag to the flow. Still this drawback is mostly balanced by the benefits of attached flow and the overall decreased drag. A method to reduce parasitic drag is to use retractable solid VGs or VGs in the form of, for example, steady or pulsed jets. These methods are not studied in this investigation.

Pearcey (1961) published one of the first extensive articles about boundary-layer control and separation prevention. The article contains a chapter about the overall design of boundary-layer control, its requirements, and passive VGs, their mechanism, types, and design criteria, as well as a part including VG jets for flow control. Concerning passive VGs, Pearcey discusses different kinds of VG settings such as corotating, counter-rotating settings, different types of VG geometries, and the influence of the vortex strength and the VG scale. The overall defining parameter for successful and unsuccessful VG designs was the VG-generated drag, and Pearcey presents successful VG designs for the application on aircraft wings and airfoils.

An experimental investigation conducted by Pauley & Eaton (1988) examines the vortex structures that are generated by delta-shaped VGs in counterrotating and corotating settings. Their VGs were attached to a flat plate in a zero-pressure-gradient (ZPG) boundary-layer and had a VG height h of approximately 150% of the local boundary layer thickness δ_{99} . Pauley and Eaton quantified the VGs by an investigation of the streamwise vorticity and circulation of the downstream development of the interacting vortex structures. They found out that a common-flow-up setting leads to higher vortex interaction compared to a common-flow-down setting. Moreover, strong interactions with neighboring vortices diffuse vorticity faster, leading to larger decreases in vorticity for common-flow-up VG pairs. The primary mechanism for decreasing the vortex circulation was found to be the spanwise component of the skin friction. Because common-flow-down VGs interact more strongly with the viscous near-wall flow, it was concluded that this setting is likely to lose more circulation strength than common-flow-up VGs.

Lin (2002) has presented a comprehensive overview of sub-boundary layer vortex-generators (SBVG) research. As a result, SBVGs are most efficient when flow separation is relatively fixed. Efficiency is further increased by the avoidance of unnecessarily large VGs, and therefore a small penetration into the flow is desired, enabling a minimal yet sufficient vortex-strength generation for flow-separation prevention. For that purpose, it is important to significantly reduce h and a maximum of 50% of δ_{99} is suffcient to increase the overall efficiency and decrease the parasitic drag.

An experimental study including VGs mounted in adverse-pressure-gradient (APG) boundary-layer flow was carried out by Godard & Stanislas (2006). The aim was to describe optimal VG parameters to control the separation bubble for such a flow case. Specifically, skin-friction distributions characterize the VG effectiveness on flow-separation control. As a conclusion, it can be said that

Godard and Stanislas showed that skin-friction measurements represent a very good tool for the investigation of VGs for flow separation control.

By using computational fluid dynamics (CFD), engineers and researchers face additional challenges when including passive VGs. Most commonly, fully-resolved VGs and the downstream vortex structures are embedded into a three-dimensional computational mesh, leading to a very high number of grid points. Even though this is a very direct strategy, the implementation is very time-comsuming and a parameter variation of VGs leads to high redesign and remeshing costs.

Consequently, the use of VG models that substitute fully-resolved VGs has become more popular during the last decade. In particular, Bender et al. (1999) introduced the Bender-Anderson-Yagle (BAY) VG model that uses a side-force source term normal to the local flow and parallel to the VG model forcing plane. The BAY VG model basically uses the Prandtl lifting-line theory (Glauert 1926; Anderson 1991) (LLT) and adjusts the local flow velocity with the VG, depending on an empirical model constant that can be difficult to define correctly. For the VG model to work, grid points that are supposed to be located within the VG vane need to be identified by the user to apply the forcing at the correct location. As pointed out by Jirásek (2005), the BAY VG model approach is therefore strongly grid dependent. Moreover, VG arrays containing more than one VG in the spanwise direction can be modelled by the BAY model. Yet, the VG array is simplified and reduced to a single distributed forcing along the spanwise direction that encloses the entire VG array that is forcing the flow.

Jirásek (2005), on the other hand, suggested an improved BAY model by removing the described disadvantages and called it jBAY model, because it is a further development of the BAY model. The two approaches have in common that computational meshes require three dimensions in order to account for the forcing source term at the modelled VG position. The jBAY model removes the need to include geometrical structures of the VGs in the mesh, and the forcing is now applied on zero-thickness surfaces, representing each VG vane. Nevertheless, the generated vorticies are resolved and, thus, the region downstream of the vortex-forcing region must be sufficiently resolved in all three dimensions.

Further simplifying the modelling and the application of VGs in a CFD analysis, Törnblom & Johansson (2007) suggested a statistical VG model that uses a Reynolds stress approach in a statistical sense. Additional vortex stresses that originate from the VGs are added to the Reynolds stress-transport (RST) equations. The core of this model is a Lamb-Oseen vortex model in combination with the Prandtl LLT that takes most of the VG's geometrical aspects into account. By spanwise-averaging the second-order correlations of the additional vortex-velocity field in the forcing plane, vortex stress contributions are computed and added to the Reynolds stress tensor. An advantage of this method is that no local mesh refinement is needed and that the computational costs

are comparable to solving the Reynolds-averaged Navier-Stokes (RANS) equations, thus enabling design and optimization studies for optimal VG settings by using CFD analysis.

The main objective of this work was to carefully examine the VG model approach by Törnblom & Johansson (2007) that statistically describes the effects of the vortex-induced mixing generated by modelled VGs. In addition, an improved VG model is presented here, and the differences in results between both approaches are compared. Firstly, a turbulent boundary layer on a flat plate in ZPG flow was used for a calibration and validation against experimental data and fully-resolved RANS computations; see also von Stillfried *et al.* (2009). Second, the VG models were validated in separated flows, such as an APG flat-plate flow and a plane asymmetric diffuser; see also Törnblom (2006).

2. Analytical and Numerical Methods

The modelling of the VGs in this investigation follows that suggested by Törnblom & Johansson (2007), who presented a model that neither requires mesh refinements nor fully-resolved computations. In this model approach, the VGs are represented by a vortex source model that uses the (LLT) (Glauert 1926) to estimate the generation of the circulation Γ by the VG vanes. The circulation distribution $\Gamma(y)$ across a wing section in free-flight conditions at a spanwise coordinate y can be estimated in accordance with the LLT:

$$\Gamma(y) = \frac{K}{2}U(y)c(y)\left[\alpha(y) - \frac{w(y)}{U(y)}\right],\tag{1}$$

where K is the local section lift slope of the wing $(K_{\text{max}} = 2\pi \text{rad}^{-1} \text{ for a thin flat plate}^1)$, U(y) is the local incoming freestream velocity, c(y) the local chord length of the wing, $\alpha(y)$ the local angle of attack, and w(y) the local downwash velocity due to the trailing vortex sheets. The ratio w(y)/U(y) is the local induced angle of attack $\alpha_{\text{ind}}(y)$ for small angles α , and the local downwash velocity w(y) reads

$$w(y) = \frac{1}{4\pi} \int_{-h}^{h} \frac{d\Gamma}{dy'} \frac{1}{y' - y} dy'. \tag{2}$$

Equations (1) and (2) are solved by means of a Fourier-series ansatz; fo example, see Anderson (1991). The LLT holds for high-aspect-ratio wings in free-flight conditions for small angles of attack α far away from obstacles in the flow. By modelling VG vanes that are mounted in wall-bounded flows by means of the LLT, some of its assumptions are not valid anymore as a result of 1) a boundary-layer velocity profile U(y) instead of a constant freestream velocity U_{∞} ; 2) VG vanes being wings with very low aspect ratios; 3) possible side effects due to the proximity of neighboring VG blades (i.e. neighboring

 $^{^{1}}$ The unit rad $^{-1}$ will generally be neglected when K is mentioned in the rest of this paper

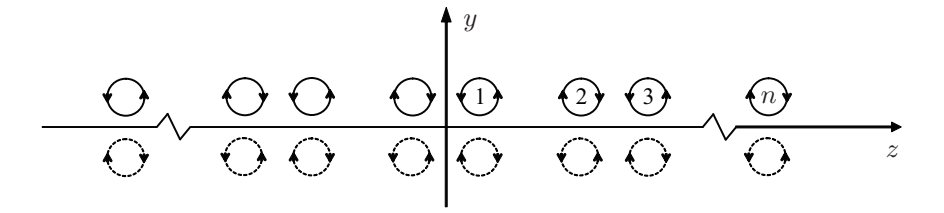


FIGURE 1. Scheme of a VG array with n counter-rotating vortex pairs and their mirror images for computing the total superposition of the vortex-induced velocity field $V_i(y,z)$ in the VG forcing plane. [Image inspired by Törnblom & Johansson (2007).]

streamwise vortices); and 4) a reasonably high angle of incidence α of the VG vanes

Therefore, the LLT should only be regarded as an approximation for the estimation of the circulation distribution $\Gamma(y)$ across the VGs. In turn, the circulation distribution $\Gamma(y)$ estimates the generated lift, the induced drag, and the vortex strength, which is again needed as an input for the vortex model that is used. The vortices are represented by a Lamb-Oseen vortex model with the azimuthal velocity distribution

$$V_{\Phi}(r) = \frac{\Gamma_{\text{max}}}{2\pi r} \left[1 - e^{-\left(\frac{r}{r_0}\right)^2} \right], \tag{3}$$

where $\Gamma_{\rm max}$ is the maximum value of the circulation distribution $\Gamma(y)$ [see equation (1)], r_0 is the vortex core radius, and r is the radial coordinate from the vortex center. A limitation of the Lamb-Oseen vortex model is that it accounts for a constant streamwise velocity component. Besides that, Velte et al. (2009) investigated vortex structures experimentally and has shown that passive VGs at higher angles of incidence (i.e. $\alpha=20$ - 40 deg) produce vortices with helical structures. These vortex structures can be modelled, using a simplified Batchelor vortex model (Batchelor 1964) for the azimuthal and axial velocity distributions.

Generally, VG arrays consist of several VG pairs that influence the total vortex-induced velocity field everywhere at the VG array position. Becasue of that, a superposition of the individual vortex-induced velocity fields $V_{\Phi}(r)$ from equation (3) is carried out for each VG vane and its mirror image, resulting in the composite vortex-velocity field $V_i(y,z)$ at the VG position; see figure 1 and equation (4):

$$[V_2, V_3](y, z) = \sum_{n=1}^{\infty} (-1)^{n+1} \sum_{m=1}^{4} (-1)^{m+1} \frac{V_{\Phi}(r_m)}{r_m} [\Delta z_m, -\Delta y_m], \tag{4}$$

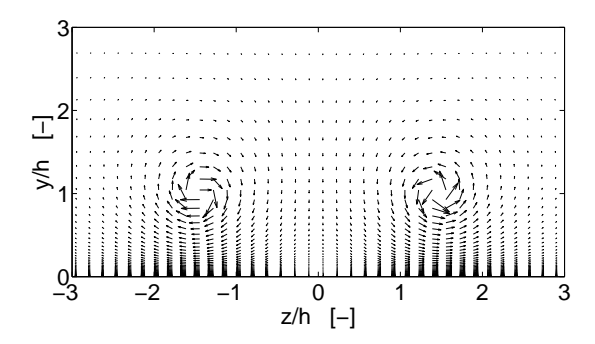


FIGURE 2. Total vortex-velocity field $V_i(y, z)$ between $-3 \le z/h \le 3$, originating from n = 5 counter-rotating VG pairs.

where

$$r_m = \sqrt{\Delta y_m^2 + \Delta z_m^2},\tag{5}$$

and

$$\Delta y_1 = y - h,$$
 $\Delta z_1 = z - z_n,$
 $\Delta y_2 = y + h,$ $\Delta z_2 = z - z_n,$
 $\Delta y_3 = y + h,$ $\Delta z_3 = z + z_n,$
 $\Delta y_4 = y - h,$ $\Delta z_4 = z + z_n,$ (6)

where this description and its total vortex-velocity distribution $[V_2, V_3](y, z)$ is only valid for a counter-rotating setting with n identical VG pairs in the absence of crossflow. For the statistical approach, n=5 VG pairs are a reasonable choice in order to obtain a converged velocity field around z=0; see figure 2. Moreover, the wall boundary at y=0 acts approximately as a symmetry condition for the vortices, which is simulated by introducing mirror image vortices. Thereby, a zero normal velocity $V_2(y=0,z=0)$ is ensured at the wall. Moreover, a wall damping function, for example $(1-\exp[-20y/h])$, needs to be introduced and applied on equation (7) because the vortex velocities V_3 in the spanwise direction at the wall boundary y=0 will not cancel out and would result in a finite value in equation (7). The wall damping function influences the $\Delta \overline{w'w'}(y)$ stresses and ensures correct boundary conditions for the $\Delta \overline{w'w'}(y)$ distribution so that $\Delta \overline{w'w'}(0)=0$. The specific choice of the wall function is not critical for the downstream distribution evolution since it only acts very close to the wall boundary (for $y \leq h/20$).

The concept of the VG model approach and describing its effects on the flow is to assume that the second-order statistics of the additional vortex-velocity field from equation (4) act as additional stresses on the mean flow. By making this assumption, the additional spanwise-averaged vortex stresses $\Delta u_i'u_j'(y)$ are

as follows [see Törnblom & Johansson (2007) for details]:

$$\Delta \overline{u_i' u_j'}(y) = \frac{1}{D} \int_{-D/2}^{D/2} V_i(y, z) V_j(y, z) dz.$$
 (7)

It is sufficient to integrate and spanwise-average the second-order statistics in equation (7) over one VG pair distance D because the resulting vortex flowfield is periodic in the spanwise direction z. Additional vortex stress contributions from equation (7) are only nonzero for $\Delta v'v'$ and $\Delta w'w'$.

2.1. Adding the
$$\Delta \overline{u_i'u_i'}$$
 Vortex Stresses

The general procedure to add the resulting vortex stresses from equation (7) to the RST equations is done via a so-called triple decomposition of the instantaneous velocity field u_i . This concept was already presented in a previous paper (von Stillfried *et al.* 2011*a*) by the authors, but it is considered to be helpful for an easier understanding of the concept so that we introduce it here again.

First, the additional total vortex velocities V_i at the forcing plane x_{VG} are added to the decomposed velocity field from the general ansatz for the RANS equations:

$$u_i(y, z, t) = U_i(y) + u'_i(y, z, t) + V_i(y, z),$$
 (8)

where U_i and u'_i are the mean velocity and the turbulent fluctuations, respectively. One possibility is to add V_i to the mean flow U_i in a RANS computation, thus resolving the generated vortices and expressing the turbulent part u'_i through a conventional turbulence model. We follow a different approach where V_i is added to the turbulent fluctuations u'_i . The combined velocity field v'_i from the turbulence and vorticies is thus

$$v_i'(y,z,t) \equiv u_i'(y,z,t) + V_i(y,z). \tag{9}$$

Note that $v_i'(y,z,t)$ is here used to denote the combination of turbulent fluctuations $u_i'(y,z,t)$ as well as the vortex-velocity field $V_i(y,z)$ and should not be confused with the instantaneous velocity component in the y-direction v(y,z,t). Then, the additional second-order statistics of the vortex-velocity field $\overline{V_iV_j}$ enter the RST equation by substituting the Reynolds stress tensor $\overline{v_i'v_j'}$, where

$$\overline{v_i'v_j'}(y) = \overline{(u_i' + V_i)(u_j' + V_j)}
= \overline{u_i'u_j'}(y) + \Delta \overline{u_i'u_j'}(y),$$
(10)

and

$$\Delta \overline{u_i' u_j'}(y) \equiv \overline{V_i V_j}(y) \tag{11}$$

are written for the additional contribution from the vortex stresses from equation (7). The cross-product terms in equation (10), containing the correlations

 $\overline{u_i'V_j}$ and $\overline{u_j'V_i}$, are zero because the mean is derived as the average in z as well as in time, and the velocity field $V_i(y,z)$ is steady.

The additional stresses $\Delta u_i' u_j'(y)$ are added to the Reynolds stress equations as surface source terms at the VG location, see Fig. 3(a). This is slightly different from the approach taken by Törnblom & Johansson (2007), who used a volume force in a region close to the VG. The downstream development of the combined stresses, $\overline{v_i'v_j'}$ is then described by an ordinary RST turbulence model without any other modifications except the forcing at the VG position.

Investigations of the VG model were also conducted with the CFD solver Edge, a general purpose CFD code developed by the Swedish Defence Research Agency FOI; see Eliasson (2002). Within Edge, the formulation of the VG model is slightly generalized compared to the analytical description in this chapter. First, a preprocessing routine localizes the grid lines that cross the VG forcing plane. Then, during processing, the input for the LLT is interpolated from the solution, and the lift distribution is computed for every iteration. The VG model is applied, and the additional vortex stresses are evaluated. In a last step, the vortex stresses are applied on the VG forcing plane. Moreover, equations (4) to (6) are generalized for an individual setting of the VG pairs and is therefore not restricted to counter-rotating settings, considering also crossflow.

2.2. Improved VG Model

The energy transfer between the different components is establised by an RST model, enabling the direct and indirect production of the $\overline{u'v'}(y)$ and $\overline{u'u'}(y)$ Reynolds stresses, which are initially not forced by the VG model. The limitation of the original VG model from equation (7) is that the $\Delta \overline{u'v'}(y)$ and $\Delta \overline{u'u'}(y)$ terms are not forced, and the development of these terms is delayed; for example, see the flat plate results in chapter 5. It is therefore chosen to also investigate an extended VG model that includes the extra $\Delta \overline{u'v'}(y)$ and $\Delta \overline{u'u'}(y)$ vortex stresses. In particular, the $\Delta \overline{u'v'}(y)$ forcing is of importance because of the direct coupling to the mean flow equation in thin shear flows. An extended vortex model with a radial variation of the streamwise velocity will not contribute to the $\Delta \overline{u'v'}(y)$ stresses because u' and v' will be uncorrelated. Instead, the main mechanism for the production of $\Delta \overline{u'v'}(y)$ is the upsweep/downsweep of the low/high-speed velocity within the boundary layer. Similar to a mixing-length turbulence model, the $\Delta \overline{u'v'}(y)$ stresses should be related to the mean flow gradient $\partial U/\partial y$. The most physical way to extend the original VG model is to include the strain rate tensor into the description. This will also force the additional vortex stresses to become zero outside of the boundary layer, and VGs with a larger height than the local boundary-layer thickness will correctly have $\Delta \overline{u'v'}(y) = 0$ for $y > \delta$. The extended assumption for the $\Delta \overline{u'v'}(y)$ and $\Delta \overline{u'u'}(y)$ vortex stresses, originating from dimensional analysis, is proposed to be

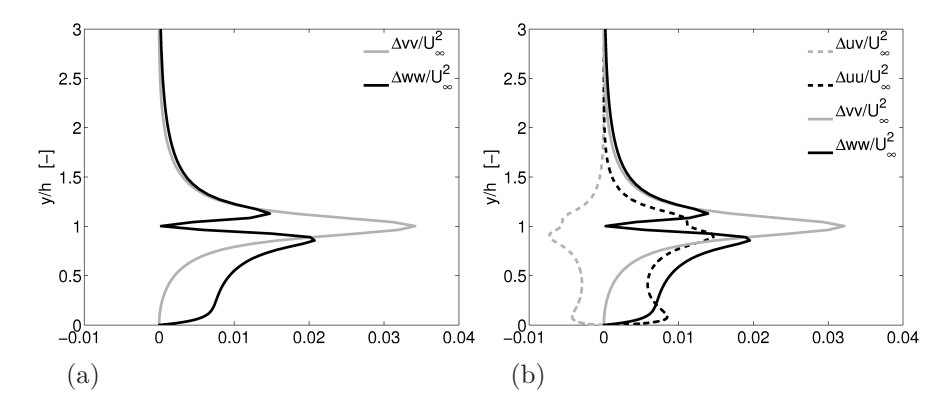


FIGURE 3. Nondimensional additional wall-normal vortex stress distributions at the VG model position originating from (a) the original VG model, and (b) the improved VG model.

$$\Delta \overline{u'v'}(y) = -C_{uv} \cdot S(y) \frac{r_0^2}{\Gamma_{\text{max}}} \left[\Delta \overline{v'v'}(y) + \Delta \overline{w'w'}(y) \right],$$

$$\Delta \overline{u'u'}(y) = C_{uu} \cdot S(y) \frac{r_0^2}{\Gamma_{\text{max}}} \left[\Delta \overline{v'v'}(y) + \Delta \overline{w'w'}(y) \right],$$
(12)

with the magnitude of the mean strain rate defined as

$$S = \sqrt{S_{ij}S_{ji}},\tag{13}$$

where the mean strain rate tensor S_{ij} is defined as

$$S_{ij} = \frac{1}{2} \left(\frac{\partial U_i}{\partial x_j} + \frac{\partial U_j}{\partial x_i} \right). \tag{14}$$

In thin shear flow, such as boundary layers, S will reduce to $\frac{1}{\sqrt{2}} \frac{\partial U}{\partial y}$. The constants C_{uv} and C_{uu} are calibrated for ZPG flat-plate boundary-layer flow (see section 5), giving

$$C_{uv} = 80,$$

 $C_{uu} = 160.$ (15)

The additional $\Delta \overline{u'u'}(y)$ and $\Delta \overline{u'v'}(y)$ vortex stresses for the improved VG model from equations (12) to (15) are shown in figure 3(b) (dashed lines).

3. Experimental Setups

3.1. Flat-Plate Boundary-Layer Flow

The VGs were experimentally investigated in ZPG and APG flat-plate boundary-layer flow by Lögdberg (2008); Lögdberg et al. (2009); cf. table 1 and figure

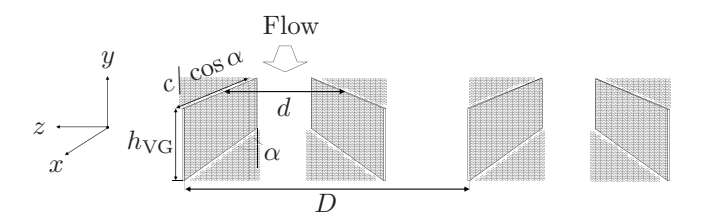


FIGURE 4. VGs in a counter-rotating common-flow-down setting.

TABLE 1. VG setups of the ZPG and APG flat-plate experiments (Lögdberg *et al.* 2009).

h, mm	d, mm	D, mm	c, mm	α , deg	x _{VG,ZPG} , m	x _{VG,APG} , m
18	37.5	150	54	± 15	1.83	1.54

4. Both setups were similar except for the VG streamwise position, and the experiments were carried out in different wind tunnels at the Royal Institute of Technology (KTH) in Stockholm. In particular, each VG pair consisted of two streamwise diverging and wall-normal-mounted vanes with a height h=18 mm and a chord length in the streamwise direction c=54 mm; see figure 4. A VG pair consisted of two VG vanes that were mounted with a mean distance d=37.5 mm from each other and at angles of incidence $\alpha=\pm15$ deg toward the free stream direction, producing counter-rotating vortices downstream of the VGs. A complete VG array consisted of total n=5 VG pairs that were mounted with a spanwise distance of D=150 mm away from each other. The experiments covered three different VG sizes, straight and yawed VG arrays.

3.1.1. ZPG Setup

The ZPG experiments were conducted by Lögdberg et al. (2009) in the minimum turbulence level (MTL) wind tunnel at KTH. This wind tunnel features a very low turbulence level of 0.03% in the central region of the test section at a speed $U_0=25.0~\rm m/s$ as well as a temperature control within $\pm 0.05^{\circ}\rm C$. The wind-tunnel test section is in total 7.0 m long and has a cross-sectional area of 1.2 x 0.8 m² at the inlet. The ZPG is established by a 5.8 m long horizontal flat plate, which was mounted in the test section 0.51 m away from the upper wall. The ceiling can be adjusted to compensate for the boundary-layer growth in order to ensure ZPG flow.

The experiments with and without VGs were carried out at a wind speed of 26.5 ± 0.1 m/s at a constant temperature $T=18.1^{\circ}\mathrm{C}$. In particular, the VGs were placed at $x_{\mathrm{VG}}=1.83$ m downstream of the leading edge in a tripped, fully-turbulent boundary layer at $Re_{\theta}=6000$, where $\delta_{99}=27.9$ mm and the ratio $h/\delta_{99}=0.65$. More details of the experiments and the MTL wind tunnel are presented in Lögdberg et al. (2009) and in Lindgren (2002).

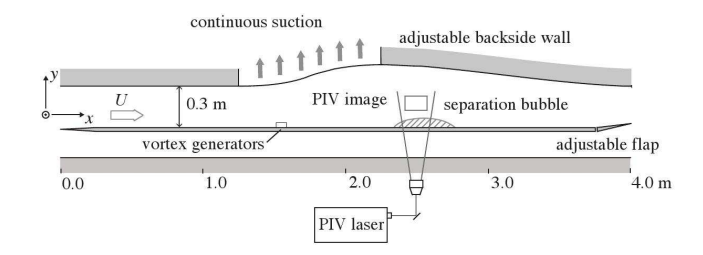


FIGURE 5. Sketch of the boundary-layer wind-tunnel test section. [From Lögdberg (2008).]

3.1.2. APG Setup

The APG experiments were also carried out by Lögdberg et al. (2010) in the boundary-layer wind tunnel at KTH. The freestream velocity U_{∞} during the experiments was set to 26.5 ± 0.1 m/s and the temperature was monitored by a temperature control at $T=20\pm0.07^{\circ}\mathrm{C}$. The wind-tunnel test section is in total 4.0 m long and has a cross sectional area of 0.75 x 0.50 m². The turbulence intensity in the test section is <0.04%; refer to Lindgren & Johansson (2004) for more details about the boundary-layer wind tunnel.

In contrast to the ZPG experiments, the VGs were mounted at $x_{VG} = 1.54$ m downstream of the flat-plate leading edge, where $\delta_{99}=27.3$ mm and the ratio $h/\delta_{99} = 0.66$. The flat plate is mounted 0.30 m away from the inlet upper wall and splits the wind tunnel's test section; see figure 5. The test section has a total height of 0.50 m at the inlet and diverges at x = 1.25 m downstream of the leading edge by means of a back side curved wall. Moreover, a suction system is installed at the upper diffuser wall so that attached flow can be established on the curved surface. The APG strength is adjusted by the suction system and a variabel suction rate at the upper curved wall. In total, three different APG cases were examined, whereas computations and their results that are presented here were only carried out for one specific suction rate [case 2 as in Lögdberg et al. (2010)]. All flowfield measurements in the experiments were performed with particle image velocimetry. Refer to Lögdberg et al. (2010) as well as to Angele (2003) for further details of the experiments, the setup and the measurement techniques. Furthermore, a recent paper (von Stillfried et al. 2011a) by the authors presents computational results of the same APG flat-plate flow without and with modelled VGs in detail.

3.2. Asymmetric Diffuser Flow

The tw-dimensional flow in a plane asymmetric diffuser with a cross-sectional height H=30 mm was experimentally and computationally studied by Törnblom (2006); Törnblom & Johansson (2007) and Gullman-Strand (2004). A sketch of the asymmetric diffuser is presented in figure 6. The inlet channel in the experiments is > 100H long and the outlet channel is > 80H long to avoid boundary-condition influences on the separating region. The diffuser itself has

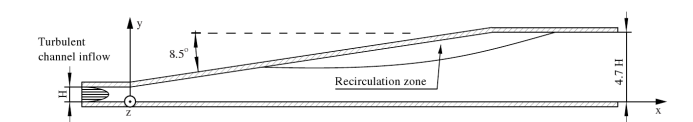


FIGURE 6. KTH diffuser geometry. [From Törnblom & Johansson (2007).]

a straight wall on the lower side and a 8.5 deg inclined wall on the upper side. The corners of the inclined walls are rounded with a radius of 10H, and the diffuser outlet is 4.7H high. The VG vanes had a rectangular shape with a height h=0.6H=18 mm, a chord c=H=30 mm and were mounted at constant angles of incidence $\alpha=20$ deg in an VG array with d=H=30 mm and D=2H=60 mm at a streamwise position $x_{\rm VG}=4.7H=141$ mm downstream of the diffuser inlet $(x_{\rm VG}/H=0)$. The bulk velocity at the diffuser inlet was $U_{\rm b}=43.4$ m/s, and the temperature in the test section was kept constant within ± 0.5 °C.

Moreover, the plane asymmetric diffuser flow case is often used as an evaluation case for turbulence modelling; for example Gullman-Strand (2004) and Obi et al. (1993). The opening angle of 8.5 deg gives a weak separation, which can be controlled rather easily and is therefore suitable for an evaluation of the VG model.

4. Computational Setup

Generally, all VG model (except for the ZPG case) and fully-resolved VG computations were carried out with the Edge CFD code (Eliasson 2002). The local airfoil-section lift slope K from equation (1) was set to 1.8π for all VG model computations, which is 10% lower than for the thin airfoil theory and the baseline case in section 4.1. This adjustment is justified due to the constant finite thickness of the VGs, the effects of viscosity that are present in real wall-bounded flows, and the rather large VG angle of incidence $\alpha = \pm 15$ deg. Refer to von Stillfried et al. (2011a), where the complete computational setup is described.

4.1. Setup for the ZPG Flat-Plate Flow

The computations with the VG model in ZPG flow were solved by means of an in-house two-dimensional ZPG boundary-layer solver; see Wallin & Mårtensson (2004), who used central differences for spatial derivatives and Euler backward differences for time derivatives. The code makes it possible to use a very fine resolution at very low computational costs. Computations of a clean flat plate without any VG model applied were carried out to determine the correct VG position in order to match the experimental results. The boundary-layer displacement and momentum thicknesses at x = 1.83 m in the experiments without VGs were $\delta^* = 4.71$ mm and $\theta = 3.38$ mm, respectively. Similar flow conditions in the computations were present further downstream at x = 2.00

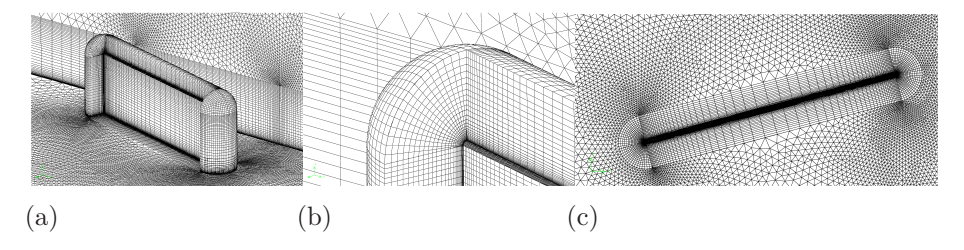


FIGURE 7. The O-grid around the VG vane, symmetry conditions at domain boundaries applied. The meshed VG vane geometry corresponds to the experimental VG vanes from Lögdberg et al. (2009); see also figure 4.

m. This difference is a result of the wind-tunnel setup that forced turbulent tripping of the boundary layer upstream of the VGs. The VG model had to be applied further downstream to match the correct streamwise position within the turbulent boundary layer. This shifting ensured $Re_{\theta} = 6000$, as suggested by Österlund (1999). The in-house boundary-layer solver was initially used for testing the original VG model on a ZPG flat plate to calibrate the free parameters (von Stillfried et al. 2009) for an implementation in the CFD code Edge. Here, additional parameters for the improved VG model needed to be tested and locked in ZPG flow first, and therefore computations were carried out with the boundary-layer solver. Moreover, the purpose here was to serve the reader with a comparison of the original and the improved VG model results in ZPG boundary-layer flow. Two-dimensional APG as well as three-dimensional cases were solely run with Edge, and three-dimensional results were spanwiseaveraged for a comparison with the two-dimensional cases from Edge and the boundary-layer solver. The in-house boundary-layer code was solely used for the ZPG flat-plate boundary-layer computations for the original and the improved VG model.

In addition, three-dimensional CFD calculations of the same flow case including fully-resolved VGs were carried out with the Edge CFD code. These results were used to compare the VG model results from the in-house boundary-layer solver with spanwise-averaged fully-resolved results. The computational domain contained in total 1.8 million nodes and fully-resolved the VGs, assuming a no-slip condition on the flat plate as well as on the VG vanes. An O-grid approach was used to resolve the VGs locally; see figure 7. Close to the wall and on the VGs, a boundary-layer grid was used and the value for the first grid point at the wall was set to $y=10^{-5}$ m throughout the domain, giving values of $y^+=\mathcal{O}(1)$. Furthermore, symmetry conditions were applied so that the computational domain could be reduced to one VG vane.

All fully-resolved computations were solved by means of the Wallin & Johansson (WJ) explicit algebraic Reynolds stress turbulence model (EARSM) (Wallin & Johansson 2000) as the constitutive relation between the stress

anisotropy and the mean flow quantities together with the Hellsten $k-\omega$ turbulence model (Hellsten 2005) as the platform equations. In contrast, all computations including the VG model were solved with a differential RST model including a pressure-strain-rate model corresponding to the WJ-EARSM turbulence model with curvature correction (Wallin & Johansson 2002) together with the Hellsten $k-\omega$ turbulence model as the platform equations. In general, the RST modelling approach in combination with the VG model adds the additional vortex stresses $\Delta \overline{u_i'u_j'}(y)$ to the Reynolds stress tensor (cf. section 2.1), whereas the EARSM approach does account for the individual transport terms of the Reynolds stress components. Nevertheless, the computations with the two turbulence models can be compared in this study and results are presented in section 5. In case of an application of the VG model, the EARSM approach accounts for an additional turbulence kinetic energy Δk originating from the vortex stresses that is in turn added to the turbulence kinetic energy k. This is not investigated here.

4.2. Setup for the APG Flat-Plate Flow

Also for the APG case, the twodimensional VG model and threedimensional computations with fullyresolved VGs were carried out. Here, and in contrast to the twodimensional ZPG case, Edge was used for both computational cases since the boundary-layer code is limited to ZPG flow. Consequently, two different computational meshes were used for this investigation: a two-dimensional mesh for the VG model computations and a threedimensional mesh for the computations with resolved VGs. meshes have a domain height and length of h = 0.25 m and l = 7.25 m, respectively, and including an additional 0.25 m long inflow region. The same O-grid as in the fully-resolved ZPG case was used here even though the domain height and length were modified here. The reason for having

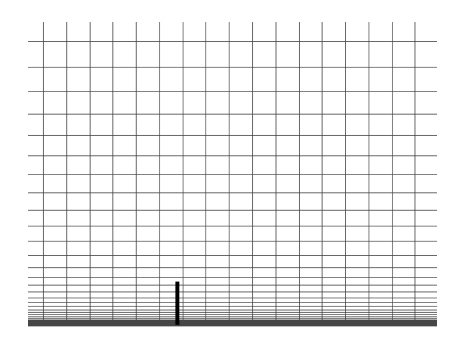


FIGURE 8. The base-line grid around the VG model forcing position used for the APG flat-plate VG model computations. The position and height of the modelled VG is indicated as a vertical black line.

a lower CFD domain than the experimental wind-tunnel height was to apply specific boundary conditions on the top boundary. A grid study (von Stillfried $et\ al.\ 2011\ a$) of the two-dimensional mesh led to the grid that is partly shown in figure 8 and consists of $321\ x\ 55$ nodes in the x and y direction, respectively, without any refinement region around the VG. Two finer meshes with a node

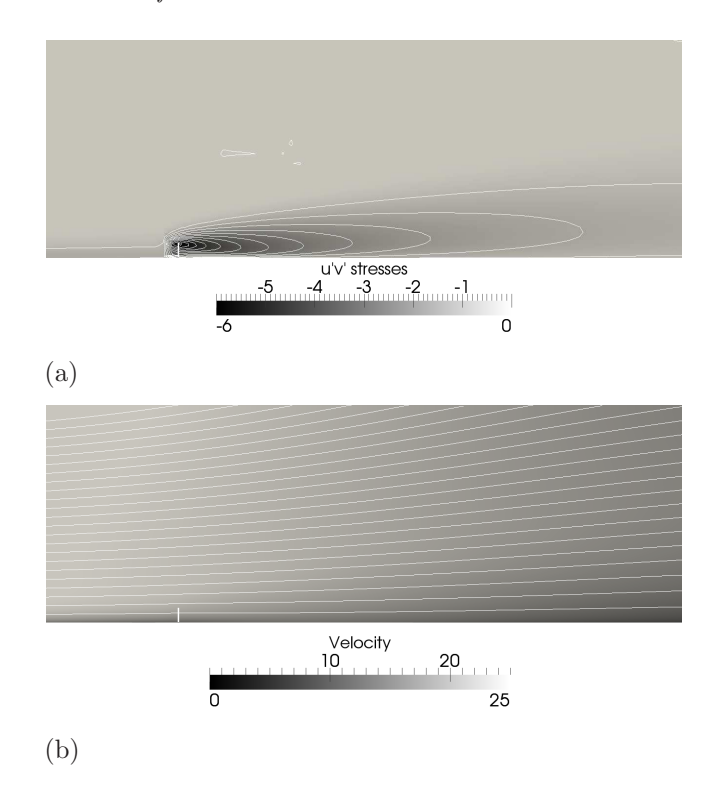


FIGURE 9. The VG model applied in APG flat-plate flow at x=1.54 m: (a) contours showing the total $\overline{u'v'}$ stresses, and (b) velocity magnitude and streamlines. The figures show a region between $1.40 \le x \le 2.10$ m.

density of 321 x 100 and 536 x 100 (high refinement in the VG region) were tested but the relative error in skin-friction results within the APG section with applied VG model forcing between the coarsest and the finest grid solutions lies within 5%, so that the coarsest grid was used for this study.

As described in section 3.1.2, the wind tunnel features a suction system on the upper curved wall, but including such a highly complicated system in the CFD domain is not practical. Instead, pressure and velocity boundary conditions from inviscid theory are applied on the upper boundary, inducing ZPG, APG and favorable pressure-gradient regions to force the flow to be similar to that in the wind-tunnel experiments. Therefore, mass flow across the top boundary was established (see figure 9), and a comparable wall-pressure distribution within the APG region could be established (von Stillfried $et\ al.\ 2011a$).

The Edge CFD code and the same turbulence model as for the ZPG flatplate computations was used for the APG case (i.e., the Hellsten $k-\omega$ platform equations together with either the WJ-EARSM approach for the fully-resolved three-dimensional computations or the differential RST approach for the two-dimensional VG model computations).

The two-dimensional computational domain was originally used for the VG model diffuser computations in von Stillfried et al. (2009). The domain has an inlet height H=30 mm, a $\approx 100H$ -long inlet channel, and a $\approx 75H$ -long outlet channel, containing 393 x 133 nodes in a structured manner in the streamwise and wall-normal direction, respectively. The expanding part consists of 160 x 133 nodes and does not feature any local refinement region around the VG position at x/H=4.7. Computations were also carried out on a finer mesh with a node density of 801 x 301 nodes, whereas the mesh was refined twofold and threefold in the streamwise and wall-normal direction, respectively, as well as increased by a factor of 5 in the region between x=H and x=8H that enclosed the VG position and the near-field downstream region.

As for the APG flat-plate flow, the same RST turbulence model was applied. Standard coefficient settings were used, but computations without the VG model (von Stillfried *et al.* 2009) revealed a too-weak separation region when compared to experiments of Törnblom (2006). Therefore, the coefficients α_1 and α_2 in the ω equation of the Hellsten $k-\omega$ turbulence model (Hellsten 2005) were increased to 0.671 and 0.593, respectively. This strategy increases the production for ω and therefore gives a better flow-separation prediction for the baseline setting without VGs and was also applied for the VG model cases.

5. Flat-Plate Boundary-Layer Flow

The baseline investigation, carried out by means of the in-house boundary-layer solver, included a variation of the independent parameters of the statistical VG modelling approach. Three different parameters were found to be independent, and the baseline reference values for the three different independent parameters K, r_0 , and C_{ω} were set as given in table 2.

K and r_0 are the local airfoilsection lift slope and the viscous core radius [see equations (1) and (3)], respectively, and C_{ω} a constant to account for the change in the turbulence specific dissipation rate ω due to the imposed vortices at the VG position. C_{ω} is defined as $C_{\omega} =$

Table 2. Baseline setting for
$$K$$
, r_0 , C_{ω} .

 $K r_0/h C_{\omega}$
 $2\pi 0.1 1$

 $\omega_{\rm out}/\omega_{\rm in}$; it multiplies the result for the computed $\omega_{\rm in}$ just before the VG position and uses the multiplied value $\omega_{\rm out}$ as a new condition just downstream of the VG position for the calculations with the VG model. For a first investigation, ω was assumed to stay constant over the VG position (i.e. $C_{\omega}=1$). The value of the lift slope $K=2\pi$ represents the maximum theoretical value of the lift slope for a flat plate in free-flight conditions. A viscous core radius

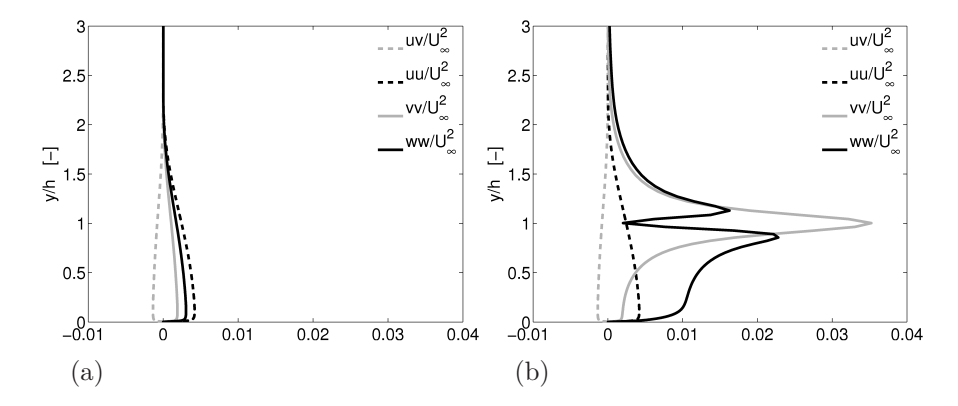


FIGURE 10. Wall-normal (a) boundary-layer stress distributions at the VG position, and (b) total stresses.

of the vortex model of $r_0/h = 0.1$ was previously investigated by Törnblom (2006) for VGs in diffuser flow.

Figures 10(a-b) show the the four Reynolds stress components for the flatplate turbulent boundary layer without and with VGs, respectively. The vortex structure is clearly observable in figure 10(b) and it is also observable that the boundary-layer stresses are about one order of magnitude smaller than the added vortex stresses; cf. figure 3(a).

Figures 11(a) shows the development of the mean velocity profiles $U(y)/U_{\infty}$ for the near-field planes at $x/h=0.0,\,0.5,\,1.1,\,1.7,\,2.2,\,$ and 2.8 downstream of the VG. It can be observed that the fully-resolved and the VG model velocity profiles collapse well, except for the velocity-deficit region around y/h=1. This defect evolves from resolving the VG vanes, which in turn introduces a momentum loss in the flow, resulting in a velocity defect in the mean-velocity profile. It is observable that the fully-resolved velocity defect is smeared out with increasing downstream distance. The Lamb-Oseen vortex model does not take any streamwise velocity defect into account.

Experimental results for a comparison with the VG model computations are available for the far-field planes at $x/h=3.3,\ 9.4,\ 23,\ 37,\ 65,\ 93,$ and 148 downstream of the VG position. Furthermore, fully-resolved computational results from Edge computations are available for both the near field and the far field. The experimental data and the fully-resolved data represent the time-averaged data of the three-dimensional flowfield. The results need to be spanwise-averaged for a comparison with the VG model computations.

The far-field velocity profiles in figure 11(b) show that the velocity profiles from fully-resolved computations are very consistent with the experimental profiles. This also applies for the last two positions for which the experiments clearly show an increase in velocity in the vicinity of the wall up to

 $y/h \approx 4$. Moreover, the experimental and fully-resolved plots clearly indicate a momentum transfer from the high-energy-containing freestream into the boundary layer and vice versa. The velocity defect in the first plots is very local around y/h = 1 and continuously diffused and transported outwards, whereas an increase in velocity takes place for lower y/h. This mechanism is directly connected to the vortices in the flow that transport low energy flow to higher y/h and, in turn, feed the near-wall flow with high-energy flow. Also the far-field development of the $\Delta \overline{u'v'}(y)$ Reynolds stresses is well predicted by the fully-resolved computations, although the stresses at x/h = 3.3 are somewhat underpredicted. The general good comparison in the far field enables us to use the fully-resolved computational results as reference data also in the near field with reasonable confidence.

The plots in figure 11(c) show the near-field development of the $\overline{u'v'}(y)$ Reynolds stresses. The VG model applied here only forces the $\Delta \overline{v'v'}(y)$ and $\Delta \overline{w'w'}(y)$ vortex stresses, but the two-dimensional boundary-layer solver takes all four Reynolds stresses into account, and the total $\overline{u'v'}(y)$ Reynolds stresses are only indirectly forced. Because the $\overline{u'v'}(y)$ stresses have the largest influence on the mean flow in thin shear flows, we focus on these stresses here. The $\Delta \overline{u'v'}(y)$ stresses were not forced by the VG model. In contrast, the fully-resolved computations exhibit significant levels of $\Delta \overline{u'v'}(y)$ stresses; see figure 11(c). Even though the initial $\overline{u'v'}(y)$ profiles are certainly totally different, they tend to approach each other further downstream, almost collapsing for the right-most plot at x/h=2.8 in figure 11(c).

It can be observed that the far-field $\overline{u'v'}(y)$ Reynolds stresses in figure 11(d) from the VG model computations are initially very similar to the experiments and to the fully-resolved computational results. The distributions of the VG model results are promising, especially when keeping in mind that the $\Delta \overline{u'v'}(y)$ component of the additional vortex stresses was not initially forced by the VG model. The trends for further downstream positions are consistent even though the VG model tends to underpredict results from x/h=23 compared to the reference data. The reason for this is that the vortex stresses are included in the turbulence stresses and are predicted by the turbulence model, which is not able to capture the much slower decay rate of the coherent vortices compared with the turbulent structures. This results in a much faster decay rate than for the vortex structures from CFD and experiments that are naturally preserved longer and that also give very similar results, mostly lying on top of each other.

Parameter variations of the independent VG model parameters as the lift slope K, the vortex core radius r_0 , and the turbulence specific dissipation rate ω were previously conducted and the authors refer to von Stillfried et al. (2009), where the complete variation study is given. In summary, all parameters influence the development of the Reynolds stresses distributions in both, the near field and the far field. The effects of these variations are visible in the near-field planes, whereas turbulence decay and redistribution have a larger impact on the far-field distributions. The different parameters act very differently on

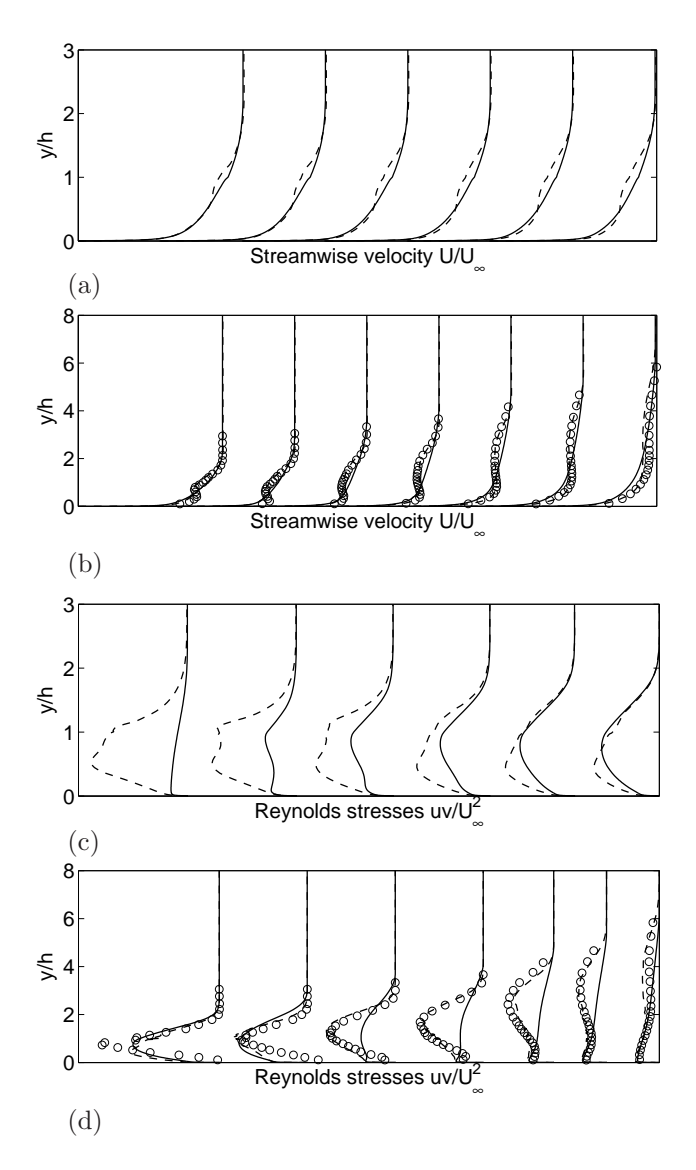


FIGURE 11. VG model baseline case (solid line), spanwise-averaged fully-resolved (dashed line), and spanwise-averaged experimental (circles) results for (a) and (c) near-field $x/h=0.0,\,0.5,\,1.1,\,1.7,\,2.2,$ and 2.8; (b) and (d) far-field $x/h=3.3,\,9.4,\,23,\,37,\,65,\,93,$ and 148 (from left to right).

the development of the Reynolds stresses, and there is some potential to create a more optimal combination of all parameters. Irrespective of the examined parameter variation, the slow development of the $\overline{u'v'}(y)$ stresses in the near

field persists, and the far-field stresses for $x/h \geq 23$ are generally much more diffused by the turbulence than the experimental vortex structures. Therefore, a further calibration of the parameters for achieving better results in the first part of the far field is not very meaningful. On the other hand, VGs should nevertheless placed not too far away from the region of interest, where they should have an effect on the flow, and thus the difference in far-field results is not as significant as it may seem. In total, the baseline parameter combination seems to represent a reasonable choice for the VG model computations at this level of modelling.

The VG model's near-field $\overline{u'v'}(y)$ vortex stresses are indirectly produced by the turbulence model mainly through the production term $\mathcal{P}_{uv} \approx -\overline{v'v'}\partial U/\partial y$ in thin shear flows. It is obvious from the near-field development in figure 11 that this mechanism is too weak. This is the main argument for forcing the $\Delta u'v'(y)$ vortex stress component by the improved VG model in section 2.2. In addition, the $\overline{u'u'}(y)$ component is forced by the improved approach. The ZPG flat-plate flow was used for a calibration of the C_{uv} and C_{uu} coefficients from equation (12) to adjust the initial near-field distribution of the Reynolds stresses downstream of the VG model. Results with the improved VG model [see equation (15)] are given in figures 12 and 13 and show a substantial improvement for the $\overline{u'u'}(y)$ and $\overline{u'v'}(y)$ Reynolds stresses compared with the original VG model; see also von Stillfried et al. (2009). In figure 12(a), it can be observed that the forcing of the $\Delta u'v'(y)$ stresses enables an improved distribution from the forcing position and throughout the whole near field. The modelled stresses match the spanwise-averaged stresses from CFD above y/h = 1 but do not match exactly below y/h = 1. Still, this change represents a substantial improvement compared to the original results. The far-field development is very similar for both VG models but indicates slight advantages for the improved VG model up to x/h = 3.3. Further downstream, both the original and the improved VG model's results are very similar, eventually lying on top of each other; see also figure 12(b). This is due to the diffusion of turbulence that includes the vortex stresses. Therefore, and with growing streamwise distance from the forcing plane, the stresses for both models cannot be distinguished anymore because they are here predicted by the same turbulence model. Again, it can also be observed that the spanwise-averaged three-dimensional vortex stresses originating from coherent vortices predict the experimental results well for each streamwise position x/h.

The $\overline{u'u'}(y)$ near-field distributions for the original and the improved VG models are given in figure 13(a). Again, it can be seen that the original VG model does not provide any initial $\Delta \overline{u'u'}(y)$ stress forcing, whereas only the incoming $\overline{u'u'}(y)$ boundary-layer stresses are present. In contrast to that, the improved VG model enables an initial forcing of $\Delta \overline{u'u'}(y)$ stresses with a very similar distribution above y/h=1 and somewhat underestimated below y/h=1. Nevertheless, it can be observed how the stress distributions for the improved VG model become more similar to the averaged fully-resolved results further

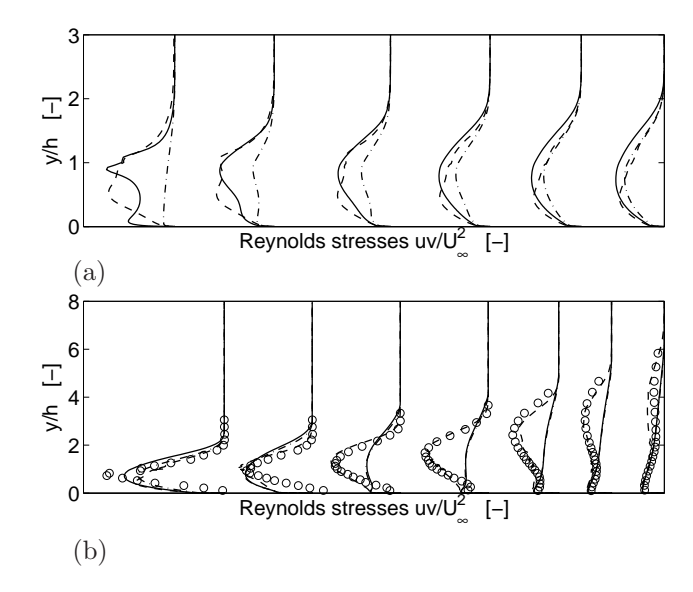


FIGURE 12. Original VG model (broken line), improved VG model (solid line), spanwise-averaged fully-resolved (dashed line), and spanwise-averaged experimental (circles) results for (a) near-field x/h = 0.0, 0.5, 1.1, 1.7, 2.2, and 2.8; (b) far-field x/h = 3.3, 9.4, 23, 37, 65, 93, and 148 (from left to right).

downstream in the near field. Further downstream in the far field in figure 13(b), the improved VG model results reveal advantages over the original VG model up to x/h = 3.3, from where on both model stress distributions lie on top of each other; see also discussion for figure 12(b).

In addition to the ZPG flat-plate case, APG flat-plate computations were carried out with the improved VG model. The flow-case setup and the complete study including the original VG model are described in detail in section 3 and in von Stillfried $et\ al.\ (2011a)$, respectively. Here, the application of the original VG model, the improved VG model, and the fully-resolved approach are compared with each other by means of wall skin-friction distributions. The modelled VGs and the fully-resolved VGs (i.e., their trailing edges) were placed at a streamwise position at $x_{\rm VG}=1.54$ m, as in the APG experiments by Lögdberg $et\ al.\ (2009)$.

Without flow control, the pressure gradient is sufficiently strong to generate a turbulent separation bubble. Results of the original VG model show that the separation is surpressed, but the local skin-friction distribution in the APG region is significantly lower than for the fully-resolved computations; see figure 14. This is a sign for the weaker influence of the original VG model on the important momentum mixing effects in the boundary layer. In contrast to that, the improved VG model shows a significant increase in local skin friction

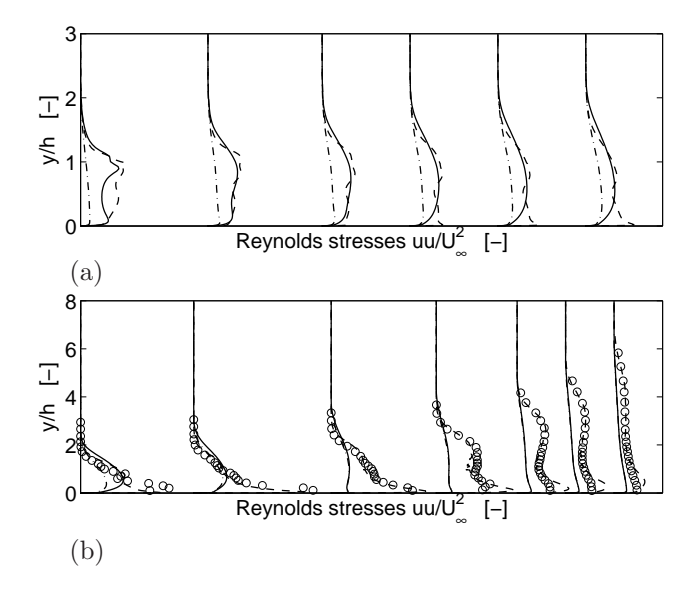


FIGURE 13. Original VG model (broken line), improved VG model (solid line), spanwise-averaged fully-resolved (dashed line), and spanwise-averaged experimental (circles) results for (a) near-field x/h = 0.0, 0.5, 1.1, 1.7, 2.2, and 2.8; (b) far-field x/h = 3.3, 9.4, 23, 37, 65, 93, and 148 (from left to right).

between the streamwise location of the VG model at $x_{\rm VG}=1.54$ m and the end of the APG region at $x\approx 3.00$ m, in particular in the near-field region up to x=1.70 m. This is consistent with the results from figures 12 and 13 that presented the enhanced stress distributions in the near-field region. Still, the improved VG model cannot capture the far-field flow physics in contrast to fully-resolved VG computations (VG3D in figure 14). This is due to the turbulence description of the vortices from equation (7). Therefore, the modelled vortex diffuses faster than fully-resolved vortex structures the further downstream they travel, underpredicting the effectiveness of the VG. Nevertheless, the overall result of the improvement of the VG model is a more stable flow through the APG section with a larger clearance to the $c_f=0$ threshold for flow separation.

6. Diffuser Flow

In addition to the flat-plate boundary layer cases, a study of the internal APG flow in the KTH asymmetric diffuser was carried out; see also von Stillfried et al. (2009).

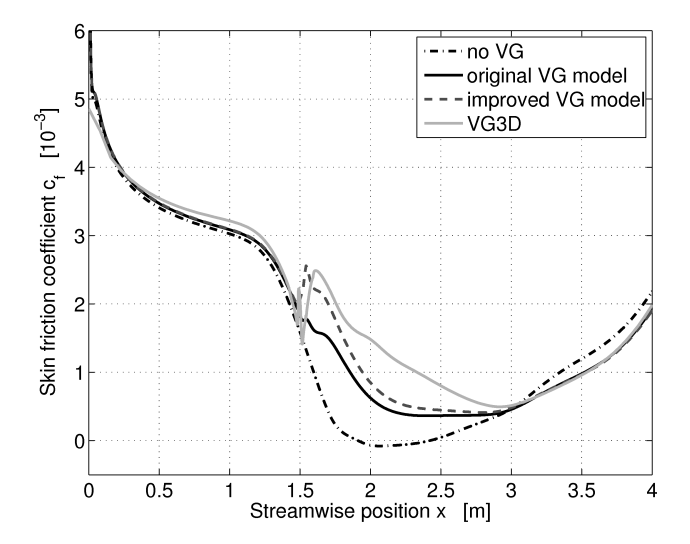


FIGURE 14. Local skin-friction coefficient distributions for computations with spanwise-averaged fully-resolved computations, without VGs, and with the different VG models for $x_{\rm VG_{TE}}=1.54$ m.

6.1. Grid Resolution Study

Two structured diffuser grids using the improved VG model were used in order to examine grid dependency on the results in terms of the local wall-pressure distribution c_p and the local skin-friction distribution c_f on the upper wall. For that, the VG setting as in the experiments was used, and differences in the pressure and skin-friction distributions were investigated. The baseline grid consists of 393 x 193 grid points in the streamwise and in the wall-normal directions, respectively, and the finer grid consists of 801 x 301 grid points, whereas the refinement in the streamwise direction was doubled in the whole diffuser downstream from x/H=0. Moreover, within the region x/H=1-8, the streamwise grid resolution is approximately five times denser. The c_p results for the baseline mesh using the improved VG model in figure 15(a) show only minor differences with a maximum deviation of <1% from the fine mesh results.

As for c_p , the much more sensitive skin-friction results in figure 15(b) generally show similar distributions. For the fine mesh solution, a deviation from the baseline mesh solution of $\approx 20\%$ occurs very locally at the VG model forcing plane at x/H=4.7 which is hard to identify in the plot. In the far-field region around x/H=9, the finer mesh solution gives locally higher c_f values in the order of maximum 10% compared to the baseline case. Nevertheless, the variation in c_f is not critical for describing the effects of the modelled VGs on the diffuser flow, and the authors have chosen the baseline mesh for the subsequent investigations. Therefore, the baseline grid was considered to be sufficiently

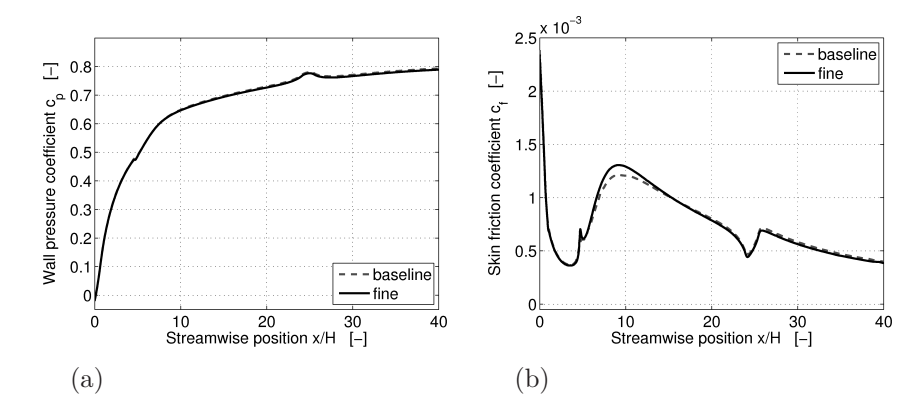


FIGURE 15. (a) Wall-pressure, and (b) skin-friction distributions for the baseline and the fine grids.

fine for the following investigations. Moreover, an important result of this grid study is that the VG model may essentially be placed anywhere in the diffuser where the mesh resolution compares to the baseline grid resolution without the need for further remeshing, supporting the grid independent results of a previous grid study for the APG flat-plate flow (von Stillfried *et al.* 2011*a*); see section 5.

6.2. Results

Figure 16 presents streamlines and plots of the turbulence kinetic energy for the computations without VG, with the original VG model, and with the improved VG model. It can be seen that computations without VGs reveal a large separation region on the inclined diffuser wall. When comparing figure 16(a) with velocity plots in figure 17, it is observable that computational and experimental results are similar to each other, and a clean baseline flow is ensured for the computations. However, the predicted separation is too thin and too weak compared to experiments and, consequently, computational results show a higher pressure distribution on the lower diffuser wall; see figure 18.

Applying the VG setting from experiments shows that the influence of the original VG model on flow separation prevention is working well. Streamlines in figure 16(b) do not show any separation region within the complete diffuser. The streamwise velocity and the pressure distributions for the experiments also reveal attached flow, and a higher pressure recovery within the diffuser is observable cf. figures 17 and 18.

The improved VG model does not show substantially different results in figure 16(c) but it can be seen how streamlines are somewhat shifted upwards compared to the original VG model results. This upward push is particularly observable in the velocity plots in figure 17, where the peak velocities occur in the upper half-section of the diffuser instead of the lower half-section as for the

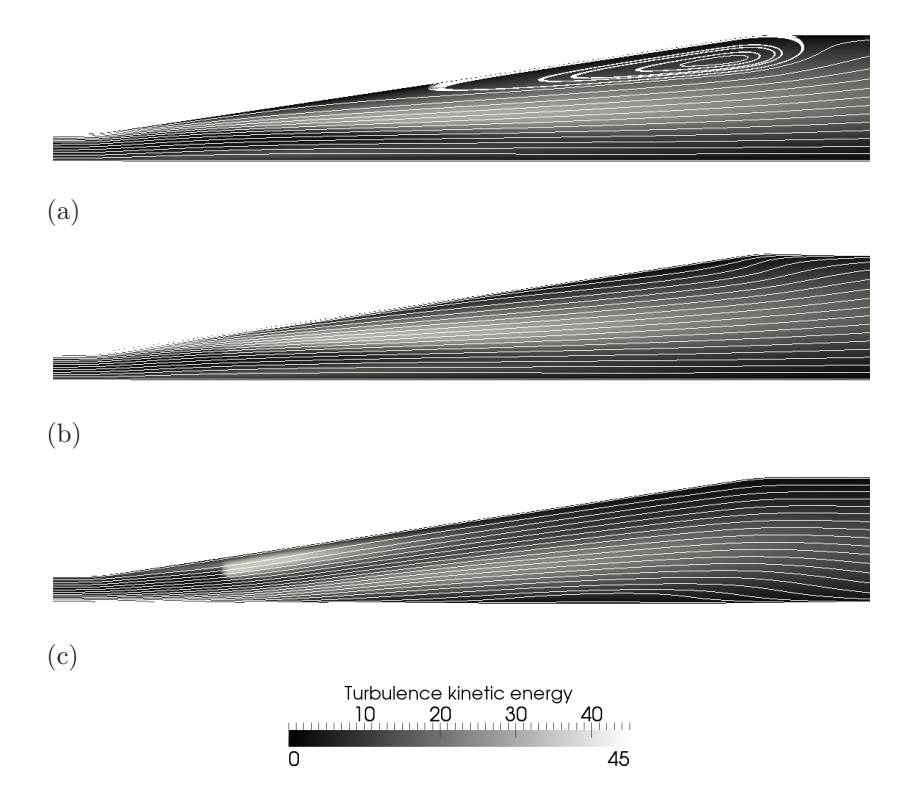


FIGURE 16. Turbulence kinetic-energy contours and streamlines for the computations: (a) without VG model, (b) with original VG model, and (c) with improved VG model.

original VG model. In addition, a very small separated region that is hardly visible in the velocity plots can be observed on the straight diffuser wall. It cannot be stated whether this flow state is correct or not because experimental results were not available for a comparison. The pressure distribution in figure 18 shows how the pressure rises more rapidly than for the original VG model but reaches a similar level further downstream. Nevertheless, experiments give a higher pressure between x=400 mm and 1000 mm, but the total pressure recovery at x=1300 mm of the VG computations is also comparable with the experiment.

In total, it can be said that the different VG model approaches are capable of describing the separation prevention qualitatively correct. As a conclusion of figures 16 to 18, it can be said that both VG models describe different flow states but pressure distributions do not differ much. Velocity plots reveal strong differences in the local streamwise velocity profiles, but it cannot be stated whether the original or the improved VG model is correct here. For that, experiments should be repeated, and velocity profiles need to be measured.

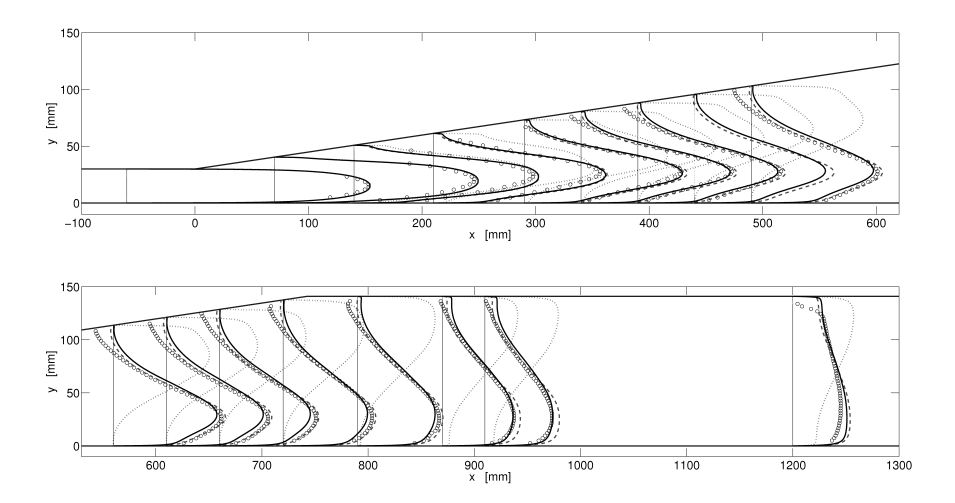


FIGURE 17. Mean streamwise velocity profiles: experiments w/o VGs (circles), computations w/o VGs (dashed line), original VG model (solid line), and improved VG model (dotted line).

7. Conclusions

The application of the statistical VG model has shown its capabilities to mimic the effects of VG arrays within turbulent boundary layers by means of introducing additional vortex stresses to the mean governing equations. Two

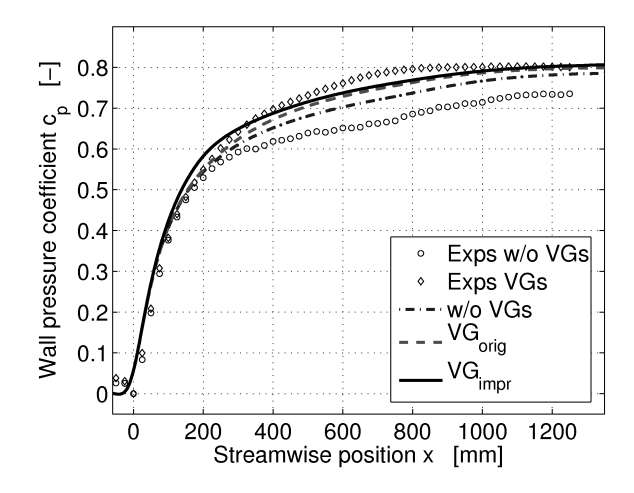


FIGURE 18. Wall-pressure distributions distributions for the experiments and the VG model computations.

different VG model approaches were investigated in this study. In particular, both VG model incorporate additional vortex stresses $\Delta \overline{v'v'}$ and $\Delta \overline{w'w'}$ that are generated in a spanwise plane at the VG forcing location. Nevertheless, the additional vortex stresses $\Delta \overline{u'u'}$ and $\Delta \overline{u'v'}$ are zero for the original VG model approach, leading to inconsistent stress distributions for $\overline{u'u'}$ and $\overline{u'v'}$ in the VG forcing plane. However, within the intial near-field transient up to x/h=2.8 in the ZPG flat plate case, $\overline{u'v'}$ is produced through a transfer of energy from the vortex stresses $\Delta \overline{v'v'}$ and $\Delta w'w'$ within the RST model. Further downstream, up to x/h=9.4, the original VG model $\overline{u'v'}$ vortex stresses become similar to both the ZPG experimental and fully-resolved CFD results. Far downstream, the influence of the VG is underpredicted using the VG model.

The proposed improved VG model also incorporates additional $\Delta \overline{u'u'}$ and $\Delta \overline{u'v'}$ vortex stresses through forcing terms that are based on the $\Delta \overline{v'v'}$ and $\Delta \overline{w'w'}$ vortex stresses from the original VG model in combination with the magnitude of the mean strain rate S, the vortex core radius r_0 , and the maximum circulation $\Gamma_{\rm max}$. A calibration of these vortex stresses was carried out through an adjustment of the improved VG model peak vortex stresses to corresponding peak vortex stresses for a VG applied in ZPG flat-plate flow. This approximation especially proves to give improved vortex stresses in the region up to x/h=3.3 behind the VG, as could be shown for the ZPG and APG flat-plate flow by means of the combined Reynolds stresses $\overline{u'v'}$, $\overline{u'u'}$, and by skin-friction distributions, respectively.

Applying either VG model in a flat-plate boundary layer has shown that they generally underpredict the influence in the far-field region behind the VG. The main reason for this is that the coherent vortices generated by the VGs are only represented by their correlations, and the evolution is predicted using a turbulence model. The generated vortices are much more stable and will persist much longer than corresponding turbulent structures with the same statistics, and the turbulence model cannot distinguish between them. Still, the investigation of the different VG models in the diffuser case showed that the VGs could completely prevent flow separation. Different flow states in the diffuser were observable for the two VG models but it could not be stated which one of them produced correct trends and tendencies.

In summary, this investigation has shown that the introduced statistical modelling of VGs as turbulent flow-separation devices is promising, producing qualitatively correct results, trends and tendencies even though the far-field stresses are underpredicted due to the model description. Nevertheless, some research should be carried out in order to further improve the VG model. In particular, it can be stated that the VG model introduces the opportunity to carry out parameter variations fastly and efficiently without the need for rebuilding the computational mesh. It is finally also important to note that this approach has the advantage of not being more computationally expensive than solving RANS equations without modelled devices, leading to much faster results than with conventional methods such as fully- or partly- resolved VGs.

Acknowledgements

The ZPG flat-plate experiments were carried out within a cooperative research program between the Royal Institute of Technology and Scania AB, Sweden. Special thanks to Ola Lögdberg and Jens Fransson for the provision of experimental results. Financial support of the Swedish Research Council, grant no. 2010-6965, is gratefully acknowledged.

References

- Anderson, J. D. 1991 Fundamentals of Aerodynamics, 2nd edn. New York, USA: McGraw-Hill.
- ANGELE, K. P. 2003 Experimental Studies of Turbulent Boundary Layer Separation and Control. PhD thesis, Department of Mechanics, KTH Stockholm.
- BATCHELOR, G. K. 1964 Axial Flow in Trailing Line Vortices. *Journal of Fluid Mechanics* **20** (4), 645 658.
- Bender, E. E., Anderson, B. H. & Yagle, P. J. 1999 Vortex Generator Modelling for Navier-Stokes Codes. *American Society of Mechanical Engineers, FEDSM* 99-6919.
- ELIASSON, P. 2002 Edge, a navier-stokes solver for unstructured grids. *Proceedings to Finite Volumes for Complex Applications III* pp. 527 534, edited by D. Kroner and R. Herbin, Hemre Penton Science London.
- GLAUERT, H. 1926 The Elements of Aerofoil and Airscrew Theory, 1st edn. Cambridge University Press, London, UK.
- GODARD, G. & STANISLAS, M. 2006 Control of a Decelerating Boundary Layer. Part
 1: Optimization of Passive Vortex Generators. Aerospace Science and Technology
 10 (3), 181 191.
- GULLMAN-STRAND, J. 2004 Numerical and Experimental Study of Separated Flow in a Plane Asymmetric Diffuser. *International Journal of Heat and Fluid Flow* **25** (3), 451 460.
- Hellsten, A. 2005 New Advanced $k-\omega$ Turbulence Model for High-Lift Aerodynamics. AIAA Journal 43 (9), 1857 1869.
- JIRÁSEK, A. 2005 A Vortex Generator Model and its Application to Flow Control. Journal of Aircraft 42 (6), 1486 – 1491.
- LIN, J. C. 2002 Review of Research on Low-Profile Vortex Generators to Control Boundary-Layer Separation. Progress in Aerospace Sciences 38, 389 – 420.
- LINDGREN, B. 2002 Flow Facility Design and Experimental Studies of Wall-Bounded Turbulent Shear-Flows. PhD thesis, Department of Mechanics, KTH Stockholm.
- LINDGREN, B. & JOHANSSON, A. V. 2004 Evaluation of a New Wind Tunnel with Expanding Corners. *Experiments in Fluids* **36**, 197 203.
- LÖGDBERG, O. 2008 Turbulent Boundary Layer Separation and Control. PhD thesis, Department of Mechanics, KTH Stockholm.
- LÖGDBERG, O., ANGELE, K. & ALFREDSSON, P. H. 2010 On the Robustness of Separation Control by Streamwise Vortices. *European Journal of Mechanics B/Fluids* **29** (1), 9 17.
- LÖGDBERG, O., FRANSSON, J. H. M. & ALFREDSSON, P. H. 2009 Streamwise Evolution of Longitudinal Vortices in a Turbulent Boundary Layer. *Journal of Fluid Mechanics* 623, 27 58.
- Obi, S., Aoki, K. & Masuda, S. 1993 Experimental and Computational Study of Turbulent Separating Flow in an Asymmetric Plane Diffuser. *Ninth Symp. on turbulent shear flows, Kyoto, Japan* p. 305.
- ÖSTERLUND, J. M. 1999 Experimental Studies of a Zero Pressure-Gradient Turbulent Boundary Layer Flow. PhD thesis, Department of Mechanics, KTH Stockholm.
- PAULEY, W. R. & EATON, J. K. 1988 Experimental Study of the Development of

- Longitudinal Vortex Pairs Embedded in a Turbulent Boundary Layer. AIAA Journal 26 (7), 816 823.
- Pearcey, H. H. 1961 Part IV: Shock-Induced Separation and its Prevention by Design and Boundary Layer Control. In *Boundary Layer and Flow Control*, its *Principles and Applications* (ed. G. V. Lachmann), pp. 1170 1344. Pergamon, Oxford, UK.
- VON STILLFRIED, F., WALLIN, S. & JOHANSSON, A. V. 2009 Statistical Modeling of the Influence of Turbulent Flow Separation Control Devices. *AIAA Paper* 2009-1501.
- VON STILLFRIED, F., WALLIN, S. & JOHANSSON, A. V. 2011 Evaluation of a Vortex Generator Model in Adverse Pressure Gradient Boundary Layers. *AIAA Journal* **49** (5), 982 993.
- TÖRNBLOM, O. 2006 Experimental and Computational Studies of Turbulent Separating Internal Flows. PhD thesis, Department of Mechanics, KTH Stockholm.
- TÖRNBLOM, O. & JOHANSSON, A. V. 2007 A Reynolds Stress Closure Description of Separation Control with Vortex Generators in a Plane Asymmetric Diffuser. *Physics of Fluids* **19** (115108).
- VELTE, C. M., HANSEN, M. O. L. & OKULOV, V. L. 2009 Helical Structure of Longitudinal Vortices Embedded in Turbulent Wall-Bounded Flow. *Journal of Fluid Mechanics* 619, 167 – 177.
- Wallin, S. & Johansson, A. V. 2000 An Explicit Algebraic Reynolds Stress Model for Incompressible and Compressible Turbulent Flows. *Journal of Fluid Mechanics* 403, 89 132.
- WALLIN, S. & JOHANSSON, A. V. 2002 Modelling Streamline Curvature Effects in Explicit Algebraic Reynolds Stress Turbulence Models. *International Journal of Heat and Fluid Flow* 23 (5), 721 – 730.
- Wallin, S. & Mårtensson, G. E. 2004 A General 1D-solver for Partial Differential Equations. *Tech. Rep* TRITA-MEK 2004:3. Department of Mechanics, KTH Stockholm, in: Licentiate thesis *Experimental and numerical study of turbulent flow in rotating ducts* by G. E. Mårtensson.

Paper 2

Evaluation of a Vortex Generator Model in Adverse Pressure Gradient Boundary Layers

By Florian von Stillfried, Stefan Wallin, and Arne V. Johansson

Royal Institute of Technology, 100 44 Stockholm, Sweden

AIAA Journal **49**(5), pp. 982 – 993, DOI: 10.2514/1.J050680.

The use of a two-dimensional statistical passive vortex-generator model, applied to an adverse-pressure-gradient boundary-layer flow, is evaluated qualitatively against experimental and fully-resolved vortex-generator computations. The modelling approach taken here has the advantage of substantially reducing the complexity of including such flow separation control devices in a computational mesh, thus giving the opportunity to carry out faster parametric studies. Additional stresses, originating from the vortex-generator-model approach, are added as additional turbulent stresses to the mean governing equations instead of resolving vortex structures in the computational domain. The vortexgenerator model has been applied to allow direct comparison with prior experiments carried out at the Royal Institute of Technology Stockholm. Variations of the vortex-generator streamwise position and tests of different vortex-generator setups, such as co- and counter-rotational settings, are presented. Distributions of wall-pressure and skin-friction coefficients are used to evaluate the vortexgenerator model against fully-resolved vortex-generator data. It is shown that the vortex-generator model successfully predicts attached and separated flow states. Moreover, the results illustrate the vortex-generator model's capability to predict flow control sensitivity with respect to the streamwise position.

1. Introduction

The use of flow control in modern engineering applications is common since flow control devices have successfully shown to prevent and delay flow separation in wall-bounded flows, such as those occurring in inlet ducts, in diffusers, or on aircraft wings. The application of passive vortex-generator (VG) vanes typically energizes low-momentum boundary-layer flow by means of increased momentum mixing near walls. Because of delayed or even vanished separation, positive effects are very often lower overall drag generation through attached flow, decreased loads, lower design weight, and increased efficiency. Negative aspects also occur, mostly in the form of parasitic drag when flow separation control is not needed and if the passive VGs cannot be retracted. However,

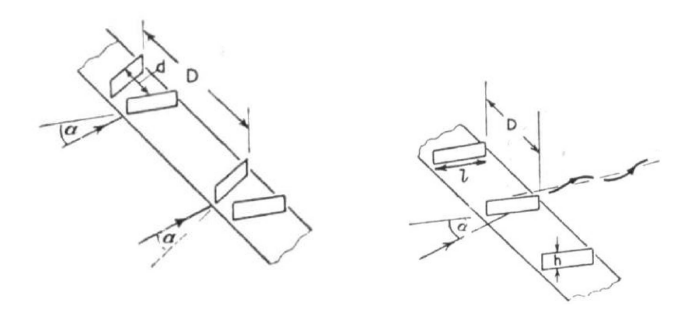


Figure 1. Pearcey's notation of VGs (Pearcey 1961).

such a tradeoff situation often favors the use of passive VGs due to their overall advantages.

One of the first comprehensive articles about flow separation control for airfoils and wings was published by Pearcey (1961). It includes a chapter about VGs, their mechanism, types and design criteria for flow control. Pearcey discusses different kinds of VG systems such as corotating, counter-rotational settings, different types of VG geometries, and a discussion about the influence of vortex strength and VG scale. The importance of vortex paths for counter-rotational systems due to induced vortex velocities as well as the importance of spacing issues for corotating systems due to velocity damping effects are described. Pearcey used the generated drag of the VGs as a defining parameter for successful and unsuccessful VG designs. Pearcey's successful designs for the application on aircraft wings and airfoils have a VG height-to-wing chord ratio h/c = 0.01, D/d = 4, D/h = 10, l/h = 1.25 and 2.5 at an angle of incidence $\alpha = \pm 15^{\circ}$ which are close to the VG parameters used in the present study (see also figure 1, with Pearcey's notation). Note that the authors use a slightly different notation throughout the paper.

Pauley & Eaton (1988) experimentally investigated vortex structures originating from delta-shaped VGs in counter-rotational common-flow-up/down and corotating setups with a height of approximately 150% of the local boundary-layer thickness δ_{99} . VGs were mounted within a zero-pressure-gradient (ZPG) turbulent boundary layer on a flat plate at a momentum thickness Reynolds number $Re_{\theta}=1700$. Pauley and Eaton studied the downstream development of the interacting vortex structures by an investigation of the streamwise vorticity and circulation. They found out that a common-flow-up setting leads to higher vortex interaction compared with a common-flow-down setting. They concluded that vorticity is diffused more quickly when there are strong interactions with neighboring vortices. This leads to a larger decrease in vorticity for common-flow-up VG pairs. Moreover, the primary mechanism for decreasing circulation was found to be the spanwise component of the skin friction. Since common-flow-down VGs interact more strongly with the viscous near-wall flow,

it was concluded that this setting is likely to lose more circulation strength than common-flow-up VGs.

Godard & Stanislas (2006) carried out an experimental study regarding optimal parameters for VGs in a decelerating boundary layer. Skin friction plots were used in order to characterize the VG effectiveness on flow separation control. They investigated several VG parameters such as the height, the shape, the position, the spanwise-spacing, and the blade distance of counter-rotational paired devices. Corotating devices were also included in this study, yet not as comprehensively as counter-rotational VGs, because counter-rotational devices turned out to perform better than corotating devices, leading to twice the skin-friction increase. In particular, the VG shape has importance for the flow control effectiveness to prevent separation since triangular VGs had advantages over rectangular VGs. The skin friction c_f is also sensitive to the VG vane angle of incidence α_{VG} , leading to an optimal value of $\alpha_{VG} \approx 18^{\circ}$. On the other hand, other parameters like the VG aspect ratio and the VG streamwise position did not show large influence on the results. In total, Godard and Stanislas showed that skin-friction measurements are an appropriate and sufficiently sensitive way for the investigation of passive VGs for flow separation control. Furthermore, they present optimal parameters for co- and counter-rotational VG arrays.

In accordance with Lin (2002), the VG parameters by Godard & Stanislas (2006) are very close to optimal values. Lin on the other hand has presented a comprehensive overview of ongoing research within the area of subboundary layer VGs (SBVG), stating that it is necessary to reduce the height h_{VG} of such devices to a maximum of 50% of the local boundary-layer thickness δ_{99} in order to maximize efficiency and decrease parasitic drag production. Lin (2002) also presents research of numerous different shapes and system settings regarding their effectiveness in terms of the percent reduction of the separation region and streamwise pressure distributions. Furthermore, different aerodynamic applications for flow control such as a high-lift airfoils, swept wings, noise reduction, and engine inlets are summarized and presented in the paper in which different methods to determine efficiency (lift/pressure/drag coefficient plots, sound pressure levels, etc., depending on the application) were used. Lin comes to the conclusion that SBVGs with device heights of $0.1 \le h_{\rm VG}/\delta_{99} \le 0.5$ are most effective and efficient when separation regions are fixed. To increase efficiency for VGs, the approach of minimal near-wall protuberances, i.e., the avoidance of unnecessary large VGs is highly desired. By that, vortex generation with just the necessary vortex strength in order to overcome separation effects is enabled. Furthermore, corotating VGs should have sufficient space between the vanes, enabling the reduction of vortex interaction and decay.

Computational fluid dynamics (CFD) introduces additional challenges to the investigation of passive VG vanes. Here, it is common to introduce VGs by resolved structures in the generated mesh. This is a very direct and intuitive approach, yet leading to many additional grid points in the vicinity of the VG. In turn, this implementation needs to be done carefully in order to resolve the vortex structures in the flow, leading to high design costs for the mesh generation. Moreover, parameter variations cannot be carried out easily because the mesh has to be changed according to new settings, giving rise to even higher grid generation costs the more comprehensive a parameter variation gets.

The development of VG modelling is the consequent approach that has become more and more used within the last decade. Bender et al. (1999) have introduced a VG model that uses a side force source term normal to the local flow and parallel to the inlet surface. The BAY (Bender Anderson Yagle) VG model is based on the lifting line theory (Glauert 1926; Anderson 1991, LLT) that adjusts the local flow velocity with the VG, depending on an empirical model constant which can be difficult to define correctly. Grid points that are supposed to be located within the VG vane need to be identified by the user in order to apply the forcing at the correct location. This method can be tricky since VGs commonly have an insignificant thickness. As Jirásek (2005) points out, this VG model approach is therefore grid dependent. Moreover, VG arrays modelled by the BAY model are simplified to a single distributed forcing along the spanwise direction enclosing the entire VG array that forces the flow.

Jirásek (2005) suggested an improved BAY model by removing some of its drawbacks, calling it jBAY model. The two approaches have in common that their meshes require three dimensions in order to account for the forcing source term at the modelled VG position. Yet, the jBAY model removes the geometrical structures of the VGs and the forcing is applied on a zero thickness surface. Still, the application of the jBAY model is not completely grid independent. A sufficient grid resolution is needed for the region downstream of the forcing region where the generated vortex structures need to be resolved in three dimensions.

Another step towards a simplification of the application of VGs within CFD is the introduction of statistical methods as done by Törnblom & Johansson (2007). Here, a Reynolds stress approach is used in a statistical sense. Additional stresses that originate from such modelled VGs and their additional vortex-velocity field are added to the differential Reynolds stress transport model (DRSM) equations. The core of this model is a Lamb-Oseen vortex model in combination with the LLT that also takes some of the VG's geometrical aspects into account. By spanwise-averaging the second-order correlations of the additional vortex-velocity field in the forcing plane, vortex stress contributions are formed and added to the Reynolds stress tensor. This method can be applied in two-dimensional as well as for three-dimensional meshes.

Investigations of this statistical VG model in a ZPG boundary-layer flow over a flat plate were presented in von Stillfried et al. (2009) based on experiments by Lögdberg et al. (2009). A calibration of the VG model was carried out and Reynolds stress results were compared to spanwise-averaged experimental data. The VG model was successfully applied on the ZPG flat plate boundary-layer flow, and in internal adverse-pressure-gradient (APG) diffuser flow. The

investigations showed that the VG model was capable of predicting correct trends and tendencies of the mean streamwise velocity and the total pressure recovery by predicting a reasonable decreased and even vanished separation region. The VG model has also the advantage of being no more computationally expensive than solving for the original Reynolds averaged Navier-Stokes (RANS) equations without the VG model forcing.

The main objective of this work is to examine the capabilities of the statistical VG model in APG flows over a flat plate, including a pressure-induced separation region. This flow case was previously carried out experimentally by Lögdberg (2008); Lögdberg et al. (2010). Firstly, the clean flat plate with APG is investigated and boundary conditions are adjusted in order to match experimental results, i.e., the wall pressure distribution in the streamwise direction without flow control. Then, the modelled VGs are introduced at the same position as in the experiment. Fully resolved VGs are also computed in order to gain additional comparison data for the evaluation of the VG modelling approach. Secondly, parameter variation studies of the VG streamwise position, the VG height, the VG spacing, as well as counter- and corotating VG setups are conducted using the VG model and are compared to the experimental results.

2. Implementation Methods

The VG model implementation method was presented in depth in Törnblom & Johansson (2007), and in von Stillfried *et al.* (2009). Nevertheless, the basic ideas are briefly presented here.

The VG model approach has its origin in the Prandtl LLT (Glauert 1926) where the circulation distribution across a wing in free flight is given by

$$\Gamma(y) = \frac{K}{2}U(y)c(y)\left[\alpha(y) - \frac{w(y)}{U(y)}\right],\tag{1}$$

where K is the local section lift slope of the wing $(K_{\text{max}} = 2\pi \text{ rad}^{-1} \text{ according})$ to thin airfoil theory), U(y) is the local incoming freestream velocity, c(y) the local chord length of the wing, $\alpha(y)$ the local angle of attack, and w(y) the local downwash velocity. The ratio w(y)/U(y) is the local induced angle of attack for small α , and the local downwash w(y) reads

$$w(y) = \frac{1}{4\pi} \int_{-h}^{h} \frac{d\Gamma}{dy'} \frac{1}{y' - y} dy'. \tag{2}$$

Because limitations regarding the application of the LLT to VGs in wall-bounded viscous flows, the LLT is only used as an approximation for deriving the circulation distribution. Here, only $\Gamma_{\rm max}$, the maximum value for the circulation distribution, is used for computing the additional vortex-velocity field when using a Lamb-Oseen vortex model. The azimuthal vortex-velocity distribution for a single VG vane reads

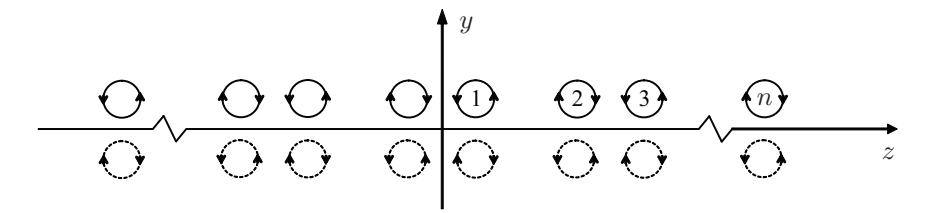


FIGURE 2. A vortex array with n counter-rotational vortex pairs and their mirror images for computing the total superposition of the vortex-induced velocity field $V_i(y,z)$ in the VG forcing plane. [Image inspired by Törnblom & Johansson (2007).]

$$V_{\Phi}(r) = \frac{\Gamma_{\text{max}}}{2\pi r} \left[1 - e^{-\left(\frac{r}{r_0}\right)^2} \right], \tag{3}$$

with $\Gamma_{\rm max}$ from the LLT circulation distribution, r_0 the vortex core radius and r the radial coordinate from the vortex center. A limitation of this vortex model is that the velocity component in the streamwise direction remains unaffected. Different approaches appear in the literature, such as Velte et~al.~(2009) who describes helical vortex structures of longitudinal vortices for high angles of incidence $\alpha=20^{\circ}$ - 40° by a simplified Batchelor vortex model (Batchelor 1964), taking also the streamwise velocity variation into account.

A VG array consists of more than one VG pair (counter-rotational setup) or more than one VG vane (corotating setup) so that all VGs influence the vortex flow field everywhere in the VG model forcing plane. Since this paper mainly discusses the investigation of counter-rotational setups, VG pairs were implemented unless stated differently. A superposition of the azimuthal vortex velocities $V_{\Phi}(r)$ for each VG pair and its corresponding vanes is needed, as shown in figure 2. Here, the wall (y=0) acts approximately as a symmetry condition for the vortices, which is simulated by introducing mirror vortices (y<0).

The additional total superimposed vortex-velocity field $V_i(y,z)$ is used in order to calculate the corresponding single-point second-order statistics which are assumed to act as additional Reynolds stresses. Spanwise averaging of the second-order statistics over one VG pair distance D is used in order to derive the VG model stresses. This is sufficient because the resulting vortex flow field is periodic:

$$\Delta \overline{u_i' u_j'}(y) = \frac{1}{D} \int_{-D/2}^{D/2} V_i(y, z) V_j(y, z) dz.$$
 (4)

Additional contributions from equation (4) for a VG array are only nonzero for $\Delta \overline{v'v'}$ and $\Delta \overline{w'w'}$. Moreover, a wall damping function, e.g. $(1-\exp{[-20y/h]})$, needs to be introduced (Törnblom & Johansson 2007) and applied in equation

(4) because the vortex velocities in the spanwise direction at the wall boundary y=0 will not cancel out and would result in a finite value in equation (4). The wall damping function influences the $\Delta \overline{w'w'}(y)$ stresses in order to impose correct boundary conditions for the $\Delta \overline{w'w'}(y)$ distribution so that $\Delta \overline{w'w'}(0)=0$. The specific choice of the wall funtion is not critical for the downstream distribution evolution since it is only assumed to act very close to the wall boundary (for $y \leq h/20$). Nevertheless, damping the local peak in the $\Delta \overline{w'w'}(y)$ distribution is preferably implemented here.

The general procedure to add the resulting vortex stresses from equation (4) to the DRSM equations is done via a so-called triple decomposition of the instantaneous velocity field u_i at the VG streamwise position x_{VG} . First, the additional vortex velocities $V_i(y,z)$ are added to the decomposed velocity field from the general ansatz for the RANS equations:

$$u_i(y, z, t) = U_i(y) + u'_i(y, z, t) + V_i(y, z),$$
 (5)

where U_i and u'_i are the mean velocity and the turbulent fluctuations, respectively. One possibility is to add V_i to the mean flow U_i in a RANS computation, thus resolving the generated vortices and expressing the turbulent part u'_i through a conventional turbulence model. We will here follow a different approach where V_i is added to the turbulent fluctuations u'_i . The combined velocity field v'_i from the turbulence and vortices is defined as

$$v_i'(y, z, t) \equiv u_i'(y, z, t) + V_i(y, z).$$
 (6)

Then, the additional time- and spanwise-averaged second-order statistics of the vortex-velocity field enter the RST equations by substituting the Reynolds stress tensor $\overline{v_i'v_j'}$ with the extended Reynolds stress tensor $\overline{v_i'v_j'}$, where

$$\overline{v_i'v_j'}(y) = \overline{(u_i' + V_i)(u_j' + V_j)}
= \overline{u_i'u_i'}(y) + \Delta \overline{u_i'u_i'}(y),$$
(7)

where

$$\Delta \overline{u_i' u_j'}(y) \equiv \overline{V_i V_j}(y) \tag{8}$$

is written for the additional contribution from the vortex stresses. At the forcing plane where the vortices are generated, the incoming turbulence has not yet been adjusted to the vortices so that the turbulence plus the vortices can be assumed to be rather uncorrelated. Thus, the cross-product terms containing the correlations $\overline{u_i'V_j}$ and $\overline{u_j'V_i}$ are assumed to be negligible.

The additional stresses $\Delta \overline{u'_i u'_j}$ at the VG model plane are added as a surface source (or line source in two-dimensional) to the DRSM. This is slightly different from the approach taken by Törnblom & Johansson (2007) who used a volume force in a region close to the VG. The downstream development of the

combined stresses, $\overline{v_i'v_j'}$, is then described by a DRSM, which takes the development of all stress components into account. The VG model approach is suitable for the use within a DRSM that naturally accounts for each Reynolds stress component. Moreover, the energy transfer between the different components is established by a RST model, enabling $\overline{u'v'}$ Reynolds stress production which is initially not forced by the VG model. This nonequilibrium relaxation process cannot be captured by eddy-viscosity models. However, a corresponding addition of the vortex kinetic energy $\Delta k = \Delta \overline{u_i'u_i'}/2$ can be added to the turbulence kinetic energy k in two-equation models such as $k-\omega$ or $k-\epsilon$ models. Such an approach can be used also for explicit algebraic Reynolds stress turbulence models (EARSM) that are derived from RST models but the dynamics of the energy transfer is lost and the results should be used with caution. The user must be aware of the possible drawbacks that come with a simplification to two-equation turbulence models.

3. Experimental Setup

As previously mentioned, VGs in a counter-rotational setup in an APG boundary layer were experimentally examined by Lögdberg et al. (2010) (see also figures 3 and 4). Each VG pair consists of two rectangular vanes of height $h_{\rm VG}$ = 18 mm and a chord length $c/\cos\alpha_{\rm VG}$ with c=54 mm being the projected VG chord in the streamwise direction. The vanes are mounted in pairs at angles of incidence $\alpha_{VG} = \pm 15^{\circ}$. The mean distance between such two blades is d = 37.5 mm and the distance between two adjacent VG pairs is D = 150mm. The VGs are mounted in an array consisting of n = 5 VG pairs with their trailing edges located at $x_{VG} = 1.54$ m from the leading edge of the flat plate in the test section of the boundary-layer wind tunnel at Royal Institute of Technology (KTH) Stockholm. Experimental results (case 2) show that the local boundary-layer thickness at $x_{\rm VG}=1.54~{\rm m}$ is $\delta_{99}=27.3~{\rm mm}$ so that the ratio $h_{\rm VG}/\delta_{99}=0.66$. The freestream velocity U_{∞} is 26.5 ± 0.1 m/s and the temperature is monitored by a temperature control system at $T=20\pm0.07^{\circ}\mathrm{C}$ over the cross-sectional area. The wind tunnel test section is 4.0 m long with a cross-sectional area of 0.75 x 0.50 m², and the turbulence intensity in the test section is <0.04\% [see also Lindgren & Johansson (2004)]. A flat plate made of acrylic glass splits the wind tunnel's test section and is mounted with a distance of 0.30 m to the test section's upper wall (see figure 4). At the wind tunnel inlet, the test section has a height of 0.50 m which is diverged by a back side curved wall at x = 1.25 m downstream of the leading edge of the flat plate in order to induce the APG. Furthermore, a suction system is installed at the curved wall so that flow separation is prevented there. Another feature of the suction system is the additional capability to change the APG strength through adjusting the suction rate at the curved wall. In total, three different APG cases were performed with different suction rates. Lögdberg's case 2 with a suction rate of 12.5-13% of the incoming mass flow is used for the investigation of the VG model, since it represents the most detailed investigated experiment (see also figure 5). All experimental measurements were performed

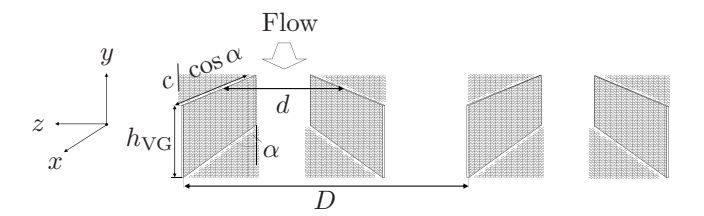


FIGURE 3. VG geometry from experiments (Lögdberg et al. 2010).

with particle image velocimetry. Refer to Lindgren & Johansson (2004) for further details of the wind tunnel, and to Lögdberg (2008); Lögdberg $et\ al.$ (2010) as well as to Angele (2003) for further details of the experiments, the setup and the measurement techniques.

The wall-pressure coefficient c_p for all c_p diagrams is here defined as

$$c_p \equiv \frac{p - p_{\text{ref}}}{q_{\infty}},\tag{9}$$

where p is the local wall static pressure, $p_{\rm ref}$ the reference wall static pressure at x=1.15 m, and q_{∞} the dynamic pressure in the freestream. The separation bubble in experiments is defined as the region where at least 50% back flow at the wall is developed, i.e. the wall back flow coefficient $\chi_{\rm wall} \geq 0.5$. According to Dengel & Fernholz (1990), χ was extrapolated to the wall from the data points in the region $y \approx 1.5$ - 10 mm in order to estimate $\chi_{\rm wall}$. The resulting geometrical properties such as the separation location $x_{\rm sep}$, the reattachment location $x_{\rm att}$, the length $l_{\rm sep}$ as well as the height of the separation bubble $h_{\rm sep}$ [defined as $U(h_{\rm sep})=0$] are given in table 2.

4. Computational Setup

This investigation includes three computational cases: a two-dimensional case of a clean flat plate, a two-dimensional case with the VG model applied and a three-dimensional case that fully-resolved the VGs on the flat plate. The following abbreviations are used for a labeling of the different computations: 1) clean flat plate computations (FP2D), for the flat plate without VG model;

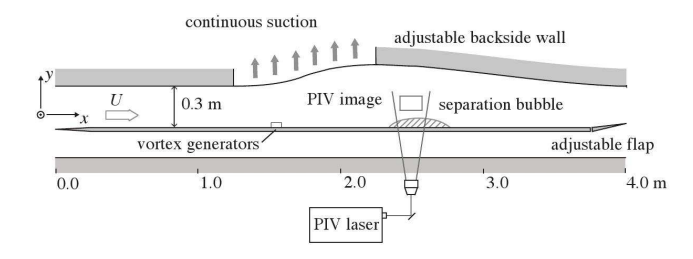


FIGURE 4. Sketch of the boundary-layer wind tunnel test section used in experiments. [From Lögdberg et al. (2010).]

2) VG model computation (VG2D), for the flat plate with VG model; and 3) fully-resolved VG computations (VG3D), for the three-dimensional flat plate with fully-resolved VGs.

Furthermore valid throughout this paper, the FP2D and VG2D computations are carried out using a differential Reynolds stress turbulence model (DRSM) with a pressure-strain rate model corresponding to the Wallin and Johansson (WJ) (Wallin & Johansson 2000, 2002) EARSM with curvature correction. The WJ-DRSM is linked to the ω -equation of the Hellsten $k-\omega$ turbulence model (Hellsten 2005). The VG3D computations are carried out by the use of the WJ-EARSM turbulence model without curvature correction (Wallin & Johansson 2000), again linked to the Hellsten $k-\omega$ turbulence model. This is done since the VG model was specially formulated for DRSM turbulence models and because the VG3D case instead resolves the vortex structures, unlike the VG model which adds the vortex stresses to the Reynolds stresses. All computations are carried out with the Edge CFD code (Eliasson 2002) and the local airfoil-section lift slope K from equation (1) is set to $1.8\pi \text{rad}^{-1}$ for all VG model computations, which is 10% lower than for the thin airfoil theory. This adjustment is justified due to the constant finite thickness of the VGs, the effects of viscosity that are present in real wall-bounded flows, and the rather large VG angle of incidence $\alpha_{VG} = \pm 15^{\circ}$. In addition, the modelling approach of the VGs is based on various other assumptions as described in section 2 and the precise value of K is not critical.

4.1. Boundary Conditions for Adverse Pressure Gradient Flow

For all computational cases, a 0.25-m-high and a 7.25-m-long rectangular computational domain was used. This domain includes a 0.25-m-long inflow region in front of the flat plate, thus giving a flat plate length of l = 7.00 m. The domain height is consequently somewhat smaller than the wind tunnel height. Instead, a specific computational boundary condition is applied on the top boundary. This strategy was applied since the upper wind tunnel wall including the suction section (see figure 4) could not be transformed identically into a computational domain. Therefore, pressure and velocity boundary conditions are applied at the upper boundary at y = 0.25 m. The upper boundary is moreover divided into two parts: first, a slip wall boundary part without pressure/velocity forcing that forces the flow in the x-direction as in the wind tunnel in the experiments from the inflow region at x = -0.25 m up to x =1.25 m in front of the APG region. Another upper boundary part from x =1.25 m up to the outflow boundary at 7.00 m with weak characteristic boundary conditions where an APG/favorable-pressure-gradient (FPG) distribution is set in order to generate a similar wall-pressure distribution on the flat plate as measured in experiments (figure 5). This upper boundary condition allowed mass flow across its boundary, enabling a similar APG/FPG distribution on the flat plate as in the experiments. The pressure p and the (u, v) velocities were set as boundary conditions according to inviscid theory.

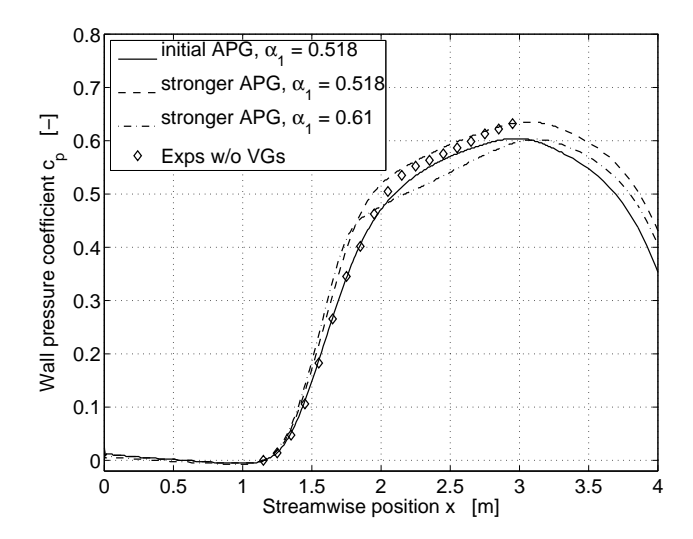


FIGURE 5. Wall pressure-coefficient distributions for the initial APG, the stronger APG, the stronger APG with the modified α_1 value, and the experiments without VGs [case 2 (Lögdberg *et al.* 2010)].

For both, the two- and three-dimensional grid, the value for the first grid point at the wall was set to $y = 10^{-5}$ m throughout the domain, giving values of $y^+ = \mathcal{O}(1)$. As mentioned previously, the three-dimensional computational domain fully-resolved the VGs, assuming a no-slip condition not only on the flat plate but also on the VGs. In addition and in contrast to experiments, the VGs were represented by very thin structures. Furthermore, symmetry conditions were applied on both xy-boundary planes so that the computational domain could be reduced to including only one VG vane, therefore leading to a three-dimensional grid width of one half VG pair distance D/2 = 75 mm (see figure 3). Generally, the computational mesh was kept fine in the vicinity of the VGs by means of an O-grid topology and consisted in total of more than 1.9 million nodes. A structured grid is wrapped around the VG surface. The VG surface and the O-grid outer surface can be seen in figure 6 and it can be observed that the structured O-grid is locally embedded in an unstructured prismatic region. Moreover, this unstructured prismatic grid is embedded in a fully-structured grid upstream and downstream of the VG region (not visible in figure 6).

In accordance with the experiments, the freestream velocity and the temperature at the inlet are set to $U_{\infty}=26.5~\mathrm{m/s}$ and $T=20^{\circ}\mathrm{C}$, respectively, giving a Reynolds number based on the plate length $Re_{l}\approx 1.42\cdot 10^{7}$. The experimental pressure distribution on the flat plate is given between $x=1.15~\mathrm{m}$ to 2.95 m (see also figure 5), and therefore does not cover the whole x-coordinate range which is needed for the computations. It was decided to mirror the given

wall-pressure distribution around its peak value at $x_{p_{\text{wall,max}}} = 2.95 \text{ m}$, and a constant pressure was imposed for the region between x = 4.75 m and the domain outlet.

An adjustment of the α_1 coefficient for the production term in the ω -equation of the Hellsten $k-\omega$ turbulence model (Hellsten 2005) was necessary since early FP2D test runs did not generate the desired separation bubble on the flat plate, even though the wall-pressure distribution was reasonably matched in the region 1.15 m < x < 1.95 m (see the "initial APG, α_1 = 0.518" graph in figure 5). Therefore, the pressure distribution on the upper boundary was forced with a slightly stronger APG in order to generate a separation re-

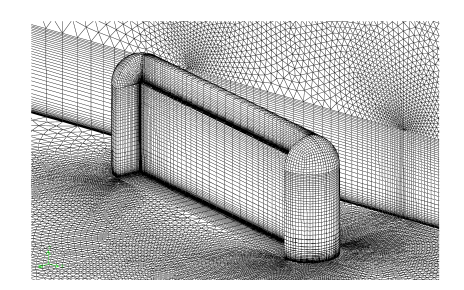


FIGURE 6. O-grid and the fully-resolved and meshed VG vane inside of it.

gion (see the "stronger APG, $\alpha_1 = 0.518$ " graph in figure 5.

Still, a separation region could not be established. A stronger amplification of the APG did not lead to any better results regarding an established separation region on the flat plate. A change of α_1 from 0.518 to 0.61 increases the production of the turbulent specific dissipation rate ω and represents a reasonable choice for the desired separation region (see "stronger APG $\alpha_1 = 0.61$ " graph in figure 5). As can be observed in figure 7(a), the velocity profiles at the inflow to the APG section are different, indicating that the change in α_1 changes the overall flow state. In addition, figure 7(b) shows a decreased c_f distribution for $\alpha_1 = 0.61$, which leads to a separated region between x = 1.91m to 2.42 m (note that $c_f < 0$). By adjusting the α_1 value, a separation region similar to that in the experiments is achieved, yet located approximately $\Delta x =$ 0.30 m further upstream as compared to the experiments. The total length of the separated region can be seen to be similar to that in the experiments (see table 2). The displacement thicknesses $\delta_{\text{sep,max}}^*$ at the location of the maximum separation bubble thickness $x_{\rm sep,max}$ for the experiments ($x_{\rm sep,max}=2.55$ m) and the FP2D computations ($x_{\text{sep,max}} = 2.25 \text{ m}$) have a value of 71.3 and 76.2 mm, respectively. The separation bubble height for the FP2D case at this streamwise position is $h_{\rm sep,max}=26$ mm. Lögdberg et al. (2010) report a separation bubble height of $h_{\rm sep,max}=17$ mm. Likewise, the momentum boundary-layer thicknesses $\theta_{\mathrm{sep,max}}$ for the experiments and the FP2D computations have a value of 14.75 and 13.5 mm, respectively. Therefore, the shape factors $H_{12,\text{sep,max}}$ at $x_{\text{sep,max}}$ have a value of 4.90 and 5.63 for the experiments and the FP2D computations, respectively. The results can be regarded as being satisfactorily close to the experimental data.

Table 1. Boundary-layer parameters at the position of the VG for two different VG positions. VG2D computations compared with experiments.

Case	x_{VG} , m	δ_{99} , mm	$h_{\rm VG}/\delta_{99}$	δ^* , mm	$h_{\rm VG}/\delta^*$
Exps case 2	1.10	15.0	1.20	3.33	5.41
VG2D	1.10	17.0	1.06	2.89	6.23
Exps case 2	1.60	29.0	0.62	6.42	2.80
VG2D	1.60	38.0	0.47	6.39	2.82

A comparison study of certain boundary-layer parameters with flow control at the VG planes for $x_{\rm VG}=1.10$ m and $x_{\rm VG}=1.60$ m is given in table 1. This was done in order to show the quality of comparability between computations and experiments with VGs. In general, the computational results show good agreement with experimental data. It must be mentioned that the boundary layer is already thickened under the influence of the APG at $x_{\rm VG}=1.60$ m. Consequently, larger differences in δ_{99} for $x_{\rm VG}=1.60$ m compared with $x_{\rm VG}=1.10$ m (located in front of the APG region) occur due to the different boundary conditions of the experiments and the computations.

This rather ad hoc method can be justified by the fact that the investigations focus on flow separation control using VGs and the resulting differences in skin friction. The computations were set up such that the baseline flow has a separation in line with the experiments. Hence, the intention was not to suggest a new turbulence model.

4.2. Grid Refinement Study

A grid refinement study was carried out for the VG2D computations in order to examine results regarding the necessary grid resolution. In particular, the resolution in the wall-normal direction around the VG model tip and the streamwise resolution in the vicinity and downstream of the VG model location

Table 2. Separation location, reattachment location, separation bubble length, location of maximum separation bubble thickness, maximum separation bubble thickness, and the shape factor at $x_{\rm sep,max}$ of the flat plate case 2 experiments (Lögdberg 2008), and corresponding computational results of the FP2D computations with adjusted $\alpha_1=0.61$ are given next

Case	$x_{\rm sep}$ m	$x_{ m att}$ m	$l_{\rm sep} \ m mm$	$x_{\rm sep,max}$ m	$h_{ m sep,max}$ mm	$H_{12,\text{sep,max}}$
Exps case 2	2.24	2.85	61	2.55	17	4.90
$DRSM_{\alpha_1=0.518}$	-	-	-	-	-	-
$DRSM_{\alpha_1=0.61}$	1.91	2.42	51	2.25	26	5.63

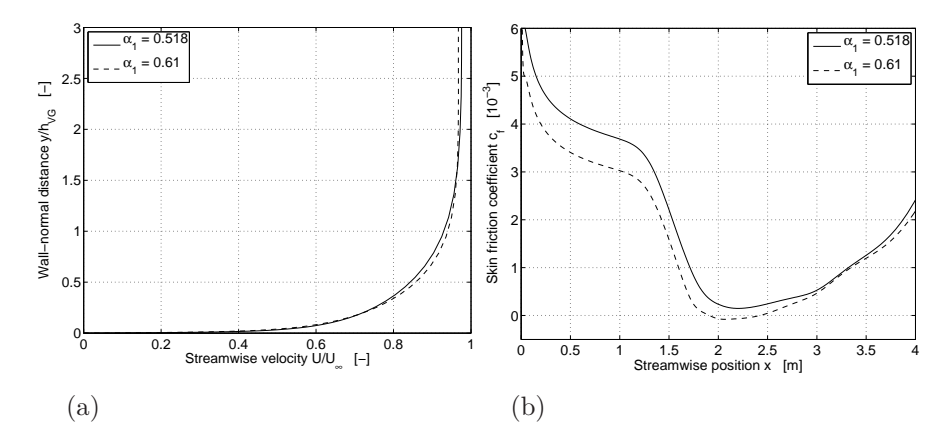


FIGURE 7. Results of the α_1 adjustment in the ω equation for the clean flat plate: (a) boundary-layer velocity profiles at a streamwise position x=1.00 m, and (b) local skin-friction coefficient distributions .

are of interest. Three different grids were generated (see also figure 8). The baseline grid in figure 8(a) consists of 321 x 55 nodes in the x and y directions without any refinement region around the VG. The fine-y grid [321 x 100 $\,$ nodes, figure 8(b) is refined only in the wall-normal direction with the grid points clustered around the VG tip (y = h) where the $\Delta \overline{u_i' u_j'}$ forcing is strong. The fine-xy grid (536 x 100 nodes) has the same distribution in the wall-normal direction as the fine-u grid, but is further refined in the streamwise direction in the vicinity of the modelled VG [see figure 8(c)]. The resulting skin-friction coefficient distribution plots are given in figure 9. As can be observed, the refinement in the wall-normal direction gives a somewhat lower skin friction upstream of the VG position. However, it is sufficient to use the baseline grid without any local refinement regions around the VG tip, in the vicinity and downstream of the VG model location. Downstream of the VG position, the skin friction reaches a state of grid independence with an error of less than 5% compared with the refined grids which are seen to give very similar results over the whole flat plate. Therefore, the baseline grid was chosen for the examination of the APG flat plate flow with the VG model. An important result of this grid study is that the VG model may be placed anywhere the mesh resolution compares to its original location without the need for further remeshing. This is very advantageous when a parameter variation of the VG model location is carried out (see also section 5 for more details).

5. Results

This chapter presents the results of the FP2D, the VG2D, and the VG3D computations. Experimental c_f and c_p distributions with VGs were unfortunately not available. A baseline case was set and a VG position, a VG setup, and

a circulation per unit width variation as examined in Lögdberg et al. (2010) are carried out. VG3D computations were nevertheless only carried out for the baseline case with $x_{\rm VG}=1.54$ m. Both for the baseline case and for the VG parameter variations, skin-friction plots are presented in the subsequent sections. Velocity profiles for the FP2D case, located in the middle of the separation bubble at $x_{\rm sep,max}=2.25$ m, are also presented and compared with experiments for the VG2D and VG3D baseline cases. The VG position and the circulation per unit width variation computational results are moreover compared quantitatively with each other and corresponding experiments.

5.1. Baseline Case

The same VG setup as in the experiment is used for the VG2D and VG3D baseline cases. The trailing edge of the fully-resolved VGs and the VG model forcing plane were consequently located at $x_{\rm VG} = 1.54$ m.

Figure 10(a) shows the wall pressure-coefficient distribution of the experiments without VGs. They describe a steep increase in wall-pressure downstream of $x_{\rm APG,start}=1.25$ m. The constant increase of c_p remains until $x\approx 2.00$ m from where the c_p distribution flattens out and quickly develops another constant slope region from x=2.25 m up to approximately $x_{\rm APG,end}=2.95$ m. This region can be identified as the separated region (cf. table 2).

The FP2D uncontrolled computation gives a very similar c_p distribution, showing a slightly steeper pressure increase and a separation region beginning at x=1.91 m. The skin-friction plots in figure 10(b) present additional information about the separation region. As expected, c_f decreases quickly from the leading edge and starts to decrease even faster beginning with the APG region at x=1.25 m. The skin-friction coefficient drops below zero between x=1.91 m to 2.42 m, describing the exact location of the back flow region close to the wall for the FP2D computation (cf. table 2).

The VG2D results in figure 10(a) show how the application of the VG model affects the c_p distribution along the flat plate. It can be observed that

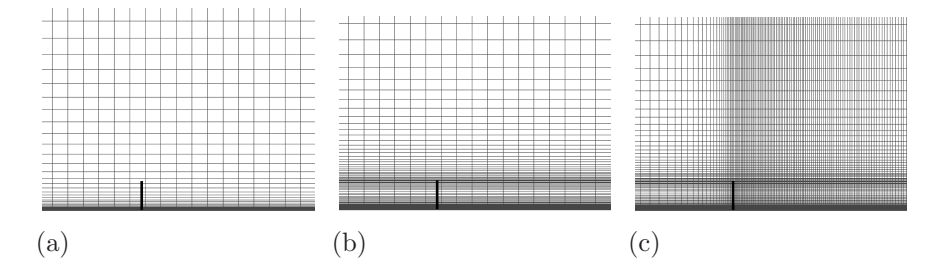


FIGURE 8. Three different grids for the VG2D grid refinement study: (a) baseline, (b) fine-y, and (c) fine-xy grid. The position and height of the modelled VG is indicated as a vertical black line.

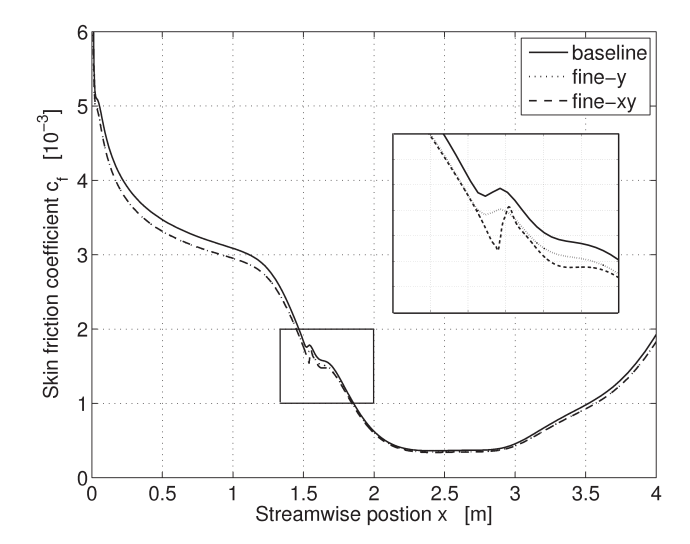


FIGURE 9. Grid comparison study: local skin-friction distributions for the baseline, the fine-y, and the fine-xy grids including a detail plot that shows the skin-friction change around the VG model location for each grid.

the pressure distribution is slightly weaker between x=1.25 m and 1.85 m when compared with FP2D computations. After that, the pressure increase is much stronger than for the uncontrolled case, indicating that the separation region has vanished. This result can be confirmed and observed in figure 10(b) where the c_f distribution does not decrease below zero anywhere.

Spanwise averaged VG3D results including the fully-resolved VGs are also presented in figure 10. It can be observed that the c_p distribution is generally slightly lower downstream of $x_{\rm VG}=1.54$ m, yet very similar to the VG2D results. The pressure loss across the VGs and the VG model location is also shown in detail in figure 10(a). Compared with the VG2D results, the c_f distribution for the VG3D case describes a higher skin-friction level throughout the whole APG section except in the vicinity of the VGs [see figure 10(b)]. This difference is a result of the VG3D vortex structures which are resolved in the computational domain and survive very far downstream. Compared with that, the VG2D turbulent stresses including the vortex stress contribution decay quickly downstream of the VG model plane. Downstream of the APG section (x>2.95 m), the curve collapses with the VG2D curve over a short section but diverges again within the FPG section.

The extended Reynolds stresses $\overline{v_i'v_j'}$ from equation (7) including the Reynolds stresses $\overline{u_i'u_j'}$ and the additional vortex stresses $\Delta \overline{u_i'u_j'}$ from equation (4) from the VG2D computations are compared with the VG3D computations at four different streamwise planes (x=1.54, 1.60, 1.70, and 1.80 m) and are

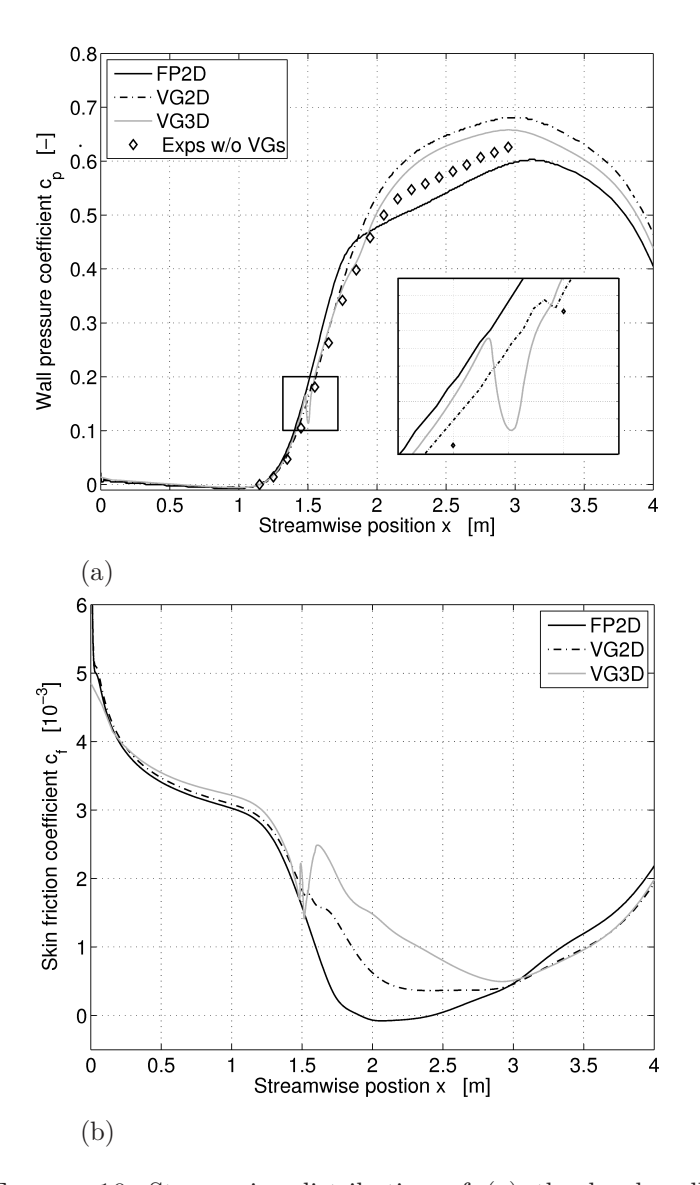


FIGURE 10. Streamwise distribution of (a) the local wall pressure-coefficient distributions including a detail plot showing the pressure drops for VG2D and VG3D at the VG position, and (b) the local skin-friction coefficient distributions for the FP2D case, the VG2D and VG3D baseline cases with $x_{\rm VG}$ = 1.54 m, and experiments without VGs [only (a)].

given in figure 11. Note that there is no forcing of the $\Delta \overline{u'v'}$ and $\Delta \overline{u'u'}$ stresses for the VG2D at the VG model forcing plane x=1.54 m. There, the stresses

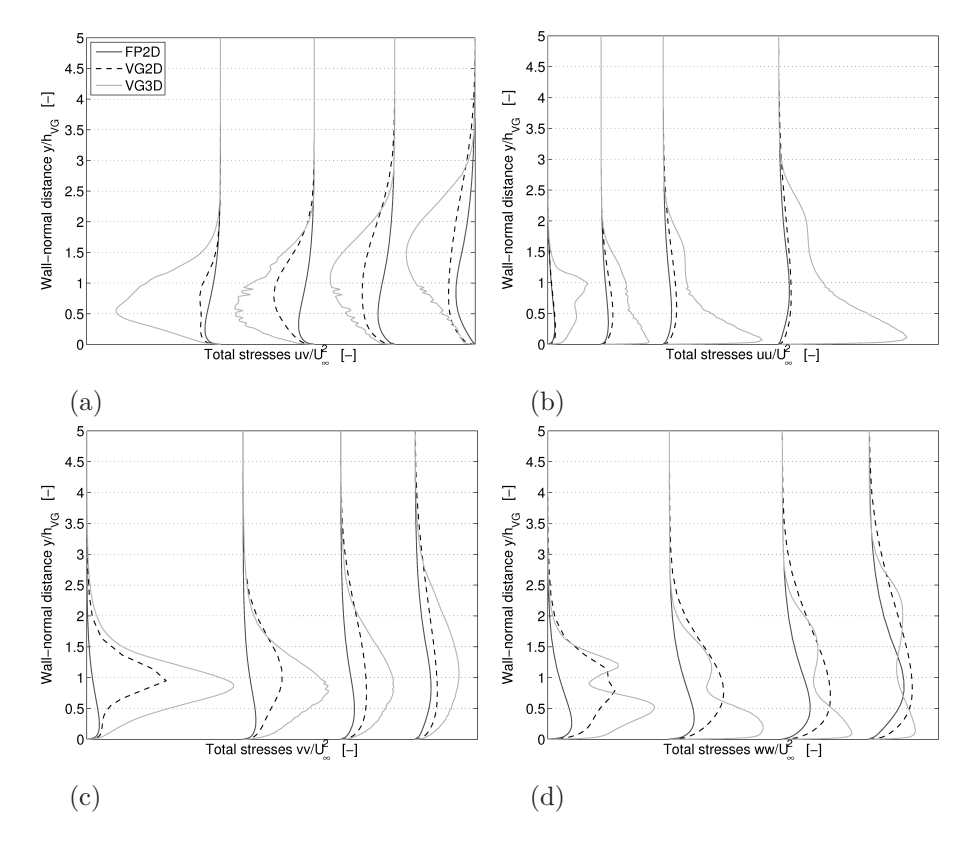


FIGURE 11. VG baseline case: total stresses $\overline{u'v'}$, $\overline{u'u'}$, $\overline{v'v'}$, and $\overline{w'w'}$ including vortex and turbulence stresses from VG2D computations compared with spanwise-averaged results from VG3D computations at streamwise positions x=1.54, 1.60, 1.70, and 1.80 m. Also, the Reynolds stresses from the FP2D computations are included for comparison.

describe a very similar distribution compared with the incoming turbulence (FP2D). Nevertheless, the total $\overline{u'v'}$ stresses of the VG model are increasing for the subsequent streamwise locations due to production and redistribution even though they do not totally catch up with results from resolved computations. In contrast to that, the VG2D $\overline{u'u'}$ stresses do not seem to change substantially when traveling downstream. Figures 11(a) and 11(b) show that the resolved computations reveal much stronger spanwise-averaged $\overline{u'v'}$ and $\overline{u'u'}$ stresses due to the existing vortex structures in the computational domain. The total $\overline{v'v'}$ and the total $\overline{w'w'}$ stress distributions [figures 11(c-d)] clearly show the effect of the vortex stress forcing at the first streamwise position. Still, differences between the VG model results and the fully-resolved results occur both in terms of amplitude and structure but the qualitative description of the

stresses is reasonable. Redistribution and diffusion result in weaker stresses further downstream. The VG model could be improved in order to investigate a more complete vortex stress forcing, including the $\Delta \overline{u'u'}$ and the $\Delta \overline{u'v'}$ stress contributions. This aspect is worth a thorough investigation and a study is currently ongoing.

5.2. Vortex Generator Position Variation

Seven streamwise VG positions using the VG model are examined here: $x_{VG} =$ 0.10, 0.50, 0.80, 1.25, 1.40, 1.54, and 1.80 m; see also figure 12. The first three positions are located in the ZPG section and the last four positions in the APG section, whereas the most downstream located VG at $x_{VG} = 1.80$ m is very close to the separation region ($x_{\text{sep}} = 1.91 \text{ m}$). The VG model computations show distinct c_f peaks at the VG positions (except for $x_{VG} = 1.80$ m), similar to the VG3D computations. The flow separation prevention works well even though the effectiveness in enhancing the c_f distribution is strongly dependent on the VG location. It can be seen that all VG positions, except the very downstream, prevent flow separation successfully. Within the APG region, the skin friction is generally further increased the further upstream the VG is located. By comparing the results in figures 12(a) and 12(b), it can be observed that there must exist a global optimal VG position in the vicinity of x = 1.25m. Further computations may be helpful to locate the exact position but this was not the aim of this investigation.

Figure 13 presents the c_p distributions for the four streamwise positions $x_{\rm VG} = 1.25, 1.40, 1.54, \text{ and } 1.80 \text{ m}$. Here, the tendency of a higher pressure increase in the APG region is clearly visible the more upstream the VGs are located. This is the result of higher streamwise velocities around the VGs due to a thinner boundary layer further upstream. Stronger vortices are therefore generated that in turn have a stronger effect on flow separation prevention, resulting in lower total pressure losses.

Further downstream at $x_{VG} = 1.80$ m, the c_f and c_p distributions in figures 12(b) and 13 are almost equal to the FP2D case [cf. figures 10(a) and 10(b)]. The separation bubble is still present because the boundary layer is already substantially decelerated at $x_{VG} = 1.80$ m so that only very weak vortices are generated. These vortices do not to have any significant effect on flow separation prevention. The trend that an increased distance between the VGs and the separation region has advantages for flow separation control is valid in the range of positions studied here. Locating the VGs further upstream, the generated vortices may nevertheless encounter sooner breakdown or strong diffusion which in turn weakens the positive influence on the mean flow before they actually reach the separated region.

Velocity profiles for the VG position variation and the VG3D baseline case at $x_{\text{sep,max}} = 2.25 \text{ m}$ are presented in figure 14. The VG3D computations provide, besides the spanwise-averaged velocity profile, two additional velocity profiles at an inflow and an outflow position in the spanwise direction. These

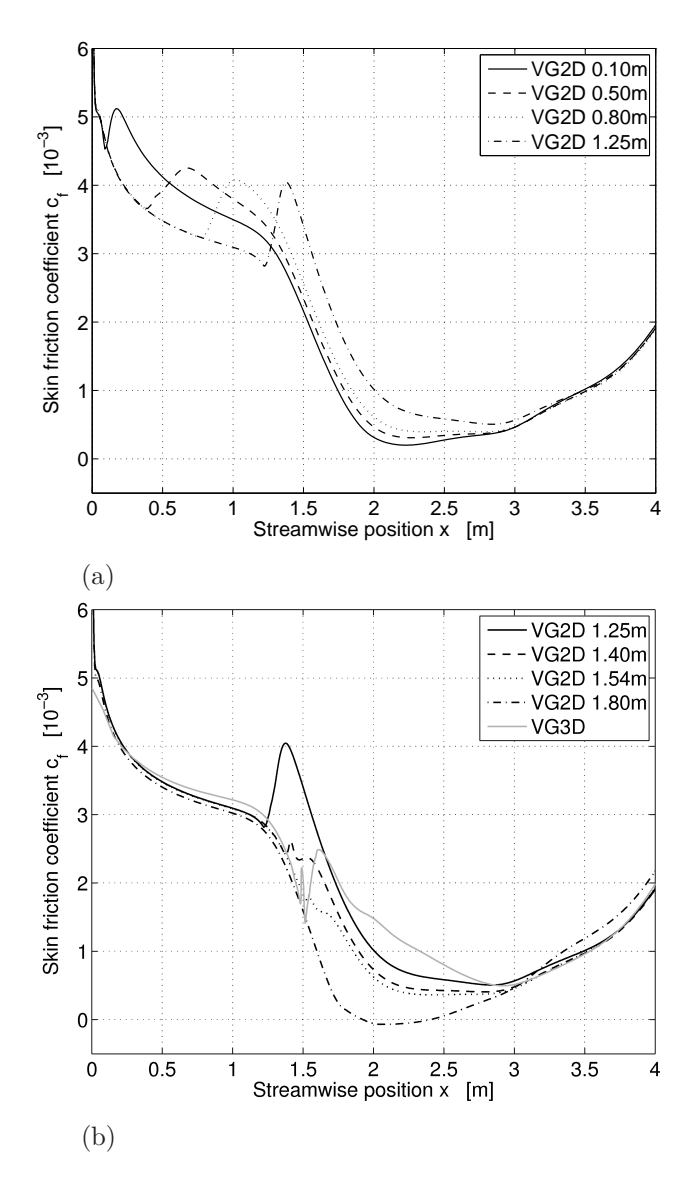


FIGURE 12. Streamwise distributions of the local skin-friction coefficient distributions for the VG position variation and for the VG3D baseline computations with $x_{\rm VG}=1.54$ m.

two positions correspond to the inflow and outflow positions from Lögdberg $et\ al.\ (2010)$ (see also figure 15). The inflow position is defined as the midposition between two VG vanes in a counter-rotational setup. Likewise, the outflow position is defined as the midposition between two VG pairs.

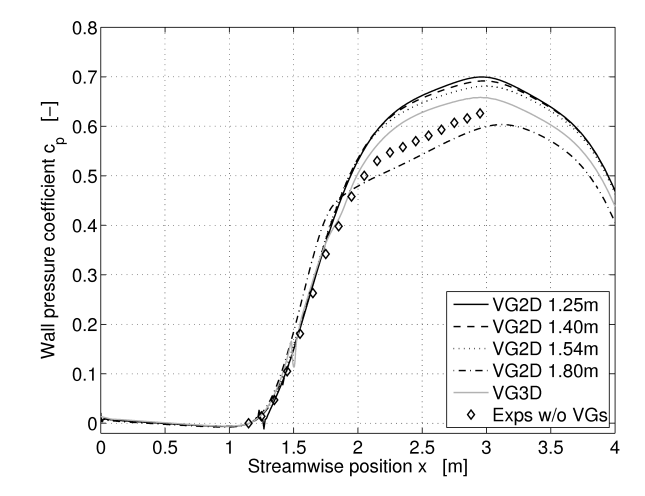


FIGURE 13. Streamwise local wall pressure-coefficient distributions for the VG position variation, for the VG3D baseline computations with $x_{\rm VG}=1.54$ m, and for experiments without VGs.

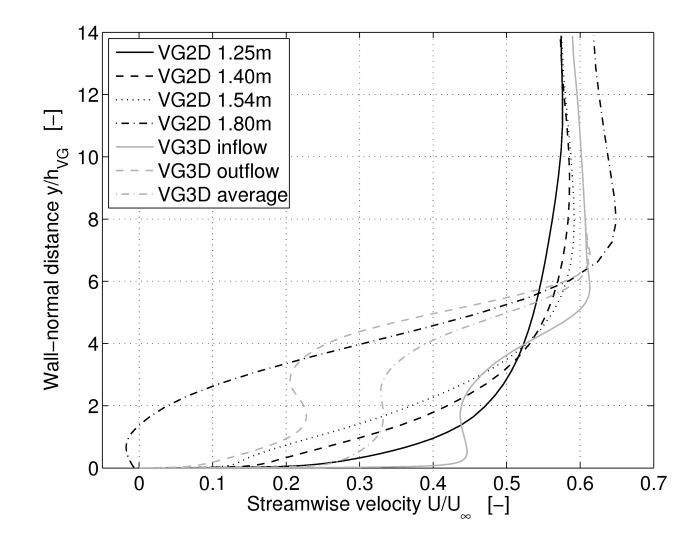


FIGURE 14. Mean velocity profiles at $x_{\rm sep,max}=2.25$ m for the VG2D streamwise position variation, and for the VG3D baseline computations with $x_{\rm VG}=1.54$ m at inflow and outflow positions as well as the corresponding averaged velocity profile for VG3D.

It can be observed from figure 14 that the four VG2D model computations indicate conforming trends for all streamwise positions. The further downstream the VG is applied, the lower are the streamwise velocities close to the

wall, indicating less momentum mixing in the boundary layer. The computations for $x_{VG} = 1.80$ m result in reversed flow, being consistent with the c_f distribution in figure 12(b). The three plots of the VG3D computations present the results of the inflow, outflow, and the spanwise-averaged velocity profiles. In general, they illustrate the velocity defect from the fully-resolved VG vanes. First, high-momentum containing fluid is pushed down towards the wall at the inflow position, increasing the near-wall velocity (gray solid line). Here, it can be observed how the flow is accelerated close to the wall. Secondly, lowmomentum fluid is pushed upwards at the outflow position, leading to lower velocities near the wall (gray dashed line). The corresponding velocity profile for $x_{VG} = 1.54$ m fits in between the VG3D velocity profiles at the inflow and outflow positions, yet lacking the velocity defect. However, the VG2D profile is not matching the spanwise-averaged VG3D profile (gray dashed-dotted line), giving a lower near-wall velocity distribution and lacking the averaged velocity defect further away from the wall. Nevertheless, it can be stated that the VG2D velocity profiles are consistent with each other regarding the trend of the VG position variation. The plots also confirm the c_f and the c_p distributions in figures 12(b) and 13. Moreover, the results of the VG3D computations show how the vortex structures propagate away from the wall boundary and therefore support the important role of boundary-layer mixing effects for flow control.

5.3. Circulation per Unit Width Variation

Lögdberg (2008) carried out a parameter variation study regarding the VG array streamwise location including different VG heights. This experimental study is used for a qualtitative comparison with the VG model computations. The experimental data were parameterized by means of the circulation per unit width for a VG array which is defined as

$$\gamma_e \equiv 2k \frac{h_{\rm VG} U_{\rm VG}}{D},\tag{10}$$

where k is a coefficient that takes the VG geometry into account [see Angele & Muhammad-Klingmann (2005)], $h_{\rm VG}$ the VG height, $U_{\rm VG}$ the VG tip velocity, and D the distance between VG pairs in the spanwise direction. For the computations, D=150 mm. In accordance with Lögdberg et al. (2010), a value of k=0.6 is used, resulting in a circulation per unit width for the present parameter variation study $\gamma_e=66.67h_{\rm VG}U_{\rm VG}$ m⁻¹. Thus, γ_e is dependent only on the VG height $h_{\rm VG}$ and the VG tip velocity $U_{\rm VG}$ which is equivalent to the streamwise position x.

To compare experiments and computations with each other, the same parameterization is also adopted in the computations, and values for γ_e were matched. This means that the VG height and the VG streamwise position need to be adjusted in order to give comparable γ_e values. The first matter is straightforward to implement into computations (identical VG heights), whereas the latter means an adjustment of the streamwise VG position in such

Table 3. The circulation per unit width, the VG height, the VG position $x_{\rm VG,exp}$ from the experiments, the resulting flow state from experiments, and the VG position $x_{\rm VG}$ of the VG model computations.

γ_e , m/s	$h_{\rm VG},{\rm mm}$	$x_{\rm VG,exp}, {\rm m}$	Flow state	x_{VG} , m
3.8	18	1.10	attached	0.80
3.1	18	1.60	attached	1.30
1.4	18	2.00	attached	1.70
1.0	10	2.00	separated	1.70

a way that VG tip velocities correspond to VG tip velocities in experiments. Since the separation bubble location and length as well as the evolution of the boundary layer from computations do not exactly match experiments, a coordinate transformation and therefore an upstream shifting of the VG position is necessary. As a result, the VG must be shifted $\Delta x=0.30$ m upstream in order to match experimental γ_e values. Table 3 presents the setup for both, the experiments and the VG model computations, as well as the resulting flow state from experiments.

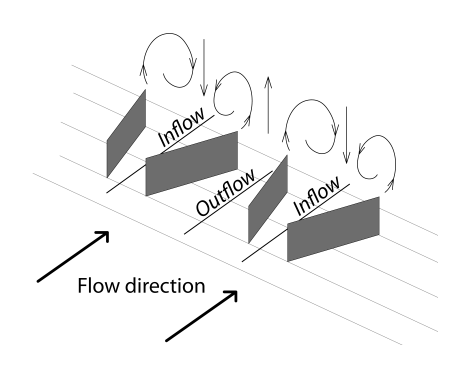


FIGURE 15. The spanwise inflow and the outflow planes of the VG3D computations.

Skin friction coefficient results of this study are presented in figure 16, though only for the VG2D computations since skin-friction data from experiments are not available. Yet, the primary focus of this VG2D study was to examine and compare the flow state prediction capabilities. From figure 16, it can be observed that the overall trend of the flow state from table 3 is predicted correctly by the VG model. Computations for the first three cases regarding the c_f plots show separation prevention $(c_f > 0)$ everywhere). In contrast to that, a reduction in $h_{\rm VG}$ from 18 mm to 10 mm results in separated flow as in the experiments (see the last case for γ_e

= 1.0 m/s in table 3). Again, the application of the VG model further upstream at $x_{\rm VG} = 0.80$ m and $\gamma_e = 3.8$ m/s shows less effectiveness for flow separation prevention than for $x_{\rm VG} = 1.30$ m, confirming the overall trend of figure 12.

5.4. Vortex Generator Setup Variation

Another interesting aspect to examine is the difference in flow separation effectiveness between co- and counter-rotational VG setups (see figure 17). Here,

four different setups were investigated: two counter-rotational settings, one given by a common-flow-down and another one by a common-flow-up setting [figures 17(a) and 17(b), respectively]. Furthermore, two corotating settings were examined: one with a VG vane distance D/2=75 mm, and another setting with an increased VG vane distance of D=150 mm, that doubles the distance between VG vanes and therefore decreases the total VG vane density in the VG array by a factor of 2 [see figures 17(c) and 17(d), respectively].

In figure 18, the results of this comparison show that counter-rotational systems are more efficient than corotating systems. This is in accordance with previous experimental results (Godard & Stanislas 2006). The c_f distributions for the corotating setups do not show much improvement when the VG vane density is doubled (when VG vane distance decreases from D to D/2, see figure 18). This is a consequence of the superposition of the single vortexvelocity fields from equation (3), resulting from the modelled VG array. Here, the induced vortex velocities partly weaken and damp out each other and this effect is higher the closer the VG vanes are located to each other, in accordance with Lin (2002). However, the VG model does not distinguish between common-flow-up and common-flow-down settings as can be observed in figure 18. Here, the c_f distributions lie on top of each other. The reason for that is the spanwise-averaging of the second-order statistics at the VG model forcing plane which results in identical contributions for the $\Delta \overline{u_i' u_i'}$ forcing. Therefore, the additional vortex stresses are also identical for both counter-rotational setups and the current VG model approach from equation (4) can hence not distinguish between these cases. However, experiments (Pauley & Eaton 1988)

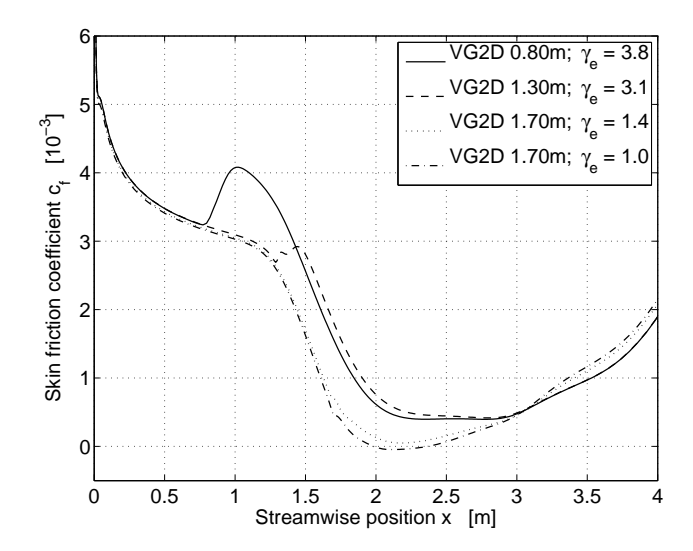


FIGURE 16. Local skin-friction coefficient distributions for the VG2D circulation per unit width variation, in accordance with table 3.

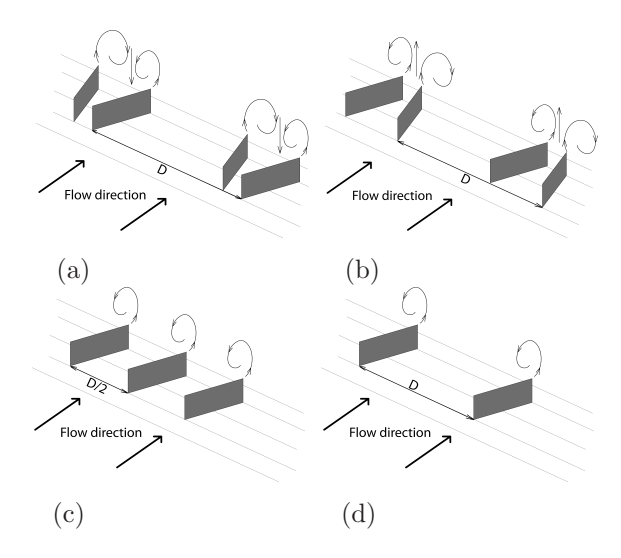


Figure 17. Different VG setups: (a) counter-rotational common-flow-down, (b) counter-rotational common-flow-up, (c) corotating with a spanwise VG vane distance D/2, and (d) corotating with a spanwise VG vane distance D.

show higher efficiency for common-flow-down setups since the vortices remain longer and closer to the wall, having a better and more persistent effect on flow separation prevention.

6. Conclusions

This investigation has shown the capabilities of the statistical VG model to mimic the effects of VG arrays in APG boundary-layer flow by means of introducing additional vortex stresses to the turbulence Reynolds stresses. Wall pressure- and skin-friction-coefficient distribution plots of the VG2D computations in APG boundary-layer flow have shown that flow separation prevention can be attained for several different configurations. Qualitative parameter variation studies and a comparison between experimental results, VG2D computations, and VG3D computations were carried out. The trends obtained in these studies successfully showed the capability of the VG model to predict flow separation prevention for identical VG setups such as in experiments and fullyresolved computations. Nevertheless, quantitative differences between the VG model and the fully-resolved VG results exist. In particular, the shear stress component $\Delta \overline{u'v'}$ is not directly forced but rather developed as a result of the production and redistribution of energy. The results indicate that the development of the shear stress component is slower and weaker than that shown in experiments. More effort should be made in formulating an improved VG model, enabling even the shear stress forcing.

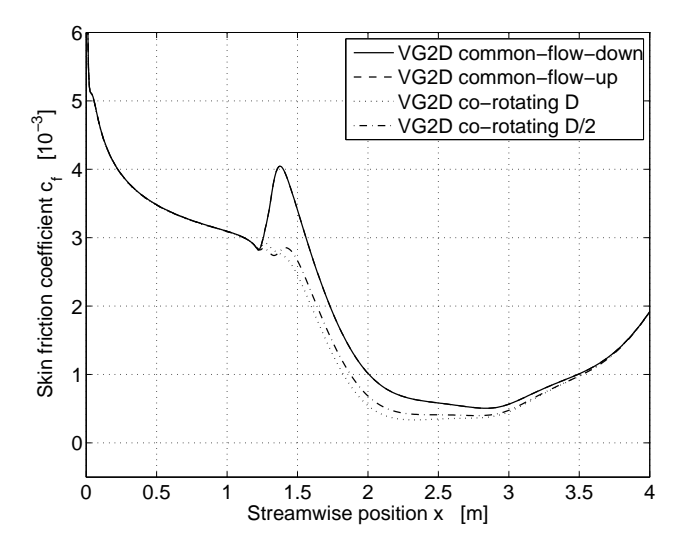


FIGURE 18. Local skin-friction coefficient distributions for different VG setups in accordance with figure 17 with a VG model forcing plane $x_{\rm VG}=1.25$ m.

A result of this examination is that the VGs' streamwise position as well as the height and the setup of the VG model strongly influence the skin-friction distribution and therefore, the effectiveness of the modelled flow control devices. The overall trends and tendencies from the parameter variations using the VG model show that there exists an optimal streamwise position for the VGs applied in the present APG boundary-layer flow case. It can be concluded that the VGs should be placed some distance upstream of the separation bubble in order to be able to generate the required vortex stresses that further develop downstream. Locating the VGs further upstream from the optimum position will generate stronger vortex stresses that in turn undergo longer-lasting diffusive processes until they reach the separation region which weakens the VGs' effectiveness. On the other hand, further downstream VG positions (also compared with the optimum) generate weaker vortex stresses with less effect on the separated flow regime due to a lower streamwise boundary-layer velocity. If the VGs are placed too close to the separation region, flow control is not attained. In total, it can be observed that all the investigated VG positions, except those very close to the separation region, give flow separation prevention.

Different combinations of the VG position and height could successfully be simulated by correctly predicting the parameter regimes for attached and separated flow when compared with the experiments. Inspection of the VG model's sensitivity to co- and counter-rotational setups showed consistency with earlier experimental results (Godard & Stanislas 2006).

In summary, this approach of modelling passive VG vanes for flow control has proved to be promising for an application to APG boundary-layer flows.

The major advantage of the VG model approach is that it is only as computationally expensive as solving the RANS equations without VGs, leading to much faster results than with conventional methods such as fully- or even partly-resolved VGs. Therefore, it could be used as a powerful tool for concept studies such as the optimal position of passive flow control devices. Results showed correct trends and tendencies in agreement with experiments and fullyresolved computations. Nevertheless, the user must also be aware of the VG model's shortcomings.

Acknowledgements

The experiments were part of a cooperative research program between the Royal Institute of Technology Stockholm and Scania AB (publ), Sweden. Ola Lögdberg is gratefully acknowledged for providing the experimental data.

References

- Anderson, J. D. 1991 Fundamentals of Aerodynamics, 2nd edn. New York, USA: McGraw-Hill.
- Angele, K. P. 2003 Experimental studies of turbulent boundary layer separation and control. PhD thesis, Department of Mechanics, KTH Stockholm.
- ANGELE, K. P. & MUHAMMAD-KLINGMANN, B. 2005 The effect of streamwise vortices on the turbulence structure of a separating boundary layer. *European Journal of Mechanics B/Fluids* **24**, 539 554.
- BATCHELOR, G. K. 1964 Axial flow in trailing line vortices. *Journal of Fluid Mechanics* **20** (4), 645 658.
- Bender, E. E., Anderson, B. H. & Yagle, P. J. 1999 Vortex Generator Modelling for Navier-Stokes Codes. *American Society of Mechanical Engineers, FEDSM* 99-6919.
- Dengel, P. & Fernholz, H. H. 1990 An experimental investigation of an incompressible turbulent boundary layer in the vicinity of separation. *Journal of Fluid Mechanics* **212**, 615 636.
- ELIASSON, P. 2002 Edge, a navier-stokes solver for unstructured grids. *Proceedings to Finite Volumes for Complex Applications III* pp. 527 534, edited by D. Kroner and R. Herbin, Hemre Penton Science London.
- GLAUERT, H. 1926 The Elements of Aerofoil and Airscrew Theory, 1st edn. Cambridge University Press, London, UK.
- GODARD, G. & STANISLAS, M. 2006 Control of a decelerating boundary layer. Part
 1: Optimization of passive vortex generators. Aerospace Science and Technology
 10 (3), 181 191.
- Hellsten, A. 2005 New Advanced $k-\omega$ Turbulence Model for High-Lift Aerodynamics. AIAA Journal 43 (9), 1857 1869.
- JIRÁSEK, A. 2005 A Vortex Generator Model and its Application to Flow Control. Journal of Aircraft 42 (6), 1486 – 1491.
- LIN, J. C. 2002 Review of research on low-profile vortex generators to control boundary-layer separation. *Progress in Aerospace Sciences* **38**, 389 420.
- LINDGREN, B. & JOHANSSON, A. V. 2004 Evaluation of a new wind tunnel with expanding corners. *Experiments in Fluids* **36**, 197 203.
- LÖGDBERG, O. 2008 Turbulent Boundary Layer Separation and Control. PhD thesis, Department of Mechanics, KTH Stockholm.
- LÖGDBERG, O., ANGELE, K. & ALFREDSSON, P. H. 2010 On the robustness of separation control by streamwise vortices. European Journal of Mechanics B/Fluids 29 (1), 9 17.
- LÖGDBERG, O., FRANSSON, J. H. M. & ALFREDSSON, P. H. 2009 Streamwise evolution of longitudinal vortices in a turbulent boundary layer. *Journal of Fluid Mechanics* 623, 27 58.
- Pauley, W. R. & Eaton, J. K. 1988 Experimental Study of the Development of Longitudinal Vortex Pairs Embedded in a Turbulent Boundary Layer. *AIAA Journal* **26** (7), 816 823.
- Pearcey, H. H. 1961 Part IV: Shock-Induced Separation and its Prevention by Design and Boundary Layer Control. In *Boundary Layer and Flow Control*, its

- $Principles\ and\ Applications$ (ed. G. V. Lachmann), pp. 1170 1344. Pergamon, Oxford, UK.
- VON STILLFRIED, F., WALLIN, S. & JOHANSSON, A. V. 2009 Statistical Modeling of the Influence of Turbulent Flow Separation Control Devices. *AIAA Paper AIAA* 2009-1501.
- TÖRNBLOM, O. & JOHANSSON, A. V. 2007 A Reynolds stress closure description of separation control with vortex generators in a plane asymmetric diffuser. *Physics of Fluids* **19** (115108).
- Velte, C. M., Hansen, M. O. L. & Okulov, V. L. 2009 Helical structure of longitudinal vortices embedded in turbulent wall-bounded flow. *Journal of Fluid Mechanics* **619**, 167 177.
- Wallin, S. & Johansson, A. V. 2000 An explicit algebraic Reynolds stress model for incompressible and compressible turbulent flows. *Journal of Fluid Mechanics* 403, 89 132.
- Wallin, S. & Johansson, A. V. 2002 Modelling streamline curvature effects in explicit algebraic Reynolds stress turbulence models. *International Journal of Heat and Fluid Flow* **23** (5), 721 730.

Paper 3

Evaluating and Parameterizing Round Vortex-Generator Jet Experiments for Flow Control

By Florian von Stillfried[†], Stefan Wallin[†], Arne V. Johansson[†], Marcus Casper[§], and Jens Ortmanns[§]

[†]Royal Institute of Technology, 100 44 Stockholm, Sweden [§]Technische Universität Braunschweig, 38 106 Braunschweig, Germany

Accepted for publication in AIAA Journal

Particle image velocimetry (PIV) experiments on the application of vortex generator jets (VGJ) with single and pair configurations in a zero-pressuregradient flat-plate boundary-layer flow have been carried out at Technische Universität Braunschweig, Germany. The experiments were analyzed at KTH Stockholm by means of a velocity triple decomposition which enables the extraction of vortex-velocity fields. The overall aim of this contribution is to identify and classify the influence of the different VGJ parameters on the generated vortex structures so that conclusions may be drawn for efficient flow-separationcontrol configurations. The spanwise-averaged second-order statistics $\overline{V_i V_i}(y)$ of the vortex-velocity field $V_i(y,z)$ are computed in order to evaluate the influence of the VGJ parameters. It could be shown that the velocity ratio λ and the skew angle β have a major influence. Furthermore, the chosen single VGJ data are compared to corresponding VGJ pair results of a similar actuator setup. It was found that the VGJ pairs could be statistically well-described by means of single VGJ vortices. Moreover, VGJ arrays should give very similar results for the configurations examined, facilitating VGJ modeling based on a statistical ansatz.

1. Introduction

As early as 1948, McCurdy (1948) was possibly the first researcher to investigate the effects of vortex generators (VG) on boundary-layer flow-separation control on an airfoil. Shortly after that, Wallis (1952, 1960) could demonstrate that an inclined active vortex generator jet (VGJ) can have the same effect as an inclined passive vane vortex generator (VVG), suggesting that VGJ arrays would have a very similar impact on a flow as an array of VVGs. In the early 1960s, PearceyPearcey (1961) published a comprehensive article about the use of VVGs and VGJs for boundary-layer-separation control, including design criteria and suggestions based on given results. Since then, many other researchers

(Pauley & Eaton 1988; Wendt 2001; Angele & Muhammad-Klingmann 2005; Godard & Stanislas 2006; Lin 2002; Lögdberg et al. 2009, 2010) have carried out basic experiments concerning the use of passive VVGs and have successfully used them for adverse-pressure-gradient (APG) boundary-layer flow-separation control. Mostly, VVGs have been applied on airfoils and wings (Bragg & Gregorek 1987; Galpin et al. 2002; Velte et al. 2007) and beneficial effects are proven.

Flow control by means of active VGJs has gained increasing interest in the flow-control community, especially during the last two decades. In contrast to passive VVGs that are mounted in a fixed manner, i.e. also leading to parasitic drag when not needed, active VGJs have the advantage that they can be switched off when not needed. Moreover, VGJs enable operation modes with different mass flow rates as well as the option for steady and periodic excitation without any changes to the surface geometry. Therefore, undesirable drag does not occur for inactive VGJs. All these parameters make a complete investigation for VGJs more demanding than for VVGs. Still, efficient combinations of the operational parameters have been found in earlier studies. For that purpose, many different experiments, mostly in ZPG boundary-layer flow, have been conducted by various research groups.

Single steady-blowing VGJ setups have been experimentally investigated by e.g. Rixon & Johari (2003), Zhang & Collins (1997), Compton & Johnston (1992), and Ortmanns & Kähler (2007). Figure 1 illustrates the general VGJ design parameters pitch angle α , skew angle β , the jet velocity U_{VGJ} , also showing a VGJ array setup with distance d within a VGJ pair and distance D between neighboring VGJ pairs. Note that the skew angle $\beta=0^\circ$ is defined against the freestream direction.

Rixon & Johari (2003) found that the circulation and the peak vorticity decrease exponentially with growing streamwise position x, and that the circulation, peak vorticity, as well as the average wall-normal position of the primary

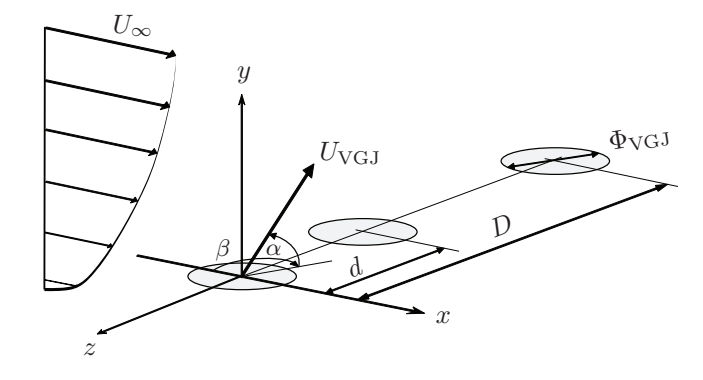


FIGURE 1. The VGJ actuator geometry and parameters, also showing additional parameters d and D for a pair and an array configuration, respectively.

vortex increase linearly with increasing the velocity ratio $\lambda = U_{VGJ}/U_{\infty}$ (for λ = 1, 2, and 3). Also the averaged wall-normal position was found to increase with downstream position with a power-law dependence on x. Moreover, they concluded that there exists an optimum VGJ actuator diameter Φ_{VGJ} that creates a strong vortex and that is not penetrating through the whole boundarylayer height δ . Zhang & Collins (1997) examined the near-field evolution of a round VGJ vortex and they concluded that a single vortex is fully developed after a streamwise distance $x = 10\Phi_{VGJ}$, and that an optimum setup is found for $\beta = 120^{\circ}$, $\alpha = 30^{\circ}$ for $\lambda = 1.0$. Also, they found that the streamwise vorticity decreases rapidly downstream, up to $x=20\Phi_{\text{VGJ}}$. Compton & Johnston (1992) examined the downstream development in terms of primaryand secondary-velocity distributions, circulation, and peak vorticity for different skew angles β and velocity ratios λ , and found that the VGJ vortices correspond to weak vortices originating from a passive VVG, and are different from strong VVG vortices at higher VVG angles of attack. In addition, they suggested the optimal skew angle β to be between 90° and 135°. Ortmanns & Kähler (2007) investigated the shear-layer interactions and the turbulent characteristics of the boundary layer affected by a VGJ. They showed that the increase of the turbulent kinetic energy is small and that the mixing is predominantly based on large-scale momentum transport.

VGJ arrays in steady-blowing mode were previously investigated by e.g. Johnston & Nishi (1990), Selby et al. (1992), Zhang (1995, 2003), and Godard & Stanislas (2006b). Johnston & Nishi (1990) evaluated VGJ arrays for different corotating and counter-rotating setups (i.e., VGJs blowing in identical and in alternating spanwise orientation, respectively) for $\alpha = 45^{\circ}$ and $\beta = 0^{\circ}$, 90° , by means of skin-friction, mean-velocity, and pressure-coefficient plots. They could show that VGJ arrays with $\beta = 90^{\circ}$ are well-suited to prevent separation in an APG boundary-layer flow and that a skew angle $\beta = 0^{\circ}$ is not suitable for separation control. Very large spanwise flow variations arise for counterrotating VGJs. Selby et al. (1992) performed a VGJ array parametric study over a rearward-facing ramp. They conducted experiments with different VGJ diameters, Φ_{VGI} , from 0.8 to 4.8 mm, pitch angles $\alpha = 15^{\circ}$ to 90°, skew angles $\beta = 90^{\circ}$ to 180°, and velocity ratios $\lambda = 0.6$ to 6.8 for corotating and counterrotating setups. The VGJ distance D was kept constant for all experiments. Streamwise pressure-coefficient distributions were used in order to quantify the flow-separation-control capability. They concluded that arrays of VGJs perform better when increasing the velocity ratio. Zhang (1995) discusses the computational investigation of corotating and counter-rotating VGJ arrays and the resulting vortices in terms of D, λ , and β . He concluded that a very high λ is not always beneficial for flow-separation control and that a change of skew angle β between 90° to 120° has only weak effects on the flow. Counterrotating vortices produced stronger vortices than corotating, whereas the latter case gave vortex-circulation levels essentially being independent of the VGJ spacing D. Furthermore, corotating vortices decayed faster than vortices from counter-rotating VGJ arrays. In a later paper, Zhang (2003) experimentally

investigated the evolution of corotating vortices with $\alpha = \beta = 135^{\circ}$ for $\lambda = 0.5, 1.0$, and 1.5. In the near field up to $x/\Phi_{\rm VGJ} = 10$, complex flow structures were revealed and the vortices of the VGJ array retained the characteristics of a single VGJ.

Godard & Stanislas (2006) conducted an extensive study in APG boundary-layer flow including counter- and corotating VGJ arrays using skin-friction results as a measure of flow-control efficiency. They found that increasing velocity ratio up to $\lambda=4.7$ increases efficiency for corotating VGJs, but that it already levels out for counter-rotating VGJs for $\lambda>3.1$. Varying β between 90° and 135° did not show significant differences for either setup, especially for high λ . Godard and Stanislas also concluded that counter-rotating VGJ arrays produce results similar to passive VVGs. Moreover, the corotating VGJs were more efficient than corotating passive VVGs, suggesting that the mechanisms are somewhat different, but the counter-rotating VGJs reach similar performance to corresponding passive VVGs.

As one can see from the different reported results, the optimum parameters for VGJs are very dependent on the actual boundary-layer conditions and many combinations are possible. Nevertheless, from the common features of the above VGJ investigations, it is possible to conclude that there exists a certain range of optimum settings for VGJs: 1) the pitch angle $\alpha=15^{\circ}$ to 45° ; 2) the skew angle $\beta=90^{\circ}$ to 135° ; 3) the velocity ratio λ should be moderate so that the jets do not penetrate through the boundary layer; 4) the region to control should be at least $x/\Phi_{\rm VGJ}=10$ downstream of the VGJs for the vortices to be fully developed; and 5) counter-rotating VG arrays tend to perform better than corotating VG arrays, even though this might be sensitive to setup.

The object of this investigation was to parameterize single VGJ experimental results in order to draw further conclusions from the parameter range examined. Furthermore, the study is aimed at developing an active VGJ array model for use in computational fluid dynamics (CFD) similar to the passive VVG array model proposed by Törnblom & Johansson (2007) and further developed by von Stillfried *et al.* (2011b,a).

2. Vortex Generator Jet Experiments

The ZPG flat-plate boundary-layer single VGJ experiments analyzed here were carried out by Ortmanns (2008) in the 1.3 x 1.3 m² and 5.7 m long test section of the closed return atmospheric low-speed wind tunnel of Technische Universität Braunschweig (TUBS), Germany. The wind tunnel's maximum freestream velocity of $U_{\infty} = 60$ m/s can be achieved with the 300 kW strong electrical power unit. The wind tunnel is equipped with a heat exchanger that keeps the air temperature constant at maximum 10.0 ± 0.5 °C above ambient temperature. Moreover, the turbulence level of the wind tunnel is 0.2% at a freestream velocity $U_{\infty} = 53$ m/s, whereas the average wind speed is uniform within $\pm0.2\%$. Stereoscopic particle image velocimetry (PIV) was used for the determination of the three velocity components $u_{PIV,i}(y,z)$ in the test planes.

The PIV method enables the ensemble-averaging of a great amount of data and for each measurement, 400 single PIV samples were recorded. Acceptable time-averaged velocities and Reynolds stresses can thereby be ensured. For a detailed description of the PIV method, the reader is referred to Raffel et al. (2007). For detailed descriptions of the individual setups used here, as well as comprehensive information on experimental accuracy, the reader is referred to Ortmanns (2008) and Casper et al. (2008), respectively.

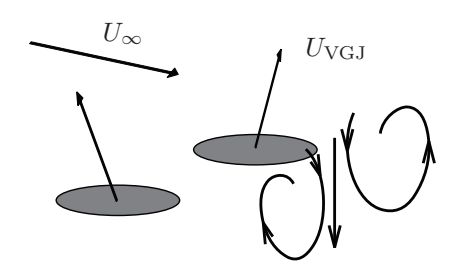


FIGURE 2. Schematic VGJ pair/array in a counter-rotating common-flow-down configuration.

The single VGJ vortices originated from a round VGJ that was placed at $x_{VG} = 4650$ mm downstream of the leading edge of the flat plate. The boundary-layer height δ (i.e. δ_{99}) was determined to be 87.6 and 86.8 mm for $U_{\infty}=25$ and 50 m/s, respectively. In the same manner, the momentum thickness was determined as $\theta = 8.0$ and 8.3 mm, respectively. The round single VGJ actuator had a diameter $\Phi_{VGJ} = 6.4$ mm, and experiments with a VGJ setup of $\alpha = 45^{\circ}$ and $\beta = 15^{\circ}$ to 105° , as well as $\alpha = 30^{\circ}$ and $\beta = 90^{\circ}$ were carried out. Moreover, the velocity

ratio $\lambda = U_{\rm VGJ}/U_{\infty}$ was set to 2.5 and 5.0 for each U_{∞} , giving four different flow cases for each VGJ setup.

Casper (2011) conducted experiments with a counter-rotating common-flow-down VGJ pair in the same wind tunnel as Ortmanns at TUBS, some of the data is published as a reference case for staggered VGJ arrays (Casper et al. 2008). The results of the VGJ pair experiments were used for a comparison with corresponding single VGJ experiments. The VGJ pair consisted of two actuators in a common-flow-down configuration, (see figure 2), causing a flow towards the wall between the actuators. The actuator diameter $\Phi_{\rm VGJ}=6.2~\rm mm$ and results are available for $\alpha=30^\circ,\,\beta=90^\circ,\,\lambda=2.5$ and 5.0 at $U_\infty=25~\rm m/s$ for two different actuator distances d=60 and 90 mm. The actuator position plane differs about $\pm 0.25\%$ of the flat-plate length compared to the single VGJ setup, whereas the measurement planes were located at the same streamwise positions as for the single VGJ case, relative to the actuator position.

The PIV measurements were obtained at three different measurement planes downstream of the single VGJ and the VGJ pair position at $x=50,\,100,\,$ and 200 mm, cf. figure 3 that is also presenting the general vortex topology for single VGJ experiments. For the investigations here, the ensemble-averaged velocity fields in the measurement planes are essential for the analysis of the

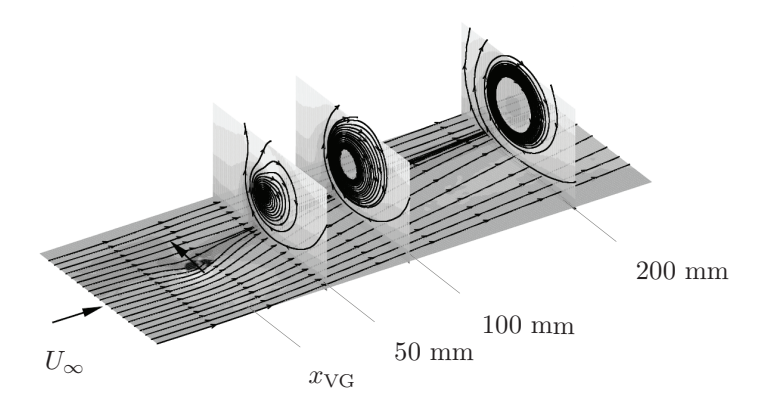


FIGURE 3. Actuator exit position at $x_{\rm VG}=4650$ mm and the measurement planes at $x=50,\,100,\,$ and 200 mm. Furthermore, exposure of the typical vortex topology of the single VGJ. [From Ortmanns (2008).]

vortex-velocity fields by means of a velocity triple decomposition. The analytical method is presented in von Stillfried $et\ al.\ (2011b)$ and is repeated for the reader's convenience in section 3.1.

The jet velocity U_{VGJ} was determined by measuring the mass flow in combination with measuring the actuator-chamber-static pressure for verification. The accuracy of determining U_{VGJ} for the jet velocities [62.5, 125, 250] m/s was $\pm [10.0, 5.1, 2.5]\%$. In terms of the pressure measurements, the accuracy for $U_{VGJ} = [62.5, 125, 250]$ m/s was determined to be $\pm [19, 5, 0.9]\%$. The actuator geometries of the single VGJs and the VGJ pairs had somewhat different inlet body structures. The single VGJ design by Ortmanns consisted of an insert of 6 mm thickness with a drilled hole as the actuator exit, see figure 4(a), whereas the VGJ pairs were equipped with additional 15-mm-long inlet pipes that enhanced the directional accuracy of the jets, see figure 4(b), and similar to the setup in the computations by Mahmood & Radespiel (2009, 2011). The accuracy of the α and β -values obtained with the single VGJ setup is moderate, because the jet can only be approximately directed when exiting the actuator. Nevertheless, it can be assumed that only very low momentum losses occur from this design that incorporated a pneumatic chamber including five highpressure-air-supply connections in total. Furthermore, Mahmood & Radespiel (2009, 2011) showed that the single VGJ results by Ortmanns (2008) could be reproduced computationally to a large extent by means of Reynolds-averaged Navier-Stokes computations and detached-eddy simulations, respectively, including a tube actuator inlet body. Therefore, the results and the accuracy of the actuator setup are assumed to be satisfactory.

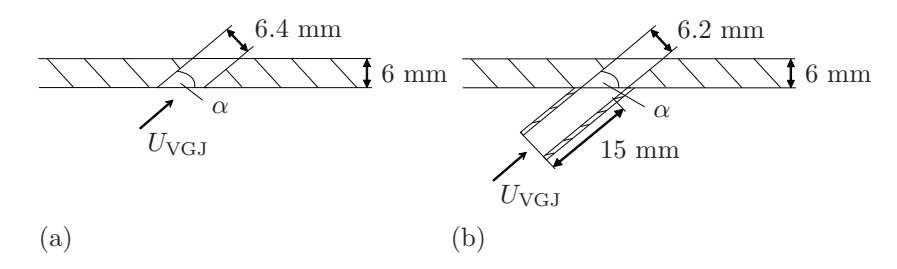


FIGURE 4. The actuator inlet cross sections for (a) the single VGJ, and (b) the VGJ pair.

3. Analysis of the Vortex Generator Jet Experiments

The aim of this investigation was to analyze the vortex-velocity fields $V_i(y,z)$ and the vortex stress distributions in the wall-normal direction y for different VGJ parameters, represented by the one-point vortex velocity correlations $\overline{V_iV_j}(y)$. These correlations represent the large-scale momentum transport which has been found to be the main mechanism for the mixing within the boundary layer (Ortmanns & Kähler 2007). Such an evaluation thereby gives new insights for VGJ parameter dependencies on the boundary-layer mixing and thus, the flow-separation-control capabilities of VGJs. The analysis of the PIV results including the vortex-velocity fields is directly carried out by a velocity triple decomposition. This reduces the need to only analyze PIV data including the vortex-velocity field for each measurement, see section 3.1. The extraction of the $\overline{V_iV_i}(y)$ vortex stresses is provided by the velocity decomposition in combination with the derivation of the second-order statistics, see section 3.2. Moreover, the determination of the vortex stresses makes it possible to further develop a statistical VGJ model for an application in CFD using Reynolds stress-transport-based turbulence models, similar to the statistical VVG model that was presented previously by the authors; see von Stillfried et al. (2011a,b).

3.1. Analyzing the Experimental Vortex Velocities

In principle, the total instantaneous velocity field $u_i(y,z,t)$ at the spanwise measurement planes perpendicular to the freestream direction can be decomposed into a mean-velocity part U_i , a turbulent-fluctuating part u'_i , and a vortex velocity part V_i

$$u_i(y, z, t) = U_i(y) + u'_i(y, z, t) + V_i(y, z).$$
 (1)

Since the experimental PIV results used here are ensemble-averaged velocities (corresponding to the time-average of statistically-steady flows), also a time-averaging of the velocity decomposition is necessary, leading to the ansatz for the velocity from PIV measurements

$$u_{PIV,i}(y,z) = \langle u_i(y,z,t) \rangle$$

= $U_i(y) + V_i(y,z)$. (2)

The velocity $u_{PIV,i}$ consists of the mean-velocity field $U_i(y)$ and the vortex-velocity field $V_i(y,z)$. A further spanwise-averaging for a infinite number of vortices in a VGJ array in the z-direction of the velocity field $u_{PIV,i}(y,z)$ yields $U_i(y)$. The spanwise average of $V_i(y,z)$ is zero for a counter-rotating vortex array because the velocity field $V_i(y,z)$ becomes symmetrical. The vortex-velocity field $V_i(y,z)$ can now be extracted from the PIV velocity field in terms of the substraction of the spanwise-averaged from the time/ensemble-averaged velocity, reading

$$V_{i}(y,z) = \langle u_{i}(y,z,t) \rangle - \overline{\langle u_{i}(y,z,t) \rangle}$$

$$= u_{PIV,i} - \overline{u_{PIV,i}}, \tag{3}$$

where the overbar denotes spanwise-averaging. Equation (3) is strictly valid only for a VGJ array configuration. However, it can be also be used for single VGJs and VGJ pairs under certain conditions. The reason for evaluating also the single VGJ and VGJ pair data in this way is that the experiments provide a comprehensive set of parameter variations. The main assumption when averaging the single VGJ data is that the single vortex will represent one vortex in a counter-rotating VGJ array. Likewise for the VGJ pair, we suggest that the given data represent a VGJ array well. Such an assumption is reasonable for the single VGJ here since the actuators in the VGJ pair setup are not too close to each other. In addition, Zhang (2003) has shown that vortices from a corotating VGJ array "retain the main characters of a single streamwise vortex". It is not clear if such an assumption may also hold for smaller distances D when vortices tend to interact stronger. CFD investigations are scheduled for the future and a comparison of results and an evaluation of this assumption will be available.

In this contribution, we use the velocity triple decomposition including the spanwise-averaging of experimental velocity results. In contrast to the spanwise distance D that is explicitly given for a VGJ array between two VGJ pairs, D is not defined for the single VGJ and VGJ pair setups. For a statistically based comparison with VGJ arrays, an artificial spanwise distance D_{sVGJ} needs to be presumed for single VGJs, as well as for VGJ pairs. D_{sVGJ} for the single VGJ is here chosen as half the symmetry distance D of a VGJ array. This is a natural choice, since $D_{sVGJ} = D/2$ contains one vortex in such a VGJ array configuration. For the VGJ pairs on the other hand, $D_{sVGJ} = D$, because two vortices are contained within the symmetry boundaries for D.

It is obvious that the actual velocity field for a single VGJ within D_{sVGJ} cannot fully represent the velocity field for a VGJ array on D/2, since the latter case includes the effects of neighboring vortices. In our case, the influence on the

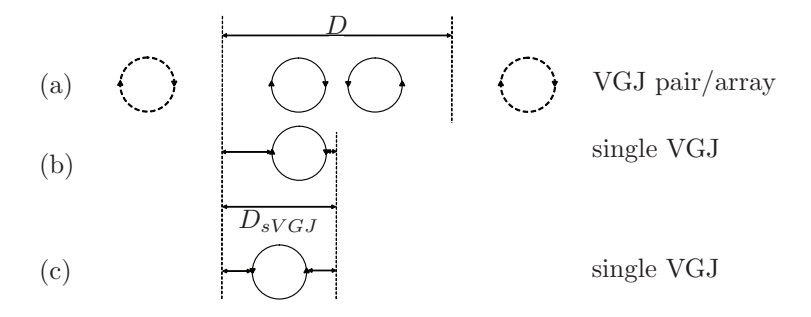


FIGURE 5. Comparing the different integration boundaries of VGJ pairs/arrays and single VGJs (a-b), and the integration boundaries switch due to different measurement window sizes (b-c).

averaged velocities on the left side of the vortex, see figure 5, is not significant as long as the distance is sufficiently long, so that effects from a neighboring vortex can be neglected. On the right side of the vortex, it is obvious that this approximation cannot account for the imposed symmetry of the vortex velocities within a VGJ pair.

In this investigation, the single VGJs and the VGJ pair were investigated in separate different wind-tunnel measurement campaigns where the PIV measurement windows are slightly different. In particular, the spanwise measurement window width for the VGJ pair incorporated integration boundaries with a spanwise distance D = 240 mm, also suitable for a VGJ array configuration; see figure 5(a). On the other hand, the single VGJ measurements made it possible to use a window width of only D/2. Moreover, the single jet in the actual measurement window from experiments [see figure 5(b)] was not exactly located as for the investigated VGJ pair, or as for the assumed virtual VGJ array settings. Therefore, the distance to the left of the single vortex, figure 5(b), was shorter while the distance to the right was longer than for D/2 in the VGJ pair/array measurement window; cf. figure 5(c). Nevertheless, the integration boundaries for the single VGJ were separated by D/2. It was found that the velocities and vortex stresses close to the integration boundaries do not contribute significantly to the mean-velocity values, see also the margins in figure 6, and therefore a sound spanwise integration can be carried out.

By means of this velocity triple decomposition and equation (3), the vortex-velocity field can finally be extracted from the PIV velocity field. Figure 7 shows vortex-velocity fields for chosen single VGJ experiments. Also, the nondimensionalised streamwise-mean-velocity contours $u_{\text{PIV},x}/U_{\infty} = [U_x(y) + V_x(y,z)]/U_{\infty}$ for a single VGJ configuration for $\alpha = 45^{\circ}$, $\beta = 90^{\circ}$, $\lambda = 2.5$ (left) and 5.0 (right) at a freestream velocity $U_{\infty} = 25$ m/s are plotted in combination with the extracted vortex-velocity field $(V_y(y,z), V_z(y,z))$ for three different streamwise locations downstream of the VGJ location. It can be observed

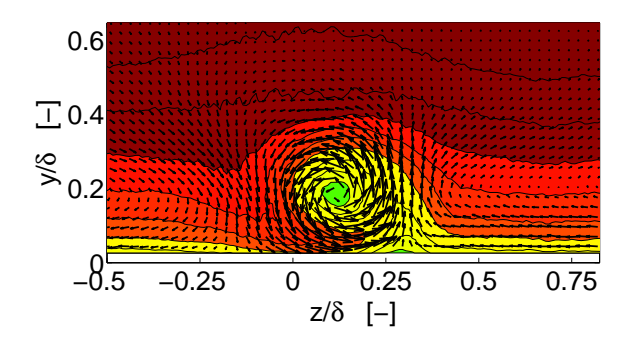


FIGURE 6. Single VGJ: mean streamwise-velocity contours $u_{\text{PIV},x}/U_{\infty}$ and the vortex-velocity field $[V_y(y,z),V_z(y,z)]$ including integration boundaries for $D_{sVGJ}=D/2$; cf. figure 5(c).

that the extracted vortex-velocity fields match the pattern of the streamwise-velocity contours well. The velocity fields for the same VGJ parameters but for a freestream velocity of 50 m/s are shown in figure 18 in Appendix A. The corresponding plots for $(\alpha, \beta) = (30^{\circ}, 90^{\circ})$ are shown in figures 19 and 20 for $U_{\infty} = 25$ m/s and 50 m/s, respectively.

In addition, it can be seen in figure 7 how the averaged wall-normal vortex core distance $h_{\rm c}$ can be said to be roughly proportional to the velocity ratio λ , in accordance with the findings of Rixon & Johari (2003). Zhang & Collins (1997) (single VGJ) and Zhang (2003) (VGJ array) found the vortices to be fully developed for $x/\Phi_{\rm VGJ}=10$. This condition is satisfied in figures 7(b-c) and figures 7(e-f) while $x/\Phi_{\rm VGJ}\approx 8$ in figures 7(a) and (d). A β -dependency is also assumed. The VGJs investigated here have a higher β than that studied by Zhang and Collins, very likely leading vortices that become fully developed earlier.

3.2. Vortex Stresses

The vortex stresses that originate from the vortex velocities $V_i(y,z)$ constitute the main source of momentum transport within the boundary layer. The aim of this investigation is to determine the vortex stresses $\overline{V_iV_j}(y)$ in order to quantify the effect of the VGJ flow-separation control capabilities in terms of the different VGJ setup parameters. In a post-processing analysis, it is possible to derive the vortex stresses $\overline{V_iV_j}(y)$ by means of spanwise-averaging the vortex velocity products $V_i(y,z)V_j(y,z)$,

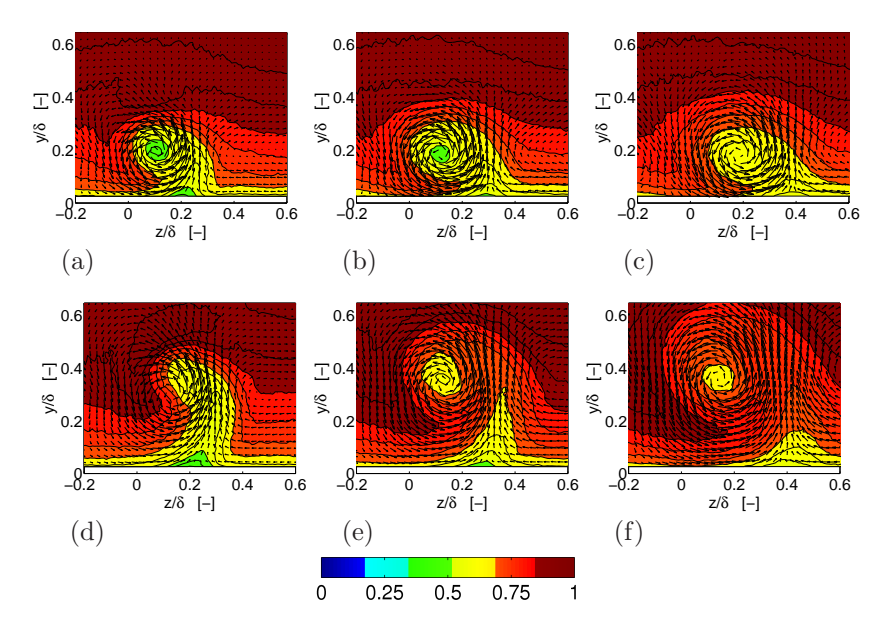


FIGURE 7. Single VGJ: $\alpha = 45^{\circ}$, $\beta = 90^{\circ}$, $U_{\infty} = 25$ m/s, $\lambda = 2.5$ (top) and 5.0 (bottom): mean streamwise-velocity contours $u_{\text{PIV},x}/U_{\infty}$ and the vortex-velocity field $[V_y(y,z),V_z(y,z)]$ at x=50, 100, and 200 mm (from left to right).

$$\overline{V_i V_j}(y) = \frac{1}{D} \int_0^D V_i(y, z) V_j(y, z) dz, \tag{4}$$

where D is the symmetry distance between two neighboring VGJ pairs in a VGJ array, or the substituted D_{sVGJ} representing the virtual symmetry distance for single VGJ and VGJ pairs; see figure 1 and section 3.1. The single VGJ is assumed to represent one VGJ in a counter-rotating VGJ array and thus, a mirror jet must be considered. This implies that the averaging can be done over the half-symmetry D_{sVGJ} for symmetric quantities, while the mean of the asymmetric correlation will vanish $(\overline{V_z} = \overline{V_x V_z} = \overline{V_y V_z} = 0)$ The vortex stresses can now be extracted for an analysis of the dependency on the VGJ setup parameters α , β , λ , and U_{∞} .

3.3. Vortex Velocity Parameterization

In order to quantify the effects of single VGJs, the experimentally generated vortices are parameterized. A vortex model allows us to describe the vortices by a set of characterizing parameters. It is then feasible to determine the values of the specific vortex-model parameters as function of the VGJ setup parameters α , β , and λ . We found earlier that it is possible to use a Lamb-Oseen vortex model in combination with the lifting-line theory (LLT) for modeling the

vortices that originate from passive VVGs; see von Stillfried *et al.* (2011a,b). It is assumed that vortices originating from VGJs can be represented in a similar way by a Lamb-Oseen vortex model.

Furthermore, the determination of the vortex stresses from VGJs provides a comparison to the VVG model (von Stillfried et al. 2011a,b) and thus, similarities between the results from modeled VVGs and experimental VGJs in terms of their stresses may be determined. Gleyzes & Pailhas (2011) have, for example, recently used the passive Bender-Anderson-Yagle (BAY) VVG model by Bender et al. (1999) and determined suitable BAY VVG model parameters that represent the examined VGJs well. The passive VVG model by Törnblom & Johansson (2007) uses additional vortex stresses instead and a possible substitution of the VGJs by a passive VVG model approach can be an alternative when compared to a future VGJ model based on this parameterization study.

The VGJ data will be fitted to a two-dimensional Lamb-Oseen vortex model with a tangential velocity, $V_{\Phi}(r)$, reading

$$V_{\Phi}(r) = \frac{\Gamma_{\text{max}}}{2\pi r} \left[1 - e^{\left(-\frac{r}{r_0}\right)^2} \right], \tag{5}$$

where $r^2 = (y - h_c)^2 + (z - z_c)^2$ is the radial distance from the vortex core (h_c, z_c) in cartesian coordinates. $\Gamma_{\rm max}$ is the maximum vortex circulation and r_0 is the vortex core radius of the modeled vortex. The spanwise-averaged vortex-stress results in von Stillfried et al. (2011a,b) showed that the Lamb-Oseen vortex model in combination with the LLT for the determination of $\Gamma_{\rm max}$ described the VVG vortices well. Here, the Lamb-Oseen vortex model for $V_{\Phi}(r)$ is used for a nonlinear least-squares data fitting to the experimental tangential vortex-velocity fields $U_{\Phi}(r)$. Thereby, a parameterization of the Lamb-Oseen vortex model parameters $\Gamma_{\rm max}$ and r_0 as well as the vortex core location (h_c, z_c) is made possible for single VGJs. A first approximation for the vortex core coordinates (h_c, z_c) for the data-fitting problem was extracted from the location of the minimum λ_2 discriminant from the experiments, reading

$$\lambda_2 = \left(\frac{\partial V_y}{\partial y} + \frac{\partial V_z}{\partial z}\right)^2 - 4\left(\frac{\partial V_y}{\partial y} \cdot \frac{\partial V_z}{\partial z} - \frac{\partial V_y}{\partial z} \cdot \frac{\partial V_z}{\partial y}\right). \tag{6}$$

The nonlinear least-squares data-fitting problem is of the form

$$\min_{x} \| (V_{\Phi}(r) - U_{\Phi}(r)) \|_{2}^{2}, \tag{7}$$

and the Lamb-Oseen vortex-model parameters $\Gamma_{\rm max}$, r_0 , $h_{\rm c}$, and $z_{\rm c}$ were fitted to the experimental results within a radial distance $r/r_0=5$ from the vortex core.

Figure 8 shows a comparison between experiments and fitted cross-plane vortex velocity distributions for three different downstream positions at x = 50, 100, and 200 mm. It can be seen that the data fitting in terms of the experiments and the vortex-model parameters shows an overall good agreement,

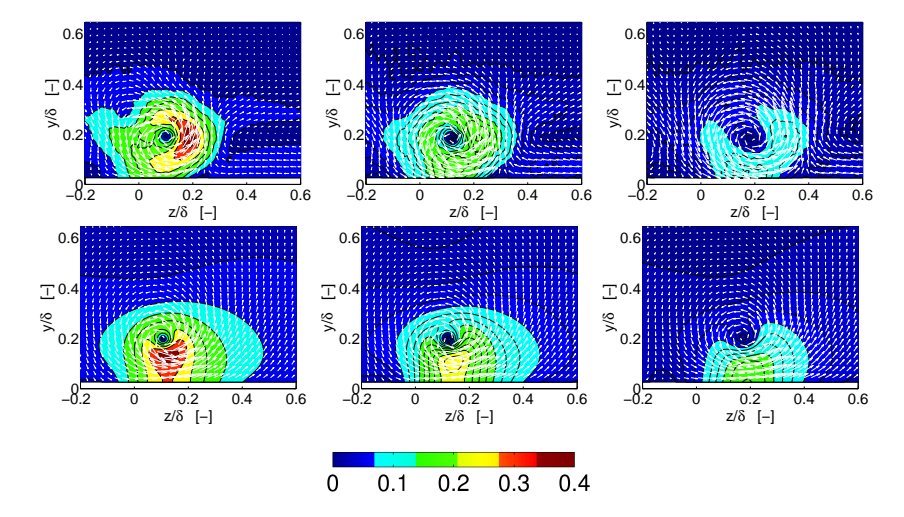


FIGURE 8. Single VGJ: experimental (top) and fitted (bottom) vortex-velocity fields $\sqrt{(V_y^2+V_z^2)}/U_\infty$. Here: $\alpha=45^\circ$, $\beta=90^\circ$, $U_\infty=25$ m/s, $\lambda=2.5$ at x=50, 100, and 200 mm (from left to right).

and indicates that the vortex-model parameterization results are satisfactory. In order to ensure the zero wall-normal velocity at the wall boundary, a mirror image with the same circulation magnitude $\Gamma_{\rm max}$ was used. Furthermore, a wall-damping function $(1-\exp[-20y/\delta])$ ensured a decrease of the spanwise velocity $V_z(y,z)$ to zero at the wall $(y/\delta=0)$.

The parameterization of the experimental results in combination with the Lamb-Oseen vortex model represents a simplified, yet a good description of the experimental results even though flow phenomena as, for example, secondary vortices cannot be captured by the vortex model and its mirror image; see figure 8. As a result and in contrast to the experiments, the peak values of the modeled velocities V_{Φ} develop between the vortex core and the wall boundary. In addition, the determination of the vortex-model-core location does not totally match the experiments. This is due to the determination of the vortex core coordinates by means of the minimum value for the λ_2 discriminant and the results differ from the experimental values because of the sensitivity to local velocity gradients.

For a more detailed verification of the experimental vortex characteristics, the experimental results $U_{\Phi}(r)$ along with the vortex-model velocities $V_{\Phi}(r)$ for the nonlinear least-squares data fitting from figure 8 are plotted in figure 9 as a function of the radial distance r/r_0 from the vortex core center. Original PIV results (dots) and averaged velocities (circles) for each radial coordinate are also given. Furthermore, the graphs show the vortex-model velocities (curves) with the fitted vortex-model parameters from tables 1 and 4. It can

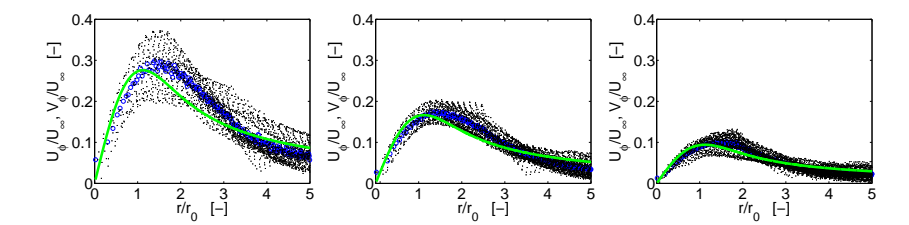


FIGURE 9. Single VGJ: nondimensional tangential vortex velocity $U_{\Phi}(r/r_0)/U_{\infty}$ from experiments (dots), corresponding averaged vortex velocity (circles), and vortex-model tangential velocity $V_{\Phi}(r/r_0)/U_{\infty}$ (curves). Here: $\alpha=45^{\circ}$, $\beta=90^{\circ}$, $U_{\infty}=25$ m/s, $\lambda=2.5$ at x=50, 100, and 200 mm (from left to right).

be observed that the Lamb-Oseen vortex model from equation (5) represents a satisfactory mean-tangential vortex velocity distribution when compared to the experimental data. The results suggest that the vortices from experiments are well-described by means of the Lamb-Oseen vortex model. Table 1 gives complete information about the fitted vortex-model parameters for experiments for $\alpha=45^\circ$ and $\beta=75^\circ$ to 105° at x=50 mm. Further information about the other streamwise planes can be found in table 4 in Appendix A.

Figure 10 presents the results of table 1 for the vortex-model parameter fitting and the parameter dependencies on the skew angle β , and the velocity ratio λ at the most upstream measurement plane x=50 mm. The parameters were made nondimensional and are defined as

TABLE 1. Chosen experimental single VGJ setups (first five columns) and fitted Lamb-Oseen vortex-model parameters Γ_{max} , r_0 , h_c and z_c (remaining four columns) at x = 50 mm.

α	β	x	U_{∞}	λ	$\Gamma_{\rm max}$	r_0	$h_{\rm c}$	$z_{ m c}$
\deg	mm	m/s	m/s		$\rm m^2/s$	mm	mm	mm
45	75	50	25	2.5	0.256	5.1	10.9	13.0
45	90	50	25	2.5	0.315	4.6	9.6	16.5
45	105	50	25	2.5	0.282	4.2	8.5	16.1
45	75	50	25	5.0	0.518	7.2	13.4	24.8
45	90	50	25	5.0	0.575	6.0	13.6	26.5
45	105	50	25	5.0	0.564	5.6	11.8	26.4
45	75	50	50	2.5	0.406	4.4	10.0	11.3
45	90	50	50	2.5	0.415	3.9	7.7	12.4
45	105	50	50	2.5	0.417	3.7	8.1	13.3
45	75	50	50	5.0	0.647	5.6	11.7	16.4
45	90	50	50	5.0	0.706	5.0	9.8	18.8
45	105	50	50	5.0	0.849	4.8	10.1	21.4

$$\Gamma_{\text{max}}^* = \Gamma_{\text{max}}/(\Phi_{\text{VGJ}}\lambda U_{\infty}),$$

$$r_0^* = r_0/\Phi_{\text{VGJ}},$$

$$h_c^* = h_c/\theta.$$
(8)

It can be seen in Figures 10(a-b) that the $\Gamma_{\rm max}^*$ results for $\lambda=5.0$ are quantitatively lower than for $\lambda = 2.5$ for the chosen nondimensional reference values. Γ_{\max}^* , representing the vortex strength, quantitatively illustrates the efficiency in terms of the momentum change in the flow caused by the VGJ. This means that the efficiency in terms of the vortex strength is not higher for higher λ -values. The Γ_{max}^* distribution and the results for $U_{\infty} = 25 \text{ m/s}$ show a clear maximum for Γ_{max}^* at $\beta = 90^\circ$ for both λ . In contrast, it can be observed that the results for $U_{\infty} = 50$ m/s generally do not show a maximum for the β range presented. Here, one can see an approximately constant distribution for λ = 2.5 and an increasing trend for $\lambda = 5.0$, for which a maximum nondimensional circulation is assumed to occur for higher skew angles than $\beta = 90^{\circ}$. In total, all results for the nondimensional Γ_{\max}^* are well within the same order, and the data for $U_{\infty}=25$ m/s reveal somewhat higher values for chosen setups, indicating a slightly higher efficiency than for $U_{\infty} = 50$ m/s. An explanation for the results being very close to each other between $0.4 \le \Gamma_{\rm max}^* \le 0.8$ is the reasonable good scaling of the experimental results from equation (8), which implies that flows with the same relation between the jet and the freestream momentum, i.e., constant λ , will be similar. However, there are some additional scaling parameters that might influence the initial formation of the vortex for different U_{∞} with constant λ . These are the Mach number Ma and the Reynolds number Re. The jet Mach number reaches levels up to $Ma \approx 0.75$ for $U_{\infty} = 50$ m/s and $\lambda = 5.0$, implying significant compressibility effects that might influence the initial development of the jet and vortex. The increasing Re may also influence how the jet flow breaks down to turbulence. However, the Reynolds number for the jet Re_{VGJ} is sufficiently high $(Re_{VGJ} = (U_{VGJ}\Phi_{VGJ})/\nu \approx 20000$ to 90000) and, hence, these interactions are expected to be of minor importance. In total, it is difficult to analyze and to draw general conclusions from such a comparison of results. More near-field experimental results, as well as detailed computational data would probably help to reveal more insight into the vortex generation and its streamwise development.

Figures 10(c-d) present results for the nondimensional viscous core radius r_0^* . Decreasing values with increasing β can be observed but the data lie closely together for the given λ values. The distance of the vortex core to the wall boundary $h_{\rm c}^*$, see figures 10(e-f), exhibits a small variation with β . A maximum value for $h_{\rm c}^*$ can be identified at $\beta=90^\circ$ for $U_\infty=25$ m/s.

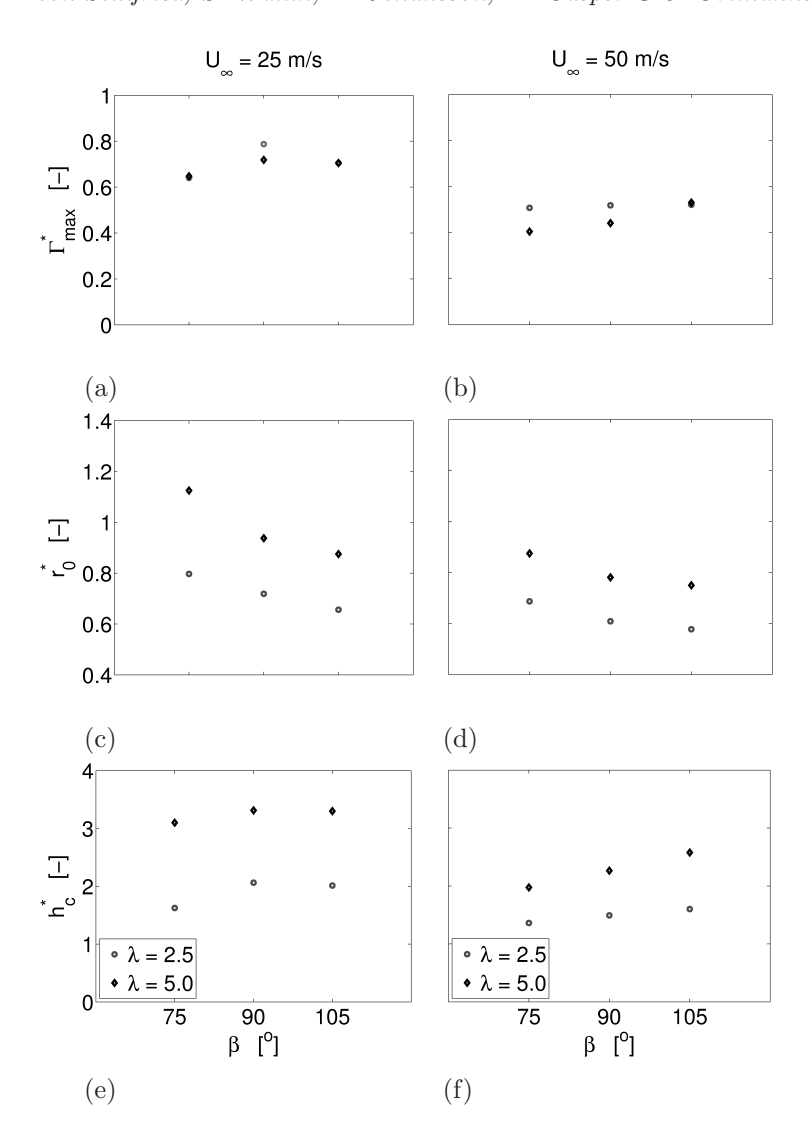


FIGURE 10. Single VGJ: nondimensional parameters based on equation (8) and table 1 for $\alpha = 45^{\circ}$, $U_{\infty} = 25$ and 50 m/s, $\lambda = 2.5$ (circles) and 5.0 (diamonds), $\beta = 75^{\circ}$, 90°, and 105° at x = 50 mm.

4. Results

$4.1.\ Single\ VGJs$

Table 2 presents the single VGJ setups that were chosen and examined by the authors. These cases were chosen from the experimental investigations by

TABLE 2. The single VGJ configurations from Ortmanns (2008) that are examined in this paper.

α , deg	β , deg	Φ_{VGJ}, mm	U_{∞} , m/s	λ
45	75	6.4	25, 50	2.5, 5.0
45	90	6.4	25, 50	2.5, 5.0
45	105	6.4	25, 50	2.5, 5.0
30	90	6.4	25, 50	2.5, 5.0

Ortmanns (2008), because they represent VGJ configurations that typically generate well-developed vortices in the boundary layer. For the $\alpha=45^{\circ}$ setup, a comprehensive skew-angle variation is provided. The single VGJ experiments for $\alpha=45^{\circ}$ were used in order to perform a parameter fitting of the experimental results and to demonstrate that the vortices from experiments can be modeled by a Lamb-Oseen vortex model as presented in section 3.3. In addition to that, an investigation and a quantification of the vortex stresses $\overline{V_i V_j}$ as presented in section 3.2 was accomplished. In terms of the vortex-stress distributions, the $\alpha=30^{\circ}$ experiments are used for a comparison of the single VGJ results with the results for a counter-rotating common-flow-down VGJ pair, see also figure 2.

4.1.1. Vortex Stresses

The investigation of the modeled spanwise-averaged vortex stresses from the experiments by Ortmanns (2008) is carried out for the single VGJ configurations in table 2. These cases produce distinct vortex stress distributions and moreover, they reveal distinguishable differences between the VGJ configurations. The interested reader is also referred to Appendix A where, for the sake of completeness of this investigation, further vortex stress distributions are presented. The $\overline{V_x V_z}$ and the $\overline{V_y V_z}$ stresses become zero in all figures, see section 3.2. The aim of this investigation was to compare single VGJ vortex stresses with vortex stresses from a VGJ pair.

Figure 11 shows the streamwise development of the spanwise-averaged stresses $\overline{V_iV_j}$ for $\alpha=45^\circ$, $\beta=75^\circ$, 90° , and 105° , $U_\infty=25$ m/s and $\lambda=2.5$. There are quantitative differences for the three different skew angles β , especially at the first measurement plane x=50 mm. It can be seen that the maximum value of $\overline{V_xV_x}$ decreases with growing β and becomes quite small for $\beta=105^\circ$. With growing β , the jet is gradually shifted from an upstream to a downstream direction with a resulting decrease in the normal vortex-stress component $\overline{V_xV_x}$. The $\overline{V_yV_y}$ and the $\overline{V_zV_z}$ components have maximum peaks for $\beta=90^\circ$, for which the vortex stresses indicate very symmetric distributions around the vortex core (i.e. where the maximum for V_yV_y and the local minimum for V_zV_z occurs). It is noteworthy that the important momentum-mixing vortex shear-stress distributions $\overline{V_xV_y}$ are very similar for all three cases without showing much variation with β . Yet, it can be assumed that the shear stresses

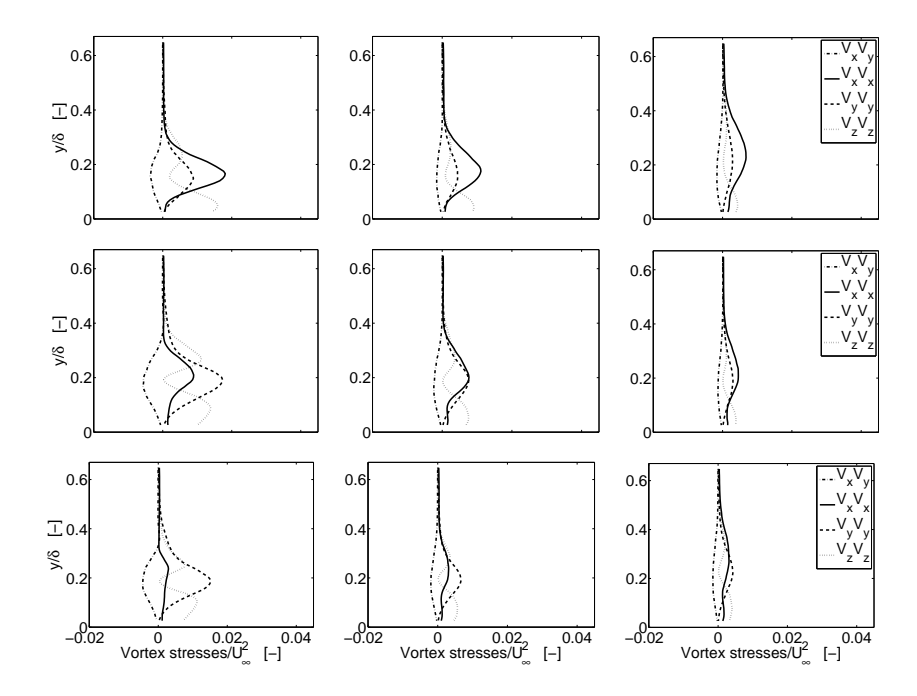


FIGURE 11. Single VGJ: $\alpha = 45^{\circ}$, $U_{\infty} = 25 \text{ m/s}$, $\lambda = 2.5$, $\beta = 75^{\circ}$, 90° , and 105° (from top to bottom): vortex-stress distributions $\overline{V_i V_j}/U_{\infty}^2$ at x = 50, 100, and 200 mm (from left to right).

are fed through the stress production $\mathcal{P}_{xy} = \overline{V_y V_y} \frac{\partial U(y)}{\partial y}$. The streamwise farfield development of the stresses reveals a general damping of all components whereas the qualitative character of the distributions remains.

The vortex-stress distributions for the $U_{\infty}=25$ m/s and $\lambda=5.0$ case in figure 12 show similar features as for the lower λ -value in figure 11, although the amplitudes are significantly larger for $\lambda=5.0$. The effect on $\overline{V_xV_x}$ is not large, since the jet is essentially pointing in the spanwise direction and, thus, does not contribute very much to increasing the spanwise averaged $\overline{V_xV_x}$ stresses; especially not for $\alpha=90^\circ$. As a result of the increase in λ , the vortex core is moved further away from the wall. Thereby, the vortices move into a region with lower shear and seem to survive for longer streamwise distances than for $\lambda=2.5$. For the second and third measurement planes, it is noticeable that the increase of $\overline{V_yV_y}$ between $\lambda=2.5$ and 5.0 is larger than for the other stress components. Stronger and more distinct vortices have developed here and the influence of the wall is diminished due to the larger wall-normal distance. This leads to less turbulence production, giving rise to a longer vortex life-time and more distinct vortices, which is expressed by the increased values for $\overline{V_yV_y}$ and

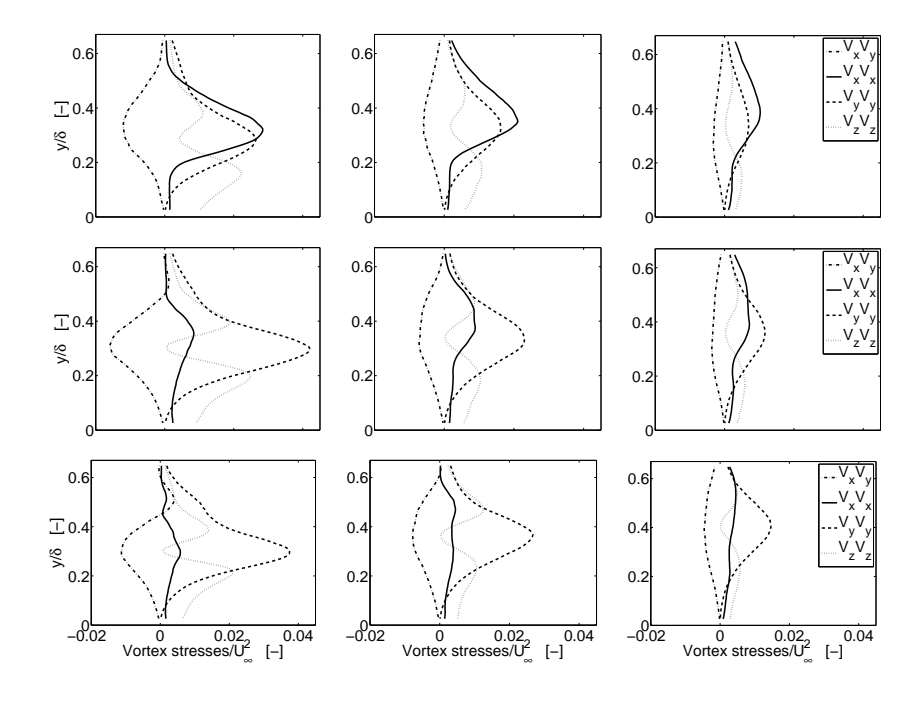


FIGURE 12. Single VGJ: $\alpha = 45^{\circ}$, $U_{\infty} = 25 \text{ m/s}$, $\lambda = 5.0$, $\beta = 75^{\circ}$, 90° , and 105° (from top to bottom): vortex-stress distributions $\overline{V_i V_j}/U_{\infty}^2$ at x = 50, 100, and 200 mm (from left to right).

 $\overline{V_zV_z}$. The vortex shear stresses $\overline{V_xV_y}$ are very similar for all β at the same streamwise positions. The larger amplitude $\overline{V_yV_y}$ distributions for $\lambda=5.0$ give a higher production of the vortex shear stresses and a longer streamwise lifespan of the vortices. Moreover, the shear stresses $\overline{V_xV_y}$ induce a higher amount of momentum-mixing in the shear layer as can be seen by the larger and more pronounced vertical vortex velocities also towards lower y/δ ; see figure 7. The $\lambda=2.5$ case, on the other hand, gives higher spanwise near-wall velocities V_z due to a lower vortex core position h_c . These vortices tend to be damped due to the interaction with the wall and the more intense shear occurring for this case.

Looking at corresponding vortex-stress distributions for $U_{\infty}=50$ m/s and $\alpha=45^{\circ}$, principally the same phenomena as in figures 11 and 12 can be observed in figures 21 and 22; see Appendix A. The qualitative distributions are very similar, and also the downstream evolution of the vortex stresses is comparable. Nevertheless, a comparison of the different freestream velocities at constant λ reveals that the nondimensional vortex stresses are generally somewhat weaker and that the vortices are located closer to the wall for $U_{\infty}=50$ m/s than for

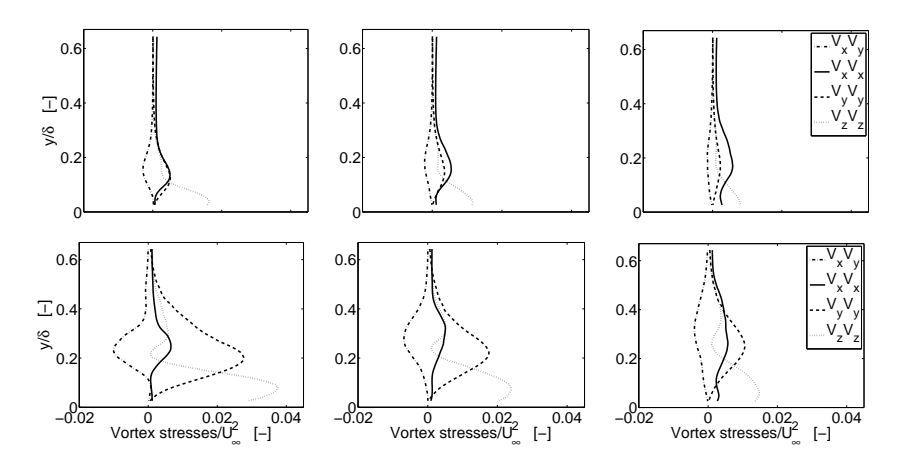


FIGURE 13. Single VGJ: $\alpha = 30^{\circ}$, $\beta = 90^{\circ}$, $U_{\infty} = 25$ m/s, $\lambda = 2.5$ (top), 5.0 (bottom): vortex-stress distributions $\overline{V_iV_j}/U_{\infty}^2$ at x = 50, 100, and 200 mm (from left to right).

 $U_{\infty}=25$ m/s. This result applies for both λ -values and may indicate a loss of flow-control efficiency for higher freestream velocities. This is also supported by figure 10 for x=50 and 100 mm, where the nondimensional maximum circulation shows higher values for $U_{\infty}=25$ m/s than for $U_{\infty}=50$ m/s. Therefore, the authors assume that there must exist a maximum efficiency in terms of the vortex stresses. In order to determine such an optimum, more experiments or detailed CFD investigations are necessary.

Figure 13 presents vortex-stress distributions for a pitch angle $\alpha = 30^{\circ}$ and a skew angle $\beta=90^\circ$ at $U_\infty=25$ m/s. For this flow case, no skewangle variations were carried out. Ortmanns & Kähler (2007) assumed that the dependency of results on a β -variation is very similar to the results for α = 45°. Thus, no further β -investigations were examined and only a λ -variation is shown, where the results need to be compared to the center plots in figures 11 and 12. Directly observable from figure 13 is that the vortices are now located much closer to the wall than for the previous cases. This is due to the reduced pitch angle α . A qualitative large difference at the first measurement position in comparison to the previous VGJ configurations occurs for the $\overline{V_z V_z}$ distribution since the lower peak of $\overline{V_zV_z}$ is larger and located closer to the wall. The $\overline{V_x V_y}$ and the $\overline{V_x V_x}$ stresses are, even though they are initially less spread, very comparable to the $\alpha=45^{\circ}$ cases whereas $\overline{V_yV_y}$ shows lower values. It may be concluded that the flow-control efficiency is higher for $\alpha = 30^{\circ}$ since the vortices are located closer to the wall and enable momentum transport closer to the wall. Nevertheless, the vortices for $\alpha = 45^{\circ}$ are possibly able to travel longer distances before they break up, and therefore may reveal better far-field flow-separation-control abilities than for $\alpha = 30^{\circ}$.

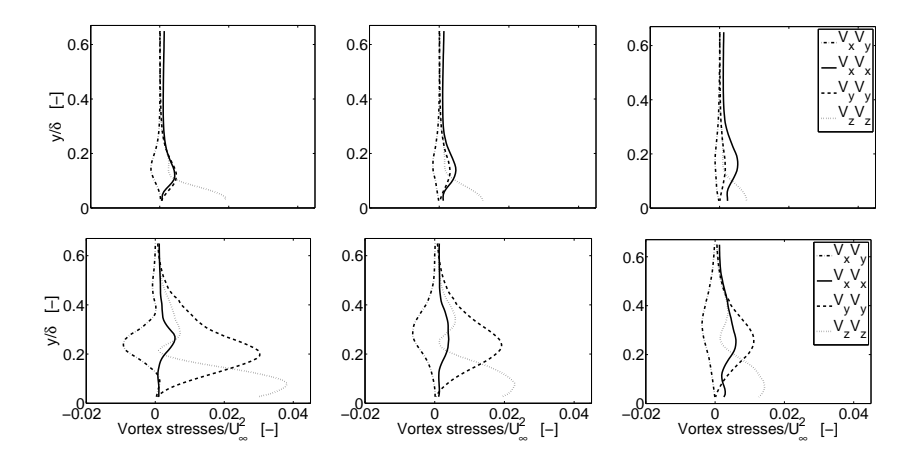


FIGURE 14. Single VGJ: $\alpha = 30^{\circ}$, $\beta = 90^{\circ}$, $U_{\infty} = 50$ m/s, $\lambda = 2.5$ (top), 5.0 (bottom): vortex-stress distributions $\overline{V_iV_j}/U_{\infty}^2$ at x = 50, 100, 200 mm (from left to right).

Figure 14 gives results for the previous VGJ configuration at $U_{\infty}=50$ m/s. It is observable that the qualitative and quantitative distributions of the nondimensional vortex-stress results of the λ -variation do not differ much from the $U_{\infty}=25$ m/s case shown in figure 13, which is in contrast to the $\alpha=45^{\circ}$ case. It can therefore be concluded that U_{∞} has negligible influence on the nondimensional vortex stresses for $\alpha=30^{\circ}$ and $\beta=90^{\circ}$. It may be assumed that different skew angles have negligible influence on results for different β , because the pitch angle α seems to be the dominant parameter here. Nevertheless, the λ -variation for $\alpha=30^{\circ}$ shows the typical distributions that are given in figure 13.

4.2. VGJ Pair

The VGJ pair experiments comprised parameter variations according to table 3. The experimental investigation encompassed a minimum actuator distance d=60 mm due to the modular actuator setup. Such a setup, including the tube actuator design from figure 4, leads to a required minimum tube distance below the flat plate, i.e., here d=60 mm. Further investigations regarding a smaller d would give insight regarding the neighboring vortex interaction, and this effect will be examined by computations. For the spanwise averaging of the vortex velocities and the vortex stresses, integration boundaries with a spanwise distance $D_{sVGJ}=240$ mm, representative for a VGJ array, were used.

TABLE 3. The VGJ pair configurations from the PIV experiments by Casper (2011).

α , deg	β , deg	$\Phi_{\mathrm{VGJ}},\mathrm{mm}$	d, mm	$U_{\infty}, \mathrm{m/s}$	λ
30	90	6.4	60, 90	25	2.5, 5.0

4.2.1. Vortex Velocities

Figures 15 and 16 present the nondimensional mean streamwise-velocity fields $u_{\rm PIV,x}(y,z)/U_{\infty}$ and the vortex velocities $[V_y(y,z),V_z(y,z)]$ for $\lambda=2.5$ and 5.0, respectively, for d=60 mm. The basic setup for the experiments by Casper (2011) was the same as for Ortmanns (2008), see section 2 enabling a close comparison.

It is observable from the figures that the vortex interaction is weak. This is the result of the common-flow-down setup that requires both jets to be pointing away from each other. The $u_{\text{PIV},x}(y,z)/U_{\infty}$ contour plots show that there is a downward motion of boundary-layer flow in between the vortices and an upward motion on the opposite sides. Secondary-vortex flows are generally not detected which is most likely a consequence of the lower pitch angle α and the symmetrical VGJ configuration. Also here, the vortex core wall-normal position h_c is proportional to λ , and h_c increases with streamwise distance x, confirming the findings of Rixon & Johari (2003). For $\lambda = 2.5$ and 5.0, the wall-normal distance of the vortex core is $h_c \approx 0.1$ -0.15 y/δ and 0.2-0.3 y/δ , respectively. A comparison with results for a single VGJ at $\alpha = 30^{\circ}$ in figure 19 in Appendix A reveals that the single vortex cores can be found at wall-normal positions within the same y/δ range. Furthermore and due to the wall interaction effects, the vortices tend to move away from each other in the direction of the vortex velocity $V_z(y,z)$ close to the wall. It is assumed that this effect weakens further downstream since the vortices decay. Nevertheless, the spanwise movement is small. By a comparison with figure 19, it is visible that the VGJ pair vortices can be well-described by the single VGJ vortices since the spanwise actuator distance is sufficiently large (d = 60 mm) for the commonflow-down configuration. This conclusion is also supported by the VGJ pair vortex stresses; see section 4.2.2. Furthermore, it can be observed that the secondary-vortex structures for the single VGJ are not visible for the VGJ pairs. The $\lambda = 5.0$ case in figure 16 generally shows a flow field very similar to that for stronger vortex velocities, generating more momentum exchange within the boundary layer. Still, the vortices can also here be seen to interact weakly, which is also supported by the vortex stresses.

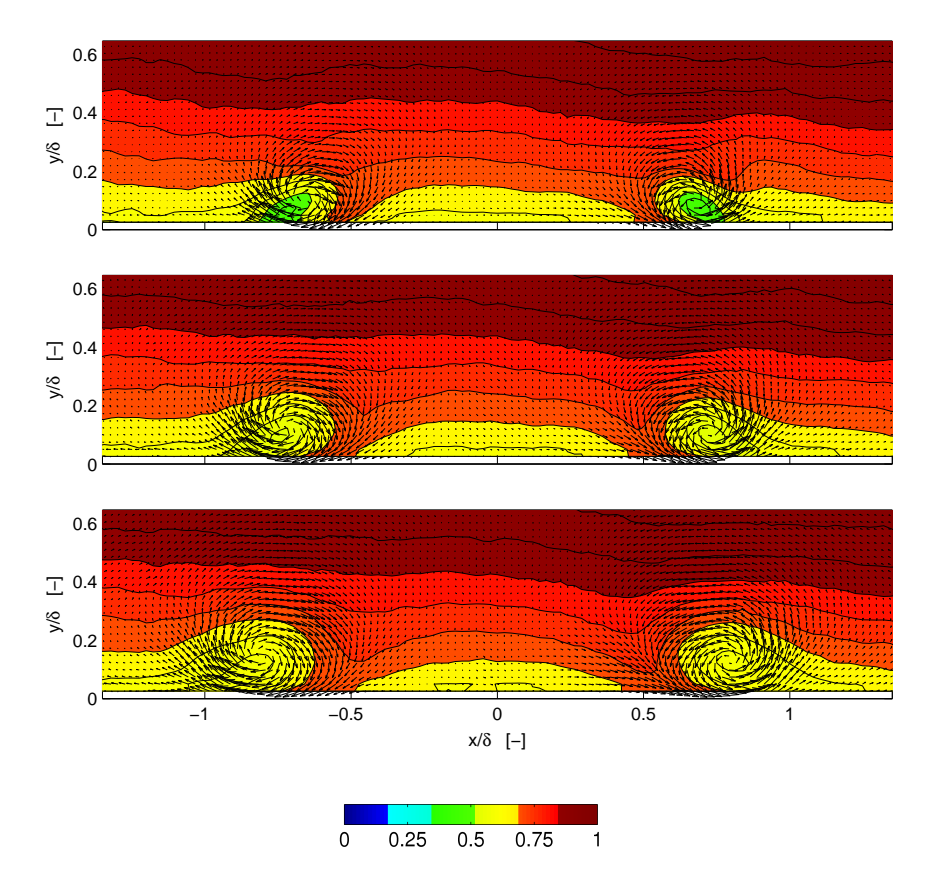


FIGURE 15. VGJ pair: $\alpha = 30^{\circ}$, $\beta = 90^{\circ}$, $U_{\infty} = 25 \text{ m/s}$, $\lambda = 2.5$, d = 60 mm: mean streamwise-velocity contours $u_{\text{PIV},x}/U_{\infty}$ and the vortex-velocity field $[V_y(y,z),V_z(y,z)]$ at x = 50, 100, and 200 mm (from top to bottom).

$4.2.2.\ Vortex\ Stresses$

The vortex stresses in figure 17 reveal results very similar compared to the vortex stresses for a single VGJ with the same setup, compare with figure 13. The stresses for the $\lambda=2.5$ case show very consistent behaviour when compared with the single VGJ vortex-stress results. For $\lambda=5.0$, the qualitative distributions are in good agreement for the single VGJ and the VGJ pair. The vortex-pair stresses $\overline{V_yV_y}$ and $\overline{V_zV_z}$ are somewhat stronger in magnitude but still in general agreement with the single VGJ case. Here, the (little) influence of the neighboring vortices is visible by means of slightly increasing values for the $\overline{V_yV_y}$ and $\overline{V_zV_z}$ stresses. The shear-stress component $\overline{V_xV_y}$ for the single VGJ is in very good agreement with the VGJ pair results, and in total, it can be stated that the single VGJ vortex stresses for $\lambda=5.0$ represent the VGJ pair-vortex stresses well. This can be expected since the vortices in the VGJ

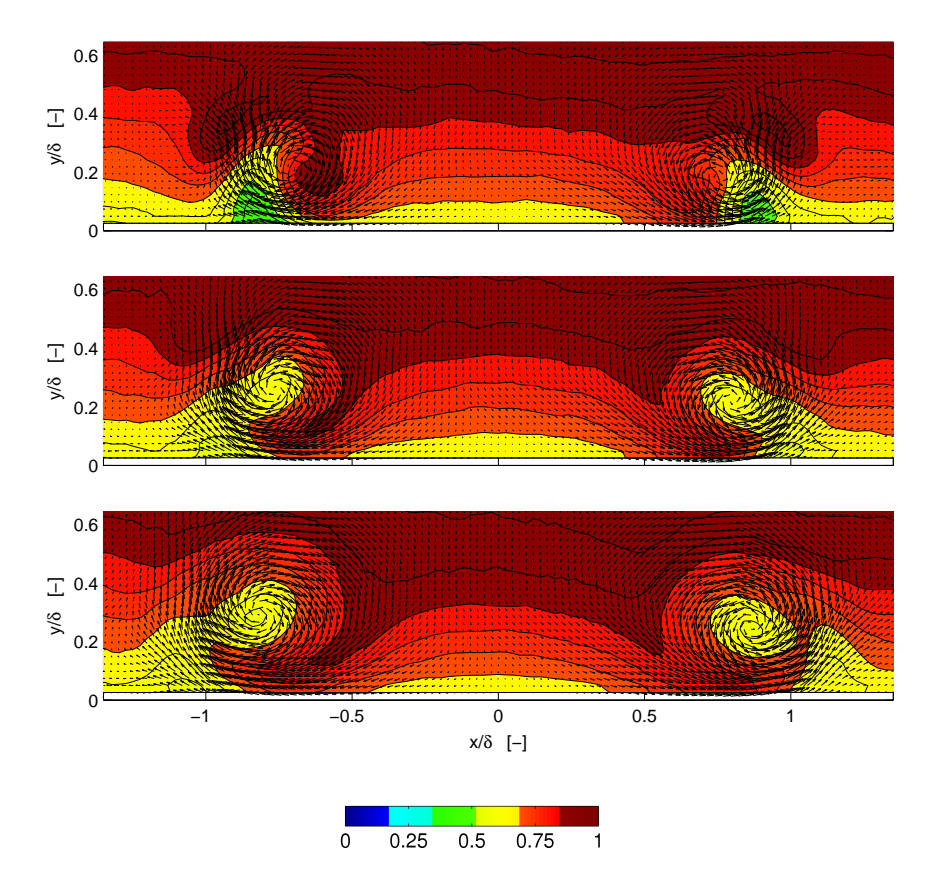


FIGURE 16. VGJ pair: $\alpha = 30^{\circ}$, $\beta = 90^{\circ}$, $U_{\infty} = 25 \text{ m/s}$, $\lambda = 5.0$, d = 60 mm: mean streamwise-velocity contours $u_{\text{PIV},x}/U_{\infty}$ and the vortex-velocity field $[V_y(y,z),V_z(y,z)]$ at x = 50, 100, and 200 mm (from top to bottom).

pair configuration only have a weak interaction with each other. Nevertheless, it is suggested that vortices for $\lambda=5.0$ have better flow-separation-control capabilities since the vortex-velocity field exhibits stronger vortices with higher momentum exchange within the boundary layer. This is also supported by the conclusion for counter-rotating common-flow-down arrays by Godard & Stanislas (2006b) who state that efficiency increases up to $\lambda=3.1$ for their specific configuration. The vortex stresses for an actuator distance d=90 mm (see figure 25 in Appendix B) lie basically on top of each other, because a spanwise-integration distance of D=240 mm (the equivalent of the VGJ array and the single VGJ symmetry distances) was chosen for all VGJ pairs which generally covers both VGJ pair vortices well.

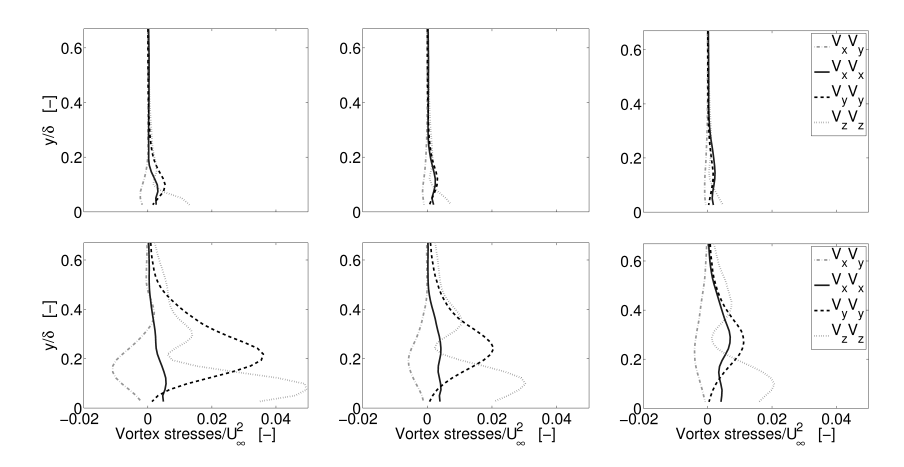


FIGURE 17. VGJ pair: $\alpha = 30^{\circ}$, $\beta = 90^{\circ}$, $U_{\infty} = 25$ m/s, d = 60 mm, $\lambda = 2.5$ (top), and 5.0 (bottom): vortex-stress distributions $\overline{V_i V_j}/U_{\infty}^2$ at x = 50, 100, 200 mm (from left to right).

5. Conclusions

This investigation presents results of a recent collaboration between TUBS, Germany, and KTH Stockholm. The study has successfully shown the ability to describe and parameterize single VGJ vortex-velocity fields by means of the Lamb-Oseen vortex model. The Lamb-Oseen vortex-model parameters Γ_{max} and r_0 , the maximum circulation and the vortex core radius, respectively, as well as the vortex core location (h_c, z_c) for each single VGJ setup, and for each measurement plane could be determined by a least-squares data fitting. The trends and tendencies of these vortex parameters as a function of chosen VGJ actuator-setup parameters could be given. It can be stated that r_0 is rather constant for different skew angles and velocity ratios β and λ , respectively. In contrast to that, the maximum circulation and the wall-normal distance of the vortex core Γ_{max} and h_c , respectively, describe similar trends that show maximum values for a skew angle $\beta = 90^{\circ}$ and $U_{\infty} = 25$ m/s. Furthermore and for $U_{\infty} = 50$ m/s the trends for the same parameters showed increasing values with possible maximum values for higher β .

The vortex velocities for the VGJ pair with the same setup as the single VGJ revealed very similar results and it is concluded that the vortices from the VGJ pair can be described by single vortices. It is furthermore inferred that the given VGJ pair setup is representative for a VGJ array when neighboring vortex pairs are located reasonably well away from each other.

As a tool to quantify the effects of the vortices on the flow, statistical vortex stresses for each setup and measurement plane were obtained. The single VGJ vortex stresses could be quantified as a function of the experimental

VGJ setup parameters, with λ and β as the dominant ones. For the important $\overline{V_xV_y}$ and $\overline{V_yV_y}$ vortex stresses, the velocity ratio λ has an approximate proportional effect on the amplitudes, whereas $\beta=90^\circ$ gives the strongest stress distributions. U_∞ has less influence on the vortex stresses, and $U_\infty=50$ m/s revealed some decrease of the nondimensional vortex circulation and corresponding nondimensional vortex stresses when compared to $U_\infty=25$ m/s.

The determination of the vortex stresses $\overline{V_iV_j}$ was carried out in order to compare the single VGJs and the VGJ pairs. It can be stated that the vortex stresses of the single VGJ describe very similar distributions when compared to the VGJ pair vortex stresses. The VGJ pair in this contribution may also represent a VGJ array with small interaction between neighboring vortex pairs. It can thereby be concluded that the vortex velocities from VGJ arrays with comparable geometrical setup are well-represented even by single VGJs distributions. This contributes to the understanding of flow-separation control and the effects of multiple vortices on the flow. The outcome can be used in order to describe trends and tendencies, as well as to draw conclusions for a VGJ array even though only single VGJs are examined.

The results of the parameterization of the single VGJs will be further used for the development of a statistical VGJ model for computational investigations using Reynolds stress turbulence models. Such a model takes the statistical vortex stresses from a VGJ array into account and adds them as additional forcing terms to the mean turbulence in the flow. Therefore, the results from the experiments and the analysis in terms of the vortex velocity parameterization, as well as in terms of the vortex stresses forms the foundation for the numerical ansatz of such a VGJ model.

References

- Angele, K. P. & Muhammad-Klingmann, B. 2005 The Effect of Streamwise Vortices on the Turbulence Structure of a Separating Boundary Layer. *European Journal of Mechanics B/Fluids* **24**, 539 554.
- Bender, E. E., Anderson, B. H. & Yagle, P. J. 1999 Vortex Generator Modelling for Navier-Stokes Codes. *American Society of Mechanical Engineers, FEDSM 99-6919*.
- Bragg, M. B. & Gregorek, G. M. 1987 Experimental Study of Airfoil Performance with Vortex Generators. *Journal of Aircraft* **24** (5), 305 309.
- Casper, M. 2011 Personal communication.
- Casper, M., Kähler, C. J. & Radespiel, R. 2008 Fundamentals of Boundary Layer Control with Vortex Generator Jet Arrays. *AIAA Paper 2008-3995*.
- COMPTON, D. A. & JOHNSTON, J. P. 1992 Streamwise Vortex Production by Pitched and Skewed Jets in a Turbulent Boundary Layer. *AIAA Journal* **30** (3), 640 647.
- Galpin, S., Rae, A. & Fulker, J. 2002 Investigation into Scale Effects on the Performance of Sub Boundary-Layer Vortex Generators on Civil Aircraft High-Lift Devices. *AIAA Paper 2002-3274*.
- GLEYZES, C. & PAILHAS, G. 2011 Flow Control using Continuous Fluidic Vortex Generators. Validation of a Simple CFD Model of the Interaction Between a Boundary Layer and an Inclined Jet. AIAA Paper 2011-3849.
- GODARD, G. & STANISLAS, M. 2006a Control of a Decelerating Boundary Layer. Part
 1: Optimization of Passive Vortex Generators. Aerospace Science and Technology
 10 (3), 181 191.
- GODARD, G. & STANISLAS, M. 2006b Control of a Decelerating Boundary Layer. Part 3: Optimization of Round Jets Vortex Generators. *Aerospace Science and Technology* **10** (6), 455 464.
- JOHNSTON, J. P. & NISHI, M. 1990 Vortex Generator Jets Means for Flow Separation Control. AIAA Journal 28 (6), 989 994.
- Lin, J. C. 2002 Review of Research on Low-Profile Vortex Generators to Control Boundary-Layer Separation. *Progress in Aerospace Sciences* $\bf 38$, 389-420.
- LÖGDBERG, O., ANGELE, K. & ALFREDSSON, P. H. 2010 On the Robustness of Separation Control by Streamwise Vortices. *European Journal of Mechanics B/Fluids* **29** (1), 9 17.
- LÖGDBERG, O., FRANSSON, J. H. M. & ALFREDSSON, P. H. 2009 Streamwise Evolution of Longitudinal Vortices in a Turbulent Boundary Layer. *Journal of Fluid Mechanics* 623, 27 58.
- Mahmood, S. & Radespiel, R. 2009 RANS Simulation of Jet Actuation in a Boundary Layer-Flow using Chimera Grids. *Deutscher Luft- und Raumfahrtkongress, September 8-10, Aachen, Germany.*
- Mahmood, S. & Radespiel, R. 2011 Detached-Eddy Simulation of Vortex Generator Jet using Chimera Grids. *International Conference on Computational Fluid Dynamics*, July 27-29, Paris, France.
- McCurdy, W. J. 1948 Investigation of Boundary Layer Control of an NACA 16-325

- Airfoil by Means of Vortex Generators. United Aircraft Corporation, Research Department, Rept. M-15038-3.
- ORTMANNS, J. 2008 Aktive Grenzschichtbeeinflussung mittels Pneumatischer Wirbelgeneratoren bei großen Reynoldszahlen. PhD thesis, Institut für Strömungsmechanik, Technische Universität Braunschweig.
- ORTMANNS, J. & KÄHLER, C. J. 2007 The Effect of a Single Vortex Generator Jet on the Characteristics of a Turbulent Boundary Layer. *International Journal of Heat and Fluid Flow* 28, 1302 1311.
- PAULEY, W. R. & EATON, J. K. 1988 Experimental Study of the Development of Longitudinal Vortex Pairs Embedded in a Turbulent Boundary Layer. AIAA Journal 26 (7), 816 – 823.
- Pearcey, H. H. 1961 Part IV: Shock-Induced Separation and its Prevention by Design and Boundary Layer Control. In *Boundary Layer and Flow Control*, its *Principles and Applications* (ed. G. V. Lachmann), pp. 1170 1344. Pergamon, Oxford, UK.
- RAFFEL, M., WILLERT, C. E., WERELEY, S. T. & KOMPENHANS, J. 2007 Particle Image Velocimetry: A Practical Guide. Springer.
- RIXON, G. S. & JOHARI, H. 2003 Development of a Steady Vortex Generator Jet in a Turbulent Boundary Layer. *Journal of Fluids Engineering* **125**, 1006 1015.
- Selby, G. V., Lin, J. C. & Howard, F. G. 1992 Control of Low-Speed Turbulent Separated Flow using Jet Vortex-Generators. *Experiments in Fluids* **12**, 394 – 400.
- VON STILLFRIED, F., WALLIN, S. & JOHANSSON, A. V. 2011a Evaluation of a Vortex Generator Model in Adverse Pressure Gradient Boundary Layers. *AIAA Journal* 49 (5), 982 993.
- VON STILLFRIED, F., WALLIN, S. & JOHANSSON, A. V. 2011b Vortex-Generator Models for Zero- and Adverse-Pressure-Gradient Flow. AIAA Journal **50** (4), 855 866.
- TÖRNBLOM, O. & JOHANSSON, A. V. 2007 A Reynolds Stress Closure Description of Separation Control with Vortex Generators in a Plane Asymmetric Diffuser. *Physics of Fluids* 19 (115108).
- Velte, C. M., Hansen, M. O. L. & Jønck, K. 2007 Flow Analysis of Vortex Generators on Wing Sections by Stereoscopic Particle Image Velocimetry Measurements. *Journal of Physics: Conference Series* **75** (012030).
- Wallis, R. A. 1952 The Use of Air Jets for Boundary-Layer Control. Aeronautical Research Laboratories (Melbourne, Australia), Aero Note 110.
- Wallis, R. A. 1960 A Preliminary Note on a Modified Type of Air Jet for Boundary Layer Control. *Aeronautical Research Council*, C.P. 513.
- Wendt, B. J. 2001 Initial circulation and peak vorticity behavior of vortices shed from airfoil vortex generators. *Tech. Rep.* NASA.
- ZHANG, X. 1995 Co- and Contrarotating Streamwise Vortices in a Turbulent Boundary Layer. *Journal of Aircraft* **32** (5), 1095 1101.
- Zhang, X. 2003 The Evolution of Co-Rotating Vortices in a Canonical Boundary-Layer with Inclined Jets. *Physics of Fluids* **15** (12), 3693 – 3702.
- Zhang, X. & Collins, M. W. 1997 Nearfield Evolution of a Longitudinal Vortex Generated by an Inclined Jet in a Turbulent Boundary Layer. *Journal of Fluids Engineering* 119, 934 – 939.

Appendix A: Single VGJ

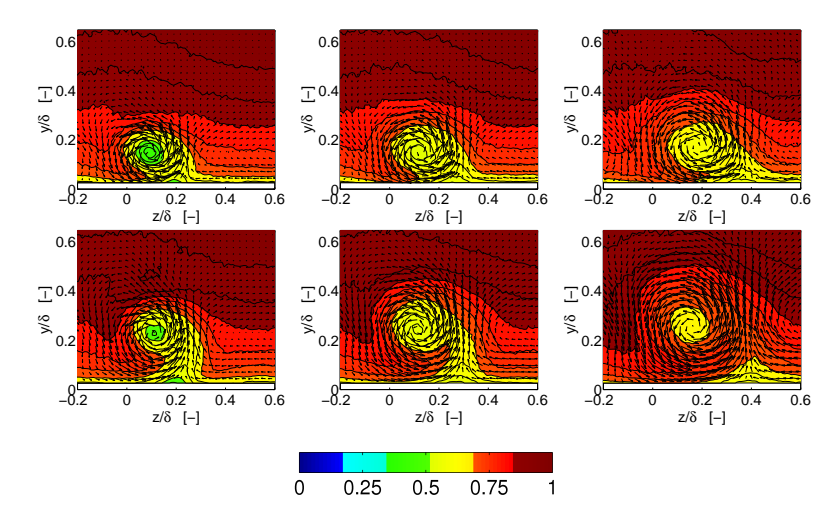


FIGURE 18. Single VGJ: $\alpha=45^{\circ}$, $\beta=90^{\circ}$, $U_{\infty}=50$ m/s, $\lambda=2.5$ (top) and 5.0 (bottom): mean streamwise-velocity contours $u_{\text{PIV},x}/U_{\infty}$ and the vortex-velocity field $[V_y(y,z),V_z(y,z)]$ at x=50, 100, and 200 mm (from left to right).

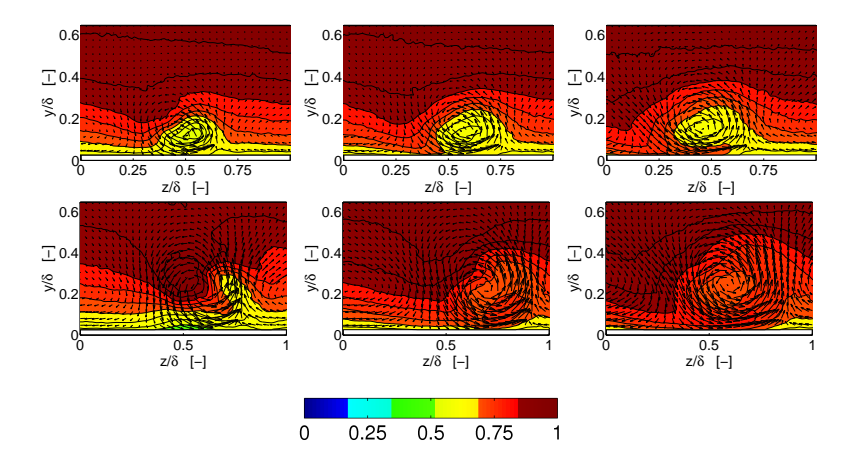


FIGURE 19. Single VGJ: $\alpha = 30^{\circ}$, $\beta = 90^{\circ}$, $U_{\infty} = 25$ m/s, $\lambda = 2.5$ (top) and 5.0 (bottom). Same information and alignement as in figure 18.

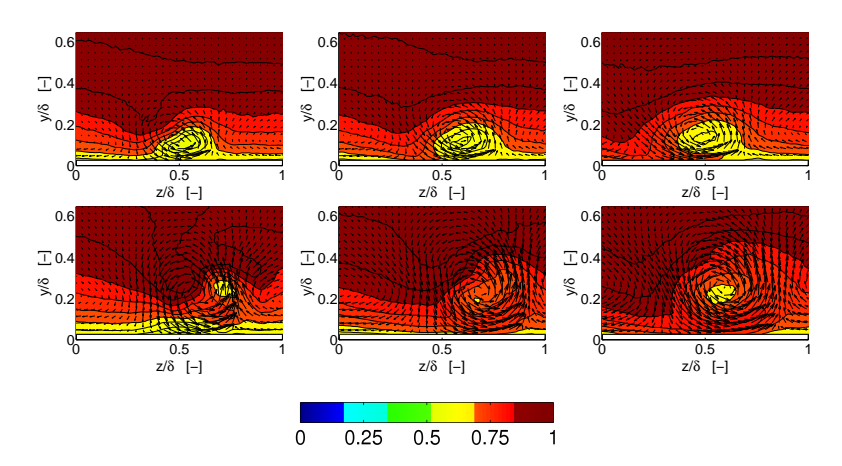


FIGURE 20. Single VGJ: $\alpha = 30^{\circ}$, $\beta = 90^{\circ}$, $U_{\infty} = 50$ m/s, $\lambda = 2.5$ (top) and 5.0 (bottom). Same information and alignement as in figure 18.

Table 4. Fitted Lamb-Oseen vortex-model parameters $\Gamma_{\rm max}$, r_0 , $h_{\rm c}$ and $z_{\rm c}$ for chosen experimental vortex-velocity fields for $\alpha=45^{\circ}$ at x=100 and 200 mm; complementing table 1.

α	β	x	U_{∞}	λ	Γ_{\max}	r_0	$h_{\rm c}$	$z_{ m c}$
\deg	mm	m/s	m/s		m^2/s	mm	mm	mm
45	75	100	25	2.5	0.210	6.4	14.6	13.4
45	75	200	25	2.5	0.199	9.6	20.6	16.7
45	90	100	25	2.5	0.230	5.6	11.1	16.1
45	90	200	25	2.5	0.167	7.2	16.0	15.6
45	105	100	25	2.5	0.211	5.3	9.4	17.2
45	105	200	25	2.5	0.203	7.4	12.4	19.5
45	75	100	25	5.0	0.453	9.3	13.2	29.3
45	75	200	25	5.0	0.363	13.6	15.6	26.0
45	90	100	25	5.0	0.486	8.3	11.8	30.1
45	90	200	25	5.0	0.408	11.2	11.8	31.2
45	105	100	25	5.0	0.506	7.5	11.0	32.3
45	105	200	25	5.0	0.427	10.1	11.1	35.0
45	75	100	50	2.5	0.325	5.6	13.6	12.4
45	75	200	50	2.5	0.242	7.1	23.9	12.2
45	90	100	50	2.5	0.340	4.9	10.9	13.4
45	90	200	50	2.5	0.275	6.6	17.8	14.9
45	105	100	50	2.5	0.356	4.6	9.9	15.0
45	105	200	50	2.5	0.300	6.3	15.2	16.1
45	75	100	50	5.0	0.546	7.4	14.1	17.8
45	75	200	50	5.0	0.438	10.2	19.5	18.7
45	90	100	50	5.0	0.590	6.5	11.6	21.1
45	90	200	50	5.0	0.517	8.8	16.8	21.8
45	105	100	50	5.0	0.688	6.3	9.7	25.4
45	105	200	50	5.0	0.583	8.5	12.2	27.3

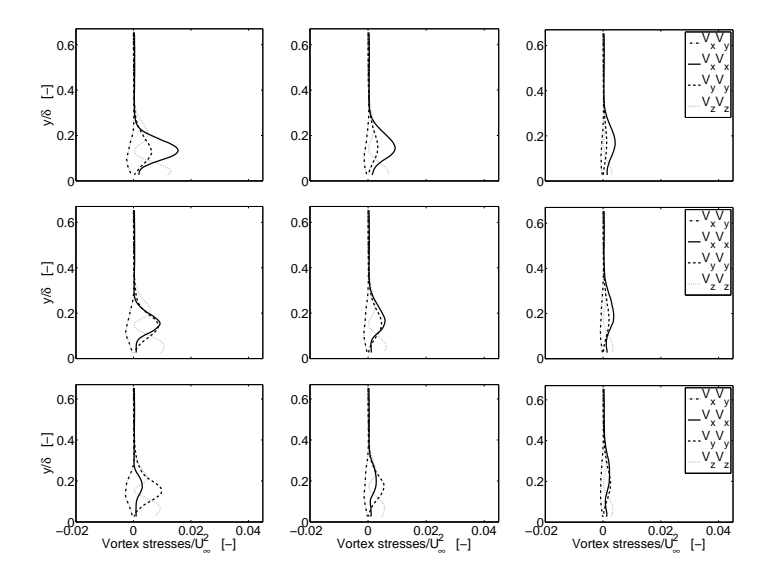


FIGURE 21. Single VGJ: $\alpha=45^\circ$, $U_\infty=50$ m/s, $\lambda=2.5$, $\beta=75^\circ$, 90° , and 105° (from top to bottom): vortex-stress distributions $\overline{V_iV_j}/U_\infty^2$ at x=50, 100, and 200 mm (from left to right).

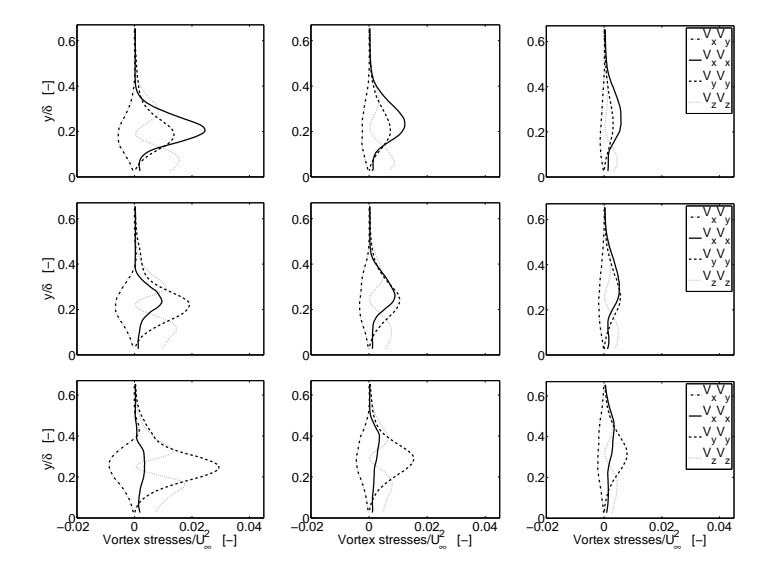


FIGURE 22. Single VGJ: $\alpha = 45^{\circ}$, $U_{\infty} = 50$ m/s, $\lambda = 5.0$. Same information and alignement as in figure 21.

Appendix B: VGJ Pair

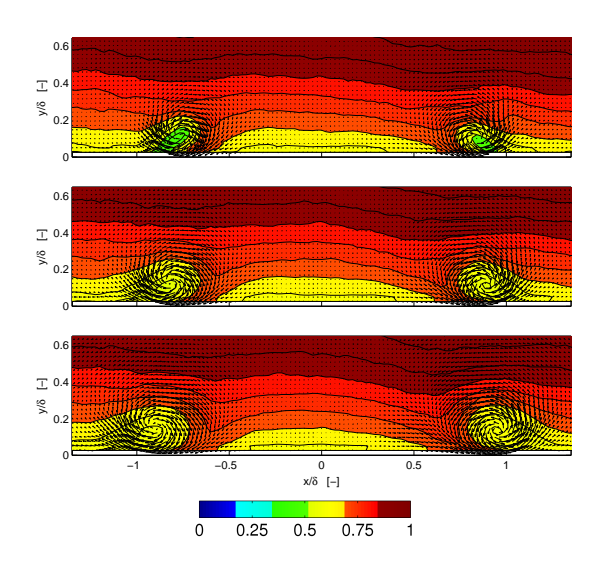


FIGURE 23. VGJ pair: $\alpha = 30^{\circ}$, $\beta = 90^{\circ}$, $U_{\infty} = 25 \text{ m/s}$, $\lambda = 2.5$, d = 90 mm: mean streamwise-velocity contours $u_{\text{PIV},x}/U_{\infty}$ and the vortex-velocity field $[V_y(y,z),V_z(y,z)]$ at x = 50, 100, and 200 mm (from top to bottom).

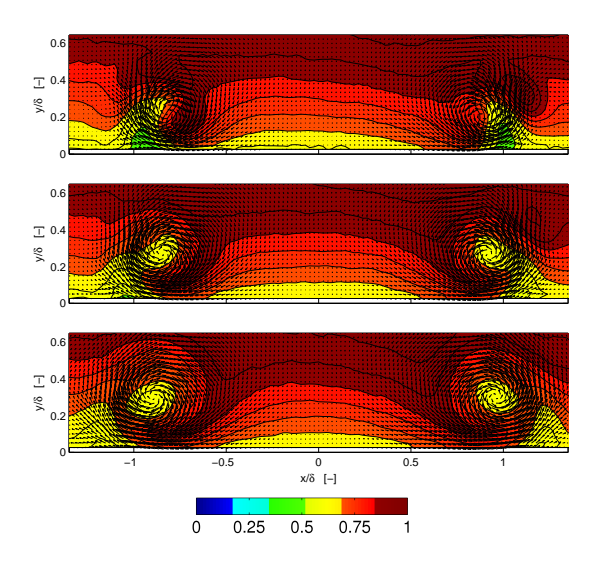


FIGURE 24. VGJ pair: $\alpha = 30^{\circ}$, $\beta = 90^{\circ}$, $U_{\infty} = 25$ m/s, $\lambda = 5.0$, d = 90 mm. Same information and alignement as in figure 23.

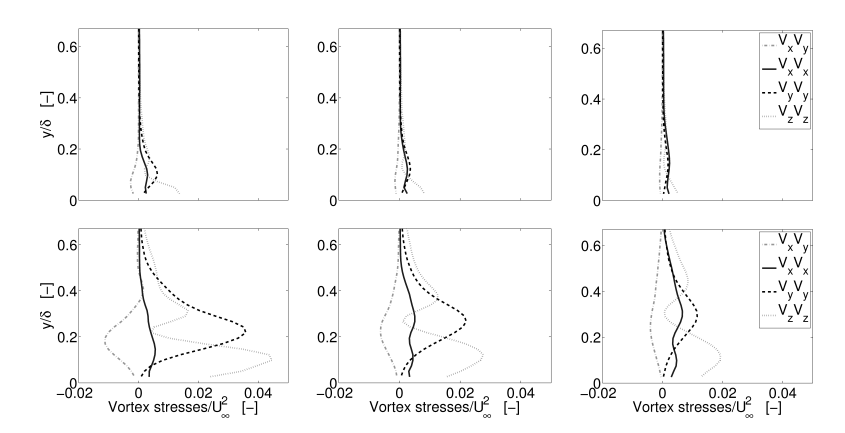


FIGURE 25. VGJ pair: $\alpha = 30^{\circ}$, $\beta = 90^{\circ}$, $U_{\infty} = 25$ m/s, d = 90 mm, $\lambda = 2.5$ (top), and 5.0 (bottom), : vortex-stress distributions $\overline{V_i V_j}/U_{\infty}^2$ at x = 50, 100, and 200 mm (from left to right).

4

A Statistical Vortex-Generator-Jet Model for Turbulent Flow-Separation Control

By Florian von Stillfried, Stefan Wallin, and Arne V. Johansson

Royal Institute of Technology, 100 44 Stockholm, Sweden

submitted to AIAA Journal

This contribution describes the development and evaluation of a new statistical-modelling approach for active vortex-generator jets. Previous experiments from Technische Universität Braunschweig, Germany, and their subsequent evaluation by the present authors showed that the induced flow field can be reasonably well represented by two-dimensional Lamb-Oseen vortices. Based on that, an analytical expression for the Lamb-Oseen vortex-model maximum circulation Γ_{max} was derived in terms of the freestream velocity U_{∞} , the jet-to-freestream velocity ratio λ , the jet skew angle β , as well as the actuator diameter Φ_{VGJ} . Based on the parameterized results, universal values for the Lamb-Oseen vortex-model parameters at the actuator position were determined for the development of the statistical vortex-generator-jet model. The idea behind the statistical-modelling approach is that the vortices are represented by their spanwise-averaged velocity correlations, or vortex stresses, that are added to the turbulence stresses in a Reynolds stress turbulence model. The spanwise-averaged vortex stresses are derived by computing the spanwise-averaged second-order statistics of the vortex-flow field. These vortexgenerator-jet model results were compared to the spanwise-averaged vortex stresses from experiments and from fully-resolved computational fluid dynamics investigations, and reasonable qualitative as well as quantitative agreement was found.

1. Introduction

Flow-separation control by means of active vortex-generator jets (VGJs) has gained increasing interest in the flow-control community recently. In contrast to fixed passive-vane-vortex generators (VVGs), the advantage of active VGJs is the possibility to activate or deactivate them when necessary, which gives the opportunity to avoid undesirable drag penalties. Moreover, VGJs make operational modes with different mass flow rates possible, and they provide the option for steady and periodic blowing. The parameters defining a complete VGJ setup are presented in figure 1, where α and β are the pitch and the skew

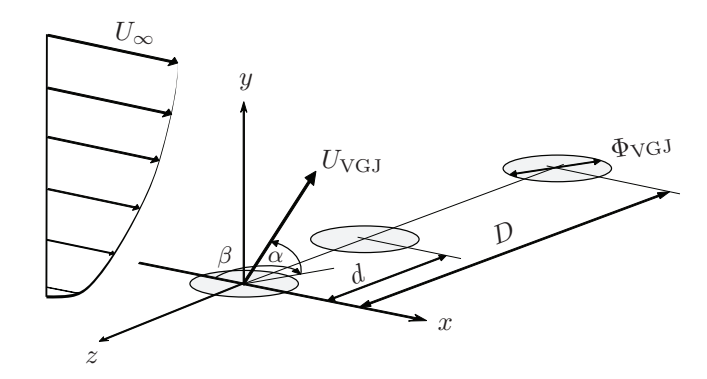


FIGURE 1. The VGJ actuator geometry and parameters, also showing the parameters d and D for a VGJ array configuration.

angle of the VGJ, respectively, and $U_{\rm VGJ}$ is the actuator-exit velocity. For setups with multiple VGJs, the parameter d represents the distance between two neighboring actuators within a VGJ pair, whereas D is the VGJ array symmetry distance between two VGJ pairs.

Rixon & Johari (2003) investigated single-steady-blowing VGJs experimentally and showed that the circulation and the wall-normal position of the primary vortex increase linearly with increasing velocity ratio $\lambda = U_{\rm VGJ}/U_{\infty}$ up to 3. Zhang & Collins (1997) investigated the near field behind a round VGJ actuator and they concluded that single vortices are fully-developed after they have traveled a streamwise distance $x=10\Phi_{\rm VGJ}$. Optimal VGJ setup parameters were, in their case, found for $\beta=120^{\circ}$, $\alpha=30^{\circ}$ for $\lambda=1.0$. Compton & Johnston (1992) investigated the far-field development and showed that the VGJ vortices can be described by weak vortices similar to those generated by passive VVGs. Ortmanns & Kähler (2007) experimentally studied the shear-layer interactions and the turbulent characteristics of the boundary layer for VGJ flow. They could show that the turbulent kinetic energy increase is rather low and that the mixing in the boundary layer is predominantly based on large-scale momentum transport by the generated vortices.

Johnston & Nishi (1990) examined corotating and counter-rotating VGJ arrays for $\alpha=45^\circ$ and $\beta=90^\circ$, and showed that such arrays could successfully establish attached flow in an adverse-pressure-gradient (APG) boundary-layer flow. Selby et~al.~(1992) performed a parametric study for VGJ arrays and boundary-layer flow over a rearward-facing ramp. They used both corotating and counter-rotating VGJ setups and concluded that such arrays perform better when λ is increased. Performance is enhanced for increasing β from 90° to 120°. Zhang (1995) concluded that a very high λ is not necessarily improving flow-separation control. Zhang (2003) also experimentally examined the evolution of corotating vortices for λ up to 1.5, and found close similarities between flow structures occuring in the near field of a VGJ array and a single VGJ setup.

Optimum parameter settings for VGJs are dependent on the actual flow case. Nevertheless, a range for an optimium VGJ setting may be determined for the pitch angle $\alpha=15^{\circ}$ to 45° , and a skew angle around $\beta=90^{\circ}$. In addition, VGJs should be positioned at $x/\Phi_{\rm VGJ}>10$ upstream of the control region in order to generate sufficiently developed vortices.

A natural approach for computational studies is to fully-resolve the VGJs as well as the downstream vortex flow structures; see, for example, V. Togiti & Knopp (2009). Even though this forms a direct way of including VGJs in a computational mesh, there seems to be fewer computational than experimental studies carried out. This is very likely because of the high computational costs associated with fully-resolved VGJs and the model uncertainties regarding the use of Reynolds-averaged Navier-Stokes (RANS) computations for resolving the subboundary-layer structures. Generally, the computational modelling of flow-control devices has become more popular as an increasing number of publications for passive VVGs has been published during the last decade (Bender et al. 1999; Jirásek 2005; Törnblom & Johansson 2007; Zhang et al. 2011; Dudek 2011; von Stillfried et al. 2011b). Yet, a weakness of general modelling strategies seems to be the dependency on good quantitative results even though the quality, the trends and tendencies of parameter changes are generally satisfactory. Nevertheless, earlier studies with a VVG model (von Stillfried et al. 2011a) applied in an APG flat-plate boundary-layer flow could, for example, verify the results of Godard & Stanislas (2006), showing the sensitivity of modeled VVGs in such flows, and giving qualitatively good results.

The present paper uses results of an experimental VGJ study, conducted by Ortmanns (2008), and previously evaluated by von Stillfried et al. (2012). The main purpose of this contribution is to present a novel VGJ modelling approach for the additional jet vortex stresses, that is similar to the passive VVG model by Törnblom & Johansson (2007). For that purpose, the given experimental vortex-velocity data was evaluated and parameterized with respect to the Lamb-Oseen vortex model. In a second step, the VGJ model based on the Lamb-Oseen vortex model was derived using an analytical ansatz. Empirical values in order to complete the VGJ model were successfully derived from the parameterization of experiments. From the VGJ model ansatz, the additional modeled vortex stresses are explicitly derived and combined with the Reynolds stress tensor in a differential Reynolds stress turbulence model (DRSM). The effect of the vortices are thereby included in the turbulence description, and consequently, influence the development of the flow field. The fact that neither resolving the VGJ actuator, nor the vortex flow structures in the boundary layer is required, leads to greatly reduced mesh generation and preprocessing times, enabling fast parameter variations. The computational costs compare with a CFD analysis without VGJs. In addition to the experiments and the VGJ model computations for a zero-pressure-gradient (ZPG) boundary-layer test case, also computations with fully-resolved VGJs are conducted and results are compared to the model results.

2. Vortex Generator Jet Experiments

The ZPG flat plate single VGJ experiments analyzed here were carried out by Ortmanns (2008) in the 1.3 x 1.3 m² and 5.7 m long test section of the closed return atmospheric low-speed wind tunnel of Technische Universität Braunschweig, Germany. The wind tunnel is equipped with a heat exchanger that keeps the air temperature constant at maximum 10.0 ± 0.5 °C above ambient temperature. Moreover, the turbulence level of the wind tunnel is 0.2% at a wind speed $U_{\infty} = 53$ m/s, whereas the average wind speed is uniform within $\pm0.2\%$. Stereoscopic particle image velocimetry (PIV) was used for the velocity measurements. For a detailed description of the PIV method, the reader is referred to Raffel et al. (2007).

The VGJ vortices originated from a single round VGJ actuator hole that was located 4650 mm downstream of the leading edge of the flat plate. The round VGJ in a modular setup had a diameter of $\Phi_{\rm VGJ}=6.4$ mm, making it possible to vary the setup in terms of the pitching angle $\alpha=30^{\circ}$ to 45°, and the skew angle $\beta=15^{\circ}$ to 105°. The freestream velocity U_{∞} for the investigations was set to 25 and 50 m/s. Moreover, the velocity ratio $\lambda=U_{\rm VGJ}/U_{\infty}$ was set to 2.5 and 5.0 for each U_{∞} , giving four different flow cases in terms of $U_{\rm VGJ}$. For $\alpha=30^{\circ}$, the experimental data were limited to $\beta=90^{\circ}$. Figure 1 illustrates the general design parameters for the VGJ, and figure 2 shows the actuator-inlet cross section.

The PIV measurements were taken at three different measurement planes downstream of the VGJ actuator at $x=50,\ 100,$ and 200 mm, or, $x/\delta_{99}=0.6,\ 1.1,$ and 2.3, with $\delta_{99}=87.6$ and 86.8 mm for $U_{\infty}=25$ m/s and 50 m/s, respectively, for the local 99% boundary-layer thickness at the actuator position, so that $\Phi_{\rm VGJ}/\delta_{99}=0.07$. These planes

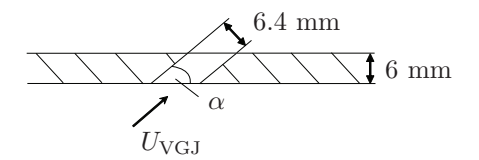


FIGURE 2. The actuatorinlet cross sections for the single VGJ.

represent far-field measurement planes where vortices already have developed. These data are the basis for the development of a statistical VGJ model, as well as for the analysis of the resulting vortex-velocity fields by von Stillfried et al. (2012). The latter is briefly repeated in section 4.1.

3. Vortex Generator Jet Computations

As mentioned in section 2, the experimental data did not cover the near field of the jet inlet where the vortex is formed. In order to gain more insight into the jet-boundary-layer interaction and the vortex development within the near field between $x/\delta_{99}=0$ and 0.6 downstream of the actuator exit, fully-resolved VGJ computations were carried out for a VGJ setup with $\alpha=30^{\circ}$ and $\beta=90^{\circ}$. Moreover, flat-plate two-dimensional computations were carried out by

using the VGJ model, which is presented in section 5, where the vortex-stress tensor is added to the Reynolds stresses at the location of the actuator exit.

3.1. Computational Setup

This computational study includes three different computational cases for the ZPG flat plate with and without VGJs. In order to make it easier to distinguish between the different cases, a labeling is introduced: 1) clean flat-plate computations (FP2D), for the flat plate without any flow control; 2) VG model computations (VGJ2D), for the flat plate with the VGJ model; and 3) fullyresolved VGJ computations (VG3D), for the three-dimensional flat plate with fully-resolved VGJs. The FP2D clean boundary-layer computations were used for finding the correct streamwise position of the VGJ actuator exit from experiments for $U_{\infty} = 25 \text{ m/s}$ and for 50 m/s. The VGJs in experiments were placed at $x_{\text{VGJ}} = 4650$ mm, where $\delta_{99} = 87.6$ mm and the momentum boundary-layer thickness $\theta = 8.0$ mm for $U_{\infty} = 25$ m/s, and $\delta_{99} = 86.8$ mm and $\theta = 8.3$ mm for $U_{\infty} = 50$ m/s. These conditions are fulfilled at FP2D streamwise positions $x_{\rm VGJ} = 5450$ and 6430 mm for $U_{\infty} = 25$ and 50 m/s. At these streamwise positions, the VGJ model is applied in the VGJ2D and the VGJ3D computations, ensuring the correct $Re_{\theta} = 1.1 \cdot 10^4$. In terms of the VGJ3D setup, a jet-velocity-inlet boundary condition was defined on the flat plate, representing the actuator exit from experiments. Here, a uniform exit-velocity profile was applied and the exit velocity was set to the theoretical velocity U_{VGJ} = [62.5, 125, 250] m/s for the different combinations of $U_{\infty} = 25, 50$ m/s and λ = 2.5, 5.0.

The FP2D and VGJ2D computations are carried out using an in-house two-dimensional ZPG boundary-layer solver (Wallin & Mårtensson 2004) using the Crank-Nicolson method with central differences for the wall-normal derivatives. The code produces results within minutes at a very fine resolution. The code uses a DRSM with a pressure-strain rate model corresponding to the Wallin & Johansson (WJ) explicit algebraic Reynolds stress model (EARSM) with curvature correction (Wallin & Johansson 2000, 2002). The DRSM is linked to the ω -equation of the Hellsten $k-\omega$ turbulence model (Hellsten 2005).

The VGJ3D computations, on the other hand, are carried out using the Edge CFD code (Eliasson 2001). Here, we use the WJ-EARSM turbulence model without curvature correction (Wallin & Johansson 2000), again linked to the Hellsten k- ω turbulence model. The EARSM approach is used here instead of the DRSM approach because the VGJ3D setup fully resolves the vortex structures in the computational grid downstream of the actuator. This is unlike the VGJ model that was specifically formulated for DRSM turbulence models, and which adds the individual vortex-stress components to the Reynolds stress tensor.

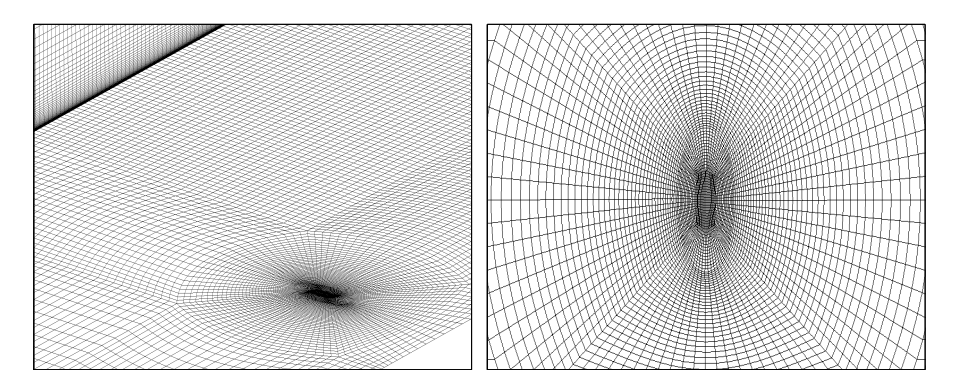


FIGURE 3. The fine grid and the fully-resolved acuator exit for $\alpha = 30^{\circ}$ and $\beta = 90^{\circ}$ in close-up isoview (left) and top-view perspective (right).

Table 1. The different meshes and the grid-refinement steps.

Grid	# nodes	refinement, %
coarse	1.1 m	-50
medium	1.8 m	± 0
fine	$3.5~\mathrm{m}$	+50
very fine	$5.6~\mathrm{m}$	+100

3.2. Grid Refinement Study

A grid-refinement study was carried out for the VGJ3D case in order to determine the required mesh resolution for the fully-resolved VGJ3D computations. In particular, the resolution around the velocity inlet and in the near field downstream of the jet exit are of interest, see also figure 3. The pitch and skew angles were $\alpha = 30^{\circ}$ and $\beta = 90^{\circ}$, and four fully-structured grids denoted: coarse, medium, fine, and very fine were created. An O-grid was wrapped around the velocity inlet so that local grid refinements have effect solely in the vicinity of the actuator exit. Close to the wall, a boundary-layer grid was used, and the wall distance to the first grid point was set to $y = 10^{-5}$ m throughout the domain, giving values of $y^+ = \mathcal{O}(1)$. Furthermore, symmetry conditions in the spanwise direction were applied so that the computational domain could be reduced to one VGJ actuator. For each grid, the node density was changed in all directions closely around the velocity inlet and in the near-field region somewhat upstream, and more extensively downstream. An overview over the different grid sizes and their total amount of nodes is given in table 1, and the refinement levels are relatively based on the medium grid. For the sake of readability, the coarse grid results are not given in the following part of this study.

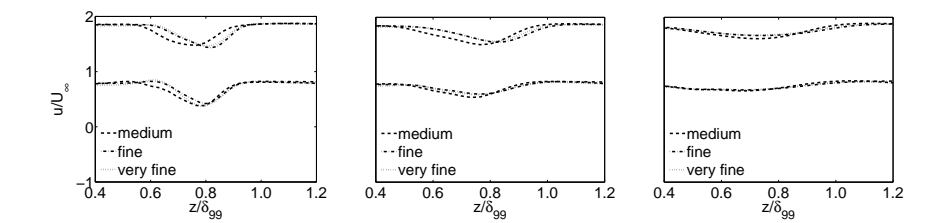


FIGURE 4. Nondimensional streamwise-velocity profiles for the grid study for $\alpha = 30^{\circ}$ and $\beta = 90^{\circ}$ (coarse results not shown) for wall-normal positions $y/\delta_{99} = 0.12$ (bottom), 0.24 (top) at streamwise positions $x/\delta_{99} = 0.6$, 1.1, and 2.3 (from left to right).

The streamwise-velocity component at three different measurement planes at $x/\delta_{99}=0.6,\,1.1,\,$ and 2.3 for two wall-normal positions $y/\delta_{99}=0.12$ and 0.24 is shown in figure 4. The differences between the fine and the very fine grids are marginal so that the fine grid was considered to be sufficient for further investigations.

3.3. Comparison of Fully Resolved Computations with Experiments

In order to compare the VGJ3D computations to experimental results from Ortmanns (2008), cross-plane contour plots of the total time/ensemble-averaged velocity fields for $\alpha=30^{\circ}$, $\beta=90^{\circ}$, $U_{\infty}=25$ m/s, and $\lambda=2.5$ at a streamwise position $x/\delta_{99}=0.6$ behind the VGJs are presented in figure 5. Note that the experimental data (top figures) represent data from a single VGJ, while the VGJ3D data (bottom figures) represent data of one single vortex in an infinitely long VGJ array. Nevertheless, the two cases are compared with each other since the vortex velocities close to and around the vortex cores are negligibly affected by their neighboring vortices; see also von Stillfried *et al.* (2012).

The resulting vortices in figure 5 are qualitatively, and to a high degree, quantitatively comparable. The u-velocity plots reveal somewhat different structures but generally, the results are satisfactory. The tangential velocities were determined by using the term $u_{\rm tan} = \sqrt{v^2 + w^2}$. In total, it can be said that the single VGJ experiments are well-represented by the VGJ3D computations and that further near-field investigations are possible with the VGJ3D results.

4. Analytical Methods

Statistical single-point vortex-velocity correlations can be analyzed from an extraction of the vortex-velocity field from experiments and computations. This analysis was previously carried out for the experimental data in von Stillfried $et\ al.\ (2012)$. Results from this analysis are given in tables 2 and 3 in the Appendix.

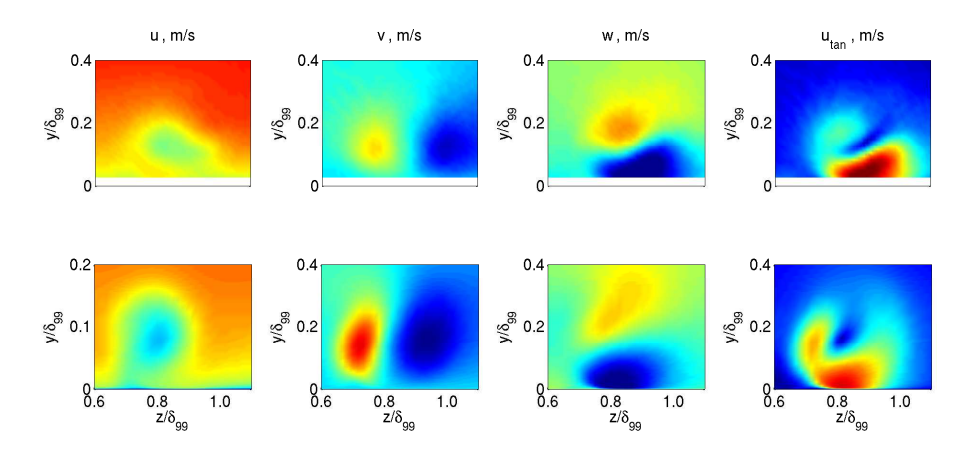


FIGURE 5. Time/ensemble-averaged velocity distributions u_i from experiments (top) and fully-resolved computations (bottom) for $\alpha = 30^{\circ}$, $\beta = 90^{\circ}$, $U_{\infty} = 25$ m/s, $\lambda = 2.5$ at a streamwise position $x/\delta_{99} = 0.6$. The range of velocities (blue: low velocity, red: high velocity) for u = 0 to 30 m/s, v = -5 to +10 m/s, w = -10 to +10 m/s, $u_{\tan} = 0$ to +10 m/s.

4.1. Analysis of the Vortex Velocities

Firstly, the velocity fields from experiments or computations are decomposed by means of a velocity triple decomposition which reads

$$u_i(y, z, t) = U_i(y) + u'_i(y, z, t) + V_i(y, z),$$
 (1)

where U_i is the time- and spanwise-averaged velocity field, $u_i'(y, z, t)$ are the time-dependent fluctuations and $V_i(y, z)$ the vortex-velocity field. Since the results that we use here are time/ensemble-averaged experimental PIV and computational RANS results, a time/ensemble-averaging of the velocity decomposition from equation (1) is already performed, so that:

$$\langle u_i(y,z,t)\rangle = U_i(y) + V_i(y,z), \tag{2}$$

since the time/ensemble-averaged value of the fluctuating part $\langle u_i'(y,z,t)\rangle$ is zero. In addition, a spanwise-averaging in the cross-plane z-direction of the time/ensemble-averaged velocity field yields

$$\overline{\langle u_i(y,z,t)\rangle} = U_i(y),\tag{3}$$

so that the vortex-velocity field $V_i(y, z)$ in a cross-plane can be extracted from the velocity field by use of the relations (2) and (3).

$$V_i(y,z) = \langle u_i(y,z,t) \rangle - \overline{\langle u_i(y,z,t) \rangle}. \tag{4}$$

The vortex-velocity field $V_i(y, z)$ can thereby be extracted from experiments and computations, and used for further post-processing for the parameter fitting in section 4.2 and the determination of statistical vortex stresses; see section 4.3.

4.2. Parameterization of the Experimental Vortex Velocities

The cross-plane vortex-velocity field $U_{\Phi}(r)$ for each measurement plane from experiments was parameterized in terms of the two-dimensional Lamb-Oseen vortex model that was previously also used for the modelling of passive VVGs (Törnblom & Johansson 2007). The Lamb-Oseen vortex model for the tangential vortex velocity uses the maximum circulation Γ_{max} , the vortex core radius r_0 , and the cross-plane vortex core position (h_c, z_c) ; see von Stillfried *et al.* (2012). In local cylindrical coordinates, the vortex velocity reads

$$V_{\Phi}(r) = \frac{\Gamma_{\text{max}}}{2\pi r} \left[1 - e^{-\left(\frac{r}{r_0}\right)^2} \right],\tag{5}$$

where $r = \sqrt{(y - h_{\rm c})^2 + (z - z_{\rm c})^2}$. A limitation of this vortex model is that it lacks a velocity component in the streamwise direction. The set of four input parameters $\Gamma_{\rm max}$, r_0 , $h_{\rm c}$, and $z_{\rm c}$, that gives the best fit for the Lamb-Oseen vortex model to the exprimental data, was found by means of solving the nonlinear least-squares fitting problem, i.e., minimizing the squared 2-norm of the difference between the experimental and the vortex-model velocities for $r/r_0 \leq 5$.

4.3. Analysis of the Vortex Stresses from Experiments and CFD

The vortex velocities $V_i(y, z)$ from equation (4) can be used in order to form the vortex-velocity correlations $V_iV_j(y, z)$; see Törnblom & Johansson (2007). From that, a statistical vortex-stress approach, i.e., the spanwise-averaged second-order statistics $\overline{V_iV_j}(y)$ can be derived and added to the Reynolds stress tensor $\overline{u_i'u_j'}(y)$ in a CFD analysis, using a DRSM. For consistency reasons with the Reynolds stress tensor, we rather use the term $\Delta \overline{u_i'u_j'}(y)$ for the additional vortex-stress tensor instead of $\overline{V_iV_j}(y)$. The vortex stress tensor reads

$$\Delta \overline{u_i' u_j'}(y) = \frac{1}{D} \int_{-D/2}^{D/2} V_i(y, z) V_j(y, z) dz,$$
 (6)

where the spanwise-averaging is performed over one VGJ pair distance D. Strictly, this spanwise-averaging only applies for an infinitely long VGJ array with a periodic variation of the vortex velocity $V_i(y,z)$ over a distance D in the cross-plane. Yet, the experimental results used here are from single VGJs, but it is assumed that single VGJs may represent a VGJ array if certain conditions are fulfilled. This includes that the neighboring vortex pairs in an array do not interact strongly with each other. Moreover, it implies that the single vortex-velocity results can be reasonably well spanwise-averaged over a

distance D/2, therefore representing a vortex pair over the symmetry distance D. This method was introduced in von Stillfried $et\ al.\ (2012)$, and has shown to generate good results when compared to VGJ pairs, confirming Zhang (2003)'s findings for VGJ arrays. The spanwise-averaging from equation (6) can be directly applied on our CFD results, since the computational setup formed an infinite VGJ array. It is also mentioned that the VGJ2D vortex stresses could not be extracted in this way, because the final VGJ2D statistical-model results were by nature already two-dimensional, and therefore, the information prior to a spanwise-averaging was not accessible. Thus, the VGJ2D vortex stresses and their development downstream of the actuator exit were calculated by a subtraction of the boundary-layer Reynolds stresses $\overline{u_i'u_j'}(y)$ from the total Reynolds stresses including the vortex stresses $\overline{u_i'u_j'}(y) + \Delta u_i'u_j'(y)$. This approach is justified since the variation of the mean-flow boundary-layer stresses is one order of magnitude smaller than the vortex stresses and thereby, essentially negligible.

The integral of the second-order statistics in equation (6) does not include the streamwise-velocity component U(y,z) since the two-dimensional Lamb-Oseen vortex model does not account for the cross-stream variation of U. Hence, the proposed model in section 5 that is based on the two-dimensional Lamb-Oseen vortex model will initially result in $\Delta \overline{u'u'}(y) = \Delta \overline{u'v'}(y) = 0$. Still, these components are to some extent formed through the production terms and redistribution mechanisms in the Reynolds stress transport model through the downstream development. Nevertheless, the authors have successfully shown that, for passive VVGs, the additional $\Delta \overline{u'u'}(y)$ and $\Delta \overline{u'v'}(y)$ components may be modeled in terms of the existing second-order statistics $\Delta \overline{v'v'}(y)$ and $\Delta \overline{w'w'}(y)$ from equation (6); see von Stillfried et al. (2011b). This aspect is however not considered in this contribution.

5. Vortex Generator Jet Modeling

The final step for the development of a VGJ model is to find relations between the Lamb-Oseen vortex-model parameters $\Gamma_{\rm max}$, r_0 , and $h_{\rm c}$ and the setup parameters for VGJs: α , β , λ , U_{∞} , and $\Phi_{\rm VGJ}$. Once these parameter dependencies are determined, the Lamb-Oseen vortex model can be used for modelling the vortex velocities, the second-order statistics can be derived and added as additional vortex stresses to the Reynolds stresses as described in section 4.3.

5.1. Theoretical Modeling Formulation for Vortex Generator Jets

In order to form a new VGJ model ansatz, a parameterization of the experimental vortices in terms of the jet and the general flow parameters is carried out based on momentum conservation. We derive an idealized model by assuming that the VGJ injects a fluidic jet with a defined impulse rate $p_{\text{VGJ}} = F_{\text{VGJ}} \Delta t$ into the boundary layer. This fluid injection results in a vortex generation and thus, in an increase of the tangential momentum in the boundary layer within a time Δt ; see figure 6.

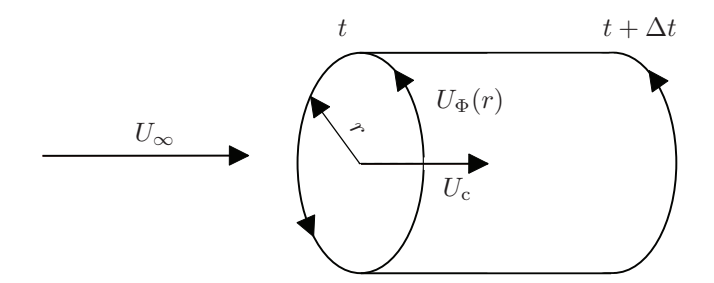


FIGURE 6. Schematic of a streamwise vortex tube of tangential vortex velocity $U_{\Phi}(r)$ that travels the distance $U_{c}\Delta t$ during the time Δt .

The magnitude of the momentum change p_{VGJ} on the boundary-layer flow by a single VGJ in a cross-plane during a time Δt for a given VGJ setup with a skew angle β can be estimated as

$$p_{\text{VGJ}} = F_{\text{VGJ}} \Delta t \sin \beta$$

$$= \dot{m}_{\text{VGJ}} U_{\text{VGJ}} \Delta t \sin \beta$$

$$= \rho \pi \frac{\Phi_{\text{VGJ}}^2}{4} U_{\text{VGJ}}^2 \Delta t \sin \beta. \tag{7}$$

The additional vortex momentum $p_{\rm V}$ contained in the vortex within a time Δt can be expressed in integral form, whereas the tangential vortex velocity U_{Φ} may be substituted by the Lamb-Oseen vortex model V_{Φ} from equation (5). This results in an additional cross-plane tangential momentum:

$$p_{V} = \int_{V} \rho U_{\Phi}(r) dV_{V},$$

$$= \rho \Delta x 2\pi \int_{0}^{R} U_{\Phi}(r) r dr,$$

$$= \rho U_{c} \Delta t 2\pi \int_{0}^{R} U_{\Phi}(r) r dr,$$

$$= \rho U_{c} \Delta t 2\pi \int_{0}^{R} \frac{\Gamma_{\max}}{2\pi r} \left[1 - e^{-\left(\frac{r}{r_{0}}\right)^{2}} \right] r dr,$$

$$= \rho U_{c} \Delta t \Gamma_{\max} \left[r - \sqrt{\pi} \frac{r_{0}}{2} \operatorname{erf}\left(\frac{r}{r_{0}}\right)^{2} \right]_{0}^{R}.$$
(8)

It is assumed that an upper integration limit of $R=5r_0$ is suitable, since this radial distance should contain most of the vortex momentum. Moreover, the vortex core convection velocity U_c is assumed to be very close to U_{∞} , i.e., $U_c \approx U_{\infty}$. We further assume that the jet impulse p_{VGJ} will be completely transformed into the vortex momentum p_{V} , leading to:

$$\Gamma_{\text{max}} = \sin \beta \frac{\Phi_{\text{VGJ}}^2 \lambda^2 U_{\infty}}{r_0} \frac{\pi}{2 \left(10 - \sqrt{\pi}\right)}.$$
 (9)

This idealized model should be used as a guide for the parameter dependencies rather than for a precise numerical value. The vortex velocities from the Lamb-Oseen vortex model in equation (5) can now be fully described by

$$\Gamma_{\text{max}} = C_{\Gamma} \sin \beta \left(\frac{\Phi_{\text{VGJ}}^2 \lambda^2 U_{\infty}}{r_0} \right),$$

$$r_0 = C_{\text{r}} \Phi_{\text{VGJ}} \sqrt{\lambda},$$

$$h_{\text{c}} = C_{\text{h}} \Phi_{\text{VGJ}} \lambda,$$
(10)

where C_{Γ} , $C_{\rm r}$ and $C_{\rm h}$ are suitable nondimensional parameters. The numerical value for

$$C_{\Gamma} = \pi / \left[2 \left(10 - \sqrt{\pi} \right) \right] \approx 0.2, \tag{11}$$

according to the idealized model from equation (9), and for an upper integration boundary $R=5r_0$. From a previous evaluation of VGJ experiments (von Stillfried et al. 2012), a dependency of r_0 on the actuator diameter $\Phi_{\rm VGJ}$ was verified. In our current analysis, a dependency on $\sqrt{\lambda}$ could be demonstrated; see section 5.2 and figure 7. The vortex core position h_c is given by the intrusion depth in terms of $\Phi_{\rm VGJ}$ that scales linearly with λ , as was also noticed by Rixon & Johari (2003). Moreover, the results from section 5.2 based on the VGJ experiments give reasonable estimates for $C_{\rm r}$ and $C_{\rm h}$ at the actuator position for the VGJ model. These estimates are later used for computations in section 6.

5.2. Streamwise Evolution of the Nondimensional Vortex Model Parameters for Experiments

Figure 7 illustrates the universality of the vortex parameter models in equation (10) by comparing the three nondimensional parameters C_{Γ} , $C_{\rm r}$ and $C_{\rm h}$, and their downstream development as a function of α , β , U_{∞} , and λ . Detailed data of the VGJ setup and the nondimensional parameters can be found in tables 2 and 3 in the Appendix. The skew-angle variation for $\alpha=45^{\circ}$ was chosen between $\beta=75^{\circ}$ to 105° , for which distinct vortices develop (von Stillfried et al. 2012). It is also mentioned that the experimental value for r_0 is used in the model equation for $\Gamma_{\rm max}$ in equation (10) when C_{Γ} is evaluated.

The model for the vortex strength in equation (10) captures the variation of $\Gamma_{\rm max}$ for different VGJ parameters reasonably well for $\alpha=30^\circ$. Therefore, the coefficient C_{Γ} lies close together around the theoretical value $C_{\Gamma}\approx 0.2$ for all flow conditions. On the other hand, the data for $\alpha=45^\circ$ show a larger spread for the different flow cases. Nonetheless, it can be observed that C_{Γ} is rather independent of β except for the flow case for $U_{\infty}=25$ m/s and $\lambda=2.5$,

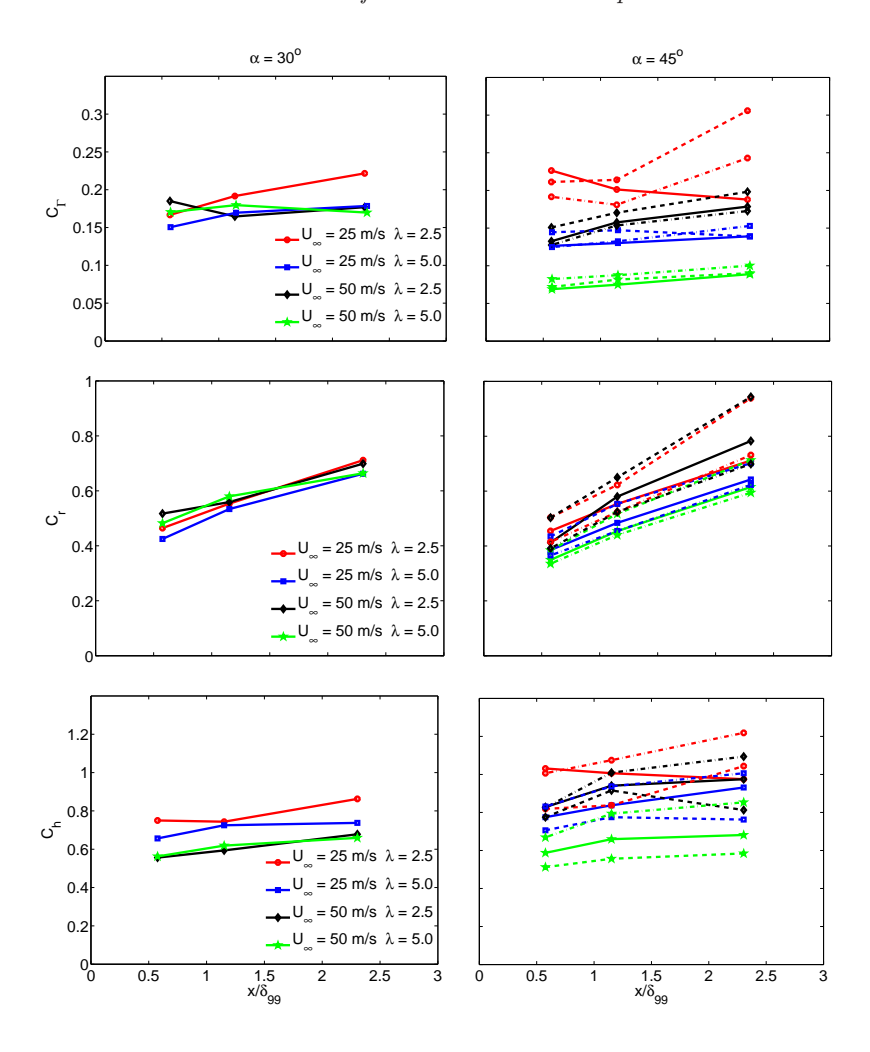


FIGURE 7. Single VGJ: streamwise development of the nondimensional parameters for the circulation C_{Γ} , the viscous core radius $C_{\rm r}$, and the wall-normal vortex core location $C_{\rm h}$ from experiments for $\alpha=30^{\circ}$ (left) and 45° (right), $\beta=75^{\circ}$ (dashed line), 90° (solid line) and 105° (broken line).

where one can observe a large variation as well as an inconsistent downstream development for the β variation. The reason for this is unclear. The plots also show that the case with the highest $U_{\rm VGJ}=250$ m/s generates a significantly weaker nondimensional circulation. Since a jet Mach number of approximately Ma=0.75 is reached with this VGJ setup, the reduced C_{Γ} is assumed to be caused by compressible effects.

The viscous core radius r_0 is well-described by the model in equation (10), as illustrated by the fact that $C_{\rm r}$ in figure 7 is rather independent on the flow conditions for $\alpha = 30^{\circ}$. It can be observed that $C_{\rm r}$ increases linearly in the streamwise direction for all VGJ settings. For $\alpha = 45^{\circ}$, the linear increase also holds, but in contrast to the $\alpha = 30^{\circ}$ setup, the $C_{\rm r}$ results are clustered with respect to λ . A lower λ , in combination with an upstream-pointing jet (β = 75°), creates the highest C_r , whereas a downstream-pointing jet ($\beta = 105^\circ$) and a higher λ achieves the lowest $C_{\rm r}$ values. In general, $C_{\rm r}$ decreases the more the jet is pointed downstream. Examining the results for a constant $\beta = 90^{\circ}$, a wider spread for $\alpha = 45^{\circ}$ compared to $\alpha = 30^{\circ}$ can be observed. Further comparing $C_{\rm r}$, it is generally observable that a smaller pitch angle $\alpha=30^{\circ}$ increases C_r slightly. Even though the differences are small, it can be said that this phenomenon very likely occurs under the influence of stronger interaction associated with the higher shear rate in the lower part of the boundary layer. A very important finding from the results is that an extrapolation for $C_{\rm r}$ to the VGJ actuator plane at $x/\delta_{99} = 0$ may be carried out for the $\alpha = 30^{\circ}$ case to determine initial settings for the proposed VGJ model in section 6. The authors suggest $C_{\rm r} = 0.4$ as a universal value for all flow cases. Moreover, the results show that vortex expansion through the linear increase in C_r , and not dissipative effects, appears to be the main mechanism for the streamwise decrease of circulation for all examined flow cases.

Also the wall-normal distance $h_{\rm c}$ is reasonably captured by equation (10), leading to a rather universal value for $C_{\rm h}$. It is suggested to follow the approach for $C_{\rm r}$, and use the $\alpha=30^{\circ}$ case for an extrapolation to $x/\delta_{99}=0$, giving $C_{\rm h}=0.6$

The four different $\alpha=30^\circ$ cases are very similar in terms of C_Γ , C_r , and C_h . The results show to be rather independent of U_∞ and λ , and it is suggested that VGJs with $\alpha=30^\circ$ represent a good choice for flow-separation control. Nevertheless, a variation of the skew angle β was not carried out regarding the experiments for $\alpha=30^\circ$, but results for $\alpha=45^\circ$ show a weak dependency on β (except for $U_\infty=25$ m/s and $\lambda=2.5$) and a similar behaviour is expected for the 30° case.

6. Comparison of the Vortex Stress Results

Results for the spanwise-averaged additional vortex stresses for the VGJ2D computations and a comparison to results from experiments, as well as from VGJ3D computations are presented for the $\Delta \overline{u'v'}$, $\Delta \overline{v'v'}$, and $\Delta \overline{w'w'}$ vortex stresses in figures 8 to 10. The near-field measurement planes between $x/\delta_{99}=0$ and 0.6, and the far-field measurement planes between $x/\delta_{99}=0.6$ and 2.3 are given in the top and bottom subfigures, respectively. For all subsequent figures, the VGJ model constants for $\alpha=30^\circ$ were set to: $C_\Gamma=0.2$, $C_r=0.4$, and $C_h=0.6$ (the first value from the theoretical determination, and the latter are two estimates from the extrapolation to the VGJ model forcing plane; see

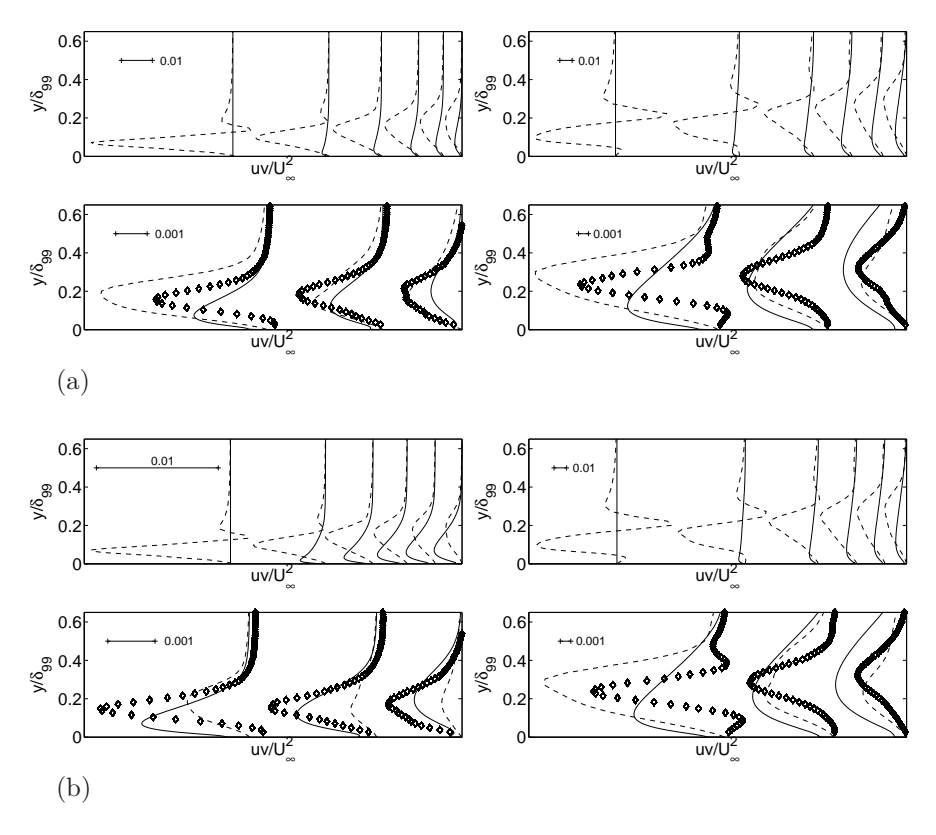


FIGURE 8. $\Delta \overline{u'v'}$ vortex-stress distributions: (a) $U_{\infty} = 25$ m/s, and (b) $U_{\infty} = 50$ m/s. $\alpha = 30^{\circ}$, $\beta = 90^{\circ}$, $\lambda = 2.5$ (left), and 5.0 (right): VGJ3D (dashed line), experiments (circles), and VGJ2D modelling results (solid line) at $x/\delta_{99} = 0.0, 0.1, 0.2, 0.3, 0.4, 0.6$ (top), and 0.6, 1.1, and 2.3 (bottom).

section 5.2). A magnitude scale is introduced in Figs. 8 to 10 so that the different results can be compared with each other.

Figures 8(a-b) present the important vortex shear stresses $\Delta \overline{u'v'}$. The initial vortex stresses at $x/\delta_{99}=0$ for the VGJ2D computations are exactly zero, since $\Delta \overline{u'v'}$ is not forced. In the near-field transient, the vortex stresses are growing through the production term $\mathcal{P}_{12}\approx -\overline{v'v'}\partial U/\partial y$ and, depending on the VGJ2D setup, reach similar magnitudes when compared to the VGJ3D distributions at the end of the near field at $x/\delta_{99}=0.6$. The far-field VGJ2D results in figures 8(a-b) show a convincing performance and a parameter dependency for the VGJ model on λ and h_c is directly visible from a comparison. The results for $\lambda=5.0$ show that the VGJ2D distributions become fuller further away from the wall, which can, to some extent, also be observed for the VGJ3D

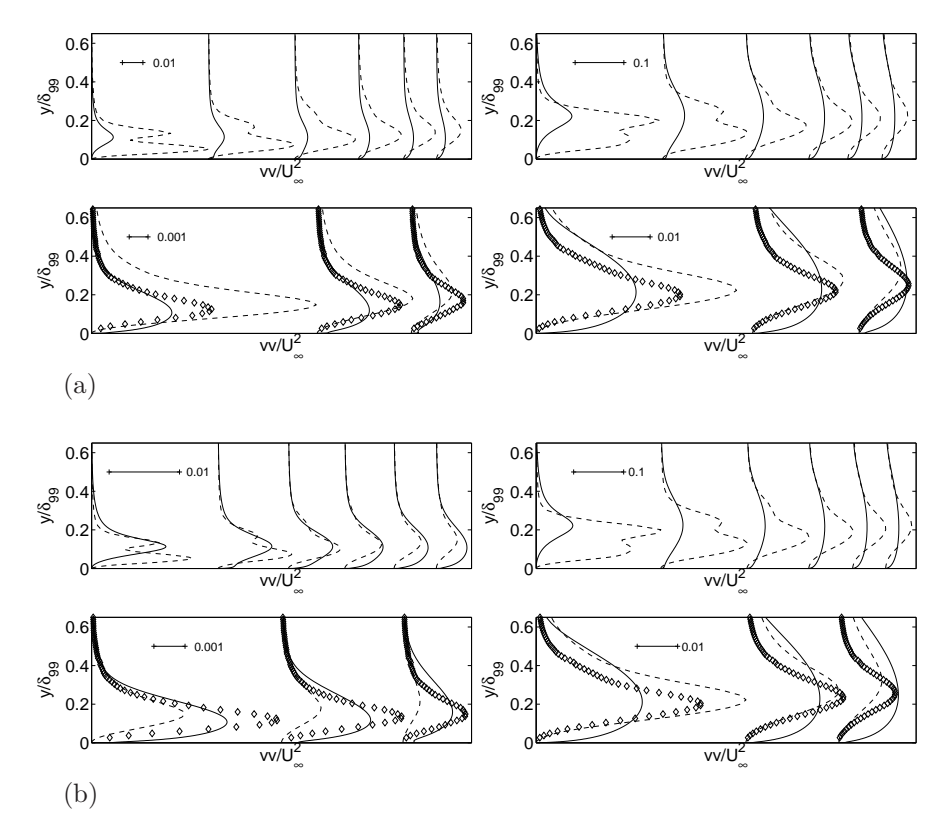


FIGURE 9. $\Delta \overline{v'v'}$ vortex-stress distributions: (a) $U_{\infty}=25$ m/s, and (b) $U_{\infty}=50$ m/s. $\alpha=30^{\circ}, \beta=90^{\circ}, \lambda=2.5$ (left), and 5.0 (right): VGJ3D (dashed line), experiments (circles), and VGJ2D modelling results (solid line) at $x/\delta_{99}=0,0.1,0.2,0.3,0.4,0.6$ (top), and 0.6, 1.1, and 2.3 (bottom).

computations and the experiments, but the influence on the VGJ2D computations is much stronger. Increasing λ to 5.0 also reveals that the distributions are generally comparable, but that especially the VGJ2D data show overestimated vortex stresses far downstream of the actuator. The vortex stresses are included in the stress tensor within the DRSM turbulence model, and unlike in the experiments, they are likely to be more rapidly redistributed than in the case when they are described by very distinct and stable vortex structures.

The $\Delta \overline{v'v'}$ in figures 9(a-b) show the forced $\Delta \overline{v'v'}$ stresses at the actuator position $x/\delta_{99}=0.0$. Depending on the VGJ model setup parameters, the change in shape and in location of the peak values can be observed for the VGJ2D stress distributions. The VGJ2D results do not perfectly describe the VGJ3D results within the near field, but also here, the $\Delta \overline{v'v'}$ stresses develop

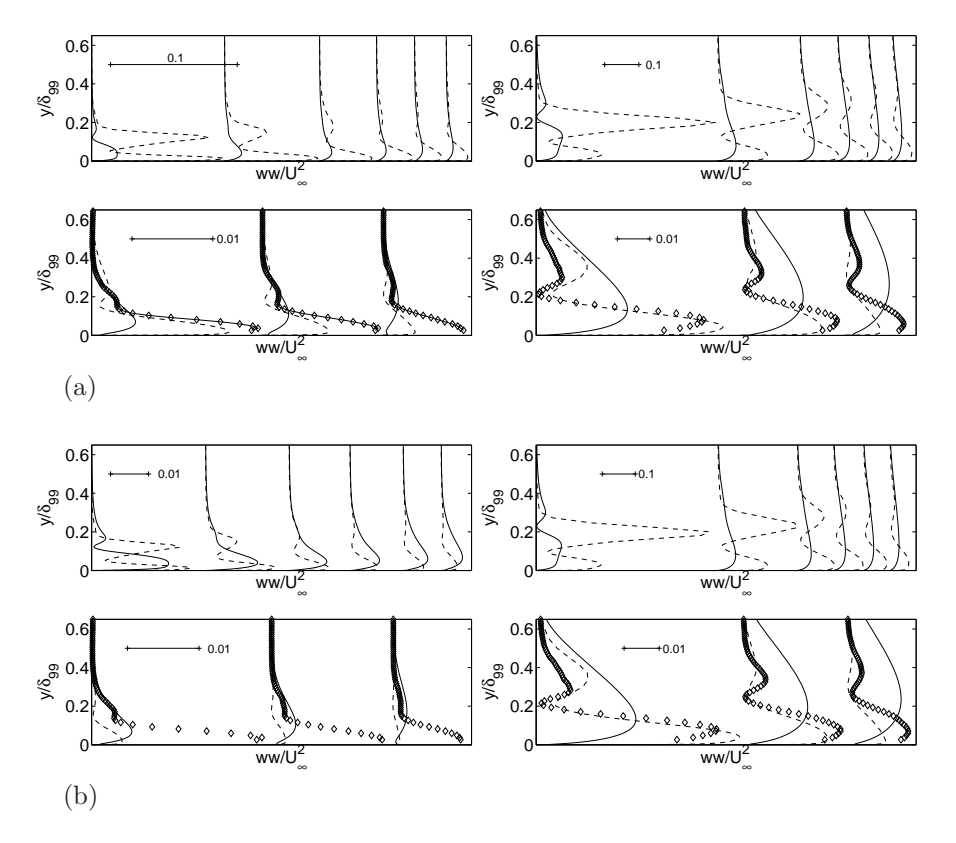


FIGURE 10. $\Delta \overline{w'w'}$ vortex-stress distributions: (a) $U_{\infty} = 25$ m/s, and (b) $U_{\infty} = 50$ m/s. $\alpha = 30^{\circ}$, $\beta = 90^{\circ}$, $\lambda = 2.5$ (left), and 5.0 (right): VGJ3D (dashed line), experiments (circles), and VGJ2D modelling results (solid line) at $x/\delta_{99} = 0$, 0.1, 0.2, 0.3, 0.4, 0.6 (top), and 0.6, 1.1, and 2.3 (bottom).

and by a streamwise position $x/\delta_{99}=0.6$, all cases have formed stress distributions that are much more comparable to experiments and to VGJ3D results. Also here, one can see how the VGJ2D stress distributions become fuller for $\lambda=5.0$.

Figures 10(a-b) present the $\Delta \overline{w'w'}$ vortex stresses that are also forced from the VGJ model. In principle, the same trends and tendencies as for $\Delta \overline{v'v'}$ can be observed. The reason for the very large deviations between computational and experimental results for $U_{\infty}=50$ m/s, $\lambda=2.5$ is not yet clear. Otherwise, the VGJ3D computations match the experiments well, and also the VGJ2D results can be regarded as satisfactory for this first attempt of a statistical VGJ model description.

In total, it can be said that the investigation of the vortex stresses and their downstream development is very encouraging for the VGJ model that uses the Lamb-Oseen vortex model and the theoretical findings from section 5. The ansatz of this new VGJ model is based on an ideal theoretical description with certain limiting approximations. It cannot be expected to generate completely consistent results with experiments or fully-resolved computations in general, but may be improved by means of new results and insights from further computational investigations. For drawing more general conclusions, the VGJ model needs to be further examined in practical flow cases such as an APG flat-plate flow or, for example, the flow around an airfoil. The present investigation should be regarded as a first effort in order to evaluate the VGJ model in ZPG flat-plate boundary-layer flow and should not yet be used to draw general conclusions about flow-separation-control capabilities.

7. Conclusions

This paper presents a novel modelling approach for active VGJs for turbulent boundary-layer flow-separation control. Additional stresses, originating from the VGJ vortices, are modeled using the additional second-order statistics $\Delta u_i' u_j'(y)$ by means of the Lamb-Oseen vortex model and its resulting vortex velocities $V_i(y,z)$. A model for the vortex parameter Γ_{max} was successfully derived by means of a theoretical ansatz from classical mechanics, and comparing the additional VGJ momentum with the momentum of a fully-developed streamwise vortex tube. Moreover, models for the vortex model parameters such as the viscous core radius r_0 , and the vortex core location (h_c, z_c) in the boundary-layer were successfully derived by an evaluation of experiments, previously carried out by Ortmanns (2008) at Technische Universität Braunschweig, Germany, and analyzed and parameterized by the authors.

The validity and generality of the models for $\Gamma_{\rm max}$, r_0 , and $h_{\rm c}$ was assessed by a comparison of the corresponding VGJ model coefficients C_{Γ} , $C_{\rm r}$, and $C_{\rm h}$, and their application on the experimental data where the VGJ pitch and skew angles, α and β , the jet blowing ratio λ and the freestream velocity U_{∞} are varied.

The theoretical value of the nondimensional circulation C_{Γ} based on $\Gamma_{\rm max}$ is approximately 0.2 and is close to the results from the parameterized experiments. It could be further shown that a VGJ for $\alpha=30^{\circ}$ shows rather small variations for C_{Γ} , $C_{\rm r}$, and $C_{\rm h}$ over the whole parameter range for λ and U_{∞} . The highest as well as the lowest value for C_{Γ} was determined for a VGJ with $\alpha=45^{\circ}$ due to a larger spread of results, making this setup apparently more sensitive to parameter variations. The streamwise development of the model coefficients reveals a linear increase of the viscous core radius $C_{\rm r}$ for all flow conditions while C_{Γ} and $C_{\rm h}$ are almost constant. The model for $\Gamma_{\rm max}$ is derived from the balance between the vortex momentum and the jet impulse and is proportional to $1/r_0$; see equation (10). The downstream decay of $\Gamma_{\rm max}$ is balanced by the linear increase in r_0 which is evidenced by the constant C_{Γ} . Hence, the vortex expansion is the primary mechanism for the vortex decay, at

least within the measurement region up to $x/\delta_{99} = 2.3$. Further downstream, turbulence diffusion and viscosity might be of bigger importance.

Based on the streamwise evolution of the nondimensional parameters for the experiments, values for $C_{\rm r}$ and $C_{\rm h}$ were extrapolated to the VGJ actuator plane $x/\delta_{99}=0$. Universal values for all flow cases based on the $\alpha=30^{\circ}$ setup were suggested with $C_{\rm r}=0.4$ and $C_{\rm h}=0.6$. These values form, together with $C_{\Gamma}\approx 0.2$, the base for the VGJ model which uses these values for the determination of additional vortex stresses as forcing terms at the VGJ actuator position.

The computations using the VGJ model and the suggested nondimensional parameter values showed satisfactory results for the resulting vortex stresses $\Delta \overline{u_i'u_j'}(y)$ and their streamwise development when compared to experiments and fully-resolved computations. This is in line with similar investigations of passive VVGs and a corresponding VVG modelling approach; see von Stillfried et al. (2011a,b). Nevertheless, the VGJ model is very idealized and still in an early development stage and cannot be considered to be completely general. Hence, further calibrations and validations are needed to draw more general conclusions about the VGJ model's flow-separation control capabilities.

It can also be stated that the creation of the VGJ vortices is different when compared to passive VVGs. This is a result of the different physics that lies behind the vortex development for the two cases, creating very distinct streamwise vortices for the passive VVG. On the other hand, the active VGJs generate vortices by means of an injection of very high-velocity jets into the boundary layer which in turn generate high-shear regions between the jet and the ambient boundary-layer flow. In contrast to VVGs, also small turbulence scales may be important for the vortex development by VGJs. This interaction on the smallest scales may weaken the VGJ vortices more quickly and thus, lead to earlier vortex breakdown since energy is dissipated much faster. Future investigations may show how this feature could be incorporated into the VGJ model description.

Acknowledgements

The Institute of Fluid Mechanics at Technische Universität Braunschweig, Germany, and especially Peter Scholz is gratefully ackowledged for providing the experimental data that were used for the evaluation of the VGJ experiments.

References

- Bender, E. E., Anderson, B. H. & Yagle, P. J. 1999 Vortex Generator Modelling for Navier-Stokes Codes. *American Society of Mechanical Engineers, FEDSM* 99-6919.
- COMPTON, D. A. & JOHNSTON, J. P. 1992 Streamwise Vortex Production by Pitched and Skewed Jets in a Turbulent Boundary Layer. *AIAA Journal* **30** (3), 640 647.
- Dudek, J. C. 2011 Modeling Vortex Generators in a Navier-Stokes Code. AIAA Journal 49 (4), 748 759.
- ELIASSON, P. 2001 EDGE, a Navier-Stokes Solver for Unstructured Grids. FOI Scientific Report FOI-R-0298-SE. FOI Swedish Defence Research Agency, iSSN 1650-19420.
- GODARD, G. & STANISLAS, M. 2006 Control of a Decelerating Boundary Layer. Part 1: Optimization of Passive Vortex Generators. Aerospace Science and Technology 10 (3), 181 – 191.
- Hellsten, A. 2005 New Advanced $k-\omega$ Turbulence Model for High-Lift Aerodynamics. AIAA Journal 43 (9), 1857 1869.
- JIRÁSEK, A. 2005 A Vortex Generator Model and its Application to Flow Control. Journal of Aircraft 42 (6), 1486 – 1491.
- JOHNSTON, J. P. & NISHI, M. 1990 Vortex Generator Jets Means for Flow Separation Control. AIAA Journal 28 (6), 989 994.
- Ortmanns, J. 2008 Aktive Grenzschichtbeeinflussung mittels Pneumatischer Wirbelgeneratoren bei großen Reynoldszahlen. PhD thesis, Institut für Strömungsmechanik, Technische Universität Braunschweig.
- ORTMANNS, J. & KÄHLER, C. J. 2007 The Effect of a Single Vortex Generator Jet on the Characteristics of a Turbulent Boundary Layer. *International Journal of Heat and Fluid Flow* 28, 1302 1311.
- RAFFEL, M., WILLERT, C. E., WERELEY, S. T. & KOMPENHANS, J. 2007 Particle Image Velocimetry: A Practical Guide. Springer.
- RIXON, G. S. & JOHARI, H. 2003 Development of a Steady Vortex Generator Jet in a Turbulent Boundary Layer. *Journal of Fluids Engineering* **125**, 1006 1015.
- SELBY, G. V., LIN, J. C. & HOWARD, F. G. 1992 Control of Low-Speed Turbulent Separated Flow using Jet Vortex-Generators. Experiments in Fluids 12, 394 – 400.
- VON STILLFRIED, F., WALLIN, S. & JOHANSSON, A. V. 2011a Evaluation of a Vortex Generator Model in Adverse Pressure Gradient Boundary Layers. *AIAA Journal* 49 (5), 982 993.
- VON STILLFRIED, F., WALLIN, S. & JOHANSSON, A. V. 2011b Vortex-Generator Models for Zero- and Adverse-Pressure-Gradient Flow. AIAA Journal **50** (4), 855 866.
- VON STILLFRIED, F., WALLIN, S. & JOHANSSON, A. V. 2012 Evaluating and Parameterizing Round Vortex Generator Jet Experiments for Flow Control. accepted for publication in AIAA Journal.
- TÖRNBLOM, O. & JOHANSSON, A. V. 2007 A Reynolds Stress Closure Description

- of Separation Control with Vortex Generators in a Plane Asymmetric Diffuser. *Physics of Fluids* **19** (115108).
- V. Togiti, V. Ciobaca, B. E. & Knopp, T. 2009 Numerical Simulation of Steady Blowing Active Flow Control using a Differential Reynolds Stress Model. *Proceedings of the KATnet II conference, Bremen, Germany.*
- WALLIN, S. & JOHANSSON, A. V. 2000 An Explicit Algebraic Reynolds Stress Model for Incompressible and Compressible Turbulent Flows. *Journal of Fluid Mechan*ics 403, 89 – 132.
- WALLIN, S. & JOHANSSON, A. V. 2002 Modelling Streamline Curvature Effects in Explicit Algebraic Reynolds Stress Turbulence Models. *International Journal of Heat and Fluid Flow* 23 (5), 721 – 730.
- Wallin, S. & Mårtensson, G. E. 2004 A General 1D-solver for Partial Differential Equations. *Tech. Rep* TRITA-MEK 2004:3. Department of Mechanics, KTH Stockholm, in: Licentiate thesis *Experimental and numerical study of turbulent flow in rotating ducts* by G. E. Mårtensson.
- ZHANG, L., YANG, K., Xu, J. & ZHANG, M. 2011 Modeling of Delta-Wing Type Vortex Generators. Science China Technological Science 54 (2), 277 285.
- ZHANG, X. 1995 Co- and Contrarotating Streamwise Vortices in a Turbulent Boundary Layer. *Journal of Aircraft* 32 (5), 1095 1101.
- Zhang, X. 2003 The Evolution of Co-Rotating Vortices in a Canonical Boundary-Layer with Inclined Jets. *Physics of Fluids* **15** (12), 3693 3702.
- Zhang, X. & Collins, M. W. 1997 Nearfield Evolution of a Longitudinal Vortex Generated by an Inclined Jet in a Turbulent Boundary Layer. *Journal of Fluids Engineering* 119, 934 – 939.

Appendix

TABLE 2. Fitted vortex-model parameters $\Gamma_{\rm max}$, r_0 and h_c for experimental vortex-velocity fields for $\alpha=45^\circ$; see equation (4). [Values partly from von Stillfried *et al.* (2012).]

	0	15	T.T.				7
α	β	x/δ_{99}	U_{∞}	λ	Γ_{\max}	r_0	$h_{ m c}$
deg	deg	mm	m/s		m^2/s	mm	mm
45	75	0.6	25	2.5	0.256	5.1	13.1
45	75	1.1	25	2.5	0.210	6.3	13.4
45	75	2.3	25	2.5	0.199	9.5	16.7
45	90	0.6	25	2.5	0.315	4.6	16.5
45	90	1.1	25	2.5	0.230	5.6	16.1
45	90	2.3	25	2.5	0.167	7.2	15.6
45	105	0.6	25	2.5	0.282	4.2	16.1
45	105	1.1	25	2.5	0.211	5.3	17.2
45	105	2.3	25	2.5	0.203	7.4	19.5
45	75	0.6	25	5.0	0.518	7.2	24.8
45	75	1.1	25	5.0	0.453	9.3	29.3
45	75	2.3	25	5.0	0.363	13.5	26.0
45	90	0.6	25	5.0	0.575	5.9	26.5
45	90	1.1	25	5.0	0.486	8.3	30.1
45	90	2.3	25	5.0	0.408	11.2	31.2
45	105	0.6	25	5.0	0.563	5.6	26.4
45	105	1.1	25	5.0	0.506	7.5	32.3
45	105	2.3	25	5.0	0.427	10.0	35.0
45	75	0.6	50	2.5	0.406	4.4	11.3
45	75	1.1	50	2.5	0.325	5.6	12.4
45	75	2.3	50	2.5	0.242	7.1	12.2
45	90	0.6	50	2.5	0.415	3.9	12.4
45	90	1.1	50	2.5	0.340	4.9	13.4
45	90	2.3	50	2.5	0.274	6.5	14.9
45	105	0.6	50	2.5	0.417	3.7	13.3
45	105	1.1	50	2.5	0.356	4.6	15.0
45	105	2.3	50	2.5	0.300	6.3	16.1
45	75	0.6	50	5.0	0.647	5.5	16.4
45	75	1.1	50	5.0	0.546	7.4	17.8
45	75	2.3	50	5.0	0.437	10.2	18.7
45	90	0.6	50	5.0	0.706	5.0	18.8
45	90	1.1	50	5.0	0.590	6.5	21.1
45	90	2.3	50	5.0	0.517	8.8	21.8
45	105	0.6	50	5.0	0.849	4.8	21.4
45	105	1.1	50	5.0	0.687	6.3	25.4
45	105	2.3	50	5.0	0.583	8.5	27.3

Table 3. Fitted vortex-model parameters $\Gamma_{\rm max}$, r_0 and $h_{\rm c}$ for experimental vortex-velocity fields for $\alpha=30^{\circ}$; see equation (4). [Values partly from von Stillfried *et al.* (2012).]

α	β	x/δ_{99}	U_{∞}	λ	Γ_{\max}	r_0	$h_{\rm c}$
\deg	deg	$\overline{\mathrm{mm}}$	m/s		m^2/s	$\overline{\mathrm{mm}}$	$\overline{\mathrm{mm}}$
30	90	0.6	25	2.5	0.227	4.7	12.0
30	90	1.1	25	2.5	0.219	5.6	11.9
30	90	2.3	25	2.5	0.197	7.2	13.8
30	90	0.6	25	5.0	0.640	7.4	17.8
30	90	1.1	25	5.0	0.527	8.0	19.0
30	90	2.3	25	5.0	0.453	10.0	21.7
30	90	0.6	50	2.5	0.448	4.3	10.5
30	90	1.1	50	2.5	0.402	5.4	11.6
30	90	2.3	50	2.5	0.341	6.7	11.8
30	90	0.6	50	5.0	1.265	6.9	18.0
30	90	1.1	50	5.0	1.108	8.3	19.8
30	90	2.3	50	5.0	0.915	9.5	21.1

5

Application of a Statistical Vortex Generator Model on the Short-Chord Flap of a Three-Element Airfoil

By Florian von Stillfried, Stefan Wallin, and Arne V. Johansson

Royal Institute of Technology, 100 44 Stockholm, Sweden

Proceedings of the KATnet II conference on Key Aerodynamic Technologies 12-14 May 2009, Bremen, Germany

Current flap designs on civil transport-type aircraft comprise approximately 30% of the undeployed wing chord. The objective of the short-chord flap project HELIX (Innovative aerodynamic high-lift concepts, 2001-2005) within the Fifth framework programe by the European Commission¹ was to reduce the trailing-edge flaps to 20% chord or less. The benefits of such a short-flap airfoil are, for example, increased fuel tank capacity within the wing, weight savings due to lighter flap-track fairings and drag reduction during cruise flight. The major challenge for a short-chord-flap airfoil to overcome is the higher flap-deflection angle during takeoff and landing phases in order to maintain the same amount of lift as for an airfoil with conventional flap size. Flow-control devices such as stationary-passive vortex generators that are mounted on such a short-chord flap can alleviate or even totally avoid flow separation at high deflection angles.

A sound computational fluid dynamics investigation of such a flow case requires an adequate grid with a corresponding large number of grid points around such vortex generators in order to obtain an accurate solution. This, in turn, leads to a time-demanding grid generation which often comes along with lots of practical challenges during the creation. An effective way to get around this time-consuming process is to introduce modelling of the vortex generators, and to add their physical effects to the governing equations rather than resolving their geometries in the computational grid. FOI, the Swedish Defence Research Agency, and KTH, the Royal Institute of Technology Stockholm, have developed computational tools for vortex-generator modelling that make it possible to simulate and to add the additional physical effects of modelled vortex generators in wall-bounded flows, whereas the need for a local mesh refinement in the vicinity of such modelled vortex generators is no longer required. A method to statistically model vortex generators is presented and applied in this paper. Experimental and computational results are compared

¹Due to confidentiality, neither absolute length, nor absolute results are given in this contribution. Instead, relative data are presented.

for the HELIX short-chord airfoil takeoff configuration for different vortex-generator-model parameter settings.

1. Introduction

The operational envelope in aeronautical and other engineering designs is in many cases limited by turbulent boundary-layer separation. The possibility of controlling and delaying the separation enables more efficient designs that can be used for improving the performance or for optimizing the design in order to reduce drag and weight. Turbulent boundary layers can be energized by introducing vortices by vortex generators (VGs) that increase the mixing of momentum in the boundary layer and, by that, increase the near-wall velocity. Experimental studies as well as computations have shown the ability of controlling separation with such devices.

Lin (2002) provides a review of the research activities in the field of passive low profile VGs. Basic fluid dynamics and applied aerodynamics research of the performance enhancement of various flow cases due to low profile VGs is presented. Low profile VGs are most efficient when flow separation is relatively fixed, and they produce "minimal near-wall protuberances" in order to overcome flow separation. The height of such low-profile VGs is typically around $0.1 \le h/\delta_{99} \le 0.5$ which, in turn, reduces drag compared to larger VGs, but still ensures the low-profile VGs acting as highly effective control devices against flow separation when compared to conventional designs. Lin states that the nondimensional geometrical-device parameters such as the VG chord-to-height ratio c/h and the VG pair distance-to-height ratio D/h are increased substantially when the height h is reduced, leading to different geometrical properties than in classical design guidelines for conventional VGs. At the same time, angles of incidence α should be increased to ensure sufficient vortex strength when low profile VGs are used for flow-separation control.

In computational fluid dynamics (CFD), the most straightforward way to mimic VGs is to fully resolve their geometry within the mesh. This leads to very fine meshes in the vicinity of such VG structures in order to resolve the developing boundary layer on the VG vane surface, as well as the developing vortex structures in its vicinity, and further downstream. Thus, fully-resolved VGs lead to rather high computational costs.

Another way to take VGs into account is to rather model the resulting effects of VGs in a flow field. This approach removes the need to mesh the VG geometry. Jirásek (2005) describes two types of different models for mimicing VGs: a vortex-source model, and a lifting-force model. The vortex-source model needs a user input such as the initial circulation of the VGs according to the Biot-Savart law. The lifting-force model, developed by Bender et al. (1999) and generally called BAY model, rather uses the lifting force that is generated by the VGs and estimated by the lifting-line theory (Glauert 1926; Anderson 1991, LLT). The lifting force is added to the Navier-Stokes equations

and therefore acts directly on the flow and, by that, forms vortices. Jirásek also presents a new so-called jBAY model that is developed from the BAY model. The jBAY model removes some of the shortcomings of the BAY model such as the lack to model the effects of multiple VGs and the difficulty to define the grid points where the model should be applied.

A statistical VG model approach was introduced in Törnblom & Johansson (2007). This model approach describes the statistical effects of VGs on the flow. Here, the vortex flow field is derived by only taking the geometrical properties of VGs into account, inspired by Wendt (2004). The circulation distribution $\Gamma(y)$ across one VG blade is needed as an input for the VG modelling and is estimated by the LLT. Then, the resulting cross-stream vortex-velocity field is added indirectly by means of the second-order statistics of the generated vortex-velocity field in a small region through forcing terms in a Reynolds stress-transport (RST) model. Furthermore, the drag generation of the modelled VGs is considered by added volume forces in the streamwise component of the momentum equation. An advantage of this method is that no mesh refinement is needed, and that the computational costs compare solely with solving the Reynolds-averaged Navier-Stokes (RANS) equations, thus, enabling design and optimization of VG settings by CFD.

Investigations of this statistical VG model in a zero-pressure-gradient boundary-layer flow over a flat plate are presented in von Stillfried *et al.* (2009). The investigation has shown that the statistical modelling of VGs was effectually deployed and truly has the advantage of not being more computational expensive than solving RANS equations.

The main objective of this work is to examine the capabilities of the statistical VG model in adverse-pressure-gradient flow over a short-chord flap of a three-element airfoil. The clean three-element airfoil at takeoff configuration was investigated at a rather high angle of attack. Second, the two-dimensional VG model was introduced at this angle of attack on the suction side of the short-chord flap. This investigation included a parameter-variation study of the modelled geometry such as the VG height, chord, and shape plus the position of the VG model plane.

2. Analytical and Numerical Methods

The modelling of the VGs in this investigation follows the way suggested in Törnblom & Johansson (2007), who presented a model that requires neither mesh refinements, nor three-dimensional computations. In this model approach, the VGs are represented by a vortex-source model that uses the LLT in order to estimate the generation of circulation by the VGs. The circulation distribution $\Gamma(y)$ across a wing according to the LLT is given by

$$\Gamma(y) = \frac{K}{2}U(y)c(y)\left[\alpha(y) - \frac{w(y)}{U(y)}\right],\tag{1}$$

where K is the local airfoil section lift slope $(K_{\text{max}} = 2\pi \text{rad}^{-1} \text{ according to thin airfoil theory})$, U(y) is the local incoming free-stream velocity, c(y) the local chord length of the wing, $\alpha(y)$ the local angle of attack, and w(y) the local downwash due to the trailing vortex sheets. The ratio w(y)/U(y) is the local induced angle of attack $\alpha_{\text{ind}}(y)$ for small angles α , and the local downwash w(y) reads

$$w(y) = \frac{1}{4\pi} \int_{-h}^{h} \frac{d\Gamma}{dy'} \frac{1}{y' - y} dy'. \tag{2}$$

Equations (1) and (2) are solved by means of a Fourier-series ansatz; see for example Anderson (1991). The LLT holds for high-aspect-ratio wings in free-flight conditions for small angles of attack α far away from obstacles in the flow. By modelling VGs that are mounted on a wall in a boundary-layer flow by means of the LLT, some of its original assumptions are not valid anymore as a result of: 1) a boundary-layer velocity profile U(y) instead of a constant free-stream velocity U_{∞} ; 2) VGs being very low-aspect-ratio wings; 3) possible side effects due to the proximity of neighbouring VG blades, i.e., neighbouring vortices; and 4) a reasonable high angle of incidence α (corresponding the angle of attack α for free flight in the LLT) of the VG blades. Therefore, the LLT is only used as an approximation to estimate the circulation distribution $\Gamma(y)$ across a single VG blade. In turn, the circulation distribution $\Gamma(y)$ quantitatively describes the generated lift, the induced drag and the vortex strength which is again needed as an input for the vortex model. The vortices are then represented by a Lamb-Oseen vortex model with the azimuthal velocity distribution

$$V_{\Phi}(r) = \frac{\Gamma_{\text{max}}}{2\pi r} \left[1 - e^{-\left(\frac{r}{r_0}\right)^2} \right],\tag{3}$$

where Γ_{max} is the maximum value of the circulation distribution $\Gamma(y)$, determined from the LLT [see equation (1)], r_0 the vortex core radius and r the radial coordinate from the vortex center. A limitation of this two-dimensional vortex model is that the velocity component in the streamwise direction is constant.

A VG array consists of more than one VG, so that all VGs influence the vortex-flow field everywhere in the VG model plane² at the streamwise position $x_{\rm VG,mod}$ from the flap leading edge. Due to that, a superposition of the vortex-induced velocities $V_{\Phi}(r)$ for each VG and their corresponding blades was needed. The wall acts approximately as a symmetry condition for the vortices, which is simulated by introducing mirror vortices.

The concept of this VG model approach and describing its effects on the flow is to assume that the second-order statistics of the additional vortex-velocity field act like additional Reynolds stresses on the mean flow. By making

 $^{^2{\}rm Throughout}$ this paper, the VG model plane is assumed to be the corresponding yz-plane at the streamwise trailing-edge location of the modelled VGs.

this assumption, the additional spanwise-averaged contributions $\Delta \overline{u_i'u_j'}(y)$ to the Reynolds stresses are

$$\Delta \overline{u_i' u_j'}(y) = \frac{1}{D} \int_{-D/2}^{D/2} u_i'(y, z) u_j'(y, z) dz.$$
 (4)

It is sufficient to integrate and spanwise-average the second-order statistics in equation (4) over one VG pair distance D since the resulting vortexflow field is periodic. Additional contributions from equation (4) are only nonzero for $\Delta \overline{v'v'}$ and $\Delta \overline{w'w'}$. Moreover, a wall-damping function, for example $[1 - \exp(-20y/h)]$, needed to be introduced and applied on equation (4), because the vortex velocities in the spanwise direction at the wall boundary y = 0 will not cancel out and would result in a finite value in equation (4).

After applying the additional vortex stresses, a RST turbulence model was used to properly describe the development of the total Reynolds stresses downstream of the VG plane. Furthermore and unlike simpler turbulence models, a RST turbulence model makes it possible to account for the energy transfer between the different components of the Reynolds stress tensor, thus enabling production of the important shear-layer $\overline{u'v'}$ Reynolds stresses.

3. Experimental Setup

In a previous study within the HELIX project, various short-chord flap designs with different shroud lengths were investigated. Finally, the short-chord flap design in figure 1 was chosen for continuative studies. The objective was to experimentally substantiate the performance predictions from previous studies, in particular since the performance enhancement by flow-separation control devices was estimated by means of ealier experiences with subboundary-layer VGs for separation control.

Experiments including a conventional three-element airfoil with a standard chord length (baseline geometry) and the new airfoil geometry with a 20% short-chord flap were carried out by VZLU, the Czech Institute of Aviation. An open jet, closed-return, low-speed wind tunnel was used and two-dimensional end-plate models of the baseline and the short-chord geometries were manufactured. These models allowed a variation in slat and flap deflections as well as a variation of flap-lap and flap-gap positions, relative to the main element. Both, the baseline and the short-chord-flap configurations were optimised in terms of the flap-lap and -gap position.



FIGURE 1. The HELIX short-chord three-element airfoil geometry.

Generally, the investigations encompassed an angle-of-attack-range from $\alpha=-5^\circ$ to $+30^\circ$ and surface-pressure measurements at 20% model semi-span were made for 13 baseline and 7 short-chord flap configurations by means of 128 pressure holes. The Reynolds number for all experiments was $Re=1.65\cdot 10^6$ based on the undeployed baseline chord $c_{\rm base}$ and the freestream Mach number was $Ma_\infty=0.13$.

In particular, the short-chord flap flow-control experiments for takeoff and landing configurations were carried out with delta-shape vane-type subboundary-layer VGs, attached at 25% flap chord $c_{\rm flap}$, in a co-rotating configuration with a height $h_{\rm VG}$, a chord $c_{\rm VG}$, and positioned with a spanwise spacing $d_{\rm VG}$ at an angle of incidence $\alpha_{\rm VG}$ towards the freestream direction. In experiments, the flap-deflection angle $\delta_{\rm F}$ of the short-chord flap was increased by 50% for the takeoff and by 0, 8 and 23% for the landing configuration compared to the baseline configuration in order to match baseline-performance results.

The experiments have shown that the short-chord flap in takeoff configuration with flow-control devices attached could provide the lift performance of the baseline-takeoff configuration even though the maximum lift coefficient $C_{L,\max}$ could not be achieved. Therefore, the ability of the short-chord flap to replace the baseline configuration in takeoff configuration was partly shown. The remaining part of this paper investigates only the short-chord flap takeoff configuration in order to evaluate the statistical VG model against the experimental results with flow control devices.

4. Computational Setup

The circular computational domain included the HELIX airfoil in its center, surrounded by ca. 70000 nodes. The circular shape made it possible to change the angle of attack by means of the free-stream velocity components without taking additional boundary conditions into account, as for a rectangular domain. The mesh around the airfoil was kept fine in region of high-flow-curvatures, i.e., especially in the vicinity of the two gaps between the three airfoil elements. The near-wall grid points were located at $y^+ = \mathcal{O}(1)$ in order to ensure capturing the viscous effects close to the wall. Yet, there is potential to increase the mesh density in the wall-normal direction in order to resolve the near-wall effects better. However, the mesh was fine enough for such an investigations that was examining the trends of such a VG model approach, rather than matching experimental results quantitatively.

Valid throughout this paper, the HELIX airfoil computations were carried out using a differential Reynolds stress model (DRSM) as a turbulence model with pressure-strain rate model corresponding to the Wallin and Johansson explicit algebraic Reynolds stress model (EARSM) with curvature correction; see Wallin & Johansson (2002). This DRSM was also linked with the Hellsten $k-\omega$ turbulence model from Hellsten (2005). The DRSM turbulence model was applied since the VG model was developed for a usage in combination with DRSM models, adding the additional vortex stresses directly to the governing



FIGURE 2. Laminar regions (black) on the airfoil-element surfaces.

equations. Corresponding to experiments, the Reynolds number based on c_{base} and the Mach number were set to $Re = 1.65 \cdot 10^6$ and Ma = 0.13, respectively.

First, test computations without the VG model applied were carried out with fully-turbulent flow as well as with pre-defined transition regions on the airfoil-element surfaces since Re was rather low, and the position of the transition point is an important aspect that neither has been triggered, nor measured, nor estimated. The purpose of this rather ad hoc procedure was to match the experimental C_P results without VGs better than with fully-turbulent flow. Figure 2 shows the laminar regions, colored in black, on the three elements for a high angle of attack, whereas the transition setting is also based on previous experience on similar cases. The analogous C_P distribution results are given in figure 3. Here, it can be seen how the blue curve for the computations with transition settings reproduces experimental results with high accuracy. Nevertheless, it is conspicuous that the C_P distribution around the flap shows a peak value close to the flap leading edge. This characteristic is a result of the nonconverged-steady RANS computations that also indicate the shedding vortices in time, whereas the experimental data represent a time-averaged flow regime. The result of introducing the laminar regions was very promising and

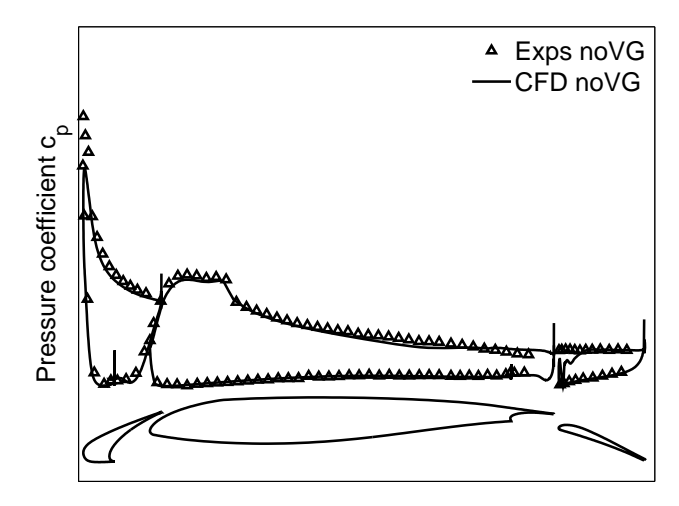


FIGURE 3. C_P distribution plots of experiments and CFD without VGs, transition settings used.

TABLE 1. Positions and configuration settings of the VG model on the HELIX short-chord flap; VG model parameters based on corresponding experimental setting.

$x_{ m VG,mod}$	4%			8%				
$c_{ m VG,mod}$	50%			100%				
$h_{ m VG,mod}$	100%		150%		100%		150%	
Shape	Δ		Δ		Δ		Δ	
Configuration	1	2	3	4	5	6	7	8

the laminar/turbulent-transition settings were therefore also applied for the flow cases with the VG model.

Second, computations including the statistical VG model were carried out for a range of high angles of attack when separation occurs on the flap. This part of the investigations included a VG model parameter variation of its corresponding modelled VG geometry in terms of shape, chord length, height, and VG model position. These input parameter can be simply set in a preprocessing step, keeping the original mesh without the need of any mesh refinement. In particular, all computations were carried out with the Edge CFD code Eliasson (2001), and for all runs, the lift slope factor K from equation (1) was set to $1.8\pi~\mathrm{rad}^{-1}$, i.e., 10% lower than for thin-airfoil theory.

5. Results

This chapter presents the experimental data with and without attached flow-control devices and the computational results with applied VG model. Previous runs have shown that the original experimental setup including the VG configuration did not lead to separation prevention in computations when the VG model was applied. At this streamwise position, i.e. at 25% $c_{\rm flap}$, the VG model plane was consequently placed in the mean-flow-separation region where the model cannot have any effect on the mean-flow characteristics. Unlike in computations, such an experimental setup can lead to separation prevention due to the fact that the flow around the flap device is fluctuating, and therefore, flow around the VGs is temporarily attached. This can be effectual to generate the needed vortex structures that ensure boundary-layer mixing and hence keep the flow attached.

It was chosen to move the VG model plane further upstream in order to place it in a smaller, as well as permantly attached boundary layer, where the VG model can successfully create the necessary vortex-stress-forcing terms that act on the mean flow. Moreover, parameter variations of the modelled geometry including the modelled VG height, chord length, and shape as well as of the VG model plane position were carried out. The parameters and their corresponding values related to the experimental setup are given in table 1.

Figure 4 displays streamline plots including velocity magnitudes in the vicinity of the main-element trailing edge and the flap for the same angle of

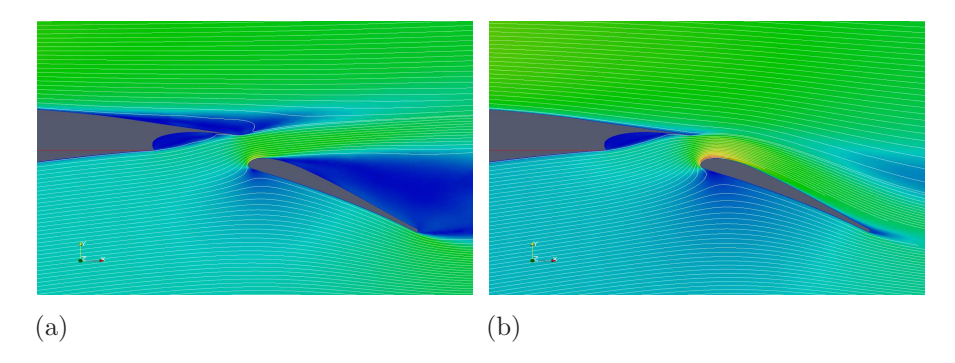


FIGURE 4. Velocity magnitude (blue: low velocity; red: high velocity) and streamline plots for (a) the airfoil without VG model, and (b) the modified airfoil with the VG model configuration 8 applied: $x_{\rm VG}/c_{\rm flap}=8\%$, $c_{\rm VG,mod}/c_{\rm VG,exp}=100\%$, $h_{\rm VG}=150\%$, rectangular shape.

attack. The comparison clearly shows the differences between the clean and the modified short-chord flap airfoil, here with VG model configuration 8. Furthermore, figures 5 and 6 show the resulting C_P plots of this investigation that include C_P distributions for all computations from table 1.

5.1. Vortex Generator Model Variation

5.1.1. Plane Variation

Figure 5 presents the different examined VG models with configuration setting 1 to 4, located at 4% c_{flap} , and in addition to the experimental results with VGs attached at 25% flap chord. Here, it can be observed that the VG model configurations 1 to 3 describe almost the same C_P curves on all three elements. Configuration 4 with larger, rectangular modelled VGs shows a visible decrease of C_P on the suction side of all airfoil elements, leading to a fully-attached flow on the flap. It should be mentioned that the VG model is located very close to the laminar/turbulent-transition point. Figure 6 shows the corresponding curves at 8% c_{flap} , yet with another value for the modelled VG chord $c_{\text{VG,mod}}/c_{\text{VG,exp}} = 100\%$, rather than 50% as in the previous case. The reason for the smaller chord was to ensure that the modelled real VG chord did not exceed the leading edge of the flap. However, figure 6 generally shows how the overall peak-pressure distribution is decreased on the flap. This might be the consequence of the double chord length that leads to a higher maximum value for $\Gamma(y)$ in equation (1). Morevover, two out of four configurations show almost congruent C_P distributions, compared to only one configuration that fully ensured separation prevention on the flap. This shows that the VG model position plays a role for an optimization of the mixing effects of flow-separationprevention devices.

5.1.2. Height Variation

The VG model height has a major influence on the effectiveness of flow separation prevention as can be seen in figure 6. There, a higher VG model is preventing the mean flow from separation, compare configurations 5 and 7 as well as 6 and 8 with each other. This is a result of the fact that the higher the VG model, the higher are the velocites around the wing tip and the higher gets $\Gamma(y)$ in equation (1), leading to larger additional forcing terms in the RANS equations. Under certain circumstances, when this height difference is of relative importance, it can have a non-negligible impact on the mean-flow field, leading to potential flow-separation prevention.

5.1.3. Shape Variation

Figures 5 and 6 show that the modelled VG shape can lead to differences in the C_P distribution, depending on where the VG model plane is located and how tall the modelled VG is. Figure 5 displays C_P distribution plots for the different VG model configurations for the further upstream located VG model plane location at 4% c_{flap} . There, configurations 3 and 4, representing delta and rectangular modelled VGs, respectively, prove to illustrate that the differences regarding a flow-separation prevention are considerable. The configurations 1 and 2 do not show this sensitivity but, for this case, it is presumed that the VG model height has more importance on results than the modelled shape. Figure 6 does not to show any sensitivities in the C_P distributions at all for a shape variation; the small differences for configurations 5 and 6 occur from the nonconverged steady computations, giving different flow states as a result of the fluctuating and separated flow region on the flap.

6. Conclusions

This investigation has shown the capabilities of the application of a statistical VG model approach on the short-chord flap of the HELIX three-element airfoil to mimic the effects of corotating VG arrays by means of introducing additional statistical vortex stresses to the governing mean-flow equations.

Pressure-distribution plots and images of the instantaneous flow regime around the three-element airfoil illustrate that the VG model computations successfully improve the flow by means of preventing separated flow on the flap for certain VG model configurations. In particular, figures 5 and 6 show the C_P distributions for the VG model parameter study; see also table 1. There, the effect of configurations 4, 7 and 8 on successfully preventing flow separation is clearly visible. Furthermore, the trends and tendencies show that the statistical VG model approach shows sensitivity for different VG model heights, shapes, and forcing plane locations. From the examined cases, it can be concluded that all VG model parameters have an effect on the flow, yet with different importance. Especially the VG height and VG model plane position are more relevant than the actual shape of the VG model, even though figure 5 shows some sensitivity according to a delta/rectangular-shape variation.

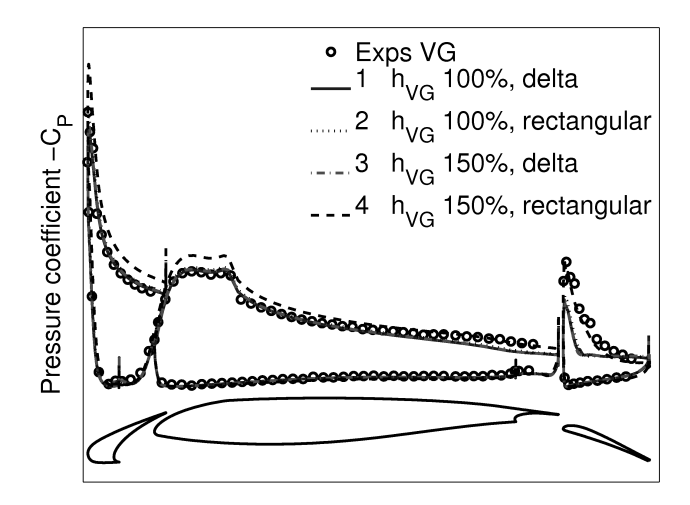


FIGURE 5. C_P distribution plots: experiments with VGs at 25% $c_{\rm base}$ and computations with different VG model configurations 1 to 4; see table 1. The VG model plane is located at $x_{\rm VG,mod}/c_{\rm flap}=4\%$ with a modelled chord length of $c_{\rm VG,mod}/c_{\rm VG,exp}=50\%$.

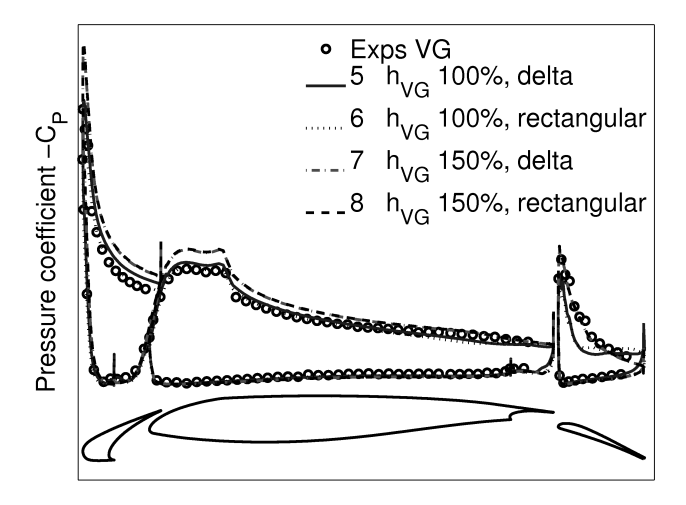


FIGURE 6. C_P distribution plots: experiments with VGs at 25% $c_{\rm base}$ and computations with different VG model configurations 5 to 8; see table 1. The VG model plane is located at $x_{\rm VG,mod}/c_{\rm flap}=8\%$ with a modelled chord length of $c_{\rm VG,mod}/c_{\rm VG,exp}=100\%$.

In total it can be said that this investigation has shown that the statistical VG model approach is very promising for an application on airfoils and has the advantage of not being more computationally expensive than solving RANS equations without modelled VGs, leading to much faster results than with conventional methods such as fully- or partly-resolved VGs.

References

- Anderson, J. D. 1991 Fundamentals of Aerodynamics, 2nd edn. New York, USA: McGraw-Hill.
- Bender, E. E., Anderson, B. H. & Yagle, P. J. 1999 Vortex Generator Modelling for Navier-Stokes Codes. *American Society of Mechanical Engineers, FEDSM* 99-6919.
- ELIASSON, P. 2001 EDGE, a Navier-Stokes Solver for Unstructured Grids. FOI Scientific Report FOI-R-0298-SE. FOI Swedish Defence Research Agency, iSSN 1650-19420.
- GLAUERT, H. 1926 The Elements of Aerofoil and Airscrew Theory, 1st edn. Cambridge University Press, London, UK.
- Hellsten, A. 2005 New Advanced $k-\omega$ Turbulence Model for High-Lift Aerodynamics. AIAA Journal 43 (9), 1857 1869.
- JIRÁSEK, A. 2005 A Vortex Generator Model and its Application to Flow Control. Journal of Aircraft 42 (6), 1486 – 1491.
- LIN, J. C. 2002 Review of Research on Low-Profile Vortex Generators to Control Boundary-Layer Separation. *Progress in Aerospace Sciences* **38**, 389 420.
- VON STILLFRIED, F., WALLIN, S. & JOHANSSON, A. V. 2009 Statistical Modeling of the Influence of Turbulent Flow Separation Control Devices. *AIAA Paper* 2009-1501.
- TÖRNBLOM, O. & JOHANSSON, A. V. 2007 A Reynolds Stress Closure Description of Separation Control with Vortex Generators in a Plane Asymmetric Diffuser. *Physics of Fluids* **19** (115108).
- Wallin, S. & Johansson, A. V. 2002 Modelling Streamline Curvature Effects in Explicit Algebraic Reynolds Stress Turbulence Models. *International Journal of Heat and Fluid Flow* **23** (5), 721 730.
- Wendt, B. J. 2004 Parametric Study of Vortices Shed from Airfoil Vortex Generators. AIAA journal 42 (11), 2185 2195.